Applications of linear plasma device studies to the improvement of power injection and handling in tokamaks

Hannah Victoria Willett

Doctor of Philosophy

University of York

Physics

June 2018

Abstract

A more advanced understanding of basic plasma physics processes is essential to the success of commercial fusion energy. Here we study two processes of considerable importance to power handling and injection in tokamak reactors, using two linear plasma devices.

Plasma detachment is vital for the reduction of heat and particle fluxes to the divertor (the exhaust region of a tokamak) below the $10\,\mathrm{MW\,m^{-2}}$ limit imposed by the material properties of the target plates. However, the physics of detachment is not fully understood. An area of particular concern is the potential influence of intermittent plasma transport perpendicular to the confining magnetic field.

In the first study, using the York Linear Plasma Device, we employ fast frame imaging and Langmuir probe diagnostics to identify fluctuations in the plasma column that are associated with the onset of detachment. Evidence is found for the intermittent outward radial transport of filamentary structures, which then cool to initiate the recombination necessary for detachment. A hypothesis suggesting the centrifugal instability as a mechanism for this transport is proposed.

The second study focuses on the potential use of helicon plasma devices as efficient, caesium-free negative ion sources for tokamak neutral beam injection (NBI) systems. A caesium catalyst is currently necessary to increase the negative ion production rate, but eliminating this is important for simplifying the maintenance requirements of these sources.

We examine the negative ion population behaviour in the helicon device MAGPIE. Peak densities of $1.25\times10^{18}\,\mathrm{m^{-3}}$ (an order of magnitude above the required NBI threshold) are measured using laser photodetachment, and a simple model of the time evolution of the negative ion population is in agreement with the experimental data. Neutral depletion is proposed as a mechanism governing the evolution of the plasma, and is consistent with additional experimental and simulation results.

Contents

List of Figures

List of Tables

List of Accompanying Material

Acknowledgements

Firstly, thanks go to my supervisor, Kieran Gibson, for continued guidance and support throughout my PhD, even when stretched across campus, and then over eight time zones. I have also benefited from the input of and discussion with the other members of my Thesis Advisory Panel, Christian Diget and Bruce Lipschultz. In Australia, thanks are due to Cormac Corr, my mentor during my time at the Australian National University, and to Jesse Santoso, with whom I worked closely throughout the collaboration.

Secondly, this research would not have fallen into place without the continual technical support provided by numerous staff at both institutions. In particular I am grateful to Richard Armitage, Andy Vick and Kari Niemi at the University of York, and Michael Blacksell and Amy Shumack at ANU.

Finally, I owe a huge thank you to my husband, parents, brother, family and friends for their unwavering belief in me: without them, navigating the successes and sticky patches of the past four (and more) years would have been a lot harder.

Declaration

I declare that this work has not previously been presented for an award at this, or any other, University. All sources are acknowledged as References. This thesis is a presentation of original work undertaken at the University of York under the supervision of Prof. K. J. Gibson (of which I am the sole author), and at the Australian National University, under the supervision of Dr. C. S. Corr and in collaboration with J. Santoso. This collaborative work is clearly labelled as such, and is presented in Chapter 6.

Some parts of this thesis have been published in conference proceedings and journals. The work presented in Chapters 4 and 5 was developed from the initial material presented in (a), and that in Chapter 6 from (b). Figure 2.9 is the work of the author of this thesis, and has been previously published in (c).

(a) H. V. Willett, K. J. Gibson and P. K. Browning. The role of plasma instabilities in the onset of detachment in the York Linear Plasma Device. In *Proceedings of the 43rd EPS Conference on Plasma Physics*, page P2.042, July 2016 [1].

(b) H. V. Willett, J. Santoso, C. S. Corr and K. J. Gibson. Negative ion studies on the RF plasma device MAGPIE. In *Proceedings of the 44th EPS Conference on Plasma Physics*, page P2.402, July 2017 [2].

(c) J. Leddy, B. Dudson, H. V. Willett. Simulation of the interaction between plasma turbulence and neutrals in linear devices. In *Nuclear Materials and Energy*, Volume 12, pages 994–998, August 2017 [3].

Chapter 1

Introduction

The need for nuclear fusion arises from the environmental problems caused by the continually increasing energy demands across the planet. The fossil fuels that we currently burn are finite resources, and are contributing to the emission of greenhouse gases into the atmosphere. Conventional renewable energy solutions, such as wind and solar power, are less reliable for baseload electricity supplies than fossil fuel plants, and nuclear fission plants produce radioactive waste that requires long-term storage. Fusion has the potential to provide a continual source of clean energy that could work alongside other renewables to fulfil our energy requirements for thousands of years into the future. However, there are still a number of issues that need to be addressed in both plasma physics and materials science before commercial fusion power plants can become a reality.

1.1 Fusion energy

Nuclear fusion is the process that fuels stars, through the 'burning' of lighter elements to create heavier elements. In general, the process involves two reactant nuclei fusing together to create a larger nucleus, plus a smaller particle such as a neutron. The total mass of the products is slightly less than that of the reactants, with the excess mass converted to energy (manifested as kinetic energy of the products). The most fundamental reactions in stars occur between protons (hydrogen nuclei), but stellar fusion goes on to involve progressively heavier elements until the most stable element, iron-56, is formed.

Fusion in stars relies on the compression of extremely large masses of fuel by gravitational forces, and occurs over million-year timescales. Clearly this is inappropriate for terrestrial fusion reactors, and alternative reactions and confinement methods must be ex-

plored. The most probable reaction at realistically achievable conditions is that between deuterium and tritium [4]:

$$^{2}_{1}\mathrm{D} + ^{3}_{1}\mathrm{T} \rightarrow ^{4}_{2}\mathrm{He}\,(3.5\,\mathrm{MeV}) + \mathrm{n}\,(14.1\,\mathrm{MeV}).$$

The products of this reaction are an alpha particle (the helium nucleus), which is trapped and acts to heat the remaining fuel, and a high-energy neutron. The neutron escapes the reaction region and is then slowed down, converting its energy to heat to produce electricity via steam (as in conventional power plants).

The neutrons will also be used to breed more tritium fuel for the reactor. Deuterium is sufficiently abundant in water (33 mg in every litre of seawater [5]) to provide an almost inexhaustible supply, but tritium is an unstable isotope, with a half-life of 12.3 years. It will therefore be necessary for a reactor to create its own tritium supply, currently intended to be done using tritium 'breeder blanket' modules surrounding the vacuum vessel. The breeder blanket will contain lithium, which reacts with neutrons to produce tritium:

$$^{6}_{3}\mathrm{Li} + \mathrm{n} \rightarrow ^{4}_{2}\mathrm{He} + ^{3}_{1}\mathrm{T} \qquad +4.8\,\mathrm{MeV};$$

$$^{7}_{3}\mathrm{Li} + \mathrm{n} \rightarrow ^{4}_{2}\mathrm{He} + ^{3}_{1}\mathrm{T} + \mathrm{n} \qquad -2.5\,\mathrm{MeV}.$$

Lithium is also an abundant resource, with proven land-based resources estimated to contain 1000 years' supply, and the potential to extract enough from seawater to last for millions of years [5].

In order to undergo fusion reactions, the nuclei must be able to overcome electrostatic repulsion and approach each other closely enough for the strong force interaction to dominate. This requires high energies (in the keV range), pushing the fuel into the plasma state. Plasma is the fourth state of matter, occurring when gas is heated to a high enough temperature to ionise the neutral atoms. The result is a gas composed of positive ions and electrons, and in some plasmas, negative ions as well. A general definition is given by Chen: "A plasma is a quasineutral gas of charged and neutral particles which exhibits collective behaviour" [6].

The fundamentals of plasma physics are covered in detail by Chen [6]; here we briefly discuss the defining features of a plasma. Firstly, "collective behaviour" refers to the long-range forces from the electromagnetic fields that arise from the motion of the charged particles in a plasma. Particles in one area are influenced by the fields produced by more remote regions in the plasma, not just the local conditions. This leads to extremely complicated behaviour and makes plasma physics a complex field to study.

The quasineutrality property stems from the concept of Debye shielding: the movement of plasma particles to reduce the effects of an applied external potential. The length scale of plasma shielding is given by the Debye length:

$$\lambda_{\mathrm{D}} = \sqrt{\frac{\varepsilon_0 T_{\mathrm{e}}}{e n_\infty}}, \tag{1}$$

where n_∞ is the bulk plasma density and T_{e} is the electron temperature in eV. This expression for λ_{D} is derived by solving Poisson's equation for the potential in the presence of an external charge. We assume that the electrons have a density determined by a Boltzmann factor, and dominate the shielding as they are much more mobile than the ions [6]. If $\lambda_{\mathrm{D}} \ll L$ (the length scale of the system), the shielding occurs in a region small compared to the size of the plasma, and no large electric fields can be applied to the bulk plasma, where the electron and ion densities are equal (generally to better than one part in 10^6 [6]). This gives rise to the concept of quasineutrality on large scales, where it can be approximated that $n_{\mathrm{i}} \simeq n_{\mathrm{e}} \simeq n_\infty$, but on the scale of λ_{D} the plasma is not perfectly neutral and electromagnetic forces are still able to exist.

A second condition for an ionised gas to be termed a plasma is that there must be sufficient particles in the shielding region for Debye shielding to be effective. This is quantified by requiring the number of particles, N_{D}, in a sphere of radius λ_{D} to be large:

$$N_{\mathrm{D}} = \frac{4}{3}\pi {\lambda_{\mathrm{D}}}^3 n \gg 1. \tag{2}$$

Finally, we consider collisions. If the charged particles collide frequently enough with neutral particles, the dominant forces controlling their motion will be hydrodynamic rather than electromagnetic [6]. We therefore require the collisional timescale (given by the mean time between collisions, τ) to be larger than the timescale of plasma behaviour. To characterise the latter, we use the frequency of plasma oscillations, $\omega = \sqrt{ne^2/\varepsilon_0 m_{\mathrm{i}}}$, leading to the third condition for a plasma: $\omega\tau > 1$.

Given the high energies and densities required to put the fuel into the plasma state and allow fusion to occur, confining the plasma presents complex technological challenges. The two common research approaches are inertial confinement fusion (ICF) and magnetic confinement fusion (MCF). There is a key condition which must be fulfilled in order to ignite fusion reactions, irrespective of which method is used. This condition (the Lawson criterion) constrains the magnitude of the fusion 'triple product': the product of the plasma density, n, plasma temperature, T, and the energy confinement time, τ_{E}, which characterises the timescale on which energy is lost from the core plasma. The Lawson

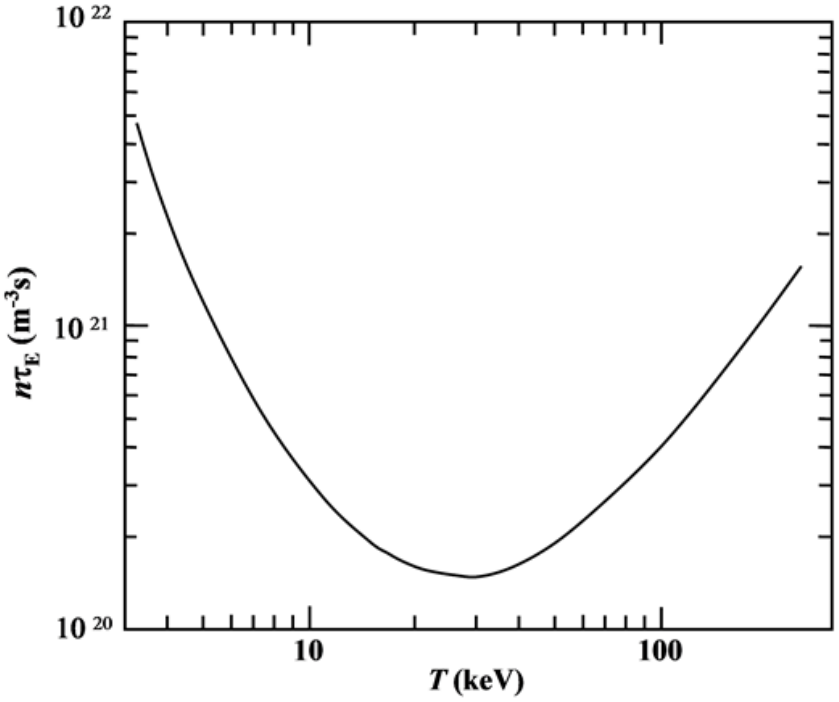

Figure 1.1: The value of $n\tau_{\mathrm{E}}$ required to obtain ignition for deuterium-tritium fusion, as a function of T. Reproduced from [4].

criterion is illustrated in Figure 1.1, which shows $n\tau_{\mathrm{E}}$ as a function of T. For a temperature range of $10 - 20\,\mathrm{keV}$ (close to the minimum of the Lawson criterion, and a reasonable goal for an MCF reactor), the condition for fusion ignition reduces to [4]:

$$nT\tau_{\mathrm{E}} > 5 \times 10^{21}\,\mathrm{m}^{-3}\,\mathrm{keV\,s}. \tag{3}$$

In ICF research, multiple lasers are focused onto a small fuel pellet to compress and heat it (see e.g. [7]). There is no confinement other than that provided by the material's own inertia, so τ_{E} is small, of the order of nanoseconds or less. Hence the densities and temperatures achieved by the laser compression must be extremely large (up to around $10^{30}\,\mathrm{m}^{-3}$ and $100\,\mathrm{keV}$ respectively once ignited). MCF, on the other hand, aims to confine the plasma on much longer timescales (on the order of seconds) using shaped magnetic fields. The most common configuration is a toroidal vacuum vessel, known as a tokamak. The largest tokamak in operation, the Joint European Torus (JET), is illustrated in Figure 1.2. With an extended confinement time, the plasma does not need to be as dense as in ICF experiments: values in the range $10^{19} - 10^{20}\,\mathrm{m}^{-3}$ are sufficient. It is MCF that the research in this thesis focuses on.

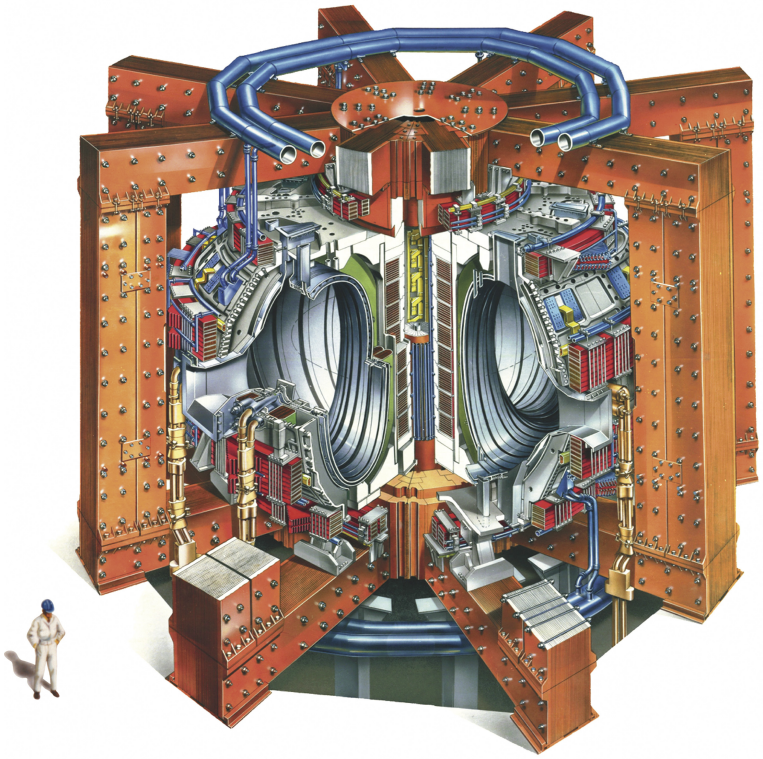

Figure 1.2: Cutaway illustration of the Joint European Torus (JET), at the Culham Centre for Fusion Energy, UK [8].

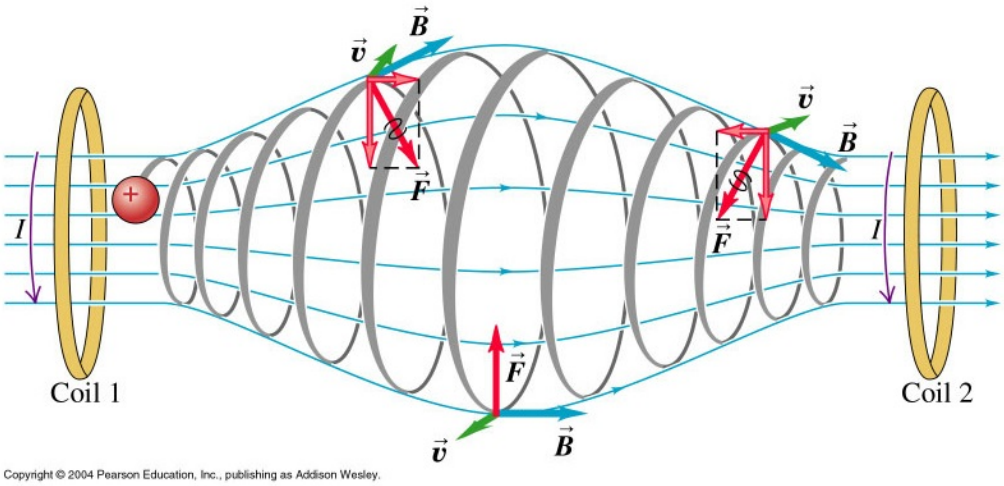

Figure 1.3: Illustration of the magnetic mirror configuration. The higher field strength at either end reflects all particles with a low enough velocity parallel to the field lines (indicated by the forces $\overrightarrow{F}$) [9].

Magnetic confinement of plasma has developed considerably over the years, from linear configurations to the toroidal geometry seen in tokamaks now. Linear confinement is based on the 'magnetic mirror' concept, shown in Figure 1.3. Charged particles are confined to helical paths around the field lines, and if their velocity parallel to the field line is low enough, they are reflected by the high-field regions. However, the more energetic particles are able to escape the mirror, and as the plasma is not perfectly collisionless, energy is transferred between particles and the plasma losses are significant.

The natural progression is to bend the magnetic mirror around to form a closed tube of plasma with toroidal field lines, thus preventing end losses. This introduces further complications, however, as the resulting gradient and curvature of the magnetic field lead to particle drifts [6]. Not only do these drifts directly degrade plasma confinement, but the dependence of the drift direction on the particle charge causes a charge separation in the plasma, creating electric fields which reduce confinement further. In order to counteract this, a small poloidal field component is added by both using more magnetic field coils and driving a toroidal current through the plasma.

This toroidal configuration with helical field lines is the basis of the tokamak, and is illustrated in Figure 1.4. This diagram shows the core plasma confinement region in pink. In the core region, the field strengths are chosen to ensure that the field lines eventually close on themselves as they wind around the tokamak. This creates surfaces of constant magnetic flux, nested within one another. In a collisionless plasma, the plasma particles would be perfectly confined to a flux surface and there would be no losses. In reality there are collisions, which together with turbulence cause plasma to be lost from the core confinement region. Outside the core plasma, the field lines are no longer closed, and eventually intersect the walls of the vacuum vessel. The structure outside the core will be discussed further in Section 1.3.

Magnetically confined fusion in tokamaks was first studied in the USSR in the 1950s (see e.g. [10]). These early experiments obtained plasma temperatures on the order of 1 keV [11], and in the past six decades, research has progressed considerably. Energy confinement times of over a second have been attained in JET, which also holds the record for the most fusion power (16.1 MW) achieved from a D-T pulse [12]. Figure 1.5 shows the progress that has been made towards reaching the $nT\tau_{\mathrm{E}}$ threshold given in (3), through research on multiple tokamak experiments around the world. The next stage in this research is ITER (projected $nT\tau_{\mathrm{E}}$ value shown in red in Figure 1.5), a global project

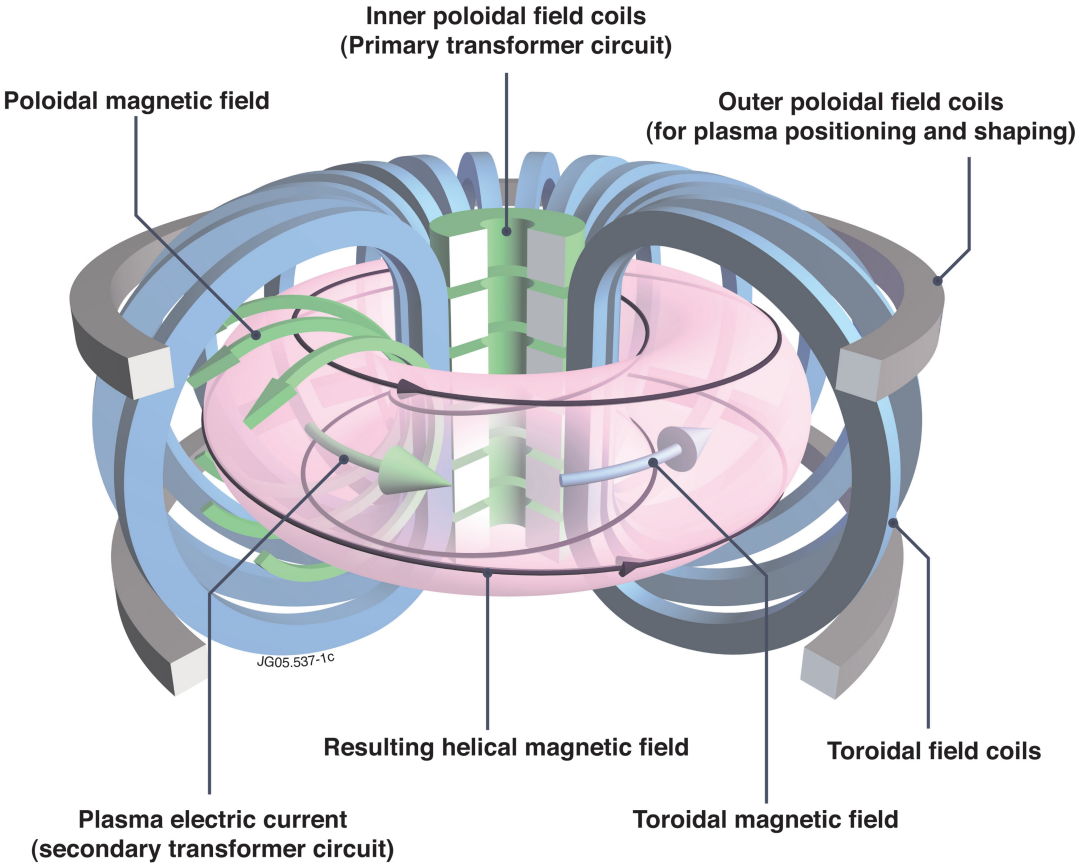

Figure 1.4: Diagram of the key features of a tokamak. The plasma is contained in a vacuum vessel (not shown) in the pink region. The confining helical magnetic field (black arrows) is produced by the toroidal and poloidal field coils, and also contains a contribution from the plasma current (toroidal green arrow) that is driven by the inner poloidal field coils [8].

designed to be the largest tokamak in the world [5]. It will be an experimental reactor that aims to test concepts for a demonstration fusion power plant, and has been designed to achieve 'breakeven', i.e. produce more energy from fusion reactions than must be supplied to ignite and sustain them.

The progress that has been made in the design and construction of tokamaks has predominantly been achieved by increasing the size of the tokamak. However, this introduces further significant problems: how to provide enough energy to ignite the fusion plasma, and how to deal with the huge amount of power that is produced.

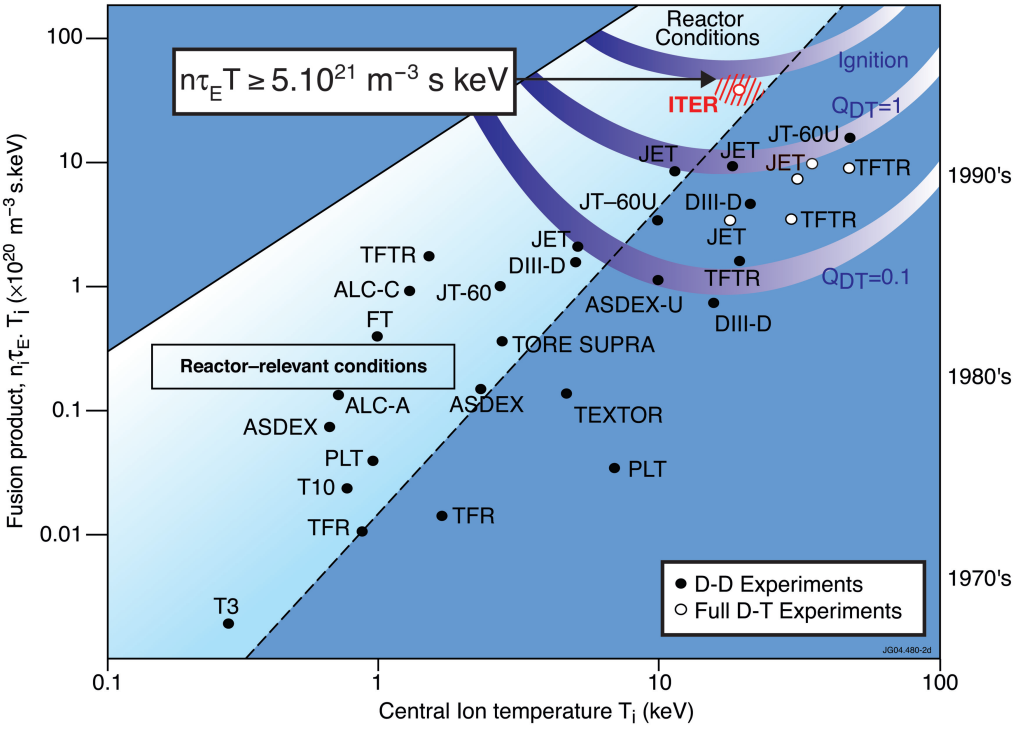

Figure 1.5: The progress that has been made over the years, using various tokamaks around the world, to meet the required $nT\tau_{\mathrm{E}}$ threshold for fusion ignition. The projected values for ITER are shown in red [8].

1.2 Power injection in tokamaks

A considerable amount of energy is required in order to create the plasma in a tokamak and initiate fusion reactions: ITER will require around 50 MW of heating power to produce 500 MW of fusion power over pulse lengths of up to 600 s [5]. The three main methods of heating a plasma are ohmic heating, microwave injection and neutral beam injection (NBI). Ohmic heating relies on inducing a current in the plasma by ramping the current through a central solenoid (cf. a transformer), and is therefore limited in both magnitude and duration by the maximum current that can be achieved. An estimate of the ohmic heating capability for ITER is an initial ramp of power up to 10 MW [13].

Injection of microwaves (RF heating) and neutral particles (NBI) can provide much higher power input over a sustained period. The RF heating systems for ITER are planned to provide up to 40 MW of power, and the NBI systems up to 33 MW, with the potential for future upgrades to add up to a further 50 MW of power [14]. These methods can be used to supply energy to the plasma as part of the initial start up phase, and during

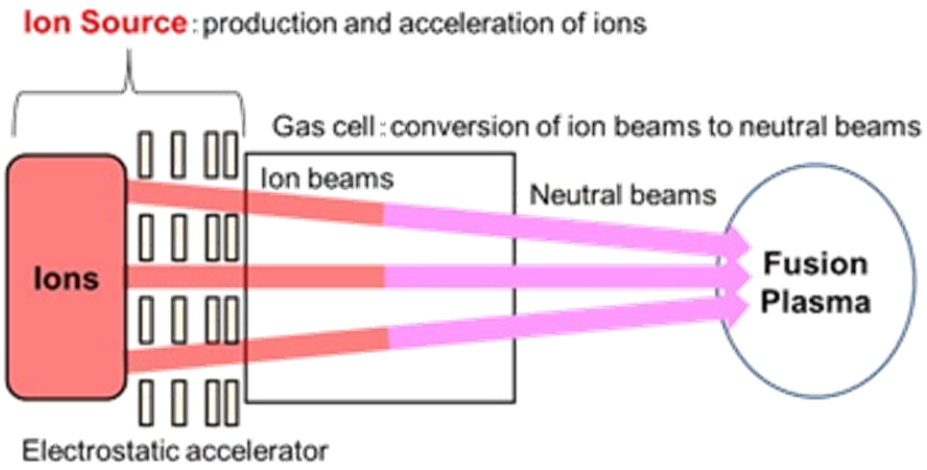

Figure 1.6: Schematic diagram of the main components of a neutral beam injection system for a tokamak fusion plasma [16].

operation if additional heating is required to sustain the fusion reaction. NBI is also able to refuel the plasma, as the neutral beams are formed from deuterium (hydrogen in some experimental campaigns), and can drive additional toroidal current around the tokamak.

The technology for these systems is sufficiently advanced to be implemented in the design for ITER, but there is room for further development (particularly in NBI) to improve efficiency for future tokamak reactors. NBI systems accelerate ions from a plasma source to form a high energy beam, which is then neutralised to produce the beam that is injected into the tokamak [15]. A schematic diagram of a typical NBI system is shown in Figure 1.6.

The deuterium beam energy required to both heat and drive current in a large tokamak such as ITER is in excess of 1 MeV [15]. These high energies are needed to allow the neutrals to reach the core of the fusion plasma, and to increase the efficiency of the current drive [17]. Either positive or negative ions can be used in NBI systems, and the selection is made based on the achievable rates of production and neutralisation.

In the case of the production rates, positive ions are more advantageous: standard plasma sources typically predominantly generate positive ions and electrons. In contrast, a caesium catalyst must be used to create a sufficient number of negative ions [18]. The catalyst is applied to a grid within the source to improve the rate of negative ion production via surface processes on the grid. The use of caesium increases both cost and safety concerns due to its high reactivity and the need to regularly replace it.

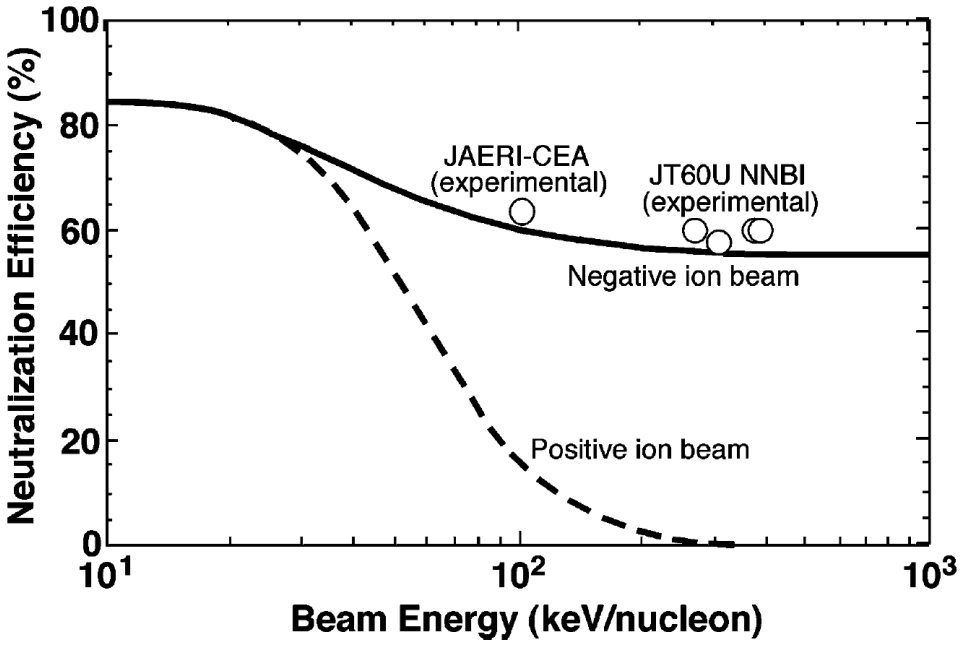

Figure 1.7: Variation of the neutralisation efficiency of negative (solid line) and positive (dashed line) hydrogen ions with energy. Circles show experimentally obtained efficiencies for negative ions. Reproduced from [17].

Figure 1.7 shows the effect of increasing the beam energy on the neutralisation efficiency for both positive and negative hydrogen ions. The efficiency for positive ions drops below 15 % at $\sim$ 100 keV, whereas that for negative ions does not reduce below 55 %. It is clear that negative ions are most appropriate to create the required high energy beams. This far outweighs the disadvantages of needing a catalyst for negative ion production, and caesiated negative ion sources are planned for ITER [15]. However, an ideal NBI source would be able to maintain a high production rate without the use of caesium, and the development of an alternative, caesium-free solution would be extremely beneficial in improving the overall efficiency of a fusion power plant.

1.3 Power handling in tokamaks

The amount of fusion power produced by a tokamak scales with the volume of the plasma; that is, it is roughly proportional to R^3, where R is the major radius of the tokamak (the distance from the central axis to the centre of the plasma), assuming that the power density remains constant. Since confinement of the plasma is not perfect, and additional heating will be required to start up and sustain the fusion reaction, not all of this power

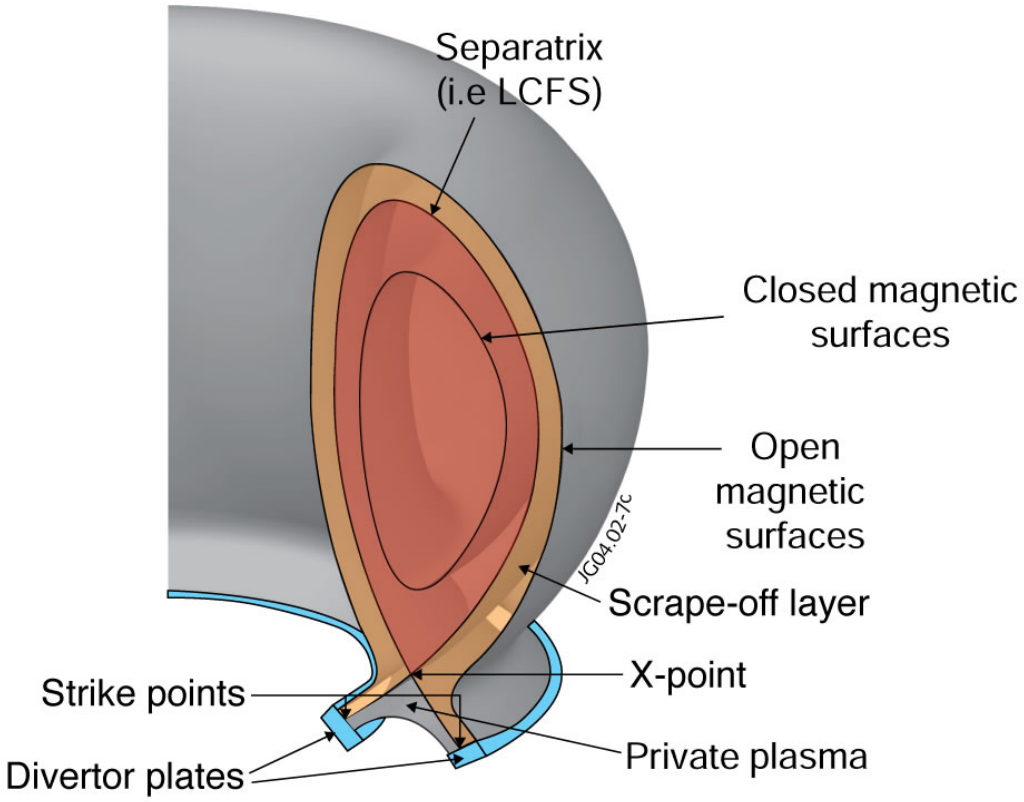

Figure 1.8: Cross-section through the magnetic flux surfaces in JET. The core plasma region, with closed magnetic flux surfaces, is represented in dark orange. The scrape-off layer, or SOL, is outside the last closed flux surface (LCFS, also called the separatrix) and is shown in light orange [8].

will be converted to electricity and there will be a considerable amount of 'exhaust' power. How to handle this without causing extensive damage to the walls of the tokamak is one of the key problems in fusion research.

Currently, exhaust power is handled using a 'diverted' tokamak configuration (illustrated in Figure 1.8). In Section 1.1 we introduced the concept of closed magnetic flux surfaces in the core plasma region, and open field lines outside the core which eventually intersect the walls of the vacuum vessel. This configuration is achieved by additional field coils at the bottom and/or top of the tokamak, which create magnetic nulls below/above the core plasma. The configuration in Figure 1.8 shows a lower single null, which will be used as the example in this discussion. The last closed flux surface, or separatrix, defines the edge of the core plasma region and contains the magnetic null, known as the X-point.

The plasma outside the separatrix is called the scrape-off layer (SOL), and in this region the field lines continue to wind helically around the tokamak until they meet the vacuum vessel wall. The exhaust power is transported out of the core of the tokamak into the SOL by the plasma particles that move across the confining magnetic flux surfaces. For the lower single null (illustrated in Figure 1.8), the field is designed so that the plasma is carried down to the bottom of the tokamak (known as the divertor), where the majority of the plasma-wall interactions occur in the vessel. The power transported into the SOL (P_{SOL}) for JET can range between $2 - 12\,\mathrm{MW}$ [19], whereas in ITER P_{SOL} is expected to be around $80\,\mathrm{MW}$ [20].

The power flux to the divertor plates depends on both P_{SOL} and the 'wetted area' (the area of the divertor plate which is impacted by the plasma). The latter is given by $A = 2\pi R\lambda_q$, where λ_q is the fall-off length of the power in the scrape-off layer. The scaling of λ_q in a tokamak has been determined to vary most strongly with the poloidal magnetic field, B_{pol}, with a small dependence on P_{SOL} and no dependence on R [19]:

$$\lambda_q \propto {B_{pol}}^{-0.8}\ {P_{\mathrm{SOL}}}^{0.1}\ {R}^{0}.$$

λ_q for JET is in the region of $1 - 2\,\mathrm{mm}$, and the scaling predicts that λ_q in ITER will be $\sim 1\,\mathrm{mm}$ [19]. The area, A, therefore scales with R, but we have already seen that the power will increase as R^3. The potential maximum divertor heat flux thus increases with tokamak size: example values are $500\,\mathrm{MW\,m^{-2}}$ for JET, and over $2\,\mathrm{GW\,m^{-2}}$ in ITER.

It is imperative that the divertor plates are able to withstand these high heat loads for a reasonable operating period before a maintenance shut-down is required. Current research suggests that the most appropriate material for the divertor plates is tungsten, but the acceptable steady-state power flux limit for a viable component lifetime is still only $10\,\mathrm{MW\,m^{-2}}$ [20, 21]. In the relatively small tokamaks that are currently operational (such as JET), there are methods of mitigating the heat flux to reduce it to a reasonable level. These measures all aim to spread the power load over an increased area, and include: angling the surface of the plates relative to the field lines; creating a region of flux expansion of the field lines next to the divertor; and sweeping the plasma strike point over the divertor plates by changing the magnetic field profile [4].

Some of these measures will be employed in ITER (for example angled divertor target plates), but the size of the machine means that they will be insufficient to reduce the $2\,\mathrm{GW\,m^{-2}}$ flux below the $10\,\mathrm{MW\,m^{-2}}$ limit. Commercial reactors are likely to be even bigger, with P_{SOL} for a large, $3\,\mathrm{GW}$ reactor estimated to be around $600\,\mathrm{MW}$ [4]. It is there-

fore essential to find further methods of limiting the divertor heat flux in order to ensure that the component lifetime is long enough. Offline maintenance periods will necessarily be relatively long, as working inside the large vacuum vessels is not straightforward, particularly once tritium (a radioactive element) has been introduced and the wall materials have become activated through neutron irradiation. Maintenance requirements must be carefully managed in order to reduce the impact on the production capacity.

One method of reducing the exhaust power flux, which will be implemented on ITER, is that of plasma detachment from the divertor plates. To achieve detachment, the neutral density in the divertor region (away from the core) must be high enough to cause significant cooling of the plasma through ion-neutral friction. This creates a low enough plasma temperature for recombination processes to occur, neutralising a high proportion of the plasma that would otherwise impact the plates over a relatively small area. In addition, the excited neutral products radiate energy over 4π steradians in the form of photons, and the rate of divertor damage decreases. The recombination can occur simply when the core density in a tokamak is increased to a sufficiently high level (as was achieved in the ASDEX tokamak, Figure 1.9 [22]), but can also be caused by injecting neutral gas (e.g. hydrogen or nitrogen) into the divertor region.

The physics of detachment will be discussed further in Chapter 2. Note that, while the phenomenon was first studied around forty years ago [24], the processes involved are still not fully understood. In particular, there has been little work that focuses on the relationship between the onset of detachment and the radial transport and instabilities present in the plasma.

1.4 The role of basic plasma experiments

Experimental tokamaks exist around the world and form the basis of a considerable proportion of experimental research into MCF: developing operation scenarios, testing component designs and increasing our knowledge of the plasma physics phenomena behind the observations. However, the toroidal geometry of a tokamak is not straightforward to study, and diagnostic access into the machines is limited. It is helpful to support tokamak research with studies carried out on basic plasma experiments, built to replicate certain aspects of tokamak plasma physics. These machines are generally constructed with a linear geometry, reducing the complexity of the problem, and have more diagnostic accessibility than tokamaks.

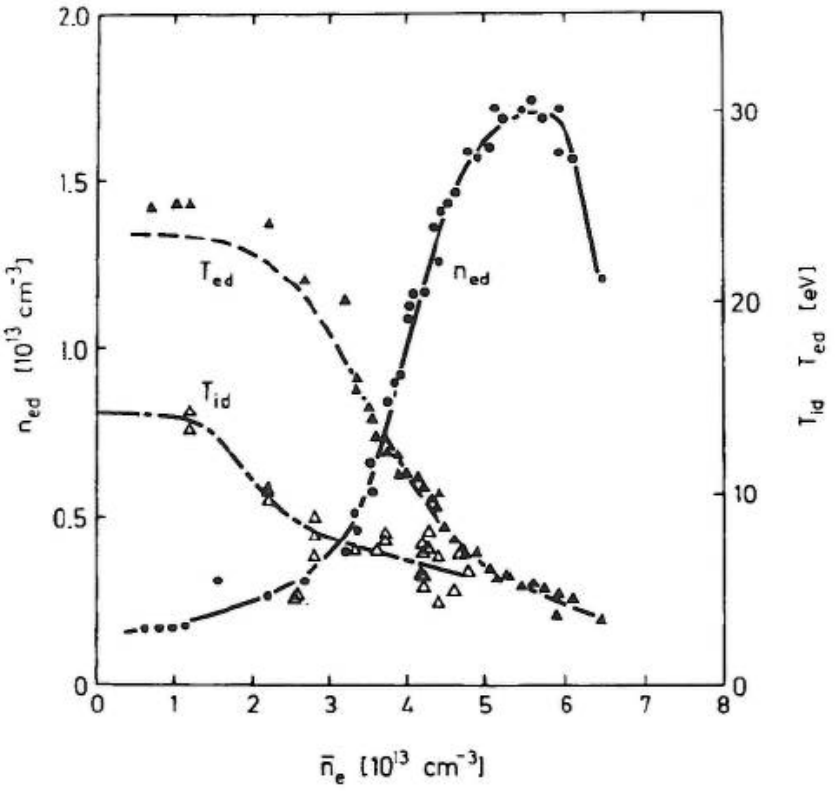

Figure 1.9: Divertor target density (n_{ed}, left-hand axis) and temperature (T_{id} and T_{ed}, right-hand axis) data from the ASDEX tokamak, plotted as a function of density in the core plasma ($\overline{n}_e$). The target density 'rollover', where n_{ed} begins to decrease at high core densities (from approximately $5.5 \times 10^{13}\,\mathrm{cm}^{-3}$), is characteristic of the reduction in particle flux to the divertor surface as the plasma undergoes detachment in the vicinity of the divertor (discussed further in Section 2.1.3). Original data from [22]; figure reproduced from [23].

A primary focus of research on many basic plasma devices is the interaction between plasma and material surfaces; for example the effects of deuterium irradiation on tungsten samples in Magnum-PSI [25] and PISCES-A [26]. Fuel retention in the reactor wall will be a major consideration, as there is a limit to the amount of tritium permitted to be on site, and unreacted tritium will need to be recycled back into the core plasma. Another key aspect is the amount of damage caused by transient events in the plasma such as edge localised modes (ELMs). These events can temporarily increase the power fluxes to as much as $10\,\mathrm{GW\,m^{-2}}$ (the projection for ITER), and studying the effects of this (for example in Magnum-PSI [27]) is an important task.

Development of diagnostics is made much more straightforward by utilising linear plasma devices. Experimental time is in demand on tokamaks, and it is more efficient to develop and test instruments on smaller machines before implementing them on tokamaks. Two examples are the development of a vorticity probe on the Large Plasma Device (LAPD) [28], and using fast imaging measurements to extract information about coherent waves in the plasma in CSDX [29].

CSDX has also been used to study turbulence in plasma flows, including transitions between turbulent states and those that exhibit shear flow (see e.g. [30, 31]). This has important applications to confinement in tokamaks. It has been suggested that shear flows in the boundary region of the plasma play a role in the appearance of the high-confinement, or H, mode, which produces more favourable conditions for fusion [32]. Turbulence and other plasma instabilities such as drift waves have been studied in other machines such as Mirabelle [33] and Mistral [34]. Mistral has also been used to look at plasma recombination for simulations of a detached divertor [35].

The most common way to induce plasma recombination for detachment studies, particularly in linear devices, is to use neutral gas puffing (see Chapter 2). The York Linear Plasma Device (YLPD) is one of several basic plasma devices capable of studying detachment in this way. Examples of previous detachment studies on linear machines will be discussed in Chapter 2, and research using the YLPD forms the major focus of this thesis.

A final application of basic linear machines is to power injection in tokamaks. Neutral beam injection (NBI) systems use compact plasma sources to produce the negative ions they require. Research is ongoing in order to improve the efficiency of these sources and develop a caesium-free alternative, for which basic plasma devices are invaluable. One potential solution is the use of a helicon plasma source, such as the Magnetised Plasma Interaction Experiment (MAGPIE). A study of the negative ion population in MAGPIE and its applications to NBI is presented in Chapter 6.

1.5 Thesis outline

This thesis is structured as follows. Chapter 2 introduces the physics of the tokamak power handling issue and discusses previous research in tokamaks and linear devices. The first section describes the scrape-off layer of a tokamak and the transportation of particles and heat from the core to the divertor, focusing on the processes involved in detachment. The second and third parts of this chapter outline some of the detachment research that

has been undertaken both in tokamaks and linear plasma machines. Chapter 3 introduces the YLPD, and the diagnostic techniques that were employed in the detachment study presented in this thesis.

Chapter 4 provides a detailed review of the previous work on detachment using the YLPD, and presents the author's own work in replicating the detached state in the machine. The third section of this chapter identifies the key research topic to be addressed: an improved understanding of the radial structure of the detached plasma in the YLPD. Chapter 5 discusses the experimental observations and analyses carried out to search for evidence of radial transport in the detached plasma in the electron-ion recombination regime, using fast frame imaging and high frequency measurements of the floating potential. Based on these results, a hypothesis for the mechanism behind the observed behaviour is presented.

Chapter 6 returns to the issue of power injection. The first section recaps the motivation for studying the negative ion population in MAGPIE, and the diagnostic methods used are described in the second part. The results of the investigation are then presented. Finally, in Chapter 7 the overall conclusions of this thesis are drawn, and the possibilities for extension of these studies are outlined.

Chapter 2

Scrape-off layer and detachment physics

This chapter discusses the physics underlying the behaviour of the scrape-off layer plasma as it transitions between operation regimes, focusing on detachment in Section 2.1.3. Following this, an overview of some of the key research concerning detachment on both tokamaks (Section 2.2) and linear plasma devices (Section 2.3) is provided, highlighting the gaps in current understanding. A summary is given in Section 2.4.

2.1 The scrape-off layer

As was seen in the previous chapter (Section 1.2), the scrape-off layer, or SOL, is the channel through which all unconfined plasma flows in order to reach the exhaust region, or divertor. For convenience, Figure 1.8, depicting the tokamak SOL, is reproduced in Figure 2.1. The behaviour of the SOL plasma can follow one of several regimes, depending on the plasma parameters both upstream (feeding into the SOL) and downstream (at the divertor target). Broadly, an increase in the upstream density causes the SOL to pass from the sheath-limited regime through the conduction-limited and high-recycling regimes, to eventually reach a state of detachment. This was illustrated by data from the ASDEX tokamak in Figure 1.9 in the preceding chapter. A key distinguishing property between these regimes is the "existence or absence of a significant temperature drop along the length of the SOL", as described by Stangeby, and the collisionality of the plasma plays an important role in determining this [23]. In this section, an overview of the four SOL regimes is given, following Stangeby's guide (see [23]) unless otherwise referenced.

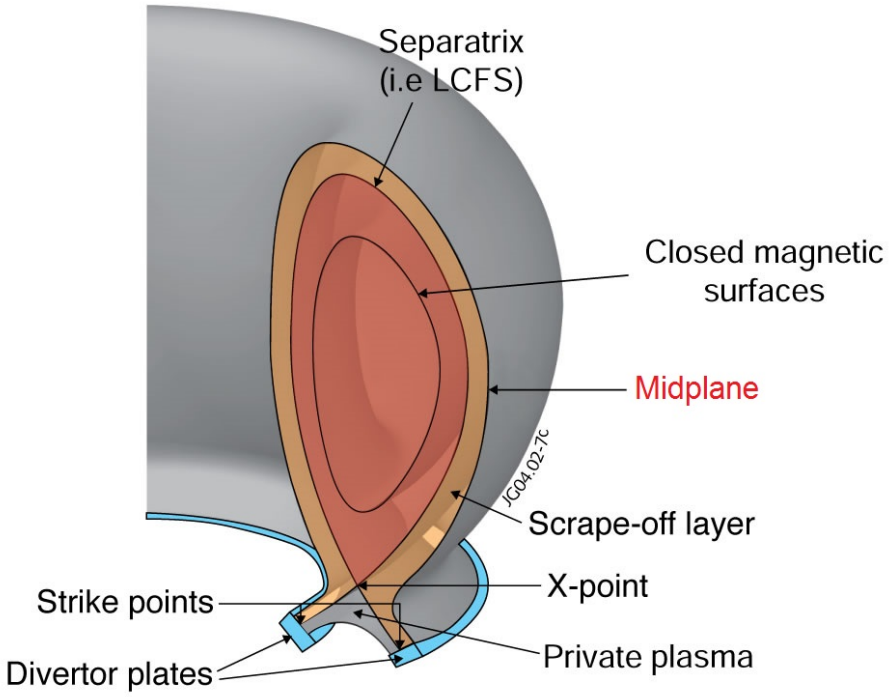

Figure 2.1: Reproduction of Figure 1.8, showing the magnetic flux surfaces in JET. The midplane of the tokamak is now labelled in red. One-dimensional models of the SOL (light orange region) 'straighten out' the section between the midplane and the divertor plate (Section 2.1.1). Diagram adapted from [8].

2.1.1 Sheath-limited regime

A scrape-off layer in the sheath-limited regime can also be termed a 'simple SOL', as a number of assumptions are made. The characteristics of a simple SOL are as follows:

1. Constant electron and ion temperatures along each flux tube;
2. Electrons and ions are thermally decoupled, and both are Maxwellian;
3. No ionisation in the SOL (cross-field transport provides the only source of particles);
4. No volumetric recombination, neutral friction or radiative cooling (the sheath at the target provides the only sink for both heat and particles).

The sheath in question refers to the region close to a material surface that is put in contact with a plasma: in this case, the divertor plates. The presence of the surface alters the plasma properties on a length scale given by the Debye length, λ_D, introduced in (1), Chapter 1.

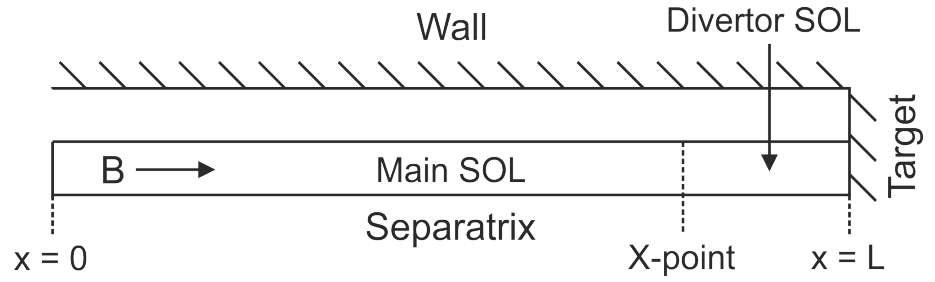

Figure 2.2: Schematic of the 'straightened-out' scrape-off layer plasma used for 1D SOL analyses (not to scale). $x = 0$ corresponds to the 'upstream' position (the midplane of the tokamak, indicated in Figure 2.1). Diagram adapted from [23].

To describe the sheath qualitatively, we first consider an isotropic, homogeneous plasma. The particle flux crossing unit area per unit time is given by $\Gamma = \frac{1}{4} n \bar{v}$ for both electrons and ions. Even if the species densities ($n_{\mathrm{i,e}}$) are equal and it is a thermal plasma (so the electron and ion temperatures are similar), the electron flux through an arbitrary plane will be greater than the ion flux, as the smaller electron mass increases their average speed, $\bar{v}$. Therefore the initial electron flux to a surface will be larger than the ion flux and the surface will become negatively charged with respect to the plasma. The plasma in the local region then adjusts to prevent the effects of this negative charge from penetrating into the bulk plasma. The fluxes to the surface are altered and the result is a shielding region around the surface (the sheath), which decays on the scale of λ_{D}.

The mathematical description of the physics of the sheath-limited SOL is discussed in multiple sources with varying degrees of complexity (e.g. [23, 36]), and Appendix A gives details of a simple derivation of the main results. The 1D sheath analysis is based on the concept of 'straightening out' the SOL, from an 'upstream' position to the divertor target (illustrated in Figure 2.2). Here we define 'upstream' as the midplane of the tokamak, as shown in Figure 2.1, but it can also be taken to be the midpoint between the two divertor plates (at the top of the tokamak). In simple SOL analyses the difference is negligible.

Sketches of the plasma density and temperature profiles in a 1D sheath-limited SOL are shown in Figure 2.3 (further details in Appendix A). The ion flux to the surface is:

$$\Gamma_i = \frac{1}{2} n_0 c_s, \tag{4}$$

where n_0 is the upstream plasma density and $c_s = \sqrt{kT_{\mathrm{e}}/m_{\mathrm{i}}}$ is the ion sound speed. This result is obtained by considering conservation of flux ($\Gamma = nv$) at the sheath edge; see Appendix A, (A.20) and (A.24), for details.

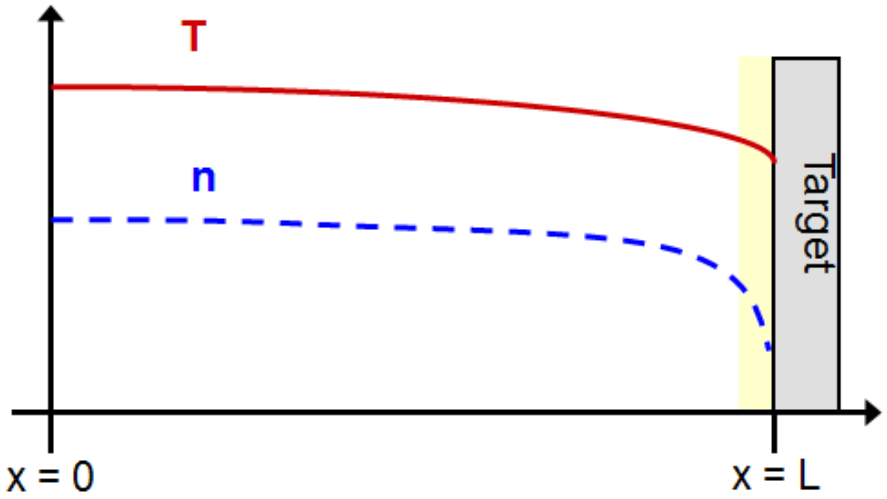

Figure 2.3: Approximate profiles of the plasma density, n, and temperature, T, throughout the SOL in the sheath-limited regime. The sheath region (not to scale) is shaded yellow. Diagram adapted from [37].

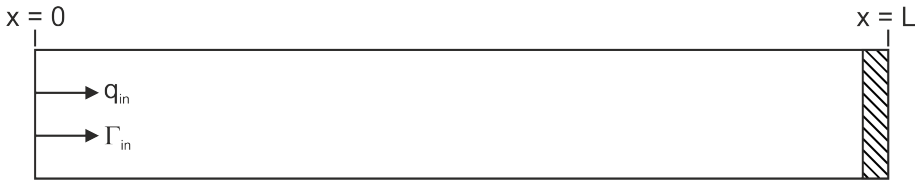

Figure 2.4: Schematic of the origins of the particle (Γ_{in}) and power (q_{in}) fluxes in the sheath-limited SOL (not to scale). The hatched section in front of the target at $x = L$ is the sheath. Diagram adapted from [23].

In the sheath-limited SOL, both the particle and power sources originate upstream, away from the divertor target. A schematic diagram is shown in Figure 2.4. This gives rise to a significant particle flow from the edge of the core plasma to the divertor target, and this convective motion transports power as well as particles. The dominance of convection is permitted by the low collisionality of the SOL plasma in this regime. In the next section, we consider the conditions on the collisionality, (5) and (6), which result in the sheath-limited and conduction-limited behaviour respectively.

The convective behaviour and low collisionality of the sheath-limited SOL mean that there is no significant temperature gradient along the field lines (again, this is discussed further in the next section). Total pressure is also conserved, although the static and dynamic pressure components vary in opposing ways throughout the SOL. The gradient

in the static pressure is caused by the presence of an upstream source and the downstream sink (surface recombination on the target), and this produces the plasma flow through the SOL (see Chapter 1 of [23]). The difference in the static pressure is then compensated for by an increase in the dynamic pressure as the electron and ion velocities increase.

In a tokamak SOL, operating in the sheath-limited regime has a considerable effect on the edge plasma properties, as it is the plasma-surface interaction at the divertor target which determines the boundary conditions. The presence of the sheath therefore affects the form of the relationship between the plasma properties that are determined by the operating conditions of the tokamak (such as the input power and total number of particles in the plasma) and those which can vary, namely the density and temperature of the edge plasma entering the SOL.

It should be noted that the analysis for the simple sheath-limited SOL is based on a fluid model, which requires relatively high collisionality in order for the approximations to be valid. However, as we have seen, the collisionality in the SOL is low, and thus the fluid model is strictly invalid. Fortunately, more rigorous analyses show that the fluid model does provide a good approximation to first-order (see Chapters 1 and 10 of [23]).

2.1.2 Conduction-limited and high-recycling regimes

The presence of a parallel temperature gradient strongly alters the behaviour of the SOL, bringing it into the conduction-limited regime. The thermal conductivity of a plasma varies as $T^{\frac{5}{2}}$, and at the very high temperatures in the core plasma, conditions are essentially isothermal. However, in the cooler SOL, conduction can be restricted and temperature gradients arise. There are still sheaths present at the divertor surfaces in this regime, but the properties of the SOL are now defined by the conductive behaviour. This regime can be accessed in a tokamak by increasing the core plasma density (the transition begins approximately in the range $(1-2)\times 10^{13}\,\mathrm{cm}^{-3}$ in Figure 1.9).

The conduction-limited SOL is more complicated than the sheath-limited SOL: a wider range of phenomena can be introduced which were not included in the simple SOL analysis. These include ionisation within the SOL, radiative cooling, collisions with neutrals and energy transfer between electrons and ions, among other possibilities. The key process we consider here is ionisation within the SOL.

Allowing ionisation of neutrals within the SOL reduces the relative strength of convection compared to conduction. As we saw in the previous section, convection plays a major

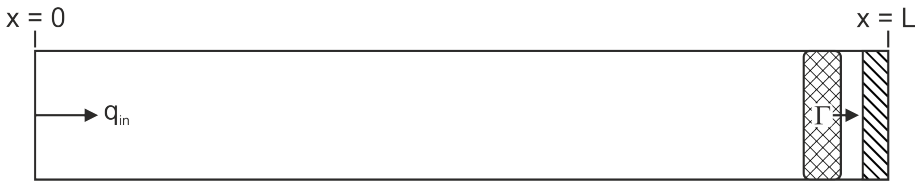

Figure 2.5: Schematic of the origins of the particle (Γ) and power (q_{in}) fluxes in the conduction-limited SOL (cf. Figure 2.4, not to scale). The hatched section in front of the target at $x = L$ is the sheath, and the cross-hatched region from which Γ originates is the ionisation region. Diagram adapted from [23].

role in particle and energy transport in the sheath-limited SOL. However, when ionisation interactions can take place downstream, the mean free path for these reactions is generally short enough compared to the SOL length that the ionisation occurs close to the source of the neutrals (recombination of ions and electrons on the target surface). This is illustrated in Figure 2.5. Plasma flow and convection processes are therefore less important in this regime, allowing conduction to dominate the heat transport and the temperature gradient to increase.

While the plasma particle source in the conduction-limited regime has moved close to the target, the power source is still upstream, as shown in Figure 2.5. The power now has to be conducted out of the core plasma and through the SOL. This implies that the collisionality in the SOL must be higher in this regime, in order to transport the power without significant particle flow. Stangeby considers criteria for the existence of the high temperature gradients required in this regime, and finds the following SOL collisionality parameter for equal ion and electron temperatures in terms of the upstream parameters (Chapter 4 in [23]):

$$\nu^*_{\mathrm{SOL}} \equiv \frac{L}{\lambda} \approx 10^{-16} \frac{n_u L}{T_u^2},$$

where L is the length of the SOL (along a field line), λ is the mean free path for collisions, and the subscript u indicates an upstream parameter. Units for the quantities are metres for lengths, m^{-3} for the density n_u, and eV for the temperature T_u (the prefactor 10^{-16} having units of $\mathrm{eV}^2\,\mathrm{m}^{-2}$). The conditions on ν^*_{SOL} for small and significant temperature gradients are found to be:

$$\nu^*_{\mathrm{SOL}} \lesssim 10 \qquad (\text{small } \nabla T); \tag{5}$$

$$\nu^*_{\mathrm{SOL}} \gtrsim 15 \qquad (\text{significant } \nabla T). \tag{6}$$

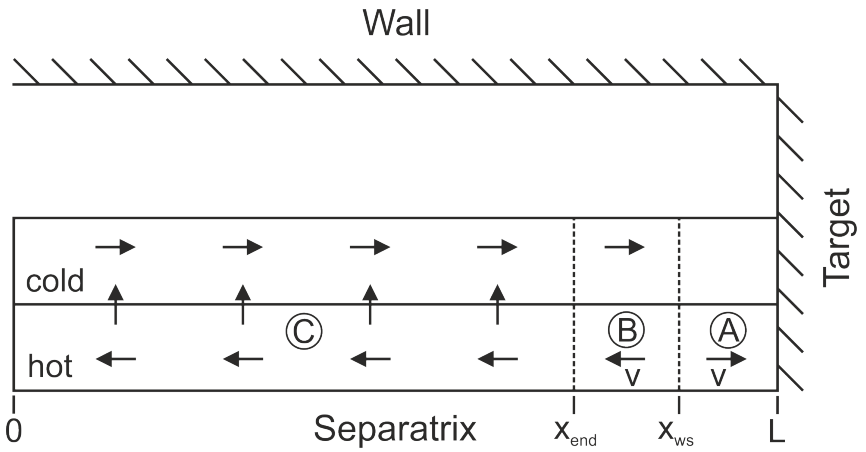

Figure 2.6: Schematic of flow reversal in a conduction-limited SOL of length L (not to scale). Ionisation occurs between $x = L$ and $x = x_{end}$. The source excess in the hot region, close to the separatrix, causes flow away from the target beyond a 'watershed' distance, x_{ws}. This sets up a convective flow in the SOL. Diagram adapted from [23].

In the one-dimensional model of the conduction-limited SOL, the presence of the particle source close to the target implies that there is no need for particle flow in the majority of the SOL, and therefore most of the plasma is stagnant (Chapter 15 in [23]). However, this is undesirable, as impurities would not be removed from the core plasma by particle flow, and is also inconsistent with measured density profiles along the SOL. A stagnant SOL plasma would be expected to have little variation in density, but measurements show that the density decreases along the SOL.

The explanation for this discrepancy is two-dimensional, and is known as 'flow reversal'. It arises from a perpendicular temperature gradient across the SOL near the target, as the plasma cools away from the separatrix. The phenomenon is illustrated in Figure 2.6. Ionisation predominantly occurs in the hotter region close to the separatrix, regardless of whether the neutrals were recycled from the target in this region or from the outer target (where the SOL plasma is cooler). Therefore the flux tubes close to the separatrix have a source excess, and the flux tubes in the outer SOL have a source deficit, compared to the number of particles that recombine on each part of the target. Flow reversal therefore occurs in the inner flux tubes in order to restore particle balance: some plasma flows away from the target, 'drains' into the outer flux tubes via cross-field transport, and returns to the target in the outer flux tubes. This plasma flow is then able to remove impurities and account for the radial density profiles observed along the SOL.

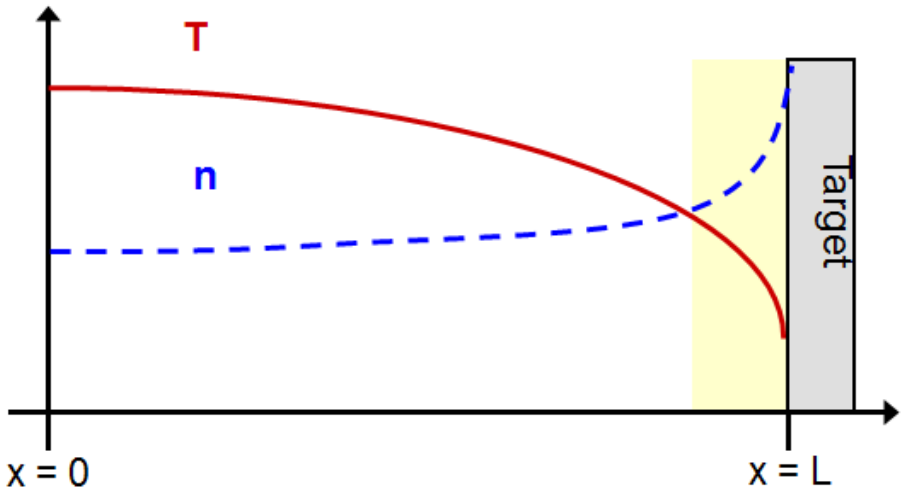

Figure 2.7: Approximate profiles of the plasma density, n, and temperature, T, throughout the SOL in the high-recycling regime. The yellow shaded region (not to scale) has strong radiative losses. Diagram adapted from [37].

If we consider the behaviour of the target density as the upstream density increases (as was shown in Figure 1.9), we see that there is an approximately linear relationship between the two initially, which then becomes a stronger, cubic dependence before rolling over into the detached region. This can be explained by the two-point model of SOL physics, which links the upstream and downstream plasma parameters [23, 38].

In the sheath-limited regime, and at lower upstream densities in the conduction-limited regime, the target flux Γ_i, and therefore target density, n_{target}, are proportional to the upstream density n_0, as seen in (4). As the upstream density increases further, however, we reach the 'high-recycling' regime. This is sometimes seen as an extension of the conduction-limited behaviour rather than necessarily an entirely different regime. The dependence of n_{target} on n_0 now becomes cubic, and Γ_i becomes proportional to ${n_0}^2$. The two-point model describing this behaviour is laid out by Stangeby (Chapter 5 of [23]), and sketches of the plasma density and temperature profiles arising in a high-recycling SOL are shown in Figure 2.7. The recycling flux, $\phi_{recycle}$, is proportional to the impacting target flux, and therefore also transitions from a linear to a quadratic dependence on n_0; hence the label 'high-recycling'. In this regime, the plasma source from ionising recycled neutrals is sufficient to sustain the plasma in the SOL.

There are significant advantages to operating a tokamak SOL in the conduction-limited regime (and beyond). The large temperature gradients mean that the upstream temper-

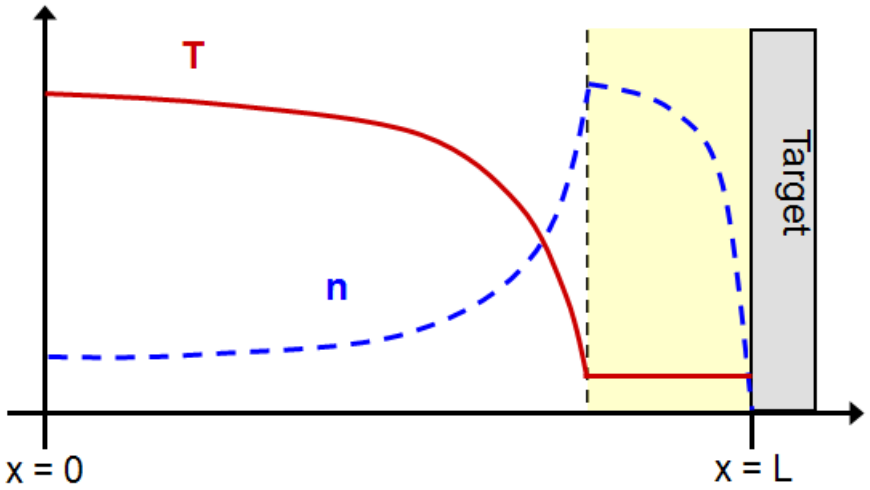

Figure 2.8: Approximate profiles of the plasma density, n, and temperature, T, throughout the SOL in the detached regime. The detached region is shaded yellow (not to scale). Diagram adapted from [37].

ature can be high (implying that the edge plasma can be hotter, which improves confinement), whilst maintaining a cooler plasma at the divertor. This reduces the amount of damage caused to the divertor plates: processes such as sputtering are mitigated by decreasing the ion energy, which can be achieved by lowering the electron temperature (as determined by sheath physics).

2.1.3 Detachment

In the detached regime, the range of phenomena occurring again increases and the SOL behaviour becomes yet more complicated. Two of the most important processes are neutral frictional drag and volume recombination. There are two key features of the detached regime: a significant decrease in the plasma flux to the divertor target; and the introduction of a pressure gradient, in addition to the temperature gradient observed in the conduction-limited regime [24]. This regime occurs when the downstream temperature in the conduction-limited or high-recycling SOL becomes so low ($< 1\,\mathrm{eV}$, compared to hundreds of eV in the core plasma) that recombination of the plasma begins to compete with ionisation in front of the divertor target, reducing the peak power and particle fluxes that reach the target surface.

The plasma density and temperature profiles arising in a detached SOL plasma are illustrated in Figure 2.8. The temperature dependence of the reaction rate coefficients for

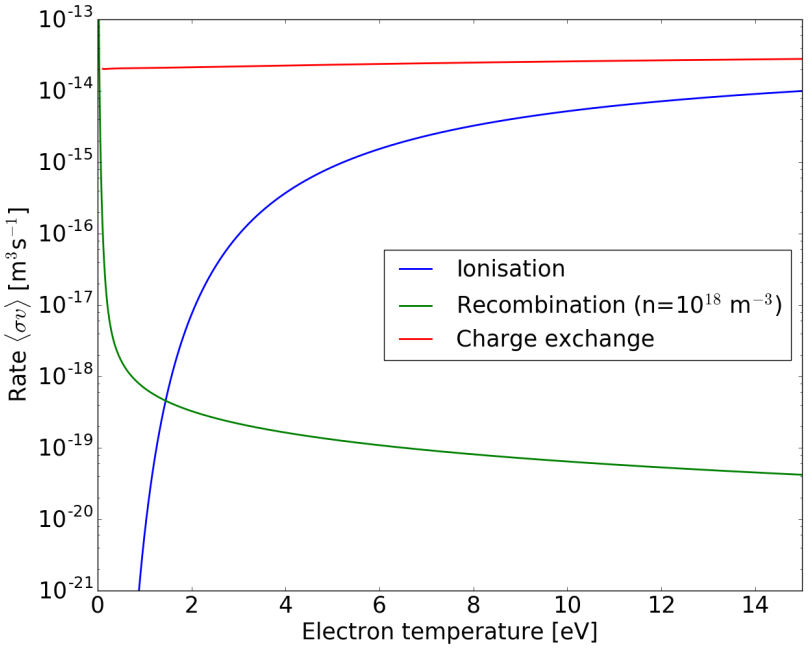

Figure 2.9: Plot of the temperature dependence of the reaction rate coefficients for ionisation, recombination (both collisional and radiative; for a plasma density of $10^{18}\,\mathrm{m}^{-3}$) and charge exchange processes in hydrogen. The fits for ionisation and charge exchange are taken from Janev [39], while the recombination curve is a fit to data taken from Bates et al. [40].

hydrogen ionisation, charge exchange and total recombination are compared in Figure 2.9. The recombination rate is calculated using both collisional and radiative processes, and is plotted for a plasma density of $10^{18}\,\mathrm{m}^{-3}$.

The detached behaviour is not simply the result of replacing the surface recombination sink at the target with a volume recombination sink in front of it, however. The level of neutral recycling from the surface, $\phi_{recycle}$, is able to take any value, as it only depends on the relative balance of the surface recombination and ionisation in front of the target. The level it reaches has to be determined by the requirement that momentum and power are conserved along the SOL.

We first consider the conservation of momentum. In the detached regime, momentum is lost through processes such as ion-neutral collisions, which cause a frictional drag force on the plasma. This gives rise to the observed drop in particle flux, and hence the pressure gradient. A simple gas discharge model of the plasma flow to the wall shows the reduction

of the particle flux, Γ, with increasing collisionality. The analysis assumes that the particle flow is due to ambipolar diffusion, with the diffusion coefficient given by:

$$D_{amb} \approx \frac{kT_{\mathrm{e}}}{m_{\mathrm{i}}\nu_{\mathrm{in}}},$$

where ν_{in} is the ion-neutral momentum-transfer frequency due to collisions. ν_{in} is proportional to $\lambda_{\mathrm{in}}^{-1}$, the inverse of the mean free path between collisions. Evaluation of the flux to the wall gives:

$$\Gamma = \frac{\pi D_{amb} n_0}{2L}.$$

We therefore see that:

$$\Gamma \propto \frac{\lambda_{\mathrm{in}}}{L},$$

i.e. the flux decreases as the collisionality increases (the mean free path of collisions goes down). Details of this and more sophisticated analyses (which also yield the same dependence) are discussed in Chapter 16 of [23].

For the conservation of energy, we must look at the radiative processes that occur in the SOL plasma, which result in the loss of energy and a reduction in the power flux to the divertor target. Upstream, closer to the edge plasma, a significant amount of power can be lost due to radiation from excited hydrogen atoms or impurities. This helps the temperature drop low enough for volume recombination processes to occur closer to the target [23].

If we look more closely at these volume recombination processes, we find that there are two main categories: electron-ion recombination (EIR); and molecular-activated recombination (MAR). Each has been observed both in tokamaks and in detachment experiments in linear plasma machines. An overview of some of these results will be given in the next two sections; here we introduce the two types of recombination.

EIR pathways create neutral hydrogen atoms in a single step, involving only a plasma ion and electron, or, in the case of three-body recombination (the third reaction in (7) below), a third species which carries off some of the energy released in the reaction. The three reaction pathways are as follows:

$$\begin{aligned} \mathrm{e}^- + \mathrm{H}^+ &\longrightarrow \mathrm{H} + h\nu \\ \mathrm{e}^- + \mathrm{H}^+ &\longrightarrow \mathrm{H}^{**} \longrightarrow \mathrm{H} + h\nu \\ \mathrm{e}^- + \mathrm{H}^+ + \xi &\longrightarrow \mathrm{H}^* + \xi'. \end{aligned} \tag{7}$$

In the final reaction in (7), the third body, ξ, is usually a second electron, making the process the direct inverse of ionisation. This is the dominant EIR pathway, as the presence

of the third body makes the conservation of both energy and momentum easier. The highly excited neutral atoms that are produced in these interactions give EIR detachment a characteristic spectroscopic signature. As they relax to the ground state, they emit photons in the blue/UV range of the electromagnetic spectrum (high-n Balmer emission lines). This gives the detached plasma a bright blue colour (as opposed to the red/pink colour of a hydrogen plasma dominated by ionisation). The reaction rate for three-body recombination is proportional to $n^2 T_e^{-\frac{9}{2}}$, and hence this regime occurs when the plasma density is high but the electron temperature drops below around 1 eV [41].

MAR occurs via the following two-step reactions:

$$H_2(v) + e^- \longrightarrow H^- + H \quad followed\,by \quad H^- + H^+ \longrightarrow H + H^* \tag{8}$$

$$H_2(v) + H^+ \longrightarrow H_2^+ + H \quad followed\,by \quad H_2^+ + e^- \longrightarrow H + H^* \tag{9}$$

$H_2(v)$ indicates a vibrationally excited molecular state. The excitation considerably increases the cross-sections of the reactions, by orders of magnitude [42]. Unlike the EIR regime, MAR detachment has few characteristics that are easily identified spectroscopically. The plasma emission fades as the onset of detachment occurs, and there is no colour change, but the presence of the vibrationally-excited molecules can be inferred from the optical spectrum, where peaks from the vibrational band occur between 600 and 640 nm. The observation of negative ions is also an indicator of MAR detachment. This regime occurs at lower densities than EIR, and the electron temperature must be around $2-3$ eV in order for the vibrationally-excited molecules to exist.

Since there are multiple processes occurring in a detached SOL plasma, and the balance between them can vary for different divertor configurations, full understanding of detachment has not yet been achieved. Processes that still need to be considered fully in models include the transition to detachment, the stability of the radiation front, and turbulence and radial transport [43]: all key areas with the potential to have a large impact on the performance of ITER and future machines. Experimental research into the behaviour of detached divertor plasmas is essential to improve our understanding and optimise the operation of fusion reactors. In the next sections, the state of current research, using both tokamaks and linear plasma machines, is considered.

2.2 Detachment in tokamaks

Detached divertor plasmas have been studied in multiple tokamaks, including JET (see e.g. [44]), JT-60U (e.g. [45]) and Alcator C-Mod (e.g. [46]). The detachment behaviour varies between machines, and it is important to study a wide range of scenarios in order to understand it fully. Boedo et al. have reviewed the experimental detachment research in tokamaks and the various diagnostic techniques employed [47]. Here, a brief overview is given of some of the experimental and computational research that has been undertaken on the DIII-D and ASDEX Upgrade tokamaks, as well as some more recent 'advanced divertor configurations' that are in place or planned on TCV and MAST-U.

2.2.1 DIII-D

Early research on DIII-D in the 1990s studied the effects of deuterium gas puffing and divertor pumping on both the control of the heat flux to the divertor and the core plasma density (see [48] and references therein). This work observed the large drop in plasma pressure between the upstream (P_{mid}) and downstream (P_{div}) regions that is characteristic of the detached state. The ratio P_{mid}/P_{div} was observed to increase from ~ 2 to ~ 40 with deuterium gas puffing near the midplane of the tokamak.

Some of the most recent work at DIII-D has established a system for the control of the detached state [49]. This system is able to change the gas puffing rate in response to changes in the measured electron temperature at the divertor target, and consequently hold the plasma in a partially detached state. It is also able to hold the plasma near the detachment threshold in an ELMing plasma (ELMs are edge localised modes: an instability which has a significant effect on the core plasma behaviour and wall heat fluxes [50]). The variation of particle fluxes throughout the ELM cycle causes multiple transitions between attached and detached plasmas, which means that DIII-D can be particularly useful for the study of the detachment transition, and its interaction with ELMs [49].

Experimental observations on DIII-D are also used to develop simulations of divertor behaviour. Recent 2D simulations using the UEDGE code are compared to Thomson scattering measurements in the DIII-D divertor in order to study the differences between the inner and outer divertor legs [51]. The results of this study showed that the detached behaviour is not always reproduced by the simulations, with the discrepancies attributed to the need for better models of plasma transport.

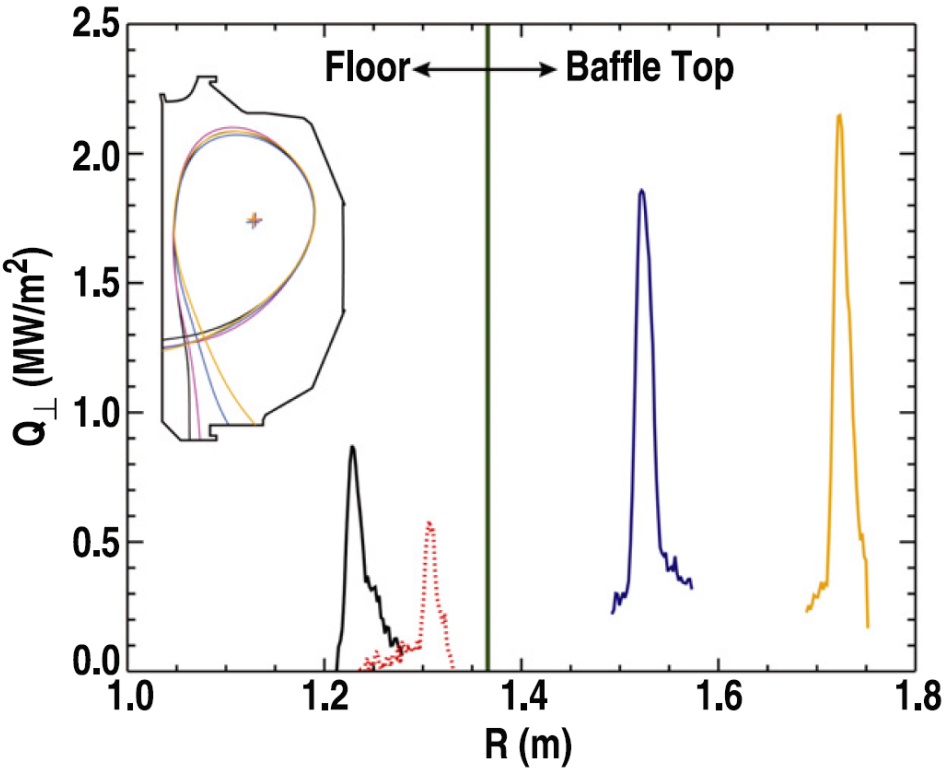

Figure 2.10: Heat flux ($Q_\perp$) profiles, based on infrared camera measurements, plotted as a function of divertor radial location, R, for the four DIII-D magnetic flux surface configurations shown in the inset. Reproduced from [52].

Research into the effects of the magnetic geometry of the separatrix and scrape-off layer on DIII-D complements the work of the wider community on advanced divertor configurations (Section 2.2.3). Petrie et al. studied multiple configurations, varying in X-point height, outer divertor leg length and outer divertor strike point radius, and their effect on the divertor heat flux, plasma density and temperature (while holding core plasma parameters steady to within 10%) [52]. The authors note that two of the configurations, with the outer divertor strike point in a 'closed' region of the vessel, were able to reach a partially detached regime. This was attributed to increased trapping of neutrals in the closed geometry versus the open geometry of the third configuration. The heat flux profiles to the divertor target for four configurations are reproduced in Figure 2.10. The experimental results were replicated relatively well with the SOLPS code, using effective diffusivity parameters to model the transport.

2.2.2 ASDEX (Upgrade)

The original ASDEX tokamak was used to obtain some of the first reported results on detached divertor plasmas [22]. The key plot showing the target density rollover as the core density is increased was reproduced in Chapter 1 (Figure 1.9). Since these early experiments, ASDEX and its upgraded version (AUG) have continued to play a key role in detachment research.

Some of the early work on AUG investigated a 'completely detached high confinement regime' [53]. This study found that the tokamak could be operated in a detached regime while still retaining a high level of core plasma confinement, and without inducing an unmanageable level of ELM activity. Deuterium and neon gas puffing were used simultaneously to obtain the detached divertor plasma, and some of the radiative cooling was due to carbon impurities in the plasma. It should be noted that carbon is no longer a relevant material for ITER due to problems with tritium retention (see e.g. [54]), but this work has nevertheless provided a starting point for further research.

More recent work, with full tungsten armour on the vacuum vessel surfaces, aimed to study divertor detachment induced by ramping the density of low-confinement modes in AUG [55]. The results indicated that there were three parts to the detachment process: an onset state (OS); a fluctuating state (FS); and finally, complete detachment (CDS). These are illustrated in Figure 2.11. The second state is characterised by the observation of fluctuations in the soft X-ray/UV emission from around the X-point of the SOL (panels (c) and (d) in Figure 2.11), and is of the most interest here.

These are the first observations of fluctuations that directly relate to detachment in AUG, and one of the few measurements of such fluctuations that have been made. Further studies of these radiative fluctuations in AUG have attributed them to oscillations in the position of the ionisation front [56]. This work also observed filamentary plasma transport in the fully detached state, which has been studied further by Nikolaeva et al., although a fully comprehensive data set has not yet been obtained [57]. The mechanisms driving the detachment and associated fluctuations are not fully understood, and it may be that the two are strongly related. The possible existence of such a link is particularly pertinent to the experimental observations of the EIR detached state in the York Linear Plasma Device, described in Chapter 5.

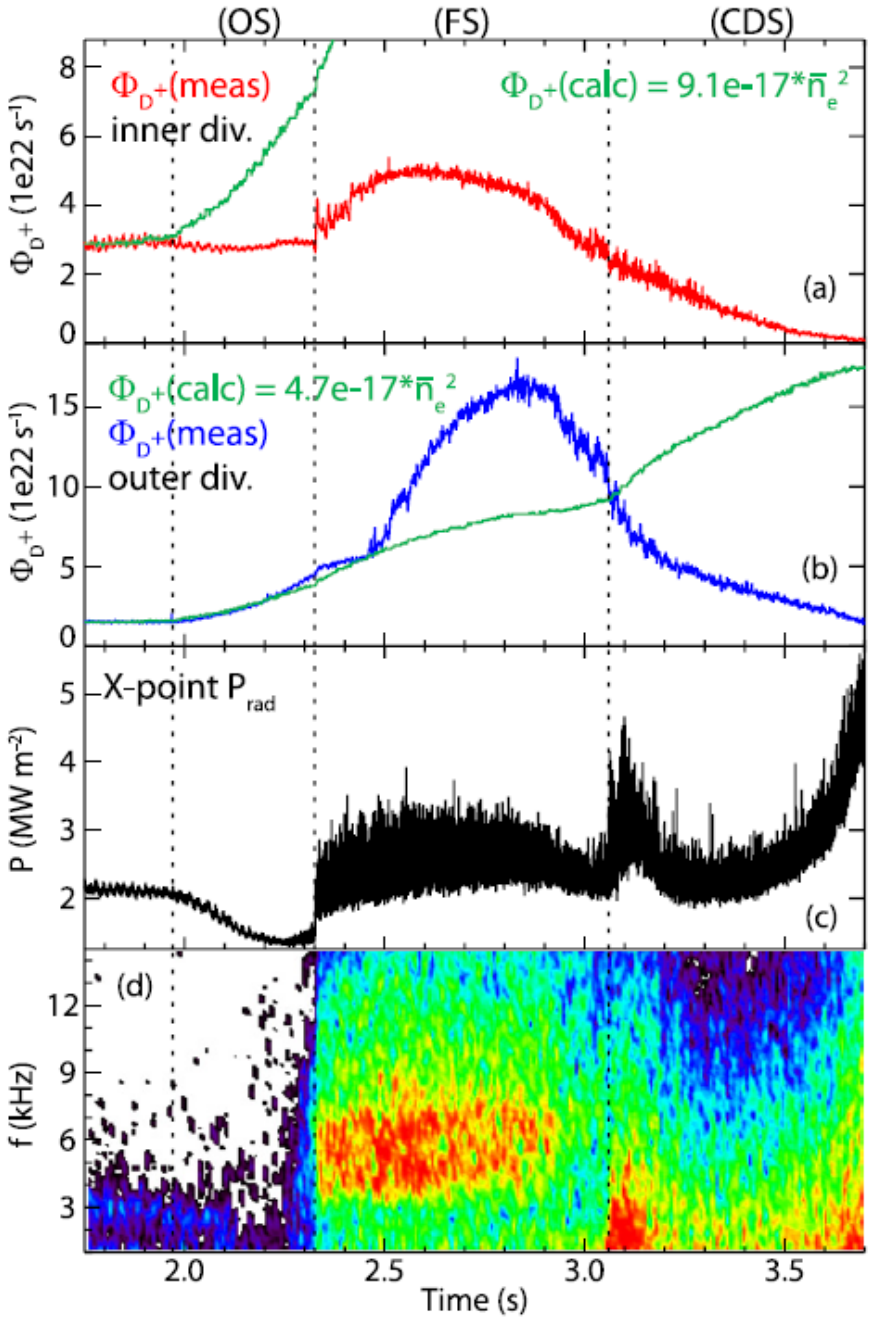

Figure 2.11: Calculated and measured total ion flux to (a) the inner and (b) the outer target; (c) the line-integrated radiated power measured by an AXUV diode; and (d) the power spectrum of the AXUV diode data from an AUG discharge. The three detachment states (OS), (FS) and (CDS) are indicated. Reproduced from [55].

2.2.3 Advanced divertor configurations

In order to achieve the reduction in divertor power flux that is required for future, larger reactors, multiple alternative tokamak divertor designs have been suggested. These are reviewed by Soukhanovskii [43]. A key feature of many of these designs is the introduction of one or more additional X-points in the magnetic configuration; either by adding extra divertors (e.g. the double null configuration with an upper and lower divertor), or by extending the existing divertor and introducing an extra X-point along the divertor leg to spread the power further. Flux expansion (weakening the magnetic field strength to spread out the field lines in the divertor) can also be included to deposit power over a larger area.

Here, two experimental tokamaks which are key to the study of these advanced divertor configurations are discussed. TCV has an open vacuum vessel configuration and 16 separate poloidal field coils, which together allow a wide variety of plasma and divertor shapes to be created [58]. Detachment studies have been carried out with several divertor configurations, including single null and flux expansion scenarios, measuring the density rollover and how this is affected by both flux expansion and divertor leg length [59]. Of particular interest is the snowflake configuration, which (in the ideal case) consists of a single null, but of second order, introducing extra divertor legs from the same X point. In practice, multiple X points are positioned in close proximity. A number of snowflake configurations are illustrated in Figure 2.12. A focus of detachment studies in this scenario is the distribution of particle and power fluxes between the different divertor legs [59].

MAST-U is currently under construction, and will be an upgraded version of the MAST spherical tokamak. A key focus of the upgrade design is the study of different divertor shapes, in particular the 'Super-X' configuration, which brings the outer divertor leg through a baffle out to a large radius [60]. The 'conventional' and Super-X double-null divertor configurations are illustrated in Figure 2.13. A number of simulations using the SOLPS code have been carried out in order to predict the behaviour of the MAST-U divertor and how detachment will be accessed (see e.g. [61–63]). Results from the operation of MAST-U will validate and inform the simulations, which in turn will continue to support the experimental research.

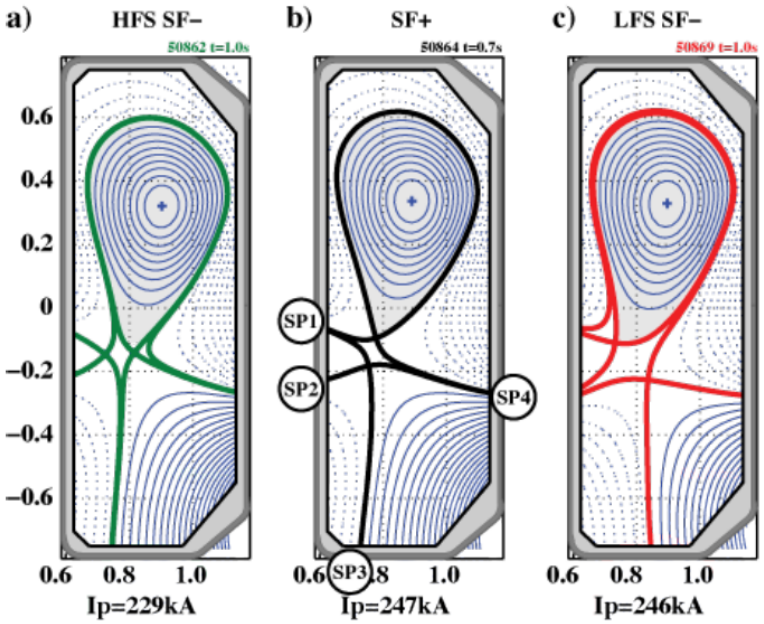

Figure 2.12: Snowflake divertor configurations produced in TCV: (a) high-field side snowflake minus; (b) snowflake plus; (c) low-field side snowflake minus. Strike points (SP) are labelled in (b). Reproduced from [59].

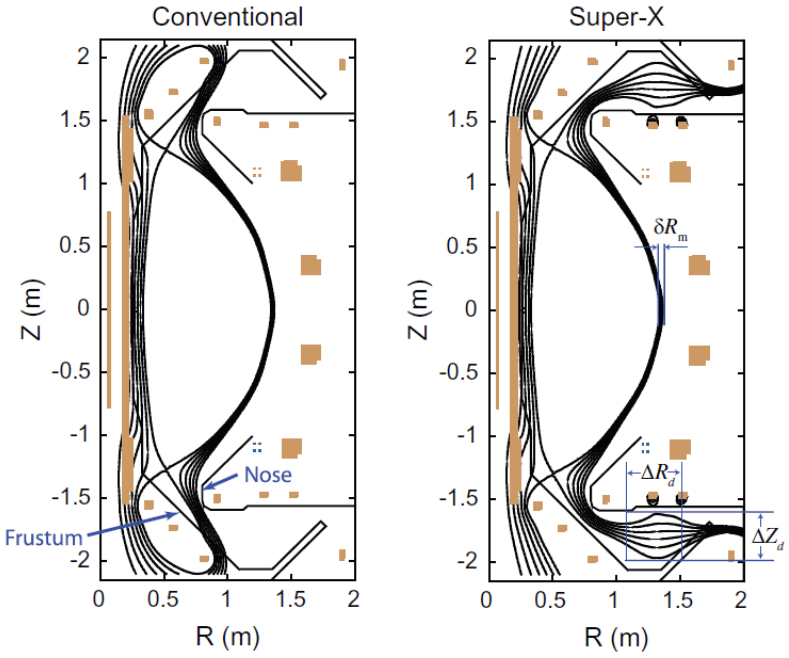

Figure 2.13: Representative double-null divertor configurations in the MAST-U tokamak. The Super-X divertor (right-hand panel) utilises flux expansion in the extended outer divertor legs. Reproduced from [60].

2.3 Linear plasma devices

Linear plasma machines are extremely useful for the study of detachment, as they are generally capable of running in steady state, allowing continuous measurements to be made at a relatively low cost (compared to a tokamak) [64]. The linear geometry makes diagnostic access more straightforward, as well as providing a simpler domain for simulations. Ohno reviews key detachment research that has been carried out on linear devices [64]; here an overview of several machines is provided, finishing with the YLPD.

2.3.1 QED device

The QED (Quiet Energetic Dense) device, illustrated in Figure 2.14, was the first to demonstrate the feasibility of the detached divertor concept [65]. The key observation made in this study was that a relatively high neutral gas pressure of a few millitorr was able to 'absorb' the entire power flux from the plasma and distribute it over the walls of the vessel. Axial heat flux measurements recorded a decrease as the neutral gas pressure increased, while the radial heat flux at the walls increased. This research provided the starting point for further detachment studies on linear devices.

2.3.2 PISCES-A

Early work on PISCES-A (shown in Figure 2.15) gave similar results to those from the QED device: observations of a 'neutraliser' (detached) regime at high neutral gas pressures, in which a density drop in front of the target was measured [66]. However, the vessel radius is larger than in the QED device, which enabled a study of radial transport in the plasma. Using experimental data to fit a classical diffusive transport model yielded an anomalously high diffusion coefficient, which the authors were unable to explain.

Later research by Schmitz et al. studied detachment in PISCES-A in more detail, investigating its causes [67]. The regime was attributed to loss of momentum due to ion-neutral collisions (supported by simulations), and radial transport reducing particle flux to the target. However, the level of radial transport observed remained anomalously high compared to a classical diffusive picture, and while the authors linked this to fluctuation-induced transport, a full understanding was not reached.

More recent research into the particle balance in detached PISCES-A plasmas (achieved via neutral gas puffing) suggests that cross-field transport can provide a dominant

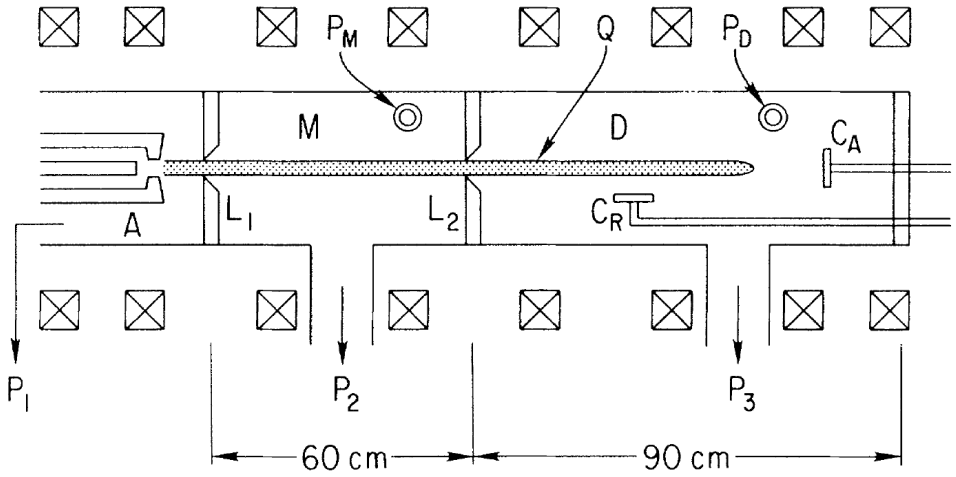

Figure 2.14: Schematic diagram of the QED linear plasma device. Key: (A) arc-jet plasma source; (Q) plasma column; ($L_{1,2}$) limiters; ($C_{A,R}$) calorimeters; (M) main plasma chamber; (D) divertor chamber; ($P_{M,D}$) pressure gauges; ($P_{1,2,3}$) pumps. Reproduced from [65].

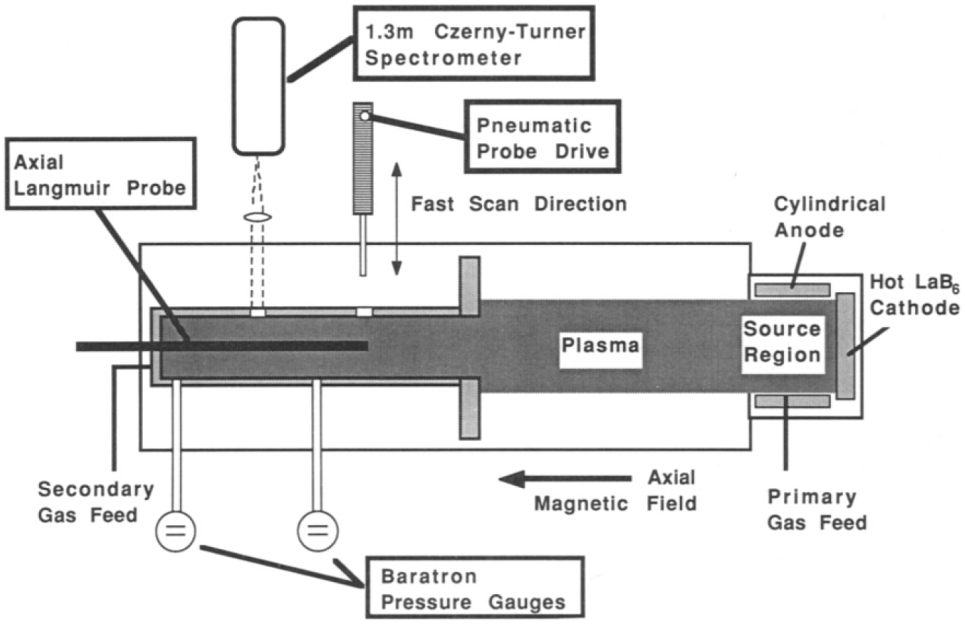

Figure 2.15: Experimental setup for the detached divertor experiments in PISCES-A. Reproduced from [66].

particle sink [68]. Measurements of particle fluxes showed that the radial flux became larger than the axial flux for the fully detached regime, and transport was not observed to be significantly affected by the neutral gas pressure. The authors conclude that turbulent radial transport, not ion-neutral collisions, is the main particle sink. However, there is some discussion as to whether this is due to the nature and geometry of the linear machine, and hence whether the same conclusions can be applied to tokamaks [69]. It is clear that further study of the relationship between turbulent transport and detachment is required to fully understand it.

2.3.3 NAGDIS-II

MAR detachment in a linear device was first observed in NAGDIS-II, illustrated in Figure 2.16 [70]. The work was carried out using hydrogen gas puffing into a helium plasma, and the emission spectra were analysed to deduce which recombination processes were occurring. Above a critical hydrogen density, the emission corresponding to the EIR regime disappeared, leaving only a contribution from MAR. To identify the dominant regime, the spectra were compared to those predicted by simulations.

The questions surrounding the role of radial transport in detached plasmas have also been considered in research on NAGDIS-II. Intermittent radial transport of blob-like plasma structures was observed using fast-frame imaging (see [71]), and analysed further by Tanaka et al. [72]. The blob transport was seen to increase between attached and detached conditions, and the authors suggest that the transport could play a significant role in the reduction of particle and power fluxes to the target.

2.3.4 MAP-II

MAR studies have also been carried out using MAP-II (shown in Figure 2.17), again by puffing molecular hydrogen gas into a helium plasma [73]. The negative ion density across the plasma column was measured using laser photodetachment (see Section 6.4), and it was found that the species was localised in the edge of the plasma. This was consistent with temperature measurements across the column: negative ions are able to exist in the cooler edge plasma, but not in the hot central region.

Development of a new monochromator system (the hetero-tandem double monochromator) for use with the Thomson scattering diagnostic technique allowed the low temperatures of EIR recombining plasmas to be more accurately measured [74]. The results were

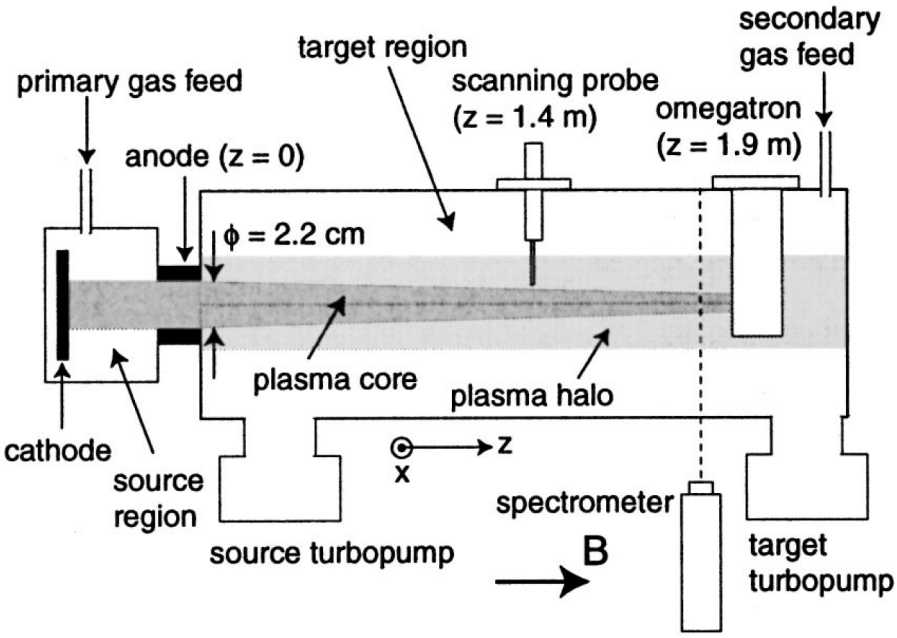

Figure 2.16: Schematic diagram of NAGDIS-II. Reproduced from [75].

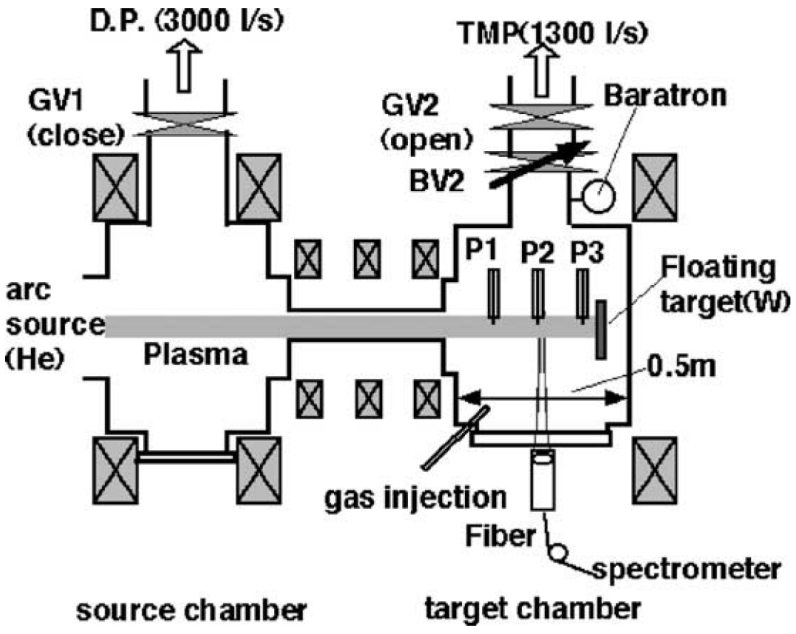

Figure 2.17: Schematic diagram of the MAP-II linear plasma device. Two vacuum pumps (D.P. 3000 and TMP) are connected to the chamber by gate valves (GV1 and 2) and a variable butterfly valve (BV2). Probes denoted by P1, 2 and 3. Reproduced from [76].

found to be consistent with those obtained using optical emission spectroscopy (Section 3.3) and simulations of a collisional radiative model.

2.3.5 YLPD (ULS)

The YLPD (previously known as the UMIST Linear System, or ULS) has been used for detachment studies since 2000 [77]. The machine is illustrated (Figure 3.2) and described in detail in Section 3.1 in the following chapter. The ion speed in this device was measured to be approximately three times the ion sound speed in the plasma, and therefore the authors acknowledge that the behaviour is unlikely to exactly replicate that of a tokamak divertor, but the results can contribute to research concerning the interaction of a plasma with neutral gas [77]. The results from this early study, based on estimated rate coefficients, indicate that MAR processes are likely to occur in this device.

The EIR and MAR regimes have both been studied on the YLPD, with a focus on how the transition between the two depends on the upstream plasma parameters [78]. It was found that higher upstream densities tended to lead to EIR detachment. The experimental measurements were compared to those predicted by a simplified model of cooling and recombination processes, and found to agree relatively well. This study also notes that the reduction of the particle flux to the end plate of the YLPD (ULS) appears to be a result of the MAR processes rather than cross-field transport.

Further characterisation of both detached regimes has been undertaken using spatially-resolved spectroscopy [79]. In the EIR regime, the emission of the high-n Balmer lines from excited atomic hydrogen provides a straightforward indication of the location of the detached region, and the axial spatial evolution along the plasma column towards the target is clear. No emission from the Fulcher bands of molecular hydrogen is seen. In contrast to this, the MAR regime does not show abrupt changes as the axial position varies; instead both the Balmer and Fulcher band emission decrease gradually towards the target. The evidence for the presence of MAR detachment is less conclusive, but the authors report that the results are consistent with 1D modelling of a plasma in this regime. These studies are reviewed in more detail in Section 4.1.

2.4 Summary

In this chapter, we have discussed the evolution of the scrape-off layer plasma as the collisionality and upstream density change. The behaviour can be broadly divided into three regimes: sheath-limited; conduction-limited; and detached. For operation of tokamak fusion reactors, the most relevant regimes are conduction-limited and, in particular, detachment. Detached divertor plasmas will be essential to sufficiently reduce divertor target heat and particle fluxes to restrict divertor damage to manageable levels.

There is already a significant amount of research into the observation and prediction of the behaviour of detached plasmas in tokamaks and in linear devices. However, the presence of an anomalous contribution to radial particle transport (and other complicated processes) means that the state is not yet fully understood, and further work is needed in order to improve our knowledge and allow us to predict and control its behaviour. One particular aspect that requires attention is the relationship between plasma fluctuations, cross-field transport and the detached state, and this is the focus of the next three chapters of this thesis.

Chapter 3

The YLPD and diagnostic techniques

The study of detachment presented in this thesis (Chapters 4 and 5) was carried out using the York Linear Plasma Device (YLPD) in the York Plasma Institute at the University of York. This machine has a DC source which creates a steady-state column of plasma. In this chapter we discuss its operation (Section 3.1) and introduce the diagnostic techniques employed in the study: Langmuir probes; optical emission spectroscopy; target plate ion flux measurements; and fast-frame imaging (Sections 3.2-3.5).

3.1 YLPD

The York Linear Plasma Device is a 1.5 m long vacuum vessel with a Demirkhanov-type duoplasmatron source [77]. The source and system are illustrated in Figures 3.1 and 3.2 respectively. The main components of the plasma source are the cathode filament, anode, intermediate electrode, reflector electrode and magnetic field coil. The cathode consists of a nickel mesh strip formed into a twisted 'U' shape and coated with powdered barium carbonate, strontium carbonate and nickel (10:10:80 wt.%), which are mixed with methanol to create an easily-applied solution. The coating increases the ability of the cathode to act as an electron emitter when heated by a current passing through it. These electrons initiate the breakdown of gas into plasma.

The duoplasmatron source is discussed in detail by Bradley et al. [80], and references therein. The following is an overview of its operation. The anode, intermediate and reflector electrodes all have a central hole of diameter 5.5 mm, through which the plasma

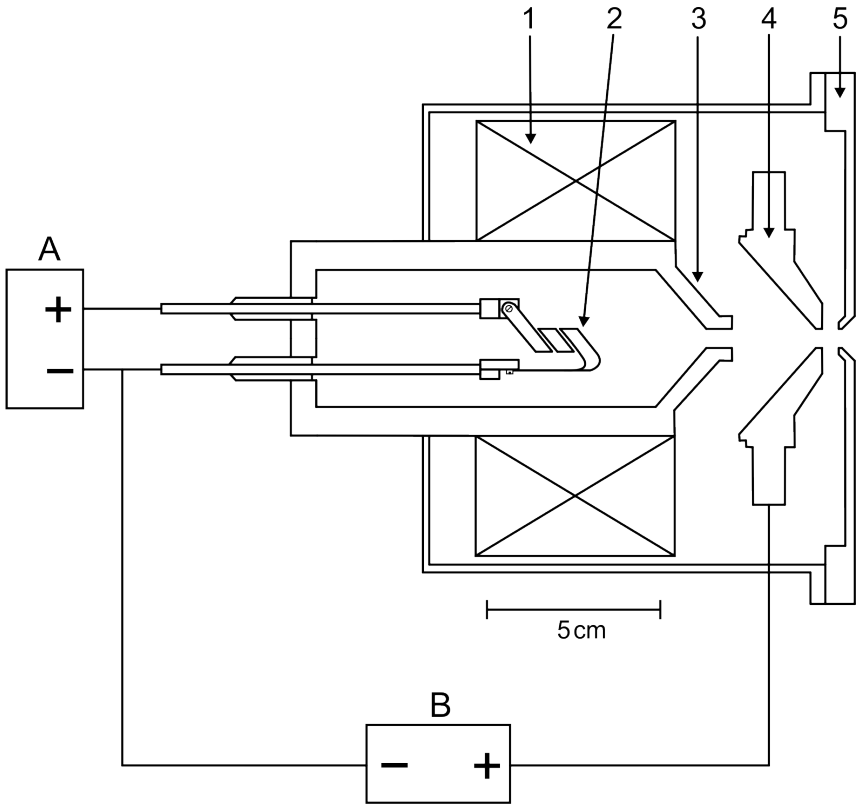

Figure 3.1: Simplified schematic diagram of the cross-section through the YLPD plasma source. Key: (1) solenoid coil; (2) cathode filament; (3) intermediate electrode; (4) anode; (5) outer casing, which acts as the reflector electrode, and through which the gas feed and the water coolant flow. A and B are the power supplies for the cathode heater and the DC bias between the anode and cathode respectively.

can travel towards the the main chamber. A constant DC bias is applied between the anode and cathode (200 V for plasma ignition, reducing to $\sim$ 80 V), and the intermediate electrode (IE) is allowed to float, taking on values in the range (-65 ± 5) V. On the cathode side of the IE, a potential sheath forms which focuses electrons through the IE towards the anode. A coil creates a uniform, axial magnetic field of magnitude (94 ± 3) mT, which also acts to focus the electrons. Neutral gas molecules are fed into the anode chamber and are ionised by the energetic electrons.

A potential 'hill' is formed between the anode and the intermediate electrode, which accelerates ions either through the anode and out of the source chamber (to create the plasma column), or back towards the IE and cathode. The impact of the ions on the cathode maintains the electron emission, causing secondary electron emission as well as

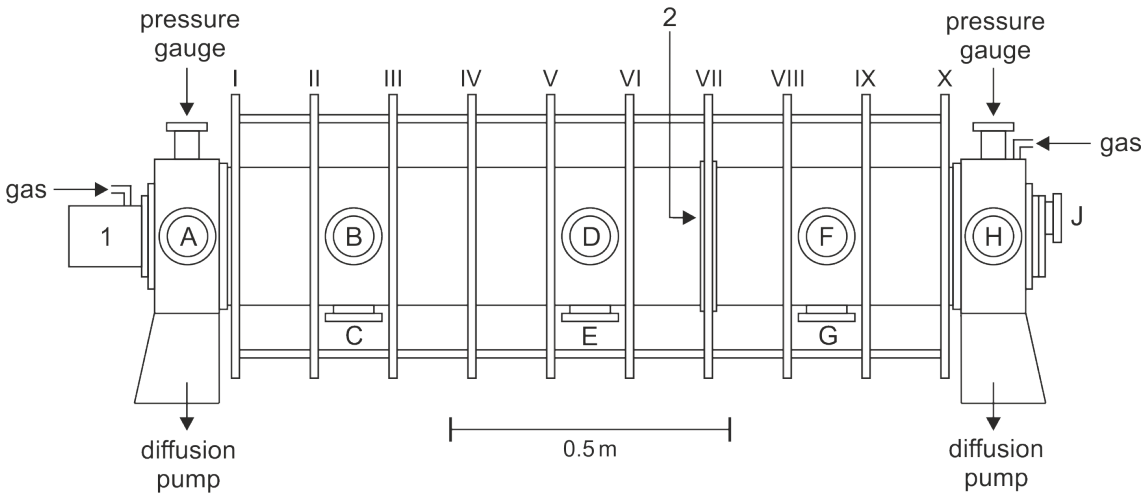

Figure 3.2: Schematic diagram of the main chamber of the YLPD machine. Key: (1) duoplasmatron source (for details see Figure 3.1); (2) position of diaphragm; (I-X) copper solenoid coils; (A-J) nine of the fourteen diagnostic ports (the remaining five are directly opposite ports A, B, D, F and H).

helping to heat the filament. The reflector electrode is also floating, and has a similar bias to that of the IE. Since this is negative with respect to the anode, most electrons oscillate between the reflector and intermediate electrodes, continuing to ionize further neutral molecules and sustain the plasma. However, as ions are accelerated out of the source chamber, some electrons are also pulled through in order to maintain quasineutrality.

Once in the main chamber, the plasma column is confined by an axial magnetic field, created by the ten water-cooled, 18-turn copper coils which are evenly spaced along the length of the chamber. The field is uniform along the majority of the length of the chamber, and can reach a maximum strength of $(98 \pm 4)\,\mathrm{mT}$. Two thirds of the way along the chamber is a diaphragm which effectively separates the chamber into two. The diaphragm supports a removable baffle plate, allowing variation of the diameter of the orifice through which the plasma passes. In this work, no baffle plate was used, and the diameter of the orifice was 40 mm.

There is a diffusion pump at each end of the chamber, meaning that each section is pumped separately. This enables neutral hydrogen to be puffed into the target chamber (the section furthest from the source), creating a 'gas box' in which plasma-neutral interactions can be studied. A sufficient increase in the target chamber pressure can induce detachment of the plasma column from the end plate of the machine.

To facilitate the observations, YLPD has fourteen ports along its length which can act as windows into the machine, or be used to attach diagnostic instruments to the chamber (e.g. Langmuir probes). A wide range ion gauge (capable of measuring down to 10^{-9} mbar) is installed at the source end of the YLPD to measure the base pressure ($\sim 10^{-6}$ mbar) before the plasma is ignited, and there is a Pirani gauge ($> 10^{-4}$ mbar) at the end of the target chamber, which monitors the pressure as detachment is induced.

Operation of the YLPD requires a balance between the magnetic field strengths (both around the source and in the main chamber), the cathode heating current, the DC bias voltage and current, and the gas flow into the source. During preliminary operation, it was found that EIR detachment could be reliably obtained using: a high magnetic field strength in the main chamber (~ 94 mT); a cathode heating current of 28 A (or the maximum available from the 6 V power supply - this depended on the cathode used); and a DC bias voltage of approximately 80 V, providing a fixed emission current of 15 A. These parameters remained fixed, but day-to-day fluctuations in the behaviour of the YLPD required slight alterations in the DC bias voltage and the source gas flow.

The alterations were found to be necessary in order to produce the same potential across the intermediate electrode (V_{IE}) for all periods of operation, as V_{IE} was identified as the key parameter in achieving EIR detachment. The value of V_{IE} was kept at (-68.0 ± 0.2) V for the current study by adjusting the gas flow to the source (between 30 and 40 cc min^{-1}) until V_{IE} stabilised. The DC bias voltage also varied as a result of this, with values of (79 ± 2) V. However, as will be discussed in Section 4.2, these variations did not affect the reproducibility of the EIR detached state within experimental error.

3.2 Langmuir probes

3.2.1 Single probe theory

There are multiple ways of measuring the temperature and density of a plasma, but a relatively simple method is to use a Langmuir probe: a small wire which is inserted into the plasma and electrically biased. The probe draws a current from the plasma which varies according to the bias applied, as the balance of collected ions and electrons changes. A plot of the probe current versus applied voltage (IV curve) can be analysed to estimate the plasma parameters. The theory of Langmuir probes has been discussed in multiple sources (e.g. [23, 81] and references therein); here we give an overview of the technique.

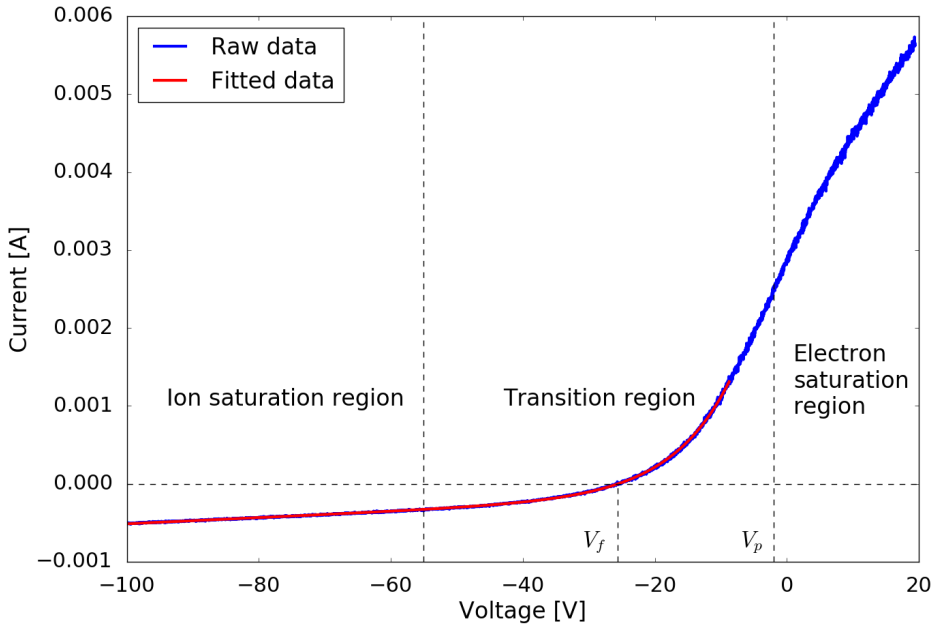

Figure 3.3: An example IV characteristic from a Langmuir probe, taken during the course of this work. Dashed vertical lines separate the ion and electron saturation regions and the transition region, and indicate the floating and plasma potentials (V_f and V_p respectively). The fit shown in red follows the four-parameter fitting equation, (18).

Before discussing the quantitative analysis of IV curves, we first give a qualitative introduction to their key features, which correspond directly or indirectly to the plasma parameters. A typical IV curve from a Langmuir probe is illustrated in Figure 3.3. Firstly, there are two important values of the potential to be noted. The plasma potential, V_p, is the true potential of the bulk plasma (away from the region perturbed by the probe). The floating potential, V_f, is the potential at which a probe insulated from the rest of the plasma device would sit if no bias were applied. In this case, the initial accumulation of negative charge from the higher electron flux repels further electrons and attracts ions, until the system balances with zero net current to the probe (as described in Section 2.1.1).

There are three key regions of the IV curve. At high-magnitude negative potentials, all electrons are reflected from the probe and only ions are collected; this is known as the ion saturation region. In practice, the magnitude of the current does not fully saturate, but slowly increases as the bias becomes more negative. This is due to sheath expansion effects, which we will return to in the discussion of the quantitative analysis. In this work, the direction of current is defined such that the ion saturation current is negative.

As the bias voltage increases, the most energetic electrons in the population (assumed to follow a Boltzmann distribution) become able to reach the surface of the probe and the net current starts to become more positive. As the bias voltage continues to rise, passing through V_f, the probe is able to collect an increasing number of electrons and the current rises exponentially. This is known as the transition region, and it is from this region that T_e can be estimated. Once the bias reaches V_p, we enter the electron saturation region, where no ions are able to reach the probe. In theory it should be possible to calculate the electron density from the electron saturation region, but in practice saturation is difficult to obtain, as more complicated effects come into play (for example secondary electron emission from the surface of the probe).

We now consider the theory behind the shape of the IV curve, assuming that the Debye length, λ_D, of the plasma (and hence the size of the sheath formed) is small compared to the size of the probe. The total current collected by the probe is:

$$I = A(j_\mathrm{e} + j_\mathrm{i}) = Ae(\Gamma_\mathrm{e} - \Gamma_\mathrm{i}), \tag{10}$$

where A is the collection area of the probe, and j_e and j_i are the current densities due to the electrons and ions respectively. The Maxwellian electron flux to the probe is given by:

$$\Gamma_\mathrm{e} = \frac{1}{4} n_p \bar{c}_\mathrm{e},$$

where $\bar{c}_\mathrm{e}$ is the average electron speed, and n_p is the electron density at the probe. Since we assume a Boltzmann distribution of the electrons in the sheath, we can substitute an expression for n_p in terms of the plasma density at the sheath edge (n_{se}), the probe bias, V, and T_e:

$$\Gamma_\mathrm{e} = \frac{1}{4} n_{se} \bar{c}_\mathrm{e} \exp\left(\frac{eV}{kT_\mathrm{e}}\right). \tag{11}$$

The ion flux at the probe is not given by an equivalent expression to that for the electrons [82]. Instead, flux conservation dictates that it is always equal to that at the sheath edge. The details are set out in Appendix A, and the result is:

$$\Gamma_\mathrm{i} = n_{se} v_{se} = \frac{1}{2} n_0 c_s. \tag{12}$$

$$c_s = \sqrt{\frac{kT_\mathrm{e}}{m_\mathrm{i}}}$$

is the ion sound speed in the plasma (m_i is the ion mass), and we have also used the key relationship (A.24):

$$n_{se} = \frac{n_0}{2}, \tag{13}$$

where n_0 is the bulk plasma density (away from the probe).

We can now consider the values of the particle fluxes at the floating potential, V_f. As no net current is drawn here, we can equate (11) and (12) for Γ_e (evaluated at V_f) and Γ_i. With varying manipulation, this gives us both an equation for Γ_i (14), and a relationship between c_s and $\bar{c}_\mathrm{e}$ (15).

$$\Gamma_\mathrm{i} = \frac{1}{4} n_{se} \bar{c}_\mathrm{e} \exp\left(\frac{eV_f}{kT_\mathrm{e}}\right); \tag{14}$$

$$c_s = \frac{1}{4} \bar{c}_\mathrm{e} \exp\left(\frac{eV_f}{kT_\mathrm{e}}\right). \tag{15}$$

Subsituting the fluxes (11) and (14) into the expression for the current (10) yields:

$$I = \frac{1}{4} A e n_{se} \bar{c}_\mathrm{e} \left[\exp\left(\frac{eV}{kT_\mathrm{e}}\right) - \exp\left(\frac{eV_f}{kT_\mathrm{e}}\right)\right].$$

Removing the first exponential term from the brackets and substituting in (13) and (15) gives our final expression for the current:

$$I = -\frac{1}{2} A e n_0 c_s \left[1 - \mathrm{e}^{\frac{e(V-V_f)}{kT_\mathrm{e}}}\right].$$

We can group the constants together as the ion saturation current, I_{sat}, to give:

$$I = -I_{sat} \left[1 - \mathrm{e}^{\frac{e(V-V_f)}{kT_\mathrm{e}}}\right]; \tag{16}$$

$$I_{sat} = \frac{1}{2} A e n_0 c_s. \tag{17}$$

A three-parameter fit to an IV curve can be used to estimate I_{sat} (and hence the plasma density, n_0, from (17)), V_f and T_e for the data set. However, this analysis is only valid for values of V for which a sheath forms, which effectively limits the upper limit of the fitting range to V_p (see Appendix A and [23, 81]).

It is possible to modify this equation to account for sheath expansion. Approximating the thickness of the sheath using Poisson's equation shows that it depends linearly on the probe potential [81]. As the sheath thickness changes, so does its surface area, which is effectively the probe's collection area. This then affects the magnitude of the current drawn by the probe. We account for this by adding an extra term into (16) to model the sheath expansion as a linear function of the bias voltage [83]. This adds a fourth fitting parameter, the sheath expansion coefficient, α:

$$I = -I_{sat} \left[1 - \alpha(V - V_f) - \mathrm{e}^{\frac{e(V-V_f)}{kT_\mathrm{e}}}\right]. \tag{18}$$

Taking IV curve data from a single Langmuir probe is quite straightforward to set up and analyse, but the technique is fairly limited. Firstly, it is an invasive diagnostic, which

disturbs the plasma around it, so may affect the phenomena that are under observation. The accuracy of the density measurements is limited to around 10% [81]. The temperature estimate is unreliable under $\sim 1\,\mathrm{eV}$, as the gradient of the transition region steepens and it becomes harder to capture and fit the behaviour accurately.

Secondly, the time required to ramp the bias voltage to obtain the full IV curve is on the order of milliseconds, which limits the time resolution that can be achieved. Events that occur on shorter timescales (including many plasma instabilities) cannot be studied using conventional IV curves, but it is still possible to gain some information by altering the approach. I_{sat} (using a constant negative probe bias) and V_f (if the probe is allowed to float) can be recorded on much faster timescales, which allows the investigation of these phenomena. These methods are discussed in more detail in Section 3.2.2. IV curves can still be used to measure the equilibrium profiles of the plasma parameters in these cases, however.

Thirdly, the application of large magnetic fields introduces further complications, as the confinement of the charged plasma particles to helical paths around magnetic field lines restricts the flow to the probe. The effect is limited if the Larmor radius of the particles is large compared to the probe dimensions, so in weak fields only the electrons are significantly affected and the above analysis still holds for bias potentials in or close to the ion saturation region. In stronger fields, the effect on the ions becomes significant, but it is still possible to use the above analysis as an approximation, if the collection area is taken to be the cross-section of the probe perpendicular to the field [81]. In the YLPD, the ion Larmor radius is of the order of a millimetre (the probe size), and for electrons it is on the order of microns. The collection area was therefore taken to be the perpendicular cross-section of the probe.

3.2.2 Fast timescale probe measurements

Recording the floating potential, V_f, at a high frequency allows statistical analyses of the data to be carried out in order to understand the fluctuating behaviour of the plasma, with spatial resolution determined by the Langmuir probe. The distributions of the V_f time series can be plotted as histograms, and the skewness and kurtosis calculated to quantify the deviation of each distribution from a Gaussian function. Random noise in the data is normally distributed, and hence these methods are useful for the identification of noise, as well as outlying intermittent events.

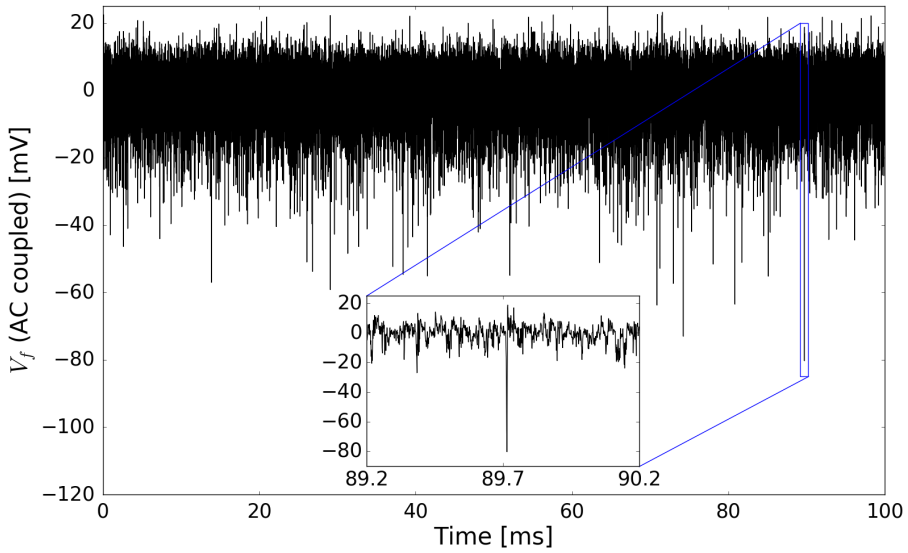

Figure 3.4: Example V_f time series data from the reference probe in the EIR detached plasma. Inset: 1 ms segment around an example large amplitude event chosen for correlation analysis.

Skewness is a measure of the asymmetry of a distribution: whether there are more high (or low) valued data points compared to the Gaussian distribution (which has a skewness of zero). Positive skew means that there is a longer high valued tail, and the mean of the distribution is larger than the median. A negatively skewed distribution has a long low valued tail, and the mean is smaller than the median. The formula for the skewness, S, of a data set with N points $(x_1, x_2, \ldots, x_N)$, mean $\bar{x}$ and standard deviation σ is:

$$S = \frac{1}{\sigma^3} \frac{\sum_{i=1}^{N} (x_i - \bar{x})^3}{N}.$$

The kurtosis indicates whether there are more, or fewer, outlying data points (both positive and negative compared to the mean) than would occur in a Gaussian distribution. In this thesis, we take the Gaussian function to have a kurtosis of zero, a definition known as 'excess kurtosis'. Distributions with positive kurtosis have longer tails (more outlying points), while a negative kurtosis value indicates that there are fewer outliers and the distribution has truncated tails compared to a Gaussian. The equation for the excess kurtosis, K, of the general data set described above is:

$$K = \frac{1}{\sigma^4} \frac{\sum_{i=1}^{N} (x_i - \bar{x})^4}{N} - 3.$$

Power spectra were also calculated for each radius by taking the fast Fourier transform of the V_f time series. Two-dimensional spectrograms were created to map the evolution of

the power spectrum as the radial position of the probe was changed. Narrow peaks in the power spectrum indicate the presence of coherent modes or waves in the plasma, whereas a broadband spectrum suggests that intermittent events are occurring which do not have a fixed frequency.

The motion of events in the plasma can be tracked by simultaneously recording data using both the moveable probe and a fixed reference probe, and considering the time delay in the appearance of significant events. The correlation between the moveable and reference probe signals was studied for 40 large negative events in the reference signal (an example event is shown in Figure 3.4).

A time window of $\pm 10\,\mu s$ around each event was selected, and its correlation with segments of equal duration in the moveable probe data was calculated (using the Python function scipy.signal.correlate). The moveable probe data window was scanned over $20\,\mu s$ either side of the event to find the time delay that yielded the maximum correlation value. The optimum time delay values for all events at each radius were then averaged, and the standard error of each set calculated. Plotting the average optimum delay versus radius can indicate whether events are travelling radially: if a straight line can be fitted to consecutive data points, events may be propagating through the plasma with a velocity given by the slope of the line.

3.2.3 Probes on the YLPD

Two Langmuir probes were mounted radially on the YLPD, at port F and its counterpart opposite (see Figure 3.2). Both probes have a full range of motion in the two-dimensional vertical plane perpendicular to the plasma column axis, with motorised insertion/retraction along the axis of the probe (radially across the column), and manual alteration of the angle of the probe to the horizontal.

The main probe in this research has a single tungsten wire tip, 1 mm in diameter and 0.72 mm in length, encased in a ceramic insulator tube. This probe was used both for the time-averaged IV measurements, and as the moveable probe in recording the fast V_f data. The reference probe for the fast measurements was the largest tip in a triple probe arrangement (with tip length and diameter both $\sim$ 1 mm), with the probe head aligned to reduce the disturbance to the plasma from the other probe tips. For the same reason, both probes were retracted out of the plasma column at all times when not in use.

IV curves were recorded using the ESPsoft software from Hiden Analytical, with the

Table 3.1: Properties of the hydrogen Balmer emission lines of interest in this study, including: upper (n) and lower (m) transition levels; the statistical weight of the upper level, g_n; the Einstein coefficient for the decay transition, A_{nm}; and the wavelength of the emitted photon, λ_{nm}.

Line	n	m	g_n	A_{nm} [s^{-1}]	λ_{nm} [nm]
H_α	3	2	18	4.410×10^{-1}	656.285
H_β	4	2	32	8.419×10^{-2}	486.128
H_γ	5	2	50	2.530×10^{-2}	434.046
H_δ	6	2	72	9.732×10^{-3}	410.174
H_ϵ	7	2	98	4.389×10^{-3}	397.007
H_ζ	8	2	128	2.215×10^{-3}	388.905
H_η	9	2	162	1.216×10^{-3}	383.538

fitting analysis code written in the Python programming language. This program allows multiple IV curves to be recorded and averaged, and the current range can be adjusted to maximise the signal to noise ratio. The 100 ms V_f time series for fast-timescale measurements were taken using a Teledyne LeCroy HDO6054 oscilloscope, on a 1 µs timescale with 1 MΩ AC coupling. These data were again analysed using a Python script.

3.3 Optical emission spectroscopy

3.3.1 Boltzmann temperature analysis

Temperature estimates obtained from Langmuir probes tend to become unreliable for low values (< 1 eV), and so it is necessary to use an alternative diagnostic in order to improve the accuracy of temperature measurements for detached plasmas. For EIR detachment, the presence of the high-n Balmer emission lines means that a spectroscopic analysis can be undertaken. The theory of this analysis is discussed in detail by e.g. Griem [84]; here we give an overview of the method used. Details of the hydrogen Balmer emission lines of interest in this work are listed in Table 3.1.

If we assume that the high-n electron energy levels of the neutral atoms are in local thermodynamic equilibrium (LTE; discussed at the end of this section), their populations, N_n, can be described by the Boltzmann relation [81]:

$$\frac{N_n}{g_n} = \frac{N_\mathrm{i}}{g_\mathrm{i}} \frac{h^3 N_\mathrm{e}}{2(\pi m_\mathrm{e} T_\mathrm{e})^{\frac{3}{2}}} \exp\left(\frac{\Delta E_n}{T_\mathrm{e}}\right). \tag{19}$$

The subscripts e, i and n refer to the electron, ion, and n^{th} energy level populations respectively. N denotes the density, T the temperature, and g the statistical weight of the

specified population. m_e is the mass of the electron, and ΔE_n is the ionisation energy of the n^{th} energy level, given by:

$$\Delta E_n = \frac{13.6}{n^2}\,\text{eV}. \tag{20}$$

The excited energy level populations, N_n, can be calculated from the spectral integration of emission lines, assuming an optically thin plasma with line of sight of length l. The transition occurs between the excited n^{th} state and a lower level, labelled m. For the hydrogen Balmer emission lines, $m = 2$. The equation for the integrated emission of a single line is:

$$\int I_{nm}(\lambda)\,\mathrm{d}\lambda = \frac{hcl}{4\pi\lambda_{nm}} A_{nm} N_n, \tag{21}$$

where λ_{nm} is the wavelength corresponding to the transition, and A_{nm} is the appropriate Einstein coefficient (both listed in Table 3.1 for the lines of interest here). Rearranging for N_n and substituting into (19) yields:

$$\frac{\lambda_{nm}}{A_{nm} g_n} \int I_{nm}(\lambda)\,\mathrm{d}\lambda = \frac{h^4 cl N_\text{i} N_\text{e}}{8\pi g_\text{i} (\pi m_\text{e} T_\text{e})^{\frac{3}{2}}} \exp\left(\frac{\Delta E_n}{T_\text{e}}\right). \tag{22}$$

We then take the natural logarithm to give the equation of a straight line:

$$\ln\left[\frac{\lambda_{nm}}{A_{nm} g_n} \int I_{nm}(\lambda)\,\mathrm{d}\lambda\right] = \frac{\Delta E_n}{T_\text{e}} + \ln\left[\frac{h^4 cl N_\text{i} N_\text{e}}{8\pi g_\text{i} (\pi m_\text{e} T_\text{e})^{\frac{3}{2}}}\right]. \tag{23}$$

A plot of the quantity on the left-hand side against ΔE_n (using multiple emission lines) can be fitted with a straight line if LTE is valid. The slope of the fit will be equal to the inverse of the electron temperature of the plasma. An example spectrum and the corresponding Boltzmann plot are shown in Figures 3.5 and 3.6.

The validity of the LTE assumption for the n^{th} energy level can be tested using a critical level threshold criterion, as set out by Griem [84]. LTE holds if $n > n_{crit}$, where:

$$n_{crit} \approx \left(\left[\frac{5Z^2}{n_\text{e}\sqrt{\pi}}\left(\frac{\alpha}{a_0}\right)^3\right]^2 \left(\frac{T_\text{e}}{Z^2 E_\text{H}}\right)\right)^{\frac{1}{17}}.$$

Here, Z is the ionisation state of the ion ($Z = 1$ for neutral hydrogen); α is the fine structure constant; a_0 is the Bohr radius; and E_H is the Rydberg energy (13.6 eV). The value of n_{crit} lies between 5 and 6 for typical plasma parameters in the YLPD as EIR detachment is approached, and hence LTE can generally be considered to be valid for the H_δ Balmer line ($n = 6$) and above. In some cases in this work, the H_δ line was not included in the analysis as it clearly did not fit a straight line with the higher-n data.

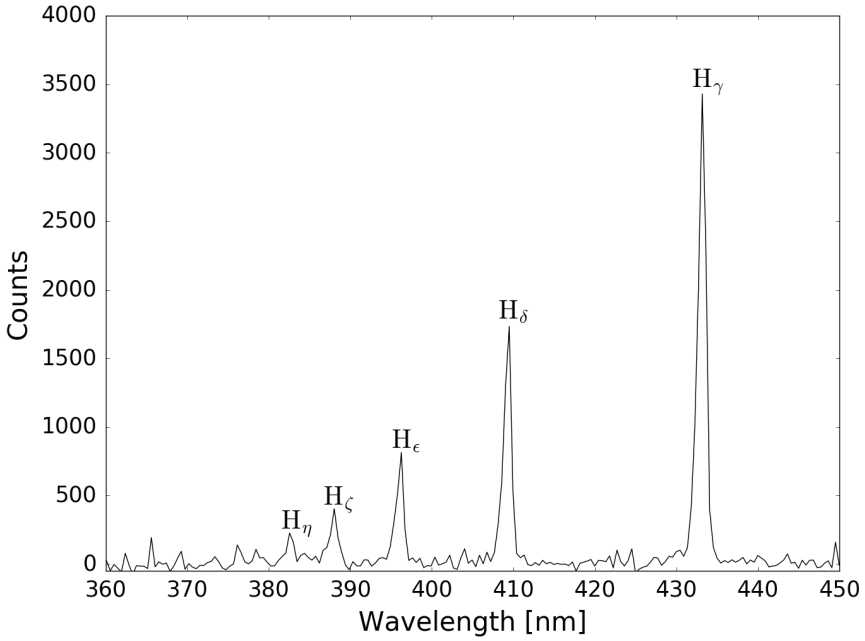

Figure 3.5: Example high-n Balmer spectrum taken from the EIR detached region of a hydrogen plasma in the YLPD. The peaks shown are the $n = 5$ transition (H_γ, $\lambda = 434.046\,\text{nm}$) to the $n = 9$ transition, H_η ($\lambda = 383.538\,\text{nm}$).

3.3.2 H_γ/H_α ratio measurements

The ratio of the strengths of different hydrogen Balmer lines is often used in tokamaks as an indicator of the behaviour of the plasma. In the normal, attached state, the emission from the plasma column is dominated by the H_α line, with small contributions from the higher-n emission lines [85]. As the pressure is increased to induce detachment, the balance of the emission alters depending on the regime. For MAR (molecular-activated recombination) detachment, the ratio of the different line strengths remains relatively constant, but in the EIR (electron-ion recombination) regime, the excited hydrogen atoms that are formed mean that the higher-n lines increase in strength relative to H_α.

In this work the H_γ and H_α lines were chosen, as lines that are further apart introduce difficulties in recording their intensities on the same scale. Every spectrum taken for the line ratio analysis in this study was an average of five exposures (700 or 1000 ms depending on the data set). A background spectrum, with no plasma present, was recorded for each exposure time in the same manner in order to correct the plasma spectra. The total line strength of each peak was calculated by integrating under a quadratic spline fit to the data. The ratio of the integrated values was then taken for each spectrum.

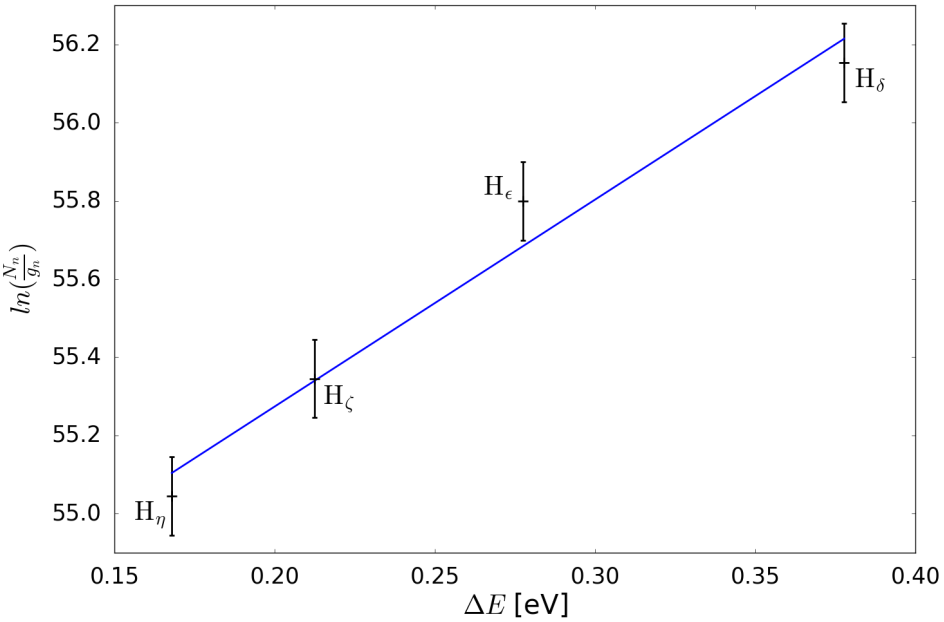

Figure 3.6: The Boltzmann plot obtained by analysing the H_δ to H_η lines in the Balmer emission spectrum in Figure 3.5. The data points are labelled with the corresponding emission line, and the blue line is the fit used to estimate the temperature. Error bars are derived from a 10% error estimate in the spectral line integration. The analysis yields a temperature of $(0.20^{+0.09}_{-0.02})$ eV.

3.3.3 OES diagnostics on the YLPD

The simple spectroscopic system in use on the YLPD consists of an Ocean Optics Maya2000 Pro spectrometer (wavelength range from $200 - 1090$ nm, with a resolution of 0.46 nm) and the Ocean Optics SpectraSuite software, capable of recording and averaging spectra covering the full range of hydrogen Balmer emission. Light was collected through port G of the YLPD (see Figure 3.2) using an optical fibre.

3.4 Target plate flux measurements

As illustrated in Figure 2.11 in Section 2.2, studies of detachment commonly use measurements of the ion flux to the divertor target plates to determine the plasma regime. The 'rollover' in flux as it peaks and then drops again is a characteristic feature of the transition to the detached state. In this study, therefore, the total ion current through the end plate of the YLPD is measured to determine the ion flux delivered to the target.

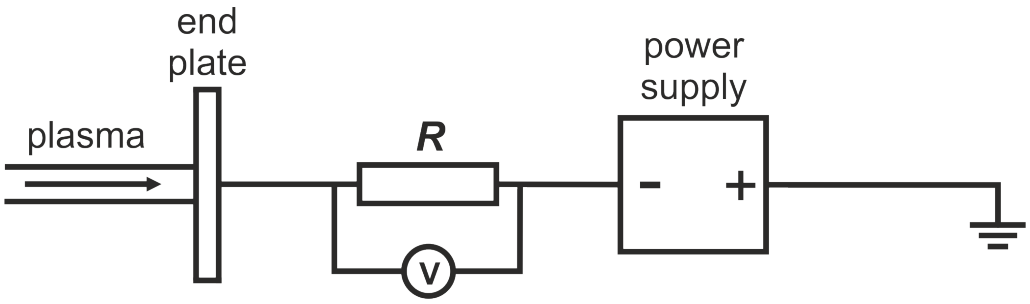

Figure 3.7: Schematic diagram of the experimental setup for measurement of the ion flux to the end plate of the YLPD. A power supply applies a negative bias to the plate in order to collect only ions, and the voltage across a resistor ($R = 0.1\,\Omega$) in series with the plate is measured. This voltage is converted to flux during analysis.

The end plate of the YLPD is electrically isolated from the rest of the chamber by an insulating spacer ring and insulating plugs around the screws. A negative bias voltage can therefore be applied to collect only the ion saturation current, which gives us a measure of the ion flux to the plate. A schematic diagram of the set up is shown in Figure 3.7. A $0.1\,\Omega$ resistor was placed between the plate and the power supply used to apply the bias voltage, which was then connected to ground. The voltage across the resistor was measured using the Teledyne LeCroy HDO6054 oscilloscope, and converted to flux values during analysis. As the plasma fluctuates over time, 100 ms of voltage data was recorded for each set of plasma conditions using $1\,\mathrm{M}\Omega$ DC coupling and a sampling rate of 1 MHz. The average and statistical error of each data set were then calculated, and converted to the total flux over the end plate (Γ_{end}) according to:

$$\Gamma_{end} = \frac{I_{end}}{e} = \frac{V}{eR}.$$

I_{end} is the ion saturation current to the end plate, given by the measured voltage, V, divided by the resistance, $R = 0.1\,\Omega$.

Following the experiments, it was recognised that problems with grounding of the measurement circuit meant that the bias voltage was incorrectly applied, and the voltage measured is likely to be in the electron transition region of the IV curve. The measurement is therefore more closely related to the electron current than the ion saturation current, and while it is still indicative of the plasma flux to the end plate, it cannot be used to infer the ion flux. However, recombination has a similar 'rollover' effect on the overall plasma flux, and the results are presented in Section 4.2.3 as an estimate of the total plasma flux.

3.5 High-speed imaging

Fast frame imaging (FFI) cameras are used to capture light emission from events that occur on rapid timescales (for an example on the MAST tokamak, see [86]). The frame rate of the camera determines the time resolution of the data. A balance must be struck between the resolution and exposure time and the light level and image processing time. In this work, a Photron Fastcam SA4 camera and a Nikon 50 mm F1.4 lens were used to view the plasma column in the YLPD target chamber through the port in the end plate (port J in Figure 3.2), with a depth of field on the order of millimetres. Continuous sequences of 5000 images were recorded for varying target chamber pressures, from the attached to the EIR detached state. The frame rate was 50 kHz, with the corresponding maximum exposure time of 20 µs. An example frame from the attached plasma is shown alongside an ordinary photograph through the same port in Figure 3.8.

Analysis of the FFI data was carried out in several ways, with the processing scripts based on those written by B. Law, with permission [87]. Firstly, mean-subtracted images were produced for each pressure value by taking the average of each pixel over the 5000 frames, and subtracting the resulting image from each individual frame. This process highlights the differences from frame to frame more clearly. Histograms were also plotted for three reference pixels to consider the distribution of the mean-subtracted intensities. The power spectra for the intensity series of each pixel through time for the 5000 frames were then calculated using the cross spectral density (CSD) function from the SciPy signal processing package (scipy.signal.csd).

Cross spectral density, $S_{xy}(\omega)$, is defined as the Fourier transform of the cross-correlation ($\gamma_{xy}(\tau)$) of two time series, $x(t)$ and $y(t)$:

$$S_{xy}(\omega) = \int_{-\infty}^{\infty} \gamma_{xy}(\tau)\, \mathrm{e}^{-i\omega\tau}\, \mathrm{d}\tau,$$
$$\gamma_{xy}(\tau) = \int_{-\infty}^{\infty} x^*(t)\, y(t-\tau)\, \mathrm{d}\tau,$$

where $x^*(t)$ is the Fourier transform of x and ω is the frequency. When $x = y$, the cross-correlation becomes the autocorrelation of x (γ_{xx}) and the cross-spectral density becomes the power spectral density, S_{xx} (PSD, the power spectrum). However, instead of taking the Fourier transform of the full time series, the SciPy function uses Welch's method, which first splits a data set into overlapping segments. The transform is carried out on each segment, and the results are averaged to reduce noise in the final answer.

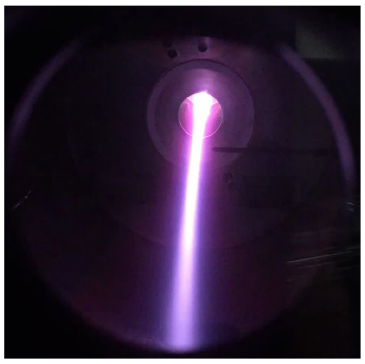

(a) Photograph of the attached plasma in the target chamber.

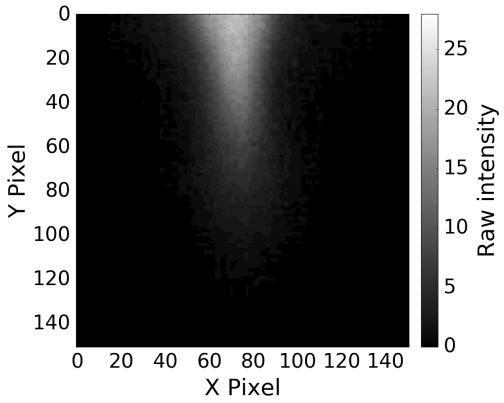

(b) Example raw FFI image of the attached plasma in the target chamber.

Figure 3.8: (a) Ordinary photo and (b) example high speed (50 kHz frame rate) camera image of the attached plasma in the target chamber of the YLPD (chamber length $\sim$ 60 cm). In both cases, the images are taken through port J (Figure 3.2) and show the plasma column entering the target chamber through the aperture in the diaphragm (diameter 40 mm) towards the top of the image. The FFI camera is focused in the plane of the Langmuir probe that enters from the right of the photograph (at approximately $y = 40$), and has a smaller field of view; the horizontal scale is approximately 0.25 mm pixel^{-1}. The vertical scale is similar in the plane of focus, but is affected elsewhere in the image by the small depth of field (of the order of mm). The line of sight from the cameras to the probe is at an angle of approximately 5° above the column axis.

The PSD measurements for the FFI data at each pressure show how the amplitude of different frequency components varies across the plasma column. To consider how the full range of frequencies (up to the Nyquist limit of 25 kHz) varies, a line of pixels can be chosen and a 2D spectrogram produced of frequency against radial position. Alternatively, the line of pixels can be used to plot the evolution of the power component at a particular frequency with pressure in the YLPD target chamber. These different types of plots are utilised in Chapter 5.

Further analysis was carried out to compare the behaviour of different pixels. If a reference pixel is chosen, the CSD calculation can be carried out between the time series of that pixel and those of all others in the image. CSD analysis for $x \neq y$ generally yields complex (rather than real) results: the amplitude at a particular frequency indicates the extent to which the two series share features at that frequency; and the phase of the CSD

gives the phase difference between the components of the series at that frequency. In this work we utilise the phase values calculated from CSD analysis to look at the phase differences between the intensity fluctuations of different regions of the plasma column.

Cross spectral density amplitude values between two time series can be compared more easily by converting them into the coherence, $C_{xy}(\omega)$. This normalises the CSD at each frequency to the amplitudes of the power spectral density for both series:

$$C_{xy}(\omega) = \frac{|S_{xy}|^2}{|S_{xx}|\,|S_{yy}|}.$$

When the two series are perfectly matched at frequency ω, $C_{xy}(\omega) = 1$. The SciPy coherence function (scipy.signal.coherence) again uses the Welch method to calculate the coherence of two series, and was used here to study how the matching of frequency components varies across the plasma column.

3.6 Summary

In this chapter, we have introduced the experimental equipment and analysis techniques employed in Chapters 4 and 5, which focus on the observations of the EIR detached state in the York Linear Plasma Device (YLPD). The design and operation of the YLPD itself have been described, along with the four diagnostic techniques employed in the study.

Langmuir probes are conventionally used to measure plasma density and temperature, but are restricted to time-averaged values due to their limited resolution. As well as using a single probe to measure equilibrium values in the YLPD (on millisecond timescales), two probes are used for analyses of microsecond-resolution time series of the floating potential.

Optical emission spectroscopy can provide more accurate temperature estimates below 1 eV, through Boltzmann analysis of the hydrogen Balmer emission lines, and the same spectra can be used to calculate Balmer emission line intensity ratios. The diagnostic setup for the measurement of the plasma flux to the end plate of the YLPD, and its implications, have been outlined. Finally, we discussed fast frame imaging using a high-speed camera, and the various techniques used to analyse the resulting data.

Chapter 4

Detachment in the YLPD

In this chapter we consider previous measurements of the detached state in the YLPD in more detail, and present further observations which complement and extend the study. The majority of these further results are the work of the author, excepting the radial optical emission profiles, which were obtained by Lisgo [88]. Insight from these measurements allows us to propose a new explanation of the behaviour of the electron-ion recombination (EIR) detachment regime in the YLPD.

The first section reviews the detachment studies carried out by Mihaljčić using the YLPD, which covered both the EIR and MAR (molecular-activated recombination) regimes [85]. We highlight the key experimental and simulation results, and identify areas in which the study can be expanded. Mihaljčić characterises the detached plasma in one dimension (along the axis of the machine) and on the relatively slow, millisecond timescales of Langmuir probe IV measurements, neglecting fast timescale behaviour and the radial broadening of the plasma column in the EIR regime.

Section 4.2 presents more recent observations of EIR detachment on the YLPD, continuing to focus on the slow timescale of Langmuir probe measurements in order to replicate the plasma conditions observed by Mihaljčić. The final experimental results detailed in this section are radial emission profiles of the hydrogen Balmer lines, which suggest that, instead of being one-dimensional, the EIR detached plasma in fact has a significantly broadened radial structure [88].

The radial observations, combined with the lack of fast-timescale measurements of EIR detachment, lead to the conclusion that there are flaws in the assumptions that fast timescale behaviour and the broadening of the plasma column are unimportant. In Section 4.3, the following alternative explanation of the behaviour is proposed. If relatively

high density plasma from the centre of the column propagates radially outwards on sub-millisecond timescales, it will no longer be connected to the source by the central core of hot plasma (emitted from the source orifice with a diameter of 5.5 mm) and will cool to create regions of low temperature, high density plasma. Simple simulations to study the time-averaged behaviour of such a broadened, cooled plasma column are carried out, showing that these conditions yield high EIR reaction rates, and are able to qualitatively reproduce the experimental EIR emission profiles.

4.1 Previous observations

The results presented in this section were predominantly obtained by Mihaljčić, who focused on characterising both the EIR and MAR detachment regimes in the YLPD, and studying the transition between them [85]. The work consists of both experimental observations (Section 4.1.1) and a computational model (Section 4.1.2).

4.1.1 Experimental data

Section 4.1.1.1 studies the threshold between the MAR and EIR regimes; and Sections 4.1.1.2 and 4.1.1.3 present axial and radial profiles of the plasma parameters in each state.

4.1.1.1 EIR/MAR threshold

An initial study mapped the threshold between the EIR and MAR regimes in density and temperature space (using the parameters measured upstream, in the main chamber where the detached state does not reach). Figure 4.1 plots the distribution of the two regimes as a function of the upstream density, n_u, and temperature, T_u, for a target chamber pressure of 1.2×10^{-2} mbar [85]. A power law fit to the approximate threshold between the two is shown as a solid grey line, and is in reasonable qualitative agreement with simple analytical models (see Section 4.1.2 for further details).

The threshold is relatively well-defined, although there is some overlap between the two regimes. We see a general trend in which the EIR regime dominates at higher densities, but the value of n_u at which the transition occurs increases as T_u increases. Mihaljčić took further data at lower target chamber pressures, and found that as the pressure was decreased, the threshold between the MAR and EIR regimes moves to higher densities. Thus lower pressures result in a wider range of conditions that produce MAR detachment.

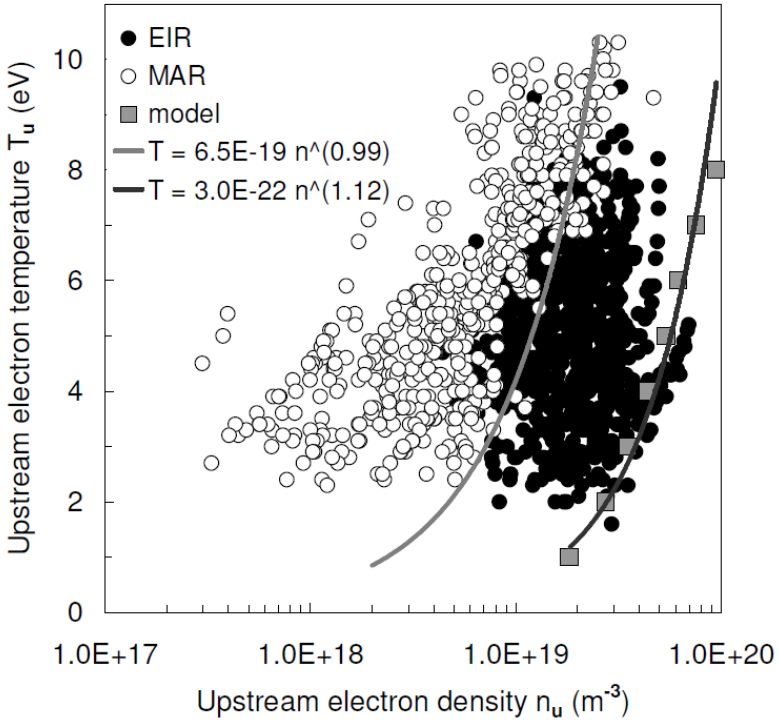

Figure 4.1: The YLPD operating space for the MAR and EIR detachment regimes in terms of the upstream (main chamber) density and temperature, for a target chamber pressure of 1.2×10^{-2} mbar. Conditions yielding MAR detachment are denoted by open circles, and EIR detachment by filled circles. The solid grey line is an approximate power law fit to the threshold between the two, based on the experimental data. Filled squares are threshold data points obtained from 1D modelling (Section 4.1.2), and the solid black is a power law fit to these points. Figure reproduced from [85].

4.1.1.2 Axial profiles

The majority of Mihaljčić's work is concerned with axial profiles of the detached plasma, using both Langmuir probe and optical emission spectroscopy (OES) techniques. He chooses a single 'case study' for each of the two detachment regimes to determine their characteristic behaviour. Both regimes have an upstream temperature of 5 eV, but for the MAR case the upstream density (n_u) is 4.7×10^{17} m^{-3}, whereas for the EIR detached plasma, $n_u = 1.5 \times 10^{19}$ m^{-3}. The target chamber pressures used to produce a stable detached plasma in each case were 1.0×10^{-2} mbar (MAR) and 1.2×10^{-2} mbar (EIR). The confining magnetic field strengths along the axis of the chamber were 30 and 50 mT for the MAR and EIR cases respectively.

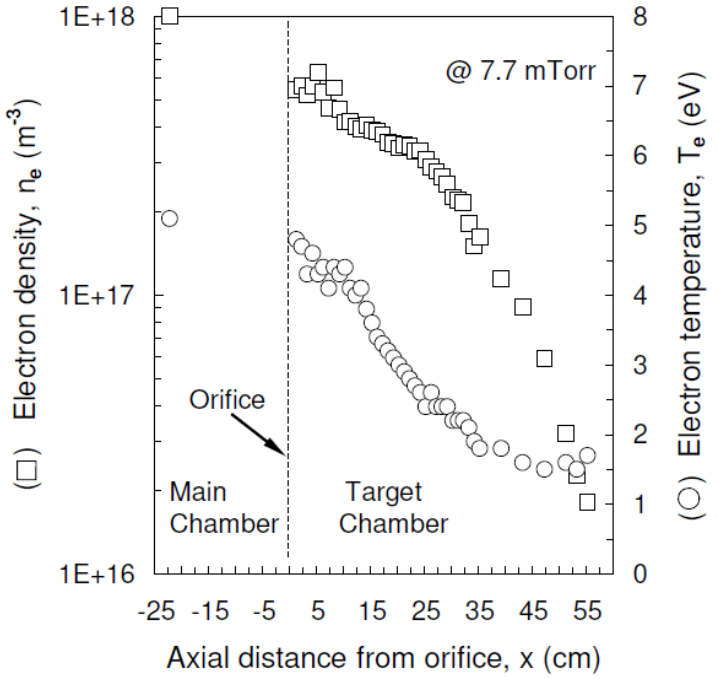

(a) MAR detachment; target chamber pressure of 7.7 mTorr (1.0×10^{-2} mbar).

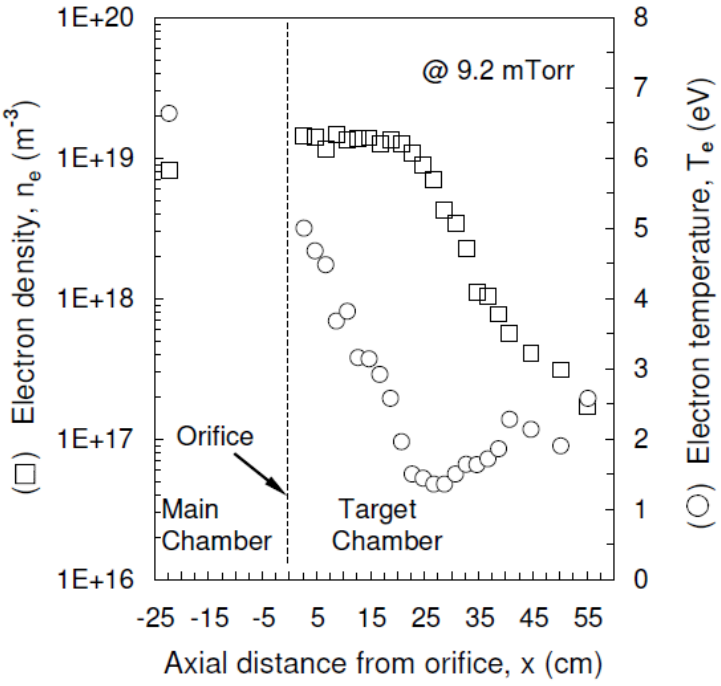

(b) EIR detachment; target chamber pressure of 9.2 mTorr (1.2×10^{-2} mbar).

Figure 4.2: Axial electron density (squares) and temperature (circles) profiles through the target chamber of the YLPD for (a) the MAR and (b) the EIR detachment regimes. The 'orifice' is the baffle; its location is taken as the 0 cm position. The target plate is located at 56 cm. Plots reproduced from [85].

An axial Langmuir probe was used to measure both density and temperature along the axis of the target chamber in the YLPD [85]. The profiles for the MAR case are shown in Figure 4.2a, and those for EIR detachment in Figure 4.2b. We see that both the density and temperature exhibit a steady decrease throughout the target chamber for the MAR case, and reflect the need for temperatures of a few eV to sustain the population of vibrationally excited molecules that is required (Section 2.1.3). In contrast, the EIR data shows that the density remains high while the temperature drops sharply, with n_e only starting to decrease once the temperature has reached $\sim 1\,\text{eV}$.

Given the unreliable nature of the Langmuir probe temperature measurements below 1 eV (see Section 3.2.1), a moveable OES probe was also employed to provide more accurate estimates of the temperature for the EIR case, by using a Boltzmann analysis of the hydrogen Balmer emission lines (discussed in Section 3.3.1). In the axial range $14-34\,\text{cm}$, termed the 'recombination zone', the OES analysis yields T_e values between 0.1 and 0.2 eV, an order of magnitude below those estimated by the Langmuir probe.

The recombination zone encompasses the position in Figure 4.2b where the density starts to drop sharply. These observations are consistent with the conditions expected for EIR: the recombination rate is fastest for high densities, but its inverse dependence on temperature ($\propto n^2 T^{-\frac{9}{2}}$) means that it can only become significant once the temperature has dropped to $\sim 1\,\text{eV}$. Hence, once T_e in the plasma is low enough, we see n_e start to decrease as the recombination process removes ions and electrons.

Full OES spectra comprise both the atomic hydrogen Balmer emission lines and Fulcher band emission, which arises from vibrationally excited states of molecular hydrogen. Mihajčić compares the behaviour of the two detachment regimes using two features of the spectra: the $^{H_\alpha}/_{H_\gamma}$ ratio (see Section 3.3.2); and the total emission from three of the strongest Fulcher band lines. The Fulcher emission is calculated by integrating over the three lines in the $v'-v''=2-2$ vibrational band, in the wavelength range $622-624\,\text{nm}$. The MAR and EIR axial profiles for both of these measures are plotted in Figure 4.3.

First, considering the $^{H_\alpha}/_{H_\gamma}$ ratio, we see that the MAR value remains fairly constant, particularly in the first 20 cm of the chamber, as the emission from all the Balmer lines decreases at the same rate. Beyond this point there is more variation, but this is likely to be attributable to difficulties in resolving the lines as they become weaker. For EIR, on the other hand, there is a significant drop between 5 and 15 cm, meaning that the population of the more highly excited state which produces the H_γ line is not decreasing as quickly

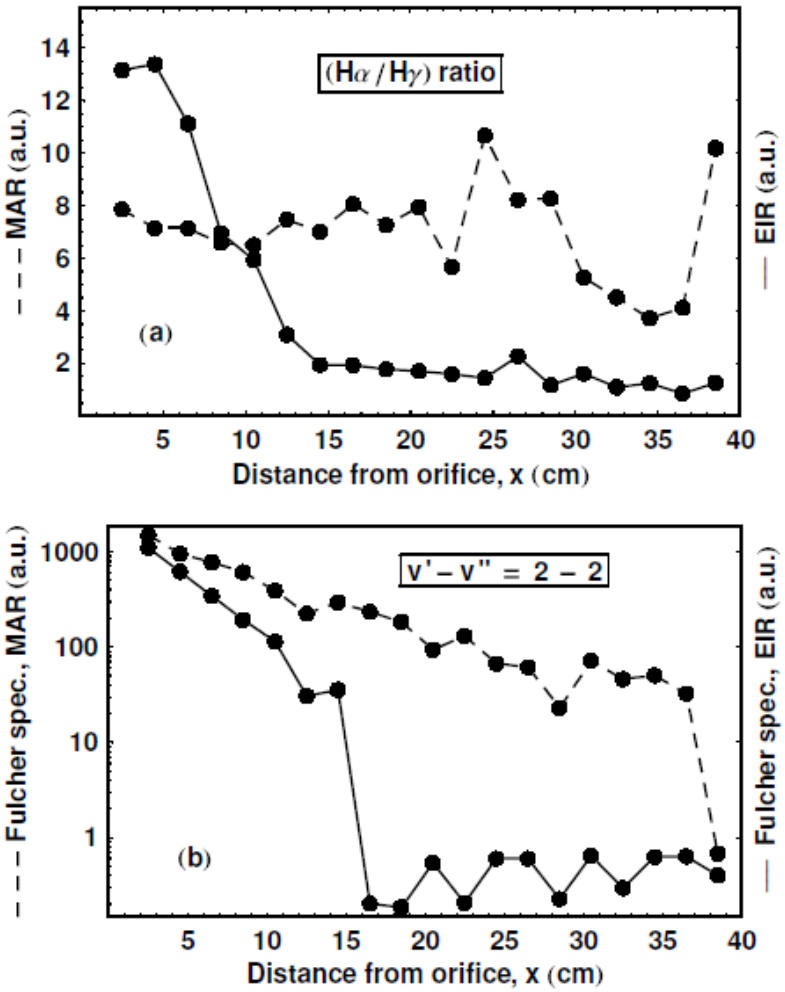

Figure 4.3: Variation of (top) the $^{H_\alpha}/_{H_\gamma}$ ratio and (bottom) the molecular Fulcher band emission throughout the target chamber for both the MAR (dashed lines) and EIR (solid lines) detachment regimes. The Fulcher band emission is calculated by integrating three lines in the $v' - v'' = 2 - 2$ vibrational band ($622 - 624\,\text{nm}$). The 'orifice' is the baffle; its location is taken as the 0 cm position. The target plate is located at 56 cm (beyond the range of the OES probe). Figure reproduced from [85].

as that which causes the H_α emission (or indeed may not be decreasing at all). The ratio remains low throughout the rest of the chamber.

The Fulcher band emission for the MAR case shows a steady decrease throughout the target chamber as the plasma cools, with a final, sudden drop at around 39 cm. OES data is not available beyond this point due to the limitations of the probe, but the low temperatures observed in the final 10 cm before the target plate (Figure 4.2a) indicate that there is no longer enough energy to excite molecules in this region. The sudden drop in the EIR case occurs at around 15 cm, coinciding with the start of the recombination zone. The extremely low temperatures in this region are undoubtedly unable to sustain vibrationally excited molecules. Prior to this point, the Fulcher emission exhibits a steady decrease similar to the MAR case, but with a steeper gradient, consistent with the faster rate of temperature decrease through the EIR detached plasma.

4.1.1.3 Radial profiles

The final experimental data considered here are radial profiles of density and temperature across the plasma column in both the MAR and EIR regimes (Figure 4.4). These profiles were taken with a Langmuir probe inserted radially from port F (see Figure 3.2), located approximately 25 cm from the baffle in the target chamber.

The MAR profiles are reasonably symmetric about the centre of the beam, peaking around the 0 cm position and decreasing as the radius increases. The full width half maximum (FWHM) value of the density plot (Figure 4.4a) is approximately 1 cm. The temperature profile (Figure 4.4b) appears to be slightly narrower (with a FWHM of $\sim$ 6 mm), but the larger errors make this plot harder to interpret, particularly outside ± 0.5 cm where the temperature drops below 1 eV.

The EIR profiles have fewer data points, and the accuracy is restricted by the low temperature values across the majority of the column. The density data (Figure 4.4c) shows a roughly symmetric peak around 0 cm, with n_e falling off by an order of magnitude within ± 0.5 cm. T_e only rises above 1 eV at the centre of the column (Figure 4.4d); all that can be inferred from the Langmuir probe data is that the temperature is likely to be below 1 eV in the edge region of the column. Mihaljčić also notes, from visual inspection of the EIR detached plasma (see Figure 4.5), that the 'blue glow' recombination zone has a radial extent that is greater than that of the plasma column that enters the target chamber through the baffle (estimating a radius of 3 cm, compared to 0.5 cm).

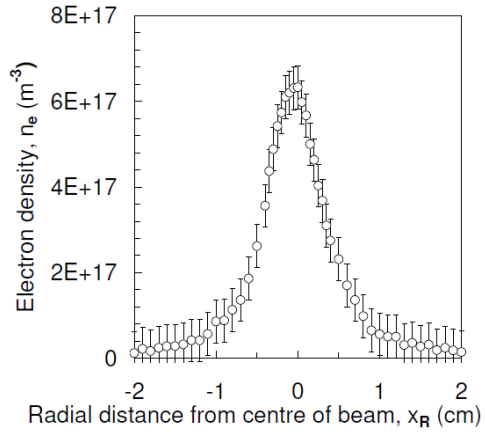

(a) Radial n_e profile (MAR).

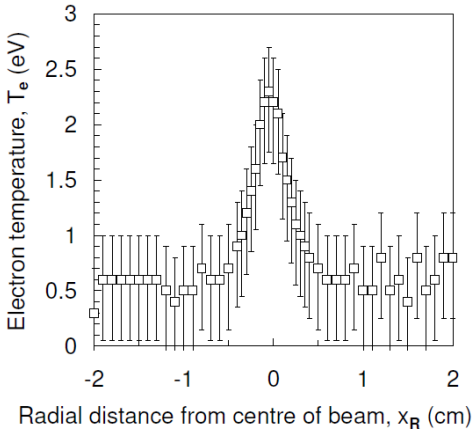

(b) Radial T_e profile (MAR).

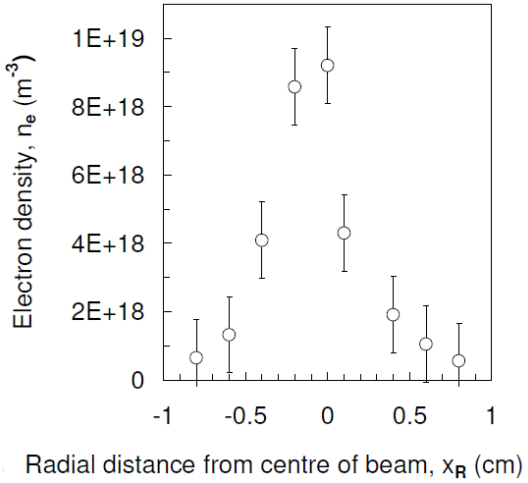

(c) Radial n_e profile (EIR).

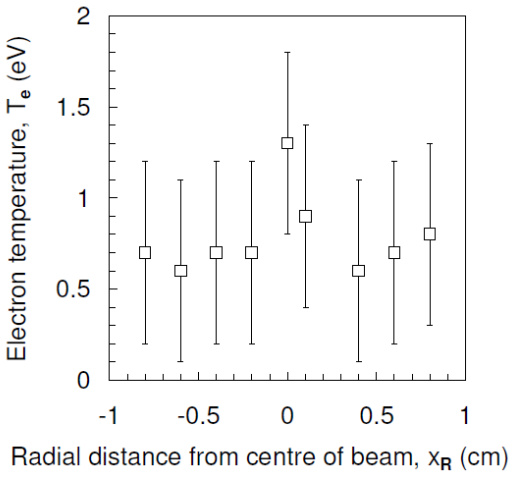

(d) Radial T_e profile (EIR).

Figure 4.4: Radial variation of density and temperature across the plasma column in the target chamber for both the MAR (top row) and EIR (bottom row) detachment regimes. The measurements were taken using a probe through port F (see Figure 3.2), approximately 25 cm downstream of the baffle. Figure reproduced from [85].

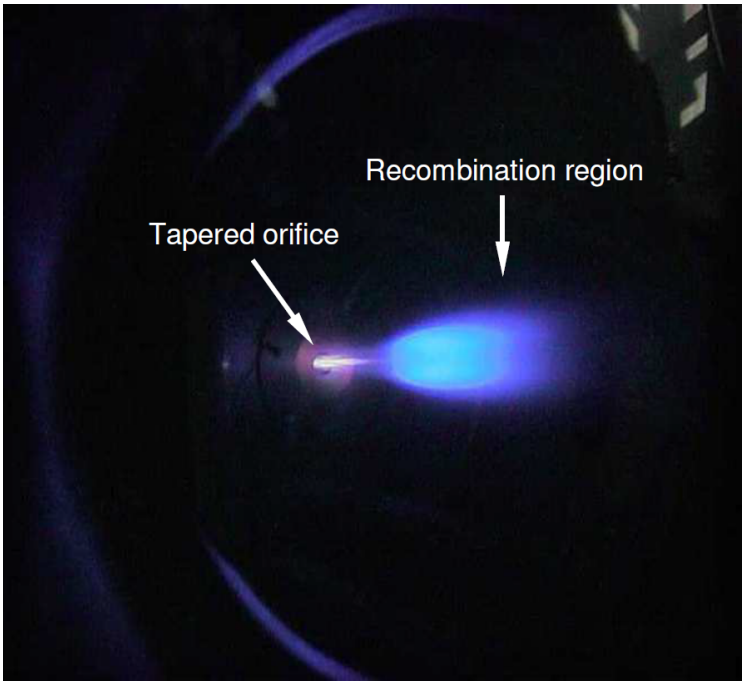

Figure 4.5: Photograph of an EIR detached plasma in the target chamber of the YLPD, as studied by Mihaljčić. In this work the aperture diameter is approximately 14 mm. Figure reproduced from [85].

These probe measurements were recorded using standard Langmuir probe methods, and thus were limited to millisecond time resolution (see Section 3.2.1). Mihaljčić acknowledges the work on the PISCES-A linear machine (Section 2.3.2), which concludes that, in that device, intermittent radial transport events ('blobs' of plasma with high radial velocities) are the most significant cause of plasma loss to the target plate, rather than recombination processes. These events can occur on shorter timescales than are detectable using a conventional Langmuir probe. To study this possibility on the YLPD, Mihaljčić employs a fast probe configuration, capable of recording data at a rate of 1 MHz.

The resulting radial profiles show the ion saturation current drawn by the probe as a proxy for density (Figure 4.6). The plot shows two pairs of profiles: one pair taken using the slow, conventional probe technique; and the other with the fast probe configuration. All profiles were recorded using the same upstream conditions (those used for the MAR case study), but one in each pair has gas injected into the target chamber, whereas the other does not. For the 'with gas' profiles, the target chamber gas pressure was raised to induce MAR detachment in the same way as for the case study. The 'no gas' profiles were taken from the attached plasma, with the target chamber gas valve remaining closed.

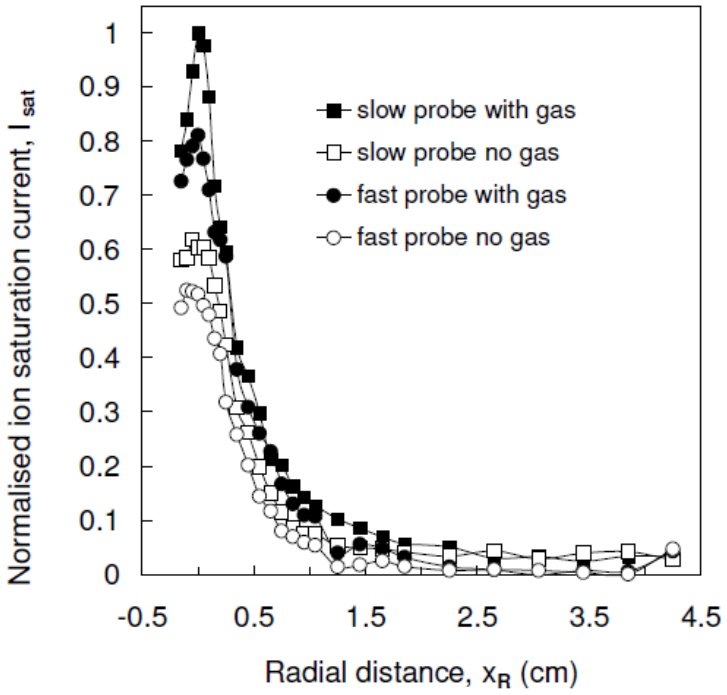

Figure 4.6: Variation of ion saturation current across the plasma column in the target chamber, as recorded by both 'slow' (< 1 kHz, square markers) and 'fast' (1 MHz, circular markers) probe methods. Data were taken for the same upstream plasma conditions as in Figures 4.4a and 4.4b: the 'with gas' data (filled markers) was taken in the detached state; and the 'no gas' data (open markers) was taken without the injection of neutral gas into the target chamber (attached conditions) for comparison. Figure reproduced from [85].

All four profiles are of similar shapes, peaking at the 0 cm position before falling away with a full width half maximum value of 1 cm, as previously observed. The slow probe technique measures peak values that are around 20% higher than those obtained from the fast configuration, but beyond a radius of $\sim$ 0.2 cm the differences are very small. This data provides no evidence that high-frequency radial transport effects are broadening the plasma column in the MAR detachment regime.

However, Mihaljčić does not repeat these measurements for EIR detachment, extending the MAR conclusion to suggest that radial transport does not play a role in either detachment regime. The failure to confirm the results for EIR may be a significant omission, particularly given the previously-noted observation that the EIR 'blue glow' recombination zone is visibly broadened compared to the upstream plasma column. This broadening is not apparent in the radial density profile obtained by the slow Langmuir probe technique, which could indicate that faster transport processes are present.

4.1.2 Modelling

To continue with the review of the previous detachment studies using the YLPD, we now consider the simulation work carried out by Mihaljčić [85]. He employs a one-dimensional fluid model (along the axis of the plasma column) to replicate some of the atomic and molecular processes which occur in the target chamber of the YLPD in both MAR and EIR detached plasmas. The model uses the particle and energy conservation equations, and includes ionisation as well as both electron-ion and molecular activated recombination.

By changing the initial conditions, Mihaljčić was able to simulate different upstream plasma conditions and use the predicted axial density and temperature profiles (along with those for particle and energy flux) to distinguish between MAR and EIR detachment cases. The EIR regime exhibits much steeper reductions in these profiles than MAR.

The resulting prediction for the threshold between MAR and EIR is plotted on Figure 4.1 in Section 4.1.1.1. This prediction is a similar shape in density and temperature space to the experimentally obtained threshold, but the density values are approximately an order of magnitude too high. The discrepancy could in part be due to the assumptions made in the model (for example ignoring convective terms for simplicity), but the limited accuracy of the Langmuir probe measurements may also contribute [85].

Another key result from the model is the attempt to replicate the axial density and temperature profiles for both the MAR and EIR case studies. These profiles are shown in Figure 4.7. The general trends of the experimental data are replicated well by the simulation, with gradual decreases in both n_e and T_e for the MAR case, and steeper gradients in the EIR regime. The temperature data are also reasonably quantitatively accurate (bearing in mind that the experimental EIR temperature data is overestimated by the Langmuir probe beyond $\sim 0.22\,\mathrm{m}$). The density values, on the other hand, are considerably overestimated by the code; again this may arise from a combination of the simplifying assumptions made in the model, and inaccuracies in the experimental technique.

The one-dimensional simulation used by Mihaljčić is able to replicate the behaviour of the plasma parameters along the axis of the YLPD relatively well. We can conclude that this simplified model provides a foundation for understanding the processes behind plasma detachment in both the MAR and EIR regimes, but the discrepancies that are observed between simulation and experiment indicate that this one-dimensional picture is insufficient for a full explanation.

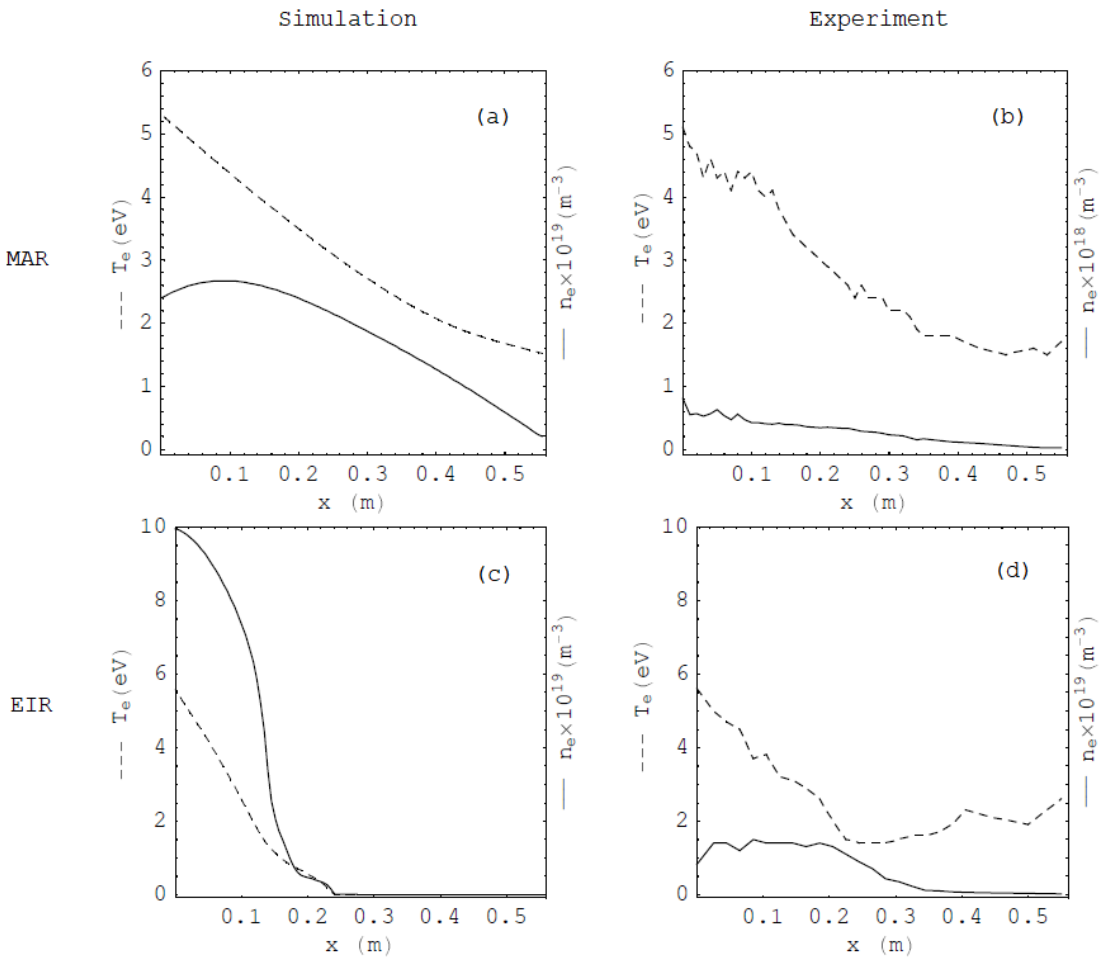

Figure 4.7: Comparison of the simulated and experimental axial profiles for temperature (T_e, dashed lines) and density (n_e, solid lines) for detached plasma regimes in the YLPD. The top row shows (a) the simulated and (b) the experimental profiles for MAR detachment. In the bottom row, we show (c) the simulated and (d) the experimental profiles for EIR detachment. Note that the experimental temperature profile beyond 0.22 m in the EIR regime, (d), is overestimated by approximately an order of magnitude (Section 4.1.1.2). The baffle is located at 0 m and the target plate at 0.56 m. Figure reproduced from [85].

4.1.3 Summary of previous work

The work carried out by Mihajčić investigates the conditions required to produce both MAR and EIR detachment in the YLPD, and provides a detailed case study of the time-averaged properties of each regime. The threshold between MAR and EIR in terms of the upstream plasma density and temperature is well characterised, and can be qualitatively reproduced by a simplified one-dimensional fluid model of the plasma (although the approximations lead to discrepancies in the predicted densities of approximately a factor of ten, as shown in Figure 4.1).

Langmuir probe and optical emission spectroscopy diagnostics are used to produce axial profiles of the plasma density and temperature for both regimes. These clearly highlight the differences between the two recombination mechanisms, particularly in the temperature profiles. In the MAR regime, the relatively high ($2 - 5\,\mathrm{eV}$) electron temperatures that are required to produce the vibrationally excited molecules are observed. In contrast, the EIR case exhibits the $< 1\,\mathrm{eV}$ temperatures that increase the three-body recombination rate. These experimental profiles are also reasonably accurately predicted by the 1D model, although again the absolute density values are overestimated by up to an order of magnitude.

Two important shortcomings of this work are: the focus on only one dimension of the system (on-axis through the target chamber); and the use of primarily time-averaged measurements, with resolution on timescales of milliseconds or longer. Mihajčić acknowledges this in discussing a range of possible improvements to his work, suggesting alternative diagnostic techniques to further investigate the intermittent radial transport of plasma 'blobs', and the use of radially resolved emission spectra to map the plasma parameters over two dimensions [85].

As noted in Section 4.1.1.3, these shortcomings are manifest in the omission of short-timescale measurements of the EIR detached plasma. The broadening of the plasma column in the recombination zone, observed through visual inspection, is not reflected in the slow probe measurements, and consequently has not been properly quantified. It is possible that this broadening may be occurring on much faster timescales. The key focus of the current study, therefore, is to extend the characterisation of the EIR detachment regime to two dimensions, and employ higher frequency diagnostic techniques to capture shorter timescale events.

4.2 Further observations

Before introducing further diagnostics, the first aim was to create an EIR detached plasma comparable to that studied by Mihaljčić, and characterise it in a similar manner. The YLPD system has altered in the intervening period, with upgrades to the vacuum pumps and power supplies, and it was therefore necessary to confirm that EIR detachment could still be obtained.

The current diagnostics are limited to a single axial position in the target chamber, approximately 25 cm downstream of the baffle. A Langmuir probe (able to move across a plane perpendicular to the plasma column) is fixed through the port opposite port F, and optical emission spectra were recorded in the same plane through port G (see Figure 3.2). The Langmuir probe was used for ion saturation current, density and temperature measurements, and optical emission spectroscopy (OES) for $^{H_\alpha}/_{H_\gamma}$ ratios, as well as a more accurate estimation of the temperature of the EIR detached plasma. In addition, the total ion saturation current to the end plate of the YLPD was measured. The results from these diagnostics are discussed in Sections 4.2.1 - 4.2.4.

These plasma characteristics were observed as the flow of neutral hydrogen into the target chamber was increased to produce a stable, EIR detached plasma (determined by visual inspection of the 'blue glow' of the EIR regime). A number of profiles were therefore obtained which show the evolution of these parameters with target chamber pressure, from the initial attached state to full EIR detachment. An example image of an EIR detached plasma from the current study is shown in Figure 4.8 (cf. Figure 4.5).

The final data presented in this section are the hydrogen Balmer emission profiles across the diameter of the EIR detached plasma column, as recorded by Lisgo (Section 4.2.5) [88]. Again, these time-averaged measurements were taken through port G, at an axial position of $\sim$ 25 cm downstream of the baffle.

It should be noted that the some of the above data sets were recorded during separate periods of operation, due to various technical limitations. In order to reproduce the starting attached plasma conditions as closely as possible for each set of data, the same magnetic field strengths and cathode and DC emission currents were used. The flow of hydrogen gas to the source was then altered to adjust the potential across the intermediate electrode, V_{IE}.

Matching V_{IE} resulted in some variation of initial gas pressure in the target chamber (ranging between 2.3×10^{-4} and 3.6×10^{-4} mbar), but only a small ($\sim$ 2 %) variation

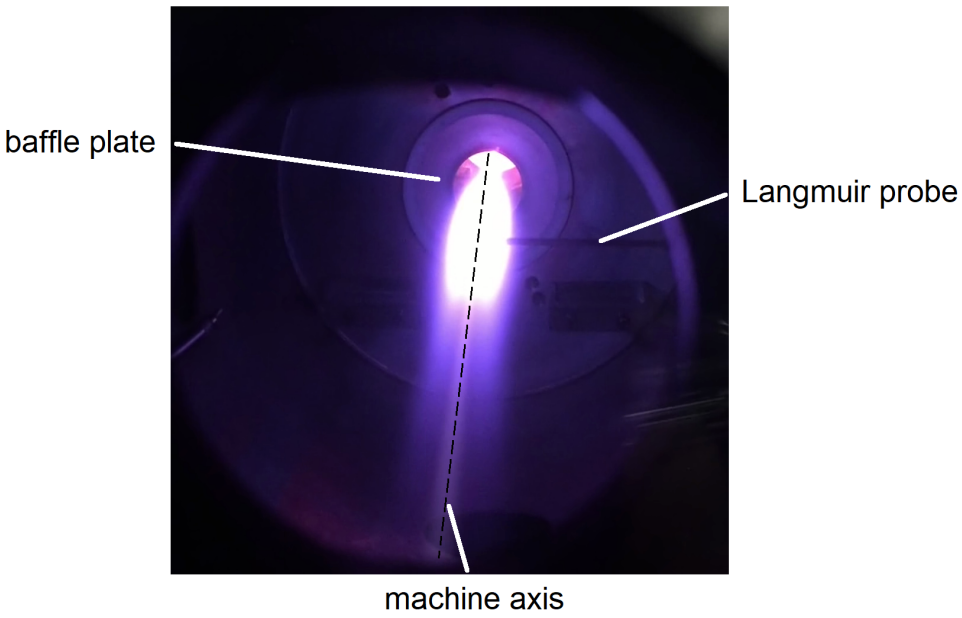

Figure 4.8: Photograph of an EIR detached plasma in the target chamber of the YLPD. The view is through the port in the end plate (port J, Figure 3.2), and the Langmuir probe used for IV measurements enters from the port on the right. The blue glow (which appears white in the brightest region) around the central plasma column is indicative of the detached regime.

in DC bias voltage, and hence in the input power to the plasma. This approach was found to yield more consistent plasma detachment than matching the gas flow and initial chamber pressure. To illustrate this, repeat data (referred to as data sets 1 and 2) for the ion saturation current, electron temperature and hydrogen emission line ratios are presented in the following sections. A comparison of the plasma conditions used for these observations and the EIR case study used by Mihaljčić is made in Section 4.2.6.

4.2.1 Ion saturation current

To improve the reliability of the results, the ion saturation current, I_{sat}, is considered as a proxy for the plasma density: the density calculation involves the temperature that is estimated from the Langmuir probe IV curve and therefore introduces further errors (Section 3.2.1). At each pressure, five IV curves were recorded, each in themselves an average of ten voltage sweeps in order to reduce noise in the data. Example IV curves for both the centre and edge probe positions in attached and EIR detached plasmas are shown in Figure 4.9.

The four-parameter fitting analysis (see (18) in Section 3.2.1) was carried out for all five IV curves at every pressure value. The resulting five I_{sat} values were averaged to produce one data point for each target chamber pressure. This was repeated with the probe positioned in the centre of the plasma column (0 mm, Figure 4.10a) and in the edge, at a radial position of 3 mm (Figure 4.10b). The error bars shown on the plots arise from the difference between the full fit to the IV curves and a fit to only the ion saturation region (excluding the exponential term) in each case.

Data sets 1 and 2 are qualitatively very similar. The 0 mm profiles initially show a slow rise, before a sharp increase at around $(1-2)\times10^{-3}$ mbar. A broad ($\sim 2\times10^{-3}$ mbar width) peak follows this jump (the 'rollover' which indicates the onset of detachment), which then decreases slowly to approximately half the maximum value in the final, detached state. There are some quantitative differences: the sharp increase occurs at a pressure that is approximately 4×10^{-4} mbar lower for Set 2 than Set 1; the peak is broader in Set 2; and I_{sat} is slightly higher for Set 1 as detachment is reached. However, given the errors, and the differing initial operating conditions (as discussed above), the agreement between the two sets of data is very good.

The edge (3 mm) profile values are generally a factor of ~ 6 weaker than the central data, in line with the radial decrease in density that Mihaljčić observed in the EIR detached plasma. The peaked 'rollover' is still seen at just over 2×10^{-3} mbar, where I_{sat} starts to decrease as the pressure increases further. In this case, however, the jump is less sharp and the final decrease appears to flatten out slightly beyond 5×10^{-3} mbar. In general, I_{sat} is slightly higher for Set 1, but the overall behaviour of the profile is reproduced well.

The 'rollover' shape of the profiles as the target chamber gas flow is increased is similar to that observed in the plots of target density against core density as detachment is induced in tokamaks (an example from ASDEX was shown in Figure 1.9). In the YLPD, the gas flow to the upstream plasma is not increased, but adding neutral hydrogen gas to the target chamber does appear to increase the ion saturation current (and hence the density) before the rollover occurs. Visual inspection of the plasma in the target chamber shows that there is an initial increase in the brightness of the attached plasma when the additional gas is first introduced, which also suggests that the density of the plasma is increasing.

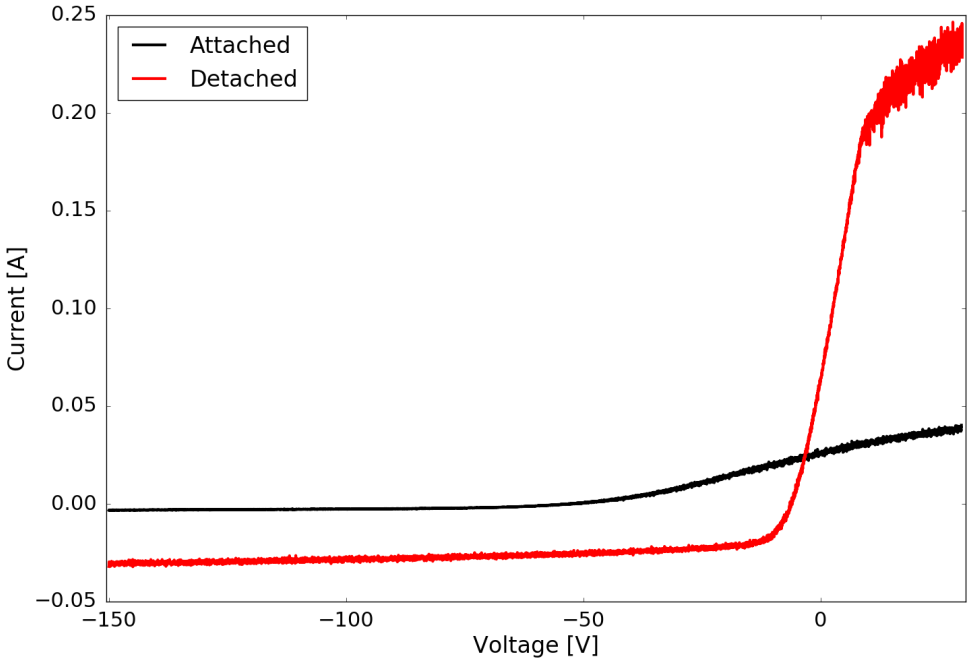

(a) IV curves from the centre of the plasma column.

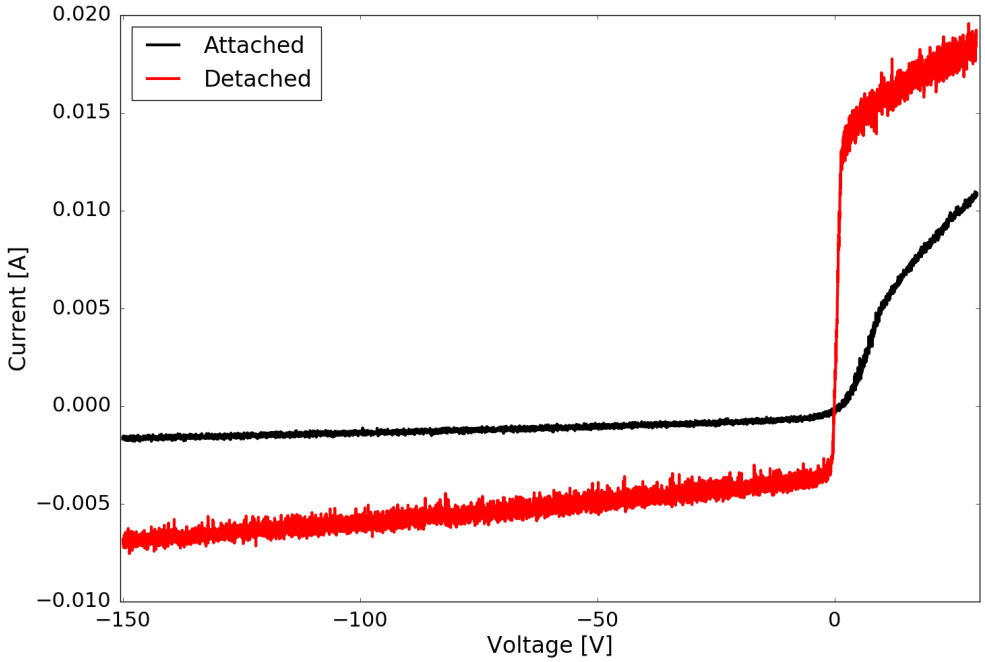

(b) IV curves from the edge (3 mm) of the plasma column.

Figure 4.9: Example IV curves from the Langmuir probe at (a) 0 mm (the centre of the column) and (b) 3 mm (in the edge of the column), for both attached (target chamber pressure 2.3×10^{-4} mbar, in black) and EIR detached (8.75×10^{-3} mbar, in red) plasmas.

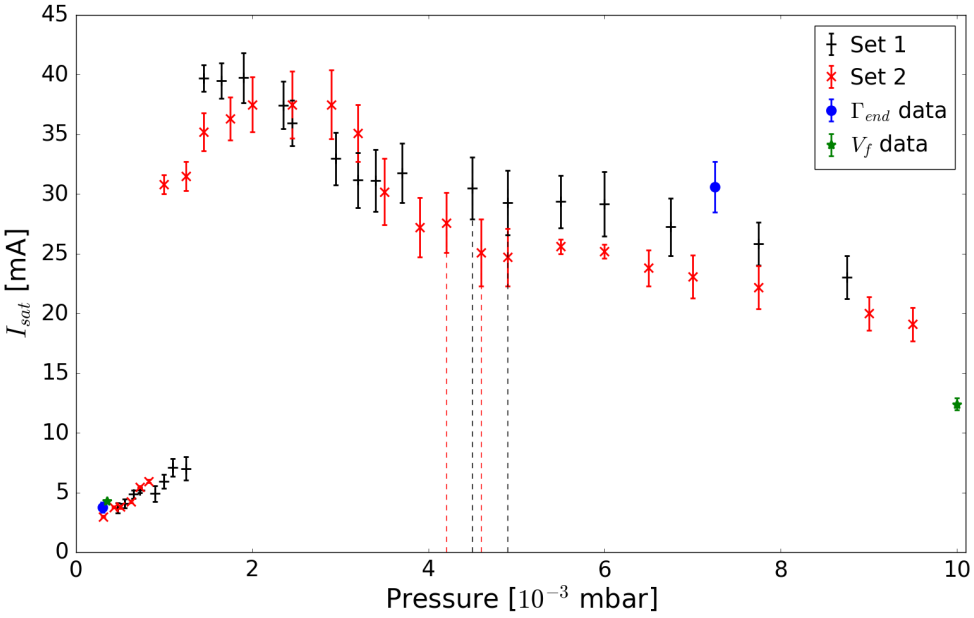

(a) Centre (0 mm) profiles.

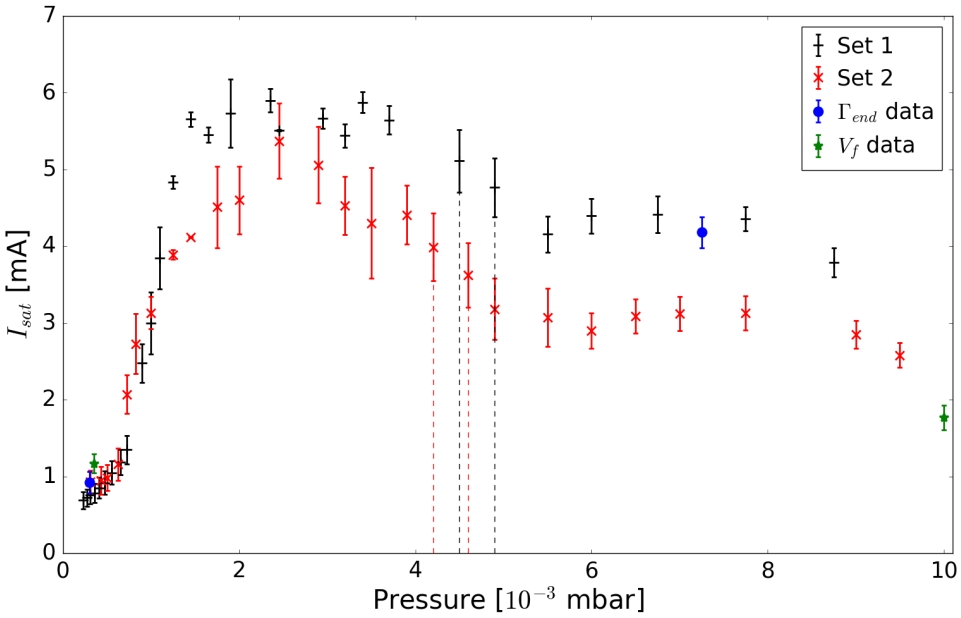

(b) Edge (3 mm) profiles.

Figure 4.10: Evolution of I_{sat} at (a) the centre (0 mm) and (b) the edge (3 mm) of the plasma column with pressure in the YLPD target chamber as EIR detachment is induced. Repeat measurements produced data sets 1 (+, in black) and 2 (×, in red). Dashed lines indicate the pressure ranges in which the onset of the 'blue glow' of the EIR detached state was first observed for each data set. Blue circles and green stars show the attached (low pressure) and detached (high pressure) Langmuir probe T_e values at both 0 and 3 mm, for the plasma in the Γ_{end} (Section 4.2.3) and V_f (Section 5.2) experiments respectively.

4.2.2 Temperature

The same IV curves which yielded the I_{sat} data above were also used to estimate the evolution of the electron temperature at the 25 cm axial position as EIR detachment was induced. Figures 4.11a and 4.11b show the resulting profiles for the centre (0 mm) and edge (3 mm) radial positions respectively. Errors were estimated by adjusting the temperature parameter in the fits to the IV data to obtain approximate upper and lower bounds.

The 0 mm data shows an initially high temperature (roughly 10−15 eV) which decreases steadily beyond $\sim 1 \times 10^{-3}$ mbar to a final value of approximately 3 eV. The start of the decrease coincides with the location of the sharp increase in I_{sat}. The difference between the initial Set 1 and Set 2 values is likely to arise from the variation in the start-up conditions that has previously been discussed. There is also some discontinuous variation within each data set at pressures below 1×10^{-3} mbar, which can be attributed to more difficulty in fitting the data (as indicated by the larger errors).

The edge profiles have a similar shape, although the absolute values are lower by a factor of three or more, starting at around 3 eV and reducing to below 1 eV. As for the I_{sat} (density) data, we expect to see lower values as we travel radially outwards from the centre of the plasma column (as seen by Mihaljčić). The decrease begins at a slightly lower pressure than for the 0 mm data, which is also to be expected, since the neutral gas will predominantly interact with the more easily-cooled plasma in the edge region. The edges of the column are less well heated by the core plasma (which is in direct contact with the source).

The onset of detachment (denoted by the dashed lines in Figure 4.11) occurs just after the temperature decreases below 1 eV in the edge of the plasma column. This is consistent with the expectation that the plasma enters the EIR detachment regime when $T_e < 1$ eV: once the temperature has cooled sufficiently, three-body recombination starts to dominate the behaviour and the 'blue glow' becomes visible. The temperature drops further as the pressure is increased and the plasma continues to cool, until stable detachment is reached.

The inaccuracy of temperature measurements below 1 eV using the Langmuir probe technique means that the 3 mm temperature profiles are likely to only provide an upper bound beyond $\sim 4 \times 10^{-3}$ mbar. Where possible, more accurate temperatures for the 'blue glow' region at the edges of the column were calculated from Boltzmann analysis of the hydrogen Balmer emission spectrum (Section 3.3.1). Spectra were collected through port G with exposure times of 700 ms (concurrent with the Set 1 Langmuir probe data) and

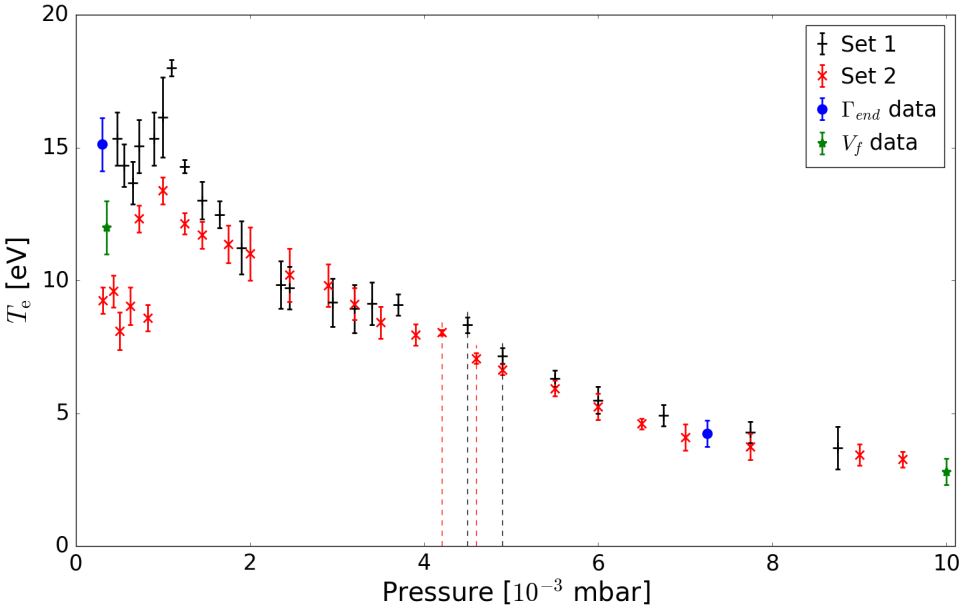

(a) Centre (0 mm) profiles.

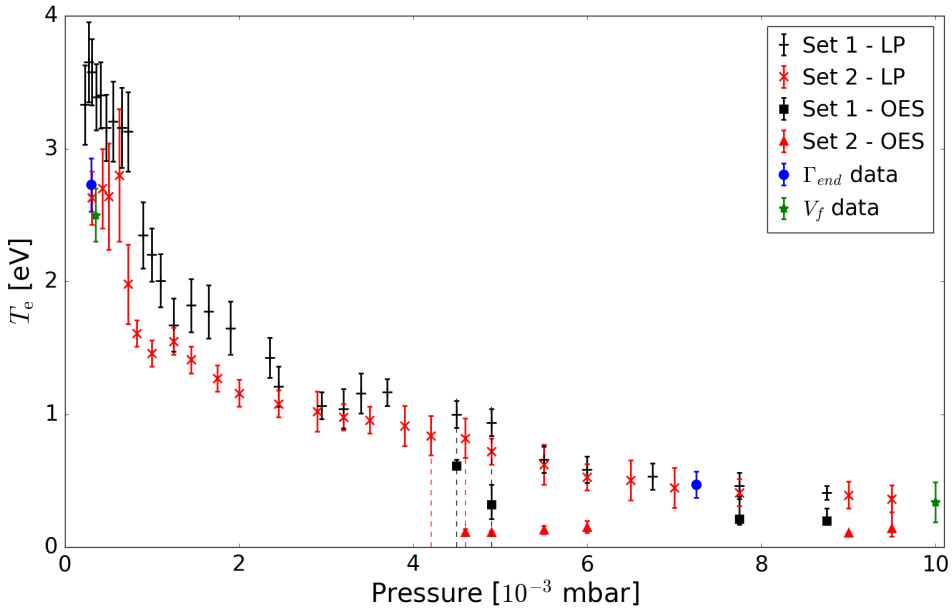

(b) Edge (3 mm) profiles (Langmuir probe: black + and red ×. OES: black ■ and red ▲).

Figure 4.11: Evolution of T_e at (a) the centre (0 mm) and (b) the edge (3 mm) of the plasma column with pressure in the YLPD target chamber as EIR detachment is induced. Repeat measurements produced data sets 1 (in black) and 2 (in red), and in (b) additional OES measurements (from the 'blue glow' in the column edge) are denoted by squares and triangles. Dashed lines indicate the pressure ranges in which the onset of the EIR detachment 'blue glow' was first observed for each data set. Blue circles and green stars show the attached and detached Langmuir probe T_e values at both 0 and 3 mm, for the plasma in the Γ_{end} (Section 4.2.3) and V_f (Section 5.2) experiments respectively.

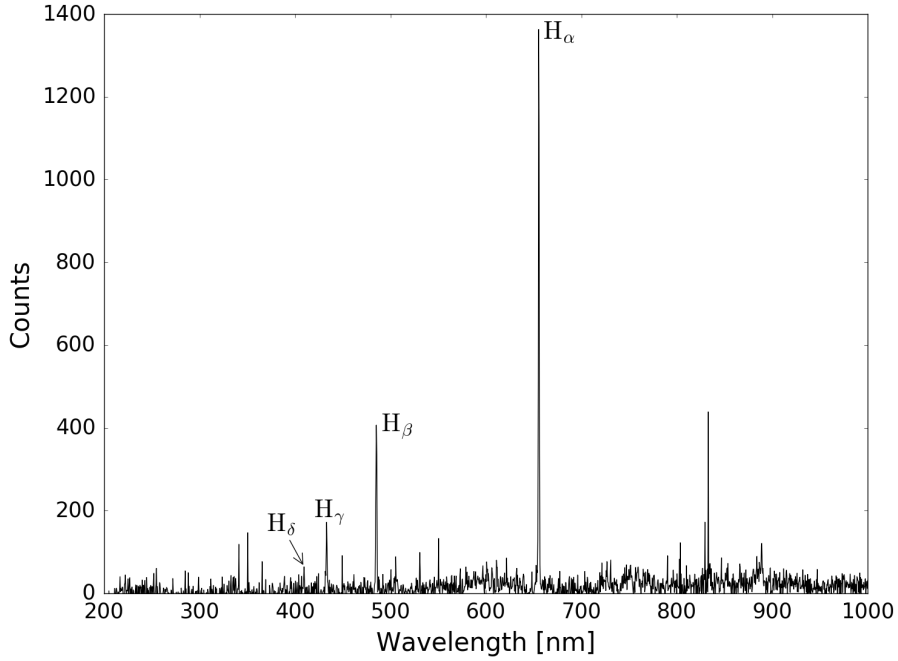

(a) Spectrum from the attached plasma column, showing H_α (656.3 nm) to H_δ (410.2 nm).

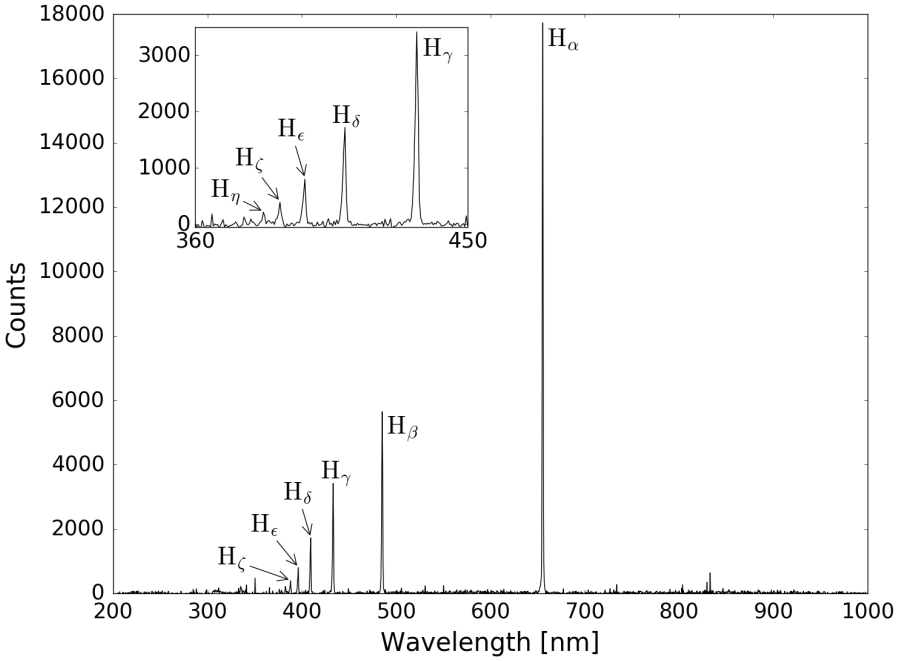

(b) Spectrum for the EIR detached plasma, showing H_α (656.3 nm) to H_η (383.5 nm, inset).

Figure 4.12: Visible emission spectra (700 ms exposure) of (a) the attached and (b) the EIR detached plasma at a position 25 cm from the baffle in the YLPD target chamber. The Balmer emission lines are labelled.

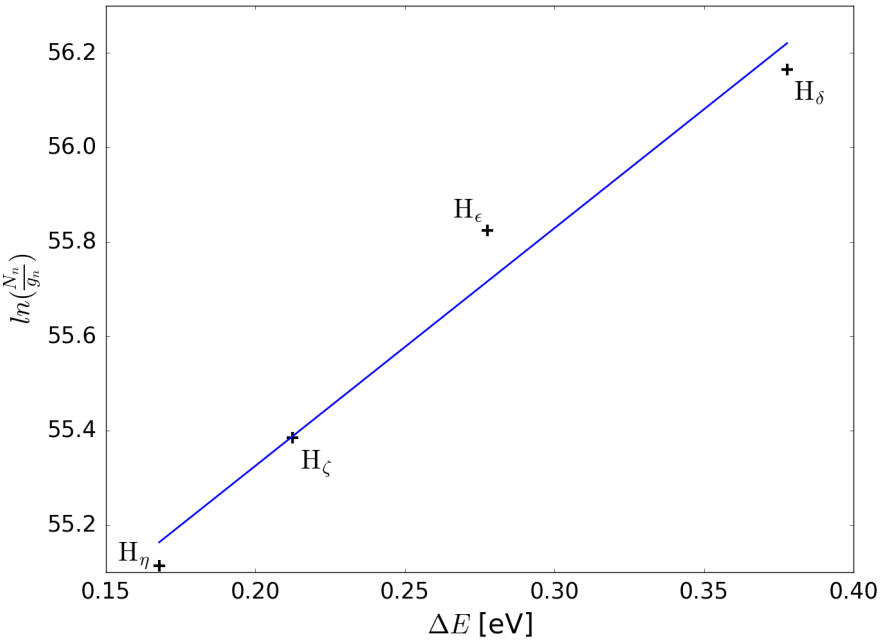

Figure 4.13: Boltzmann analysis plot from the spectrum shown in Figure 4.12b. Data points are labelled with the corresponding emission line; the blue line is the fit used to estimate the temperature, yielding a value of $(0.20^{+0.09}_{-0.03})$ eV. Error bars are derived from a 10% error estimate in the spectral line integration.

1000 ms (concurrent with Set 2). Examples for the Set 1 pressures of 2.30×10^{-4} mbar (attached) and 8.75×10^{-3} mbar (detached) are shown in Figures 4.12a and 4.12b respectively. The spectra are analysed further in Section 4.2.4, but here only those pressures where Boltzmann analysis is possible are considered. These vary between the two data sets. Enough high-n lines must be measurable, and the excited levels must meet the local thermal equilibrium approximation (see Section 3.3.1).

The resulting T_e estimates are plotted in Figure 4.11b, for all pressures in data sets 1 and 2 where the Boltzmann analysis could be carried out. An example Boltzmann plot, corresponding to the detached plasma in Set 1 (8.75×10^{-3} mbar), is shown in Figure 4.13. In this case, the H_δ to H_η lines are used, as a reasonable linear fit to the data can be obtained. For all other OES data points, the H_δ line was not included: its population was not in local thermodynamic equilibrium and the data point did not fit a straight line.

The OES temperature estimates suggest that the Langmuir probe results overestimate T_e by up to a factor of two in the edge of the detached plasma (above $\sim 4 \times 10^{-3}$ mbar),

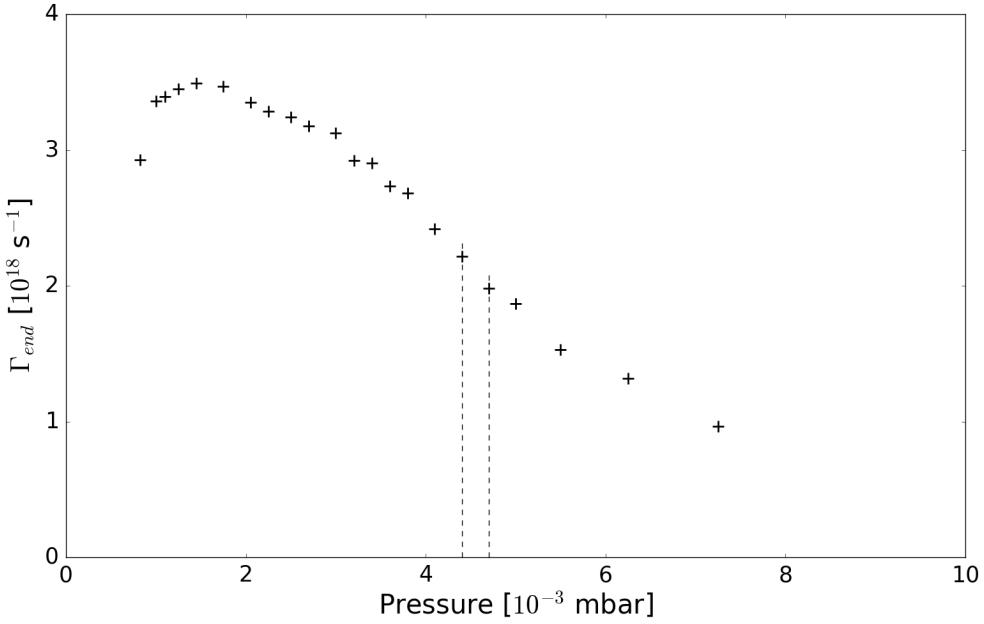

Figure 4.14: Variation of the plasma flux to the end plate with pressure in the YLPD target chamber. The dashed lines indicate the pressure range in which the onset of the 'blue glow' of the EIR detached state was first observed.

although there is greater variation between the data sets around the onset of detachment. The larger T_e values calculated from the probe data in the centre of the column are likely to be more reliable, as they do not decrease below $\sim$ 3 eV. Visual inspection of the detached region of the plasma suggests that the blue glow region dominates in the edges of the column (see Figure 4.8), meaning that it is possible that the electron temperature remains higher in the centre.

If these T_e profiles are again compared with those obtained from ASDEX (Figure 1.9), we find that the behaviour is similar. The initial high temperature decreases steadily as the density peaks and rolls over, although the absolute values differ (to be expected given the differences between the machines).

4.2.3 Target plate flux measurements

The total plasma flux to the end plate of the machine (Γ_{end}) was measured as a function of target chamber pressure (see Section 3.4 for details), in a separate experiment. As noted in Section 3.4, a grounding issue meant that the plate was not biased to the ion saturation region, and hence the data are presented as a measure of the total plasma flux to the

plate. Data were not acquired below a target chamber pressure of 8×10^{-4} mbar, but the measurements made are still sufficient to show the expected rollover in Γ_{end} as the pressure increases and the plasma detaches. The results are plotted in Figure 4.14. For this data the rollover peak occurs at approximately 1.5×10^{-3} mbar: a slightly lower pressure than was observed in the I_{sat} profiles. Standard errors for the data were calculated, but are negligibly small.

The Langmuir probe at the 25 cm axial position was used to measure the ion saturation currents and electron temperatures at the 0 and 3 mm radial positions for the initial and final pressure values in the Γ_{end} data set. These data points are plotted in Figures 4.10 and 4.11 in the previous section, in order to compare the operating conditions with those that produced the full I_{sat} and T_{e} pressure profiles. The data for the Γ_{end} plasma are consistent with the previous profiles, indicating that the observed behaviour of Γ_{end} is representative of the general EIR detached state in the YLPD.

The shape of the Γ_{end} profile is reasonably consistent with that of the ion saturation current, as is expected given the dependence of both of these quantities on the plasma density. The peak of the rollover appears at a slightly lower pressure than that of I_{sat}, but given that the Langmuir probe is positioned $\sim$ 30 cm upstream of the target plate, and the detachment front propagates up from the target, this observation is not inconsistent with expectations.

4.2.4 Hydrogen emission line ratio

Finally, the ratio of the α and γ hydrogen Balmer emission lines ($^{\mathrm{H}_\gamma}/_{\mathrm{H}_\alpha}$) was studied. Spectra, such as those shown in Figure 4.12, were recorded concurrently with the Langmuir probe IV curves that produced the I_{sat} and T_{e} data as the pressure in the target chamber was increased (see Section 3.3.2). The exposure times were 700 ms for Set 1 and 1000 ms for Set 2. $^{\mathrm{H}_\gamma}/_{\mathrm{H}_\alpha}$ is plotted against target chamber pressure for both sets in Figure 4.15. The errors were estimated by varying the width of the integration region for each peak.

The general trends for each data set are similar, although there is some variation (up to a factor of two) in the values, which is likely to relate to the differing temperatures estimated by the OES analysis (Figure 4.11b). An initial sharp decrease in $^{\mathrm{H}_\gamma}/_{\mathrm{H}_\alpha}$ indicates the rising dominance of the H_α line, with the minimum coinciding with the pressure at which I_{sat} (and hence the plasma density) is highest. In this region, ionisation is the main process occurring in the plasma. As the pressure in the target chamber increases further,

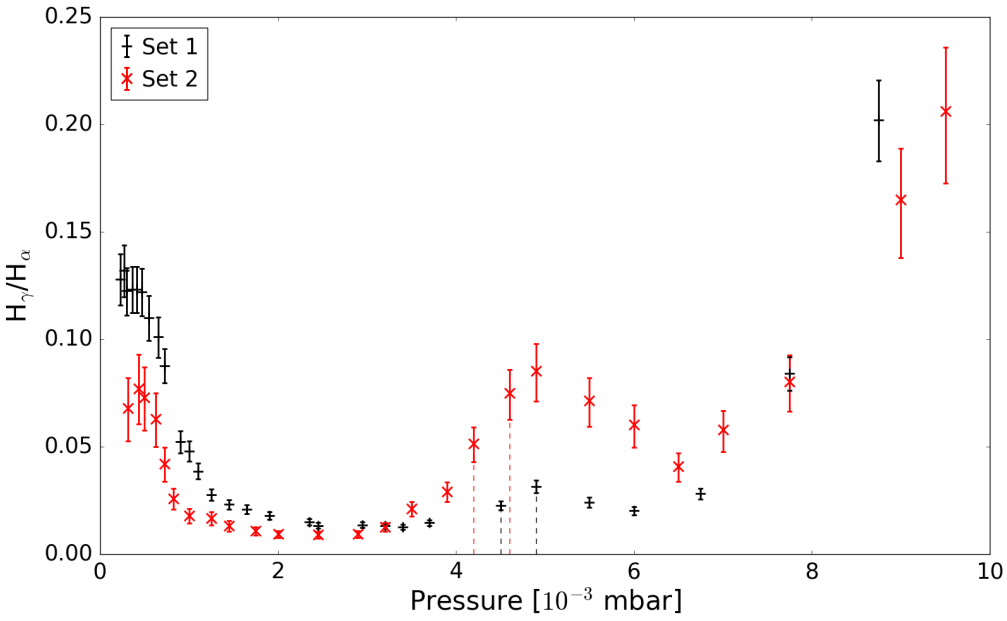

Figure 4.15: Variation of the H_γ/H_α ratio at 25 cm from the baffle as a function of pressure in the YLPD target chamber. The measurements were repeated to produce data sets 1 (+, in black) and 2 (×, in red). The dashed lines indicate the pressure ranges in which the onset of the 'blue glow' of the EIR detached state was first observed for each data set.

the ratio increases, and a local maximum occurs just after the initial appearance of the 'blue glow' of the detached state. H_γ/H_α then decreases again before rising sharply to reach the maximum value in the fully stable, EIR detached state. The relative strength of the H_γ line is therefore greatest in the detached plasma, which is consistent with the excited high-n atomic states that are expected to be produced by the recombination reactions which result in EIR detachment.

4.2.5 Radial emission profiles

The radial emission profiles of the EIR detached plasma produced by Lisgo are now considered [88]. These profiles were calculated for the H_α to H_δ Balmer lines using Abel inversion of optical emission imaging data. Figure 4.16 shows the radial profiles for the 25 cm axial position, with an inset showing a 2D colour map of the H_γ emission.

These profiles are symmetrical about the axis, but hollow: peaks appear in all four lines at approximately ±6 mm. The 'blue glow' of the Balmer emission therefore arises predominantly in the edges of the plasma column (the central column having a diameter

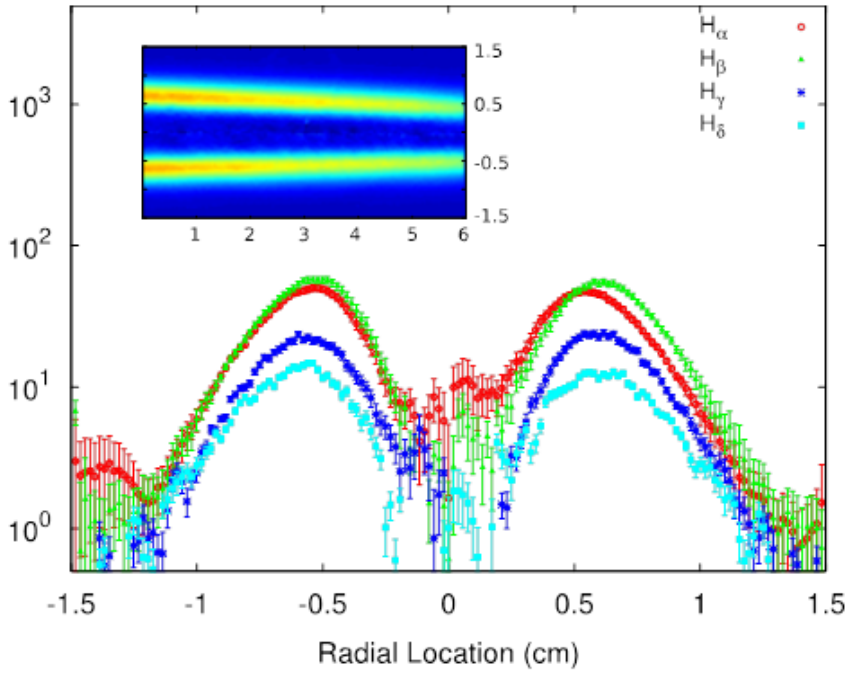

Figure 4.16: Main plot: Abel inverted radial profiles of four Balmer emission lines (H_α, H_β, H_γ and H_δ) across the EIR detached plasma column in the YLPD, at an axial position of 25 cm. Inset: 2D colour map of the radial and axial variation of the H_γ emission throughout the target chamber for the EIR detached plasma, with axial (x) and radial (y) dimension units in centimetres. Figure courtesy of S. Lisgo [88].

of a few millimetres), confirming the observations made from visual inspection of the EIR detachment regime. This is consistent with the Langmuir probe temperature estimates: in the column edges, the observed < 1 eV temperatures mean that T_e is low enough for three-body recombination to take place. In the centre of the column, however, the ~ 3 eV temperatures reduce the recombination rate, leading to less Balmer emission. These data provide strong evidence for the broadening of the plasma column when EIR detachment occurs.

4.2.6 Comparison to previous EIR case study

To enable a comparison between the above plasma conditions and Mihaljčić's EIR case study, the plasma density was estimated from the 0 mm IV curves. The initial downstream density is approximately $1 \times 10^{18}\,\mathrm{m}^{-3}$, with the peak value around a factor of ten higher. The low temperatures in the detached state make the density estimate at the highest pressures unreliable, but it lies in the range $10^{18} - 10^{19}\,\mathrm{m}^{-3}$.

Mihaljčić measures the density of the EIR detached plasma at 25 cm into the target chamber to be just under $1 \times 10^{19}\,\mathrm{m}^{-3}$ [85]. In the main chamber (effectively in the attached state) in the centre of the plasma column, he records $1.5 \times 10^{19}\,\mathrm{m}^{-3}$. These values are reasonably consistent with our more recent observations.

The central temperatures observed by the Langmuir probe in the attached plasma in the current study (around 15 eV) are almost a factor of three higher than the values obtained by Mihaljčić (5 eV at the baffle). The probe estimate of T_e in the centre of the detached plasma also remains relatively high at $3 - 4\,\mathrm{eV}$, whereas the previous study recorded $1 - 2\,\mathrm{eV}$. T_e in the edge region of the plasma column, however, is more consistent with the temperatures observed by Mihaljčić. In the attached plasma, it is below 4 eV, dropping to $< 1\,\mathrm{eV}$ (measured by the Langmuir probe) for the detached plasma. The OES temperature results for the detached plasma at the 25 cm axial position differ by a factor of two: 0.2 eV compared to the previous value of 0.1 eV.

These temperature differences are likely to arise from the altered operation conditions of the YLPD. The increased axial magnetic field strength (previously 50 mT, now 95 mT) and variation in cathode size, the emission current provided by the DC bias voltage, and the gas flow change the optimum operating parameters for the machine, which may affect the plasma parameters. In particular, the increased emission current (15 A compared to 8 A) means that the input power is greater, which is the most likely cause of the increased electron temperature in the centre of the plasma. It is harder to determine the effect on the density due to the errors in the Langmuir probe analysis. It is possible that the higher power results in the central region remaining dense and hot, while the behaviour observed by Mihaljčić is more accurately replicated in the cooler edge of the column.

Despite the differences in quantitative values, particularly in the column centre, the general behaviour of the plasma parameters follows the trends expected from the onset of EIR detachment, and the visual observations of the detached state match well (Figures 4.5 and 4.8). The results suggest that it is the cooler edge region of the plasma that is most important for EIR detachment, in the broadened 'blue glow' recombination zone.

4.3 Modelling the time-averaged radial behaviour

In light of the observations presented above, we propose that the inclusion of the radial behaviour of the plasma is vital to a full description of EIR detachment in the YLPD, and that fast (sub-millisecond timescale) events could play an important role in this. We

suggest a hypothesis in which 'blobs' of plasma are intermittently ejected radially outwards from the centre of the plasma column. If these blobs occur frequently enough, and cool quickly as they disconnect from the hot core of the column, they could create high density, low temperature regions in the plasma edge in which three-body recombination could occur at a sufficiently high rate to produce the observed detached plasma.

Such transient events would not be individually discernable on the timescales of the measurements discussed thus far, but when averaged over time could lead to a broadened radial density profile. As an initial study of the plausibility of this hypothesis, a simple model is presented to estimate the extent to which changing the density and temperature profiles across the plasma column affects the balance between EIR and excitation processes.

The simulation compares the two sets of plasma density (n) and electron temperature (T_e) profiles shown in Figure 4.17. One set of profiles corresponds to the peak density attached plasma, and the other to the final stable EIR detached state (target chamber pressures of $\sim 2\times10^{-3}$ and $\sim 9\times10^{-3}$ mbar respectively). Simple, Gaussian-like Pearson VII functions, covering the radial range over ±4 mm, were chosen to reflect the approximate densities and temperatures indicated by the most recent Langmuir probe measurements at the 0 and 3 mm radial positions at these two pressure values (Figures 4.10 and 4.11).

The n and T_e profiles for the attached plasma parameters (Figure 4.17a) both have the same width parameter of 3.5 mm (N.B. this is not the full width half maximum value), and are allowed to fall to zero beyond the ±4 mm range. In the detached plasma profiles, shown in Figure 4.17b, the density width parameter is broadened to 4.3 mm in order to match the 0 and 3 mm experimental measurements; this also reflects the average broadening of the column due to the proposed fast timescale events. The temperature profile, on the other hand, is narrower (2.0 mm width parameter), and sits on a constant pedestal of height 0.2 eV. This profile was chosen to replicate the $(0.20^{+0.09}_{-0.03})$ eV temperature of the blue glow region in the edge, as measured by the OES diagnostic, without causing unrealistically small T_e values at the outermost points where the plasma density is still relatively high.

As three-body recombination is the dominant process in EIR detachment, initial calculations estimated the reaction rate per unit volume for this process (S_{rec}) across the predicted plasma profiles, according to [41]:

$$S_{rec} = 8.75\times10^{-39}\, n^3\, T_\mathrm{e}^{-\frac{9}{2}},$$

where n is the plasma density in m^{-3}, and the electron temperature, T_e, is in eV. The resulting profiles are plotted in Figure 4.18. The peak recombination is much stronger

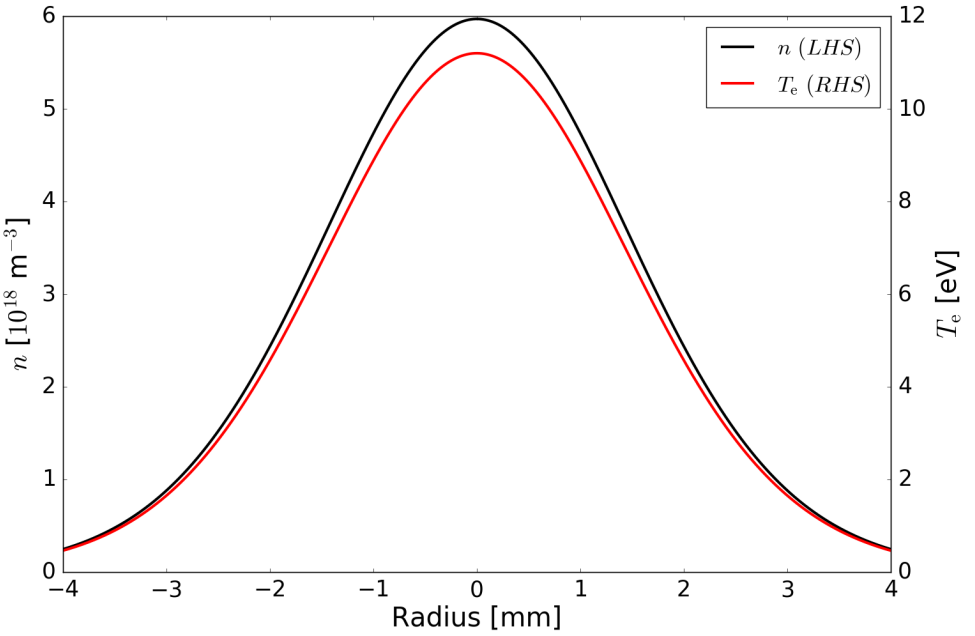

(a) Attached plasma.

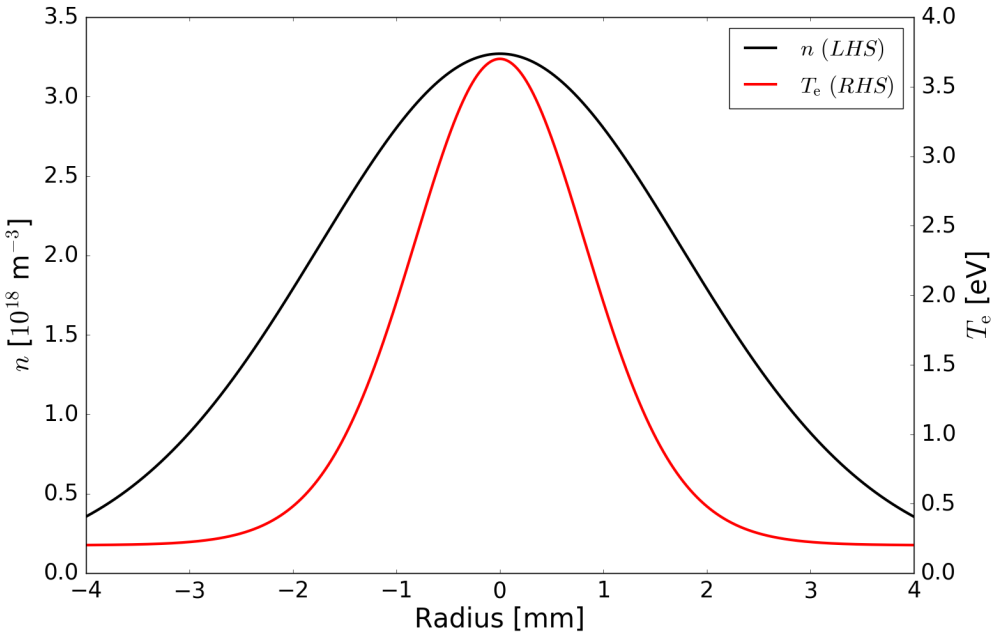

(b) EIR detached plasma.

Figure 4.17: The plasma density (n, in black) and temperature (T_e, in red) profiles used to simulate (a) the attached and (b) the EIR detached plasmas.

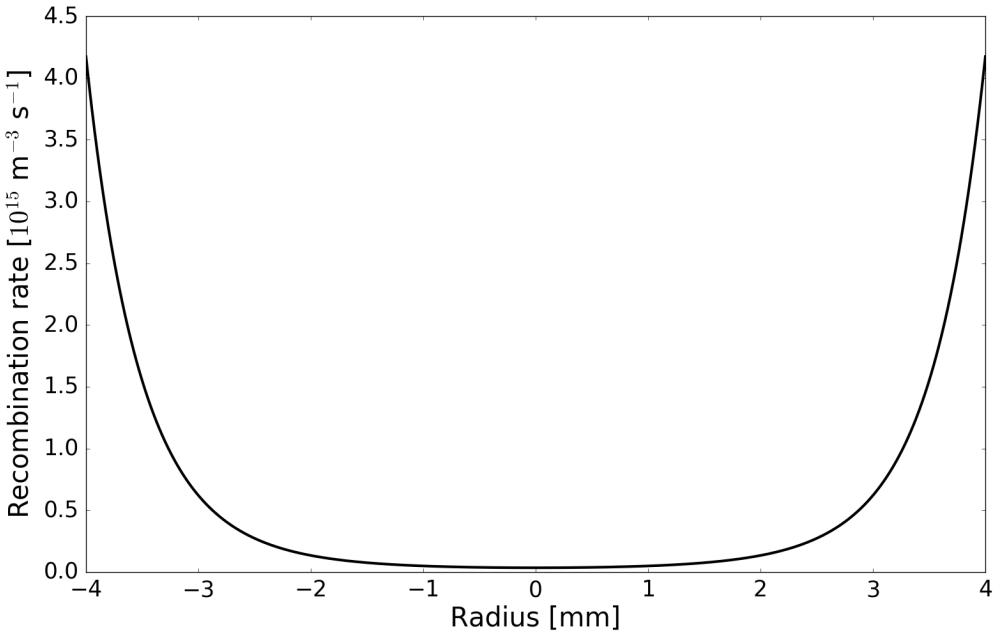

(a) Attached plasma.

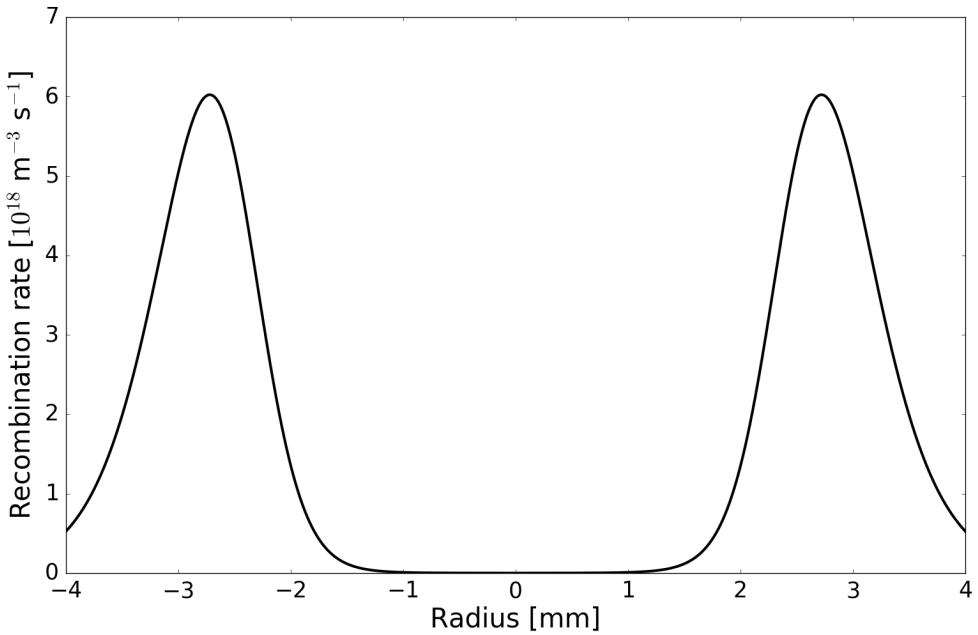

(b) EIR detached plasma.

Figure 4.18: Simulated radial profiles of the three-body recombination rate per unit volume in (a) the attached and (b) the EIR detached plasmas (note the difference in scale factor between the two).

(by three orders of magnitude) in the EIR detached case than in the attached plasma, as expected. Most significantly, the hollow profile observed in the experimental radial profiles of the Balmer emission (Figure 4.16) is replicated by the model of the EIR detached plasma.

The model was then extended further to consider the excited atomic energy level populations responsible for the H_α ($p = 3$) and H_δ ($p = 6$) Balmer emission. p is used instead of n here to denote the principle quantum number of the energy levels to avoid confusion with densities. The contributions to the level populations from both excitation and three-body recombination processes were estimated, employing the equations and coefficients of Johnson and Hinnov in the same way as Lumma et al., which we summarise here (Johnson and Hinnov [89]; Lumma et al. [90]).

The population of excited level p that is produced by three-body recombination is given by:

$$n_{rec}(p) = r_0(p)\, n_{\mathrm{E}}(p), \tag{24}$$

and the population produced by collisional excitation of ground state atoms (for which $p = 1$) by:

$$n_{ex}(p) = r_1(p)\, n(1)\, \frac{n_{\mathrm{E}}(p)}{n_{\mathrm{E}}(1)}. \tag{25}$$

$n(1)$ is the density of hydrogen atoms in the ground state, which we assume to take a constant value of $1 \times 10^{18}\,\mathrm{m}^{-3}$ here. The dimensionless coefficients $r_0(p)$ and $r_1(p)$ are tabulated by Johnson and Hinnov for a range of plasma density and temperature values, and have been interpolated between these points for the purposes of this analysis. The original data tables are reproduced in Appendix B for reference. Note that the tables do not contain $r_1(p)$ data for temperatures below 0.34 eV, and extrapolation of the fit was only possible for the $p = 3$ (H_α) level. For the $p = 6$ (H_δ) level, an upper value of $r_1(6) = 3 \times 10^{-5}$ (an overestimation of at least a factor of three) was used for all points in the EIR detached profile where $T_\mathrm{e} < 0.34\,\mathrm{eV}$.

In the notation of Johnson and Hinnov, the quantity $n_{\mathrm{E}}(p)$ in (24) and (25) denotes the Saha equilibrium density of level p, given by:

$$n_{\mathrm{E}}(p) = n(\mathrm{H}^+)\, n_\mathrm{e}\, p^2 \left(\frac{h^2}{2\pi m_\mathrm{i} e T_\mathrm{e}}\right)^{\frac{3}{2}} \exp\left(\frac{I_p}{T_\mathrm{e}}\right), \tag{26}$$

where in this case quasineutrality of the plasma means that the ion and electron densities, $n(\mathrm{H}^+)$ and n_e, are assumed to be equal ($n(\mathrm{H}^+) = n_\mathrm{e} = n$). I_p is the ionisation energy of level p ($I_1 = 13.6\,\mathrm{eV}$, $I_3 = 1.51111\,\mathrm{eV}$ and $I_6 = 0.37778\,\mathrm{eV}$), T_e is in eV, and all constants have their usual values (m_i being the mass of the hydrogen ion).

The resulting population density profiles are shown for the attached and detached cases in Figures 4.19 and 4.20 respectively. In both cases, the populations due to collisional excitation of ground state atoms (n_{ex}, Figures 4.19a and 4.20a) have centrally-peaked profiles, with the H_α level population a factor of $\sim$ 8 higher than that for the H_δ level. This is to be expected: collisional excitation of atoms is more likely to occur in the central region, where the temperature is highest and the more energetic electrons are located; and the higher-energy H_δ level is less likely to be reached than the lower lying H_α level. The hotter, broader temperature profile of the attached plasma compared to the detached case is reflected in the populations of both levels.

The population profiles due to three-body recombination (n_{rec}) show very different features. The H_δ level is preferentially populated over the H_α level, by factors of 4 and 16 in the attached and detached cases respectively. The profiles for the attached plasma (Figure 4.19b) again show single, central peaks, but they are broader than the attached n_{ex} profiles due to the $T_e^{-\frac{9}{2}}$ dependence of the recombination rate. The detached case (Figure 4.20b) differs even more significantly, with two peaks centred at approximately ± 2.6 mm for both lines. This hollow profile structure is very similar to that observed in the radial Balmer emission line profiles (Section 4.2.5).

The assumption that $n(1)$ (the density of ground-state atomic hydrogen) has a uniform value of $1 \times 10^{18}\,\mathrm{m}^{-3}$ across both the attached and detached plasmas is a considerable simplification. However, consideration of the ratio of the contributions of the excitation and recombination processes for each emission line across the plasma in both cases shows that it is still possible to gain some understanding from this model.

For the attached plasma, taking the ratios $n_{ex}(3)/n_{rec}(3)$ and $n_{ex}(6)/n_{rec}(6)$ (Figure 4.21a) shows that the contribution from excitation is dominant at all radii except in the very edges of the modelled region. This conclusion can be tested by estimating the effect of changing the assumed $n(1)$ value. If the value of $n(1)$ is an underestimate in this region, a more accurate higher value would further increase this dominance. Conversely, even an overestimation of two orders of magnitude would not cause recombination to become significant at radii smaller than 3.5 mm. Thus it is not implausible to conclude that three-body recombination is negligible in the bulk of the attached plasma column.

In the detached case, the balance of the two processes varies considerably across the plasma column (Figure 4.21b). In the centre, both the $p = 3$ and $p = 6$ levels are again predominantly populated by excitation, but at radii beyond approximately ± 1.85 mm,

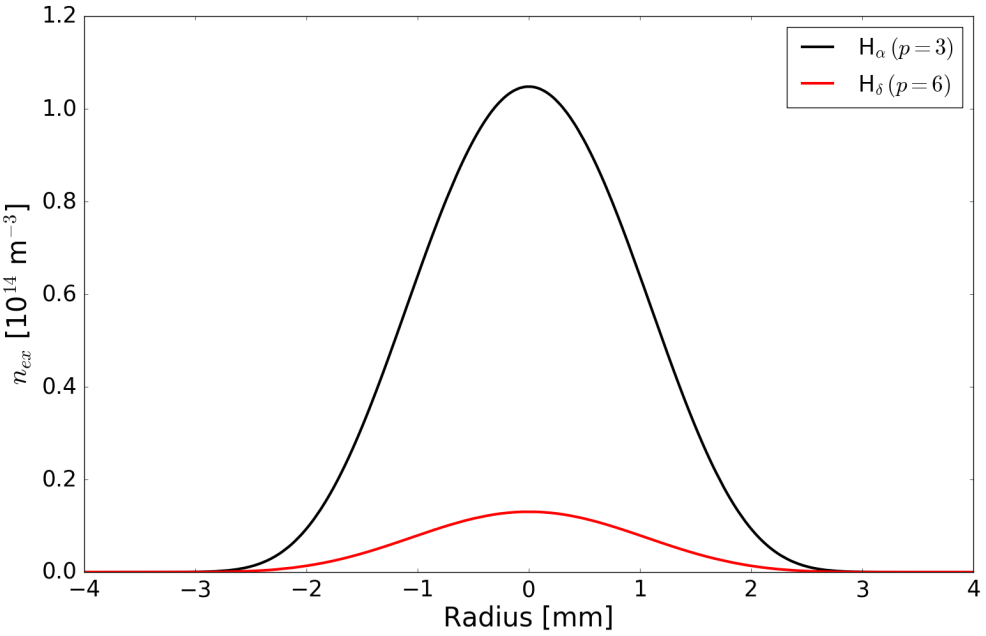

(a) Level populations due to excitation.

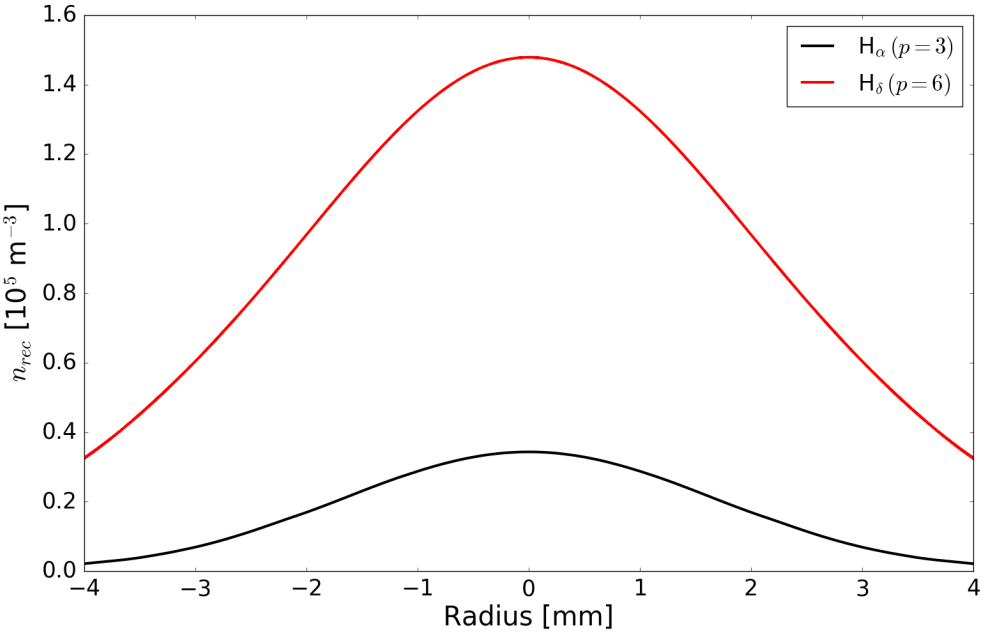

(b) Level populations due to three-body recombination.

Figure 4.19: Simulated radial profiles of the H_α ($p = 3$, in black) and H_δ ($p = 6$, in red) upper level populations produced by (a) excitation, n_{ex}, and (b) three-body recombination, n_{rec}, for the attached plasma. Note the much larger density scale factor in (a).

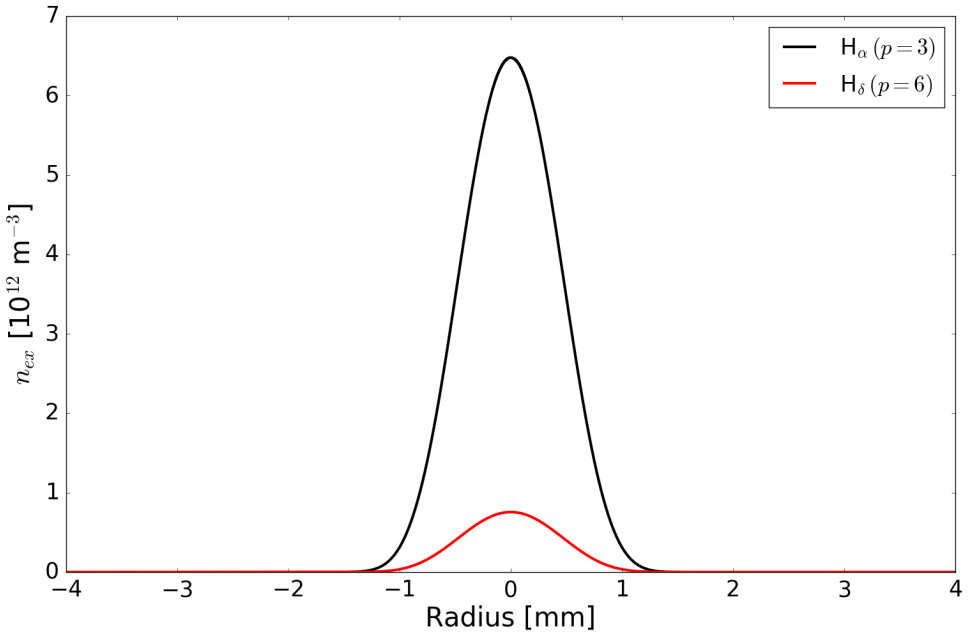

(a) Level populations due to excitation.

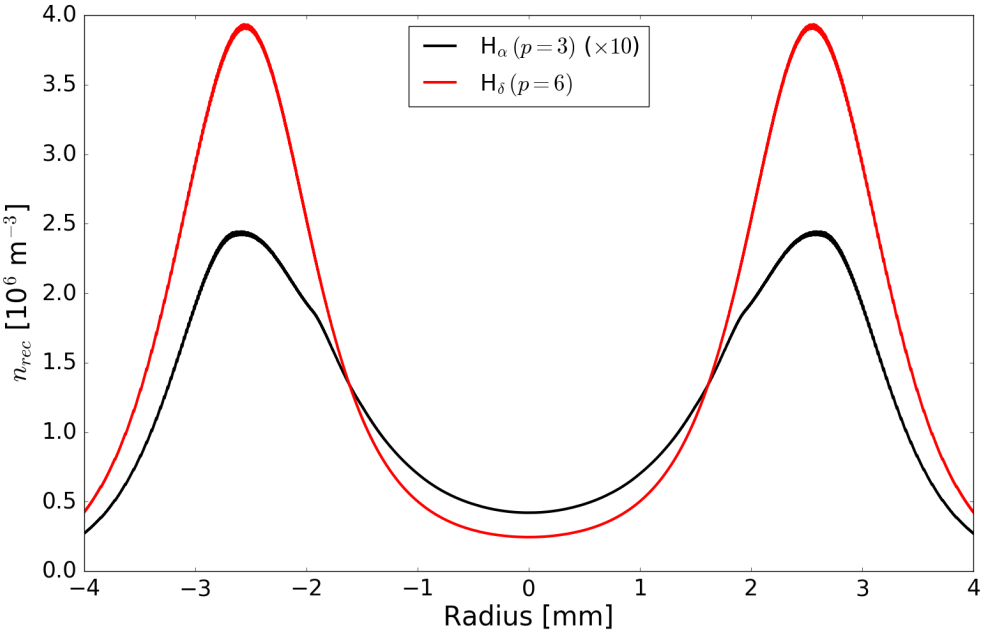

(b) Level populations due to three-body recombination.

Figure 4.20: Simulated radial profiles of the H_α ($p = 3$, in black) and H_δ ($p = 6$, in red) upper level populations produced by (a) excitation, n_{ex}, and (b) three-body recombination, n_{rec}, for the EIR detached plasma. Note the increase in density scale factor between the two.

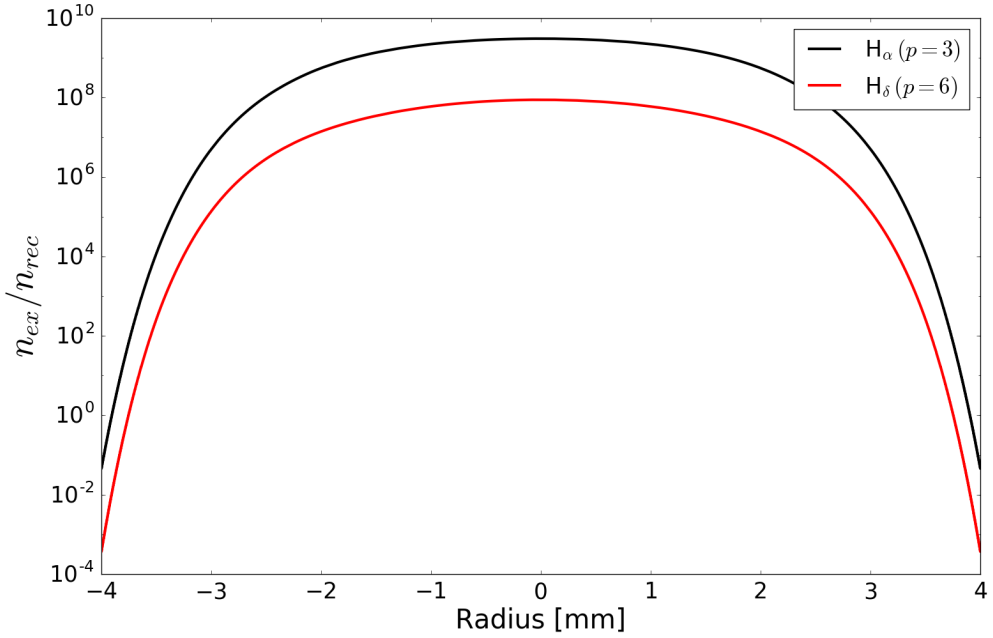

(a) Attached plasma.

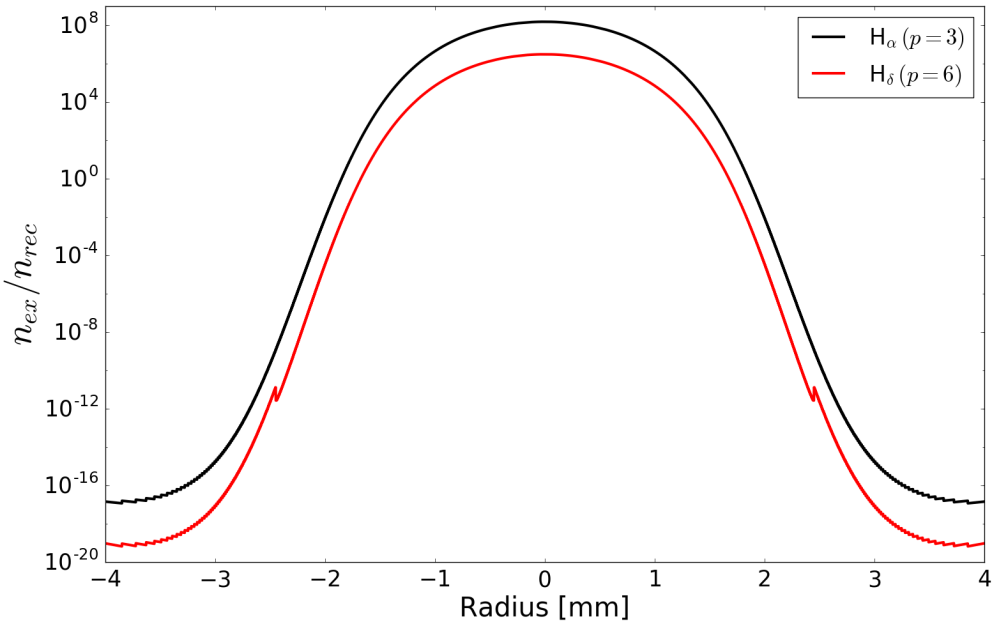

(b) EIR detached plasma.

Figure 4.21: Ratios of the excitation and three-body recombination contributions to the H_α ($p = 3$, in black) and H_δ ($p = 6$, in red) upper level populations in (a) the attached and (b) the EIR detached plasmas.

recombination becomes the more important process. Decreasing $n(1)$ by two orders of magnitude moves the boundary radius inwards by $\sim$ 0.25 mm, but this is insufficient to overcome the dominance of excitation in the centre of the column. If, on the other hand, $n(1)$ is an underestimation by even four orders of magnitude (bringing it to $10^{22}\,\mathrm{m}^{-3}$), the influence of excitation would still not extend beyond ± 2.2 mm, and three-body recombination would remain the dominant process in the column edges.

The small step-like structure in the edges of Figure 4.21b is caused by the limited density and temperature resolution of the interpolated coefficient values, which becomes significant when taking the ratios. The larger jump at approximately ± 2.3 mm is caused by the introduction of the constant upper bound on the $r_1(6)$ coefficient used at temperatures below 0.34 eV. This is a considerable overestimate at this position, but it is clear that the overall effect on the behaviour is minimal.

The $p = 3$ and $p = 6$ level populations can be used to estimate the Balmer emission from the H_α and H_δ lines for the detached profile, in order to compare it to the experimental profiles measured by Lisgo (Figure 4.16, Section 4.2.5). Since the peaks of the hollow profile lie outside the ± 2.2 mm position which bounds the excitation-dominated region, only the contribution from the three-body recombination process is considered. Inclusion of the excitation contribution merely produces a central peak which is much stronger than the edge emission, but the exact magnitude of this peak is entirely dependent upon the chosen value of $n(1)$, as previously discussed. As the excitation peak does not obscure the contribution from recombination in the edges, it can be removed from consideration without affecting the qualitative conclusions.

The spontaneous emission from an excited atomic level is calculated by multiplying the level population by the relevant Einstein A coefficient, A_{pq}. The values used here are $A_{32} = 4.410 \times 10^{-1}$ (H_α) and $A_{62} = 9.732 \times 10^{-3}$ (H_δ), as noted in Table 3.1 (Section 3.3.1). The profiles for both emission lines are plotted, along with their ratio ($^{H_\delta}/_{H_\alpha}$), in Figure 4.22a. For the purposes of comparing the simulation with the experimental data, Figure 4.16 is reproduced for convenience in Figure 4.22b. The radial range of the simulated profiles has also been extended to ± 15 mm for comparison, using the 4 mm values of $r_0(p)$ to provide an upper bound on the emission.

From Figure 4.22a, it can be seen that the H_α emission always dominates due to its larger A_{pq} value, but the maximum ratio ($\sim$ 0.35) is achieved in the edges of the column where the emission peaks are located. Comparing these profiles with the experimental

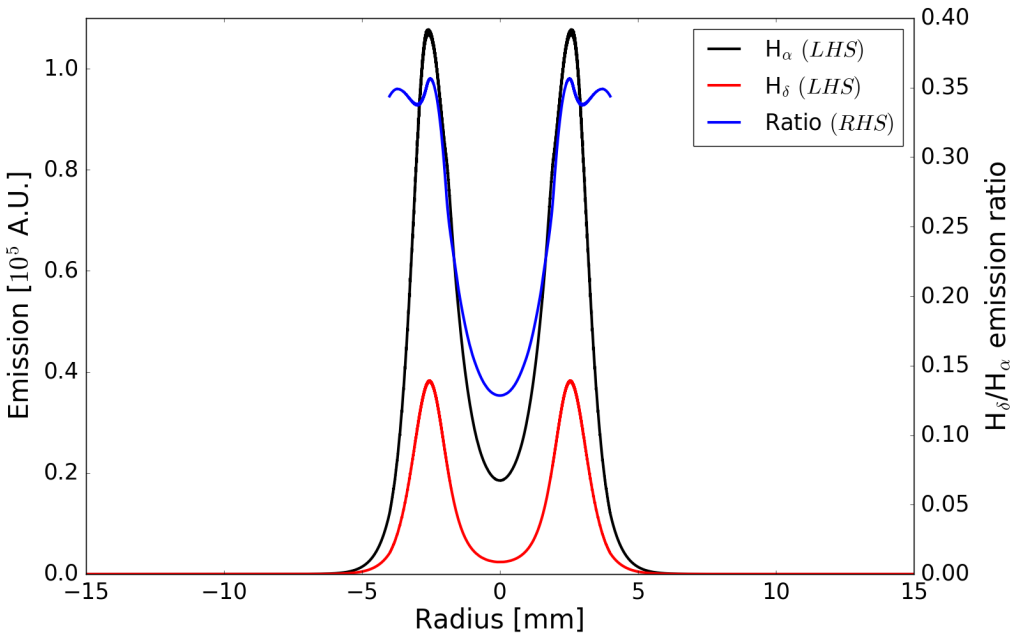

(a) Simulated radial emission profiles for the H_α (in black) and H_δ (in red) emission lines (left-hand axis). Plotted on the right-hand axis is the ratio of the two, $^{H_\delta}/_{H_\alpha}$ (in blue).

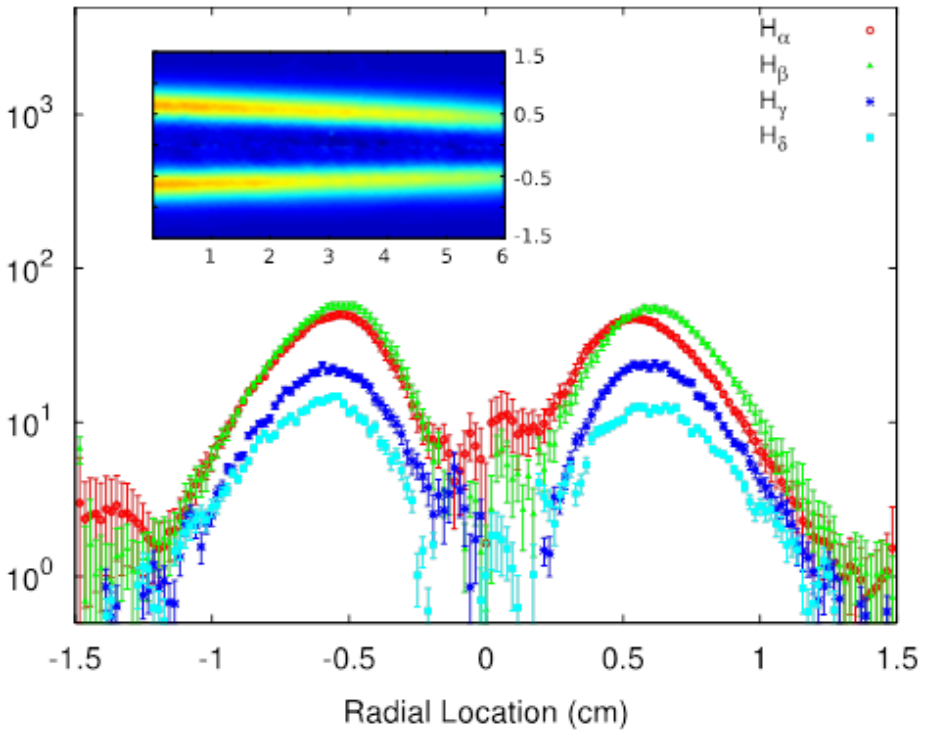

(b) Experimental radial emission profiles for the H_α, H_β, H_γ and H_δ lines (reproduced from Figure 4.16) [88]. Note the logarithmic counts scale on the y-axis.

Figure 4.22: (a) Simulated and (b) experimental profiles of hydrogen Balmer emission line intensities across the EIR detached plasma column.

data shows that the hollow profile is qualitatively well replicated, and the ratio between the peak values of H_δ and H_α emission is also in good agreement.

The most significant difference occurs in the radial scale: the peaks of the hollow profile in the simulation appear at a radius approximately half that observed in the experimental emission, and the overall radial extent of the emission is smaller by a factor of three. This is likely to be the result of choosing n and T_e profiles for the model which do not accurately replicate the experimental profiles, as only two data points were used.

Despite the uncertainty in the model n and T_e profiles, the qualitative agreement between the modelled and experimental data indicates that the process of three-body recombination is extremely important in the EIR detachment regime, and a cooler, broadened density profile is necessary for producing the high density, low temperature regions in the edges of the plasma column that allow recombination to take place. These simulations support the two-dimensional nature of the proposed hypothesis, but cannot exactly reproduce the experimental data: the correct forms of the n and T_e profiles are not known, as the mechanism which causes the broadening of the plasma column is not understood.

4.4 Summary

The first section of this chapter provided an overview of previous detachment studies using the YLPD, which covered both the molecular-activated and electron-ion recombination regimes (abbreviated to MAR and EIR respectively). This work formed a comprehensive study of the time-averaged behaviour of the plasma in each regime, with a focus on the variation along the axis of the machine. Results from a simple one-dimensional fluid model were found to agree relatively well with the experimental measurements, but the work neglected the possible importance of both fast timescale (sub-millisecond) events and radial broadening of the plasma column, particularly in the EIR regime.

More recent observations were then presented, which aimed to reproduce the conditions for EIR detachment and characterise the onset of this regime as the pressure in the target chamber is increased. These measurements continued to focus on slow (millisecond and above) timescale events, but included measurements in both the centre and edge of the plasma column. It was found that, despite alterations in the operation of the YLPD, the behaviour of the previously-studied EIR detached plasma could be replicated.

The final experimental observations discussed were the radial profiles of hydrogen Balmer emission across the EIR detached plasma column, which showed a distinctive

hollow structure in which the emission predominantly arose from the edges of the column [88]. These results, coupled with the clear broadening of the 'blue glow' region of the detached plasma that is visible by eye, strongly suggest that the radial dimension must also be included in a full explanation of the behaviour of EIR detachment.

A hypothesis was therefore proposed in which 'blobs' of plasma are intermittently ejected from the centre of the column, and travel radially outwards on sub-millisecond timescales. Cooling of these blobs in the edges of the column as they disconnect from the hot core plasma could result in high-density, low-temperature regions where three-body recombination could occur. As a preliminary exploration of the effects of broadening the plasma column, a simple simulation of the time-averaged radial density and temperature profiles was carried out for both the attached and EIR detached regimes. This work investigated the effects of broadening and cooling the column on the relative importance of three-body recombination (the key process in EIR detachment) and excitation of hydrogen atoms.

The results showed that a detached regime with a time-averaged, broadened density profile and cooler temperatures in the edges of the plasma would be dominated by three-body recombination in the edges. In addition, calculation of the resulting H_α and H_δ Balmer line emission produced hollow radial profiles that were qualitatively very similar to those measured experimentally. The ratio of the peak H_α and H_δ emission also matched the experimental data well, but the positions of the hollow profile peaks were closer to the centre of the column than was observed experimentally.

We conclude that the average broadened, cooled plasma profiles yield similar recombination emission profiles to those that have been measured experimentally. However, the mismatch in radial scale between the simulated and observed emission indicates that further work is required to understand the mechanism which causes the broadening of the column, as the plasma profiles used in the model are not fully capturing the behaviour. To fully test the 'blob' transport hypothesis, it is necessary to increase the time resolution of the experimental measurements in order to discern transient events. In the following chapter, the possible presence of such events in the plasma is investigated using high frequency diagnostics.

Chapter 5

Evidence for radial transport in the YLPD detached plasma

Having proposed an explanation for the radial broadening of the EIR detached plasma column that relies on sub-millisecond timescale events, this chapter presents observations to investigate this. Fast frame camera imaging (Section 5.1) and fast Langmuir probe floating potential measurements (Section 5.2) are used to study the plasma column on the short timescales required. The results from these diagnostics suggest that radial transport processes intermittently eject filamentary plasma structures from the column.

In Section 5.3, we hypothesise that the presence of centrifugal instabilities in the detached plasma column causes the observed radial transport. This explanation is found to be in relatively good agreement with the experimental measurements that have been made, but is not capable of explaining all the observations without further development of both theory and experiment. The findings are summarised in Section 5.4.

5.1 Fast frame imaging

The fast frame imaging (FFI) data were taken through port J in the end plate of the YLPD (Figure 3.2): the line of sight is tilted at an acute angle above the axis of the plasma column in the target chamber. To orient the reader, Figure 5.1 shows both ordinary camera images and example raw FFI frames for the attached and detached plasmas. The FFI camera is focused in the plane of the Langmuir probe that is visible in the ordinary photographs (approximately $y = 40$). Video 5.1 (see [91]) shows the YLPD plasma detaching in real time.

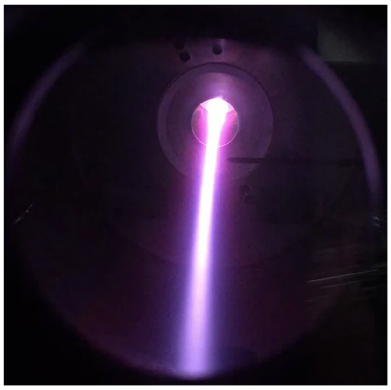

(a) Photograph; attached.

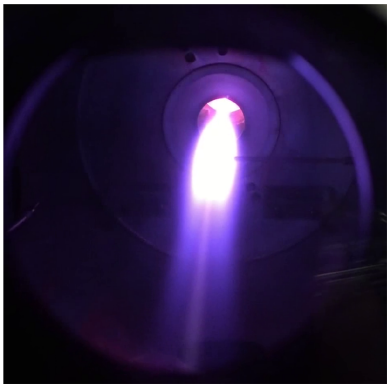

(b) Photograph; EIR detached.

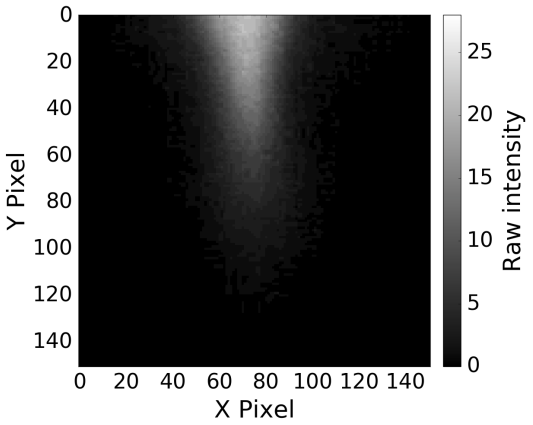

(c) Example raw FFI image; attached.

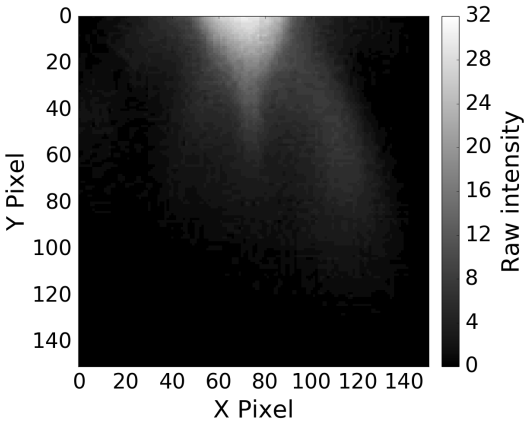

(d) Example raw FFI image; EIR detached.

Figure 5.1: Ordinary photographs (top row) and example high speed (50 kHz frame rate) camera images (bottom row) of the attached and EIR detached plasmas in the target chamber of the YLPD. The Langmuir probe that enters horizontally from the right of the photographs has a tip 1 mm in diameter, encased in a ceramic sheath of 3 mm diameter. The FFI camera is focused in the plane of the Langmuir probe (approximately $y = 40$ in the FFI images), and the x pixel scale is approximately $0.25\,\mathrm{mm\,pix^{-1}}$. The viewing angles are not identical: the FFI camera is rotated clockwise about the vertical compared to the ordinary camera.

Data were recorded and analysed (as described in Section 3.5) at a range of target chamber pressures as EIR detachment was induced. 5000 images were recorded at a frame rate of 50 kHz, with an exposure time of 20 µs. The results presented here predominantly focus on the initial (attached) and final (EIR detached) states, which occur for this set of data at target chamber pressures of 3.1×10^{-4} and 7.25×10^{-3} mbar respectively. Excerpts from the FFI data for these pressures are shown in Videos 5.2 (attached) and 5.3 (detached) [91].

Firstly, mean-subtracted image frames are considered (see Section 3.5), which show the variation between frames more clearly than the raw images, and allow us to begin to understand how the plasma varies through time (Section 5.1.1). Analysis then moves to the frequency domain, with power spectra calculated for each pixel and pressure (Section 5.1.2). Finally, three reference pixels are used to study the coherence and phase differences (Sections 5.1.3 and 5.1.4 respectively) between these pixels and the rest of the image. These results are discussed in Section 5.1.5.

Video 5.1: Detachment of the hydrogen plasma column in the YLPD in real time. The target chamber gas valve is opened over approximately 15 seconds to increase the flow of neutral hydrogen into the chamber. The onset of detachment occurs between 11 and 12 seconds, as the column dims and begins to turn blue. The fully stable detached state (characterised by the bright blue glow) is reached by 14 seconds, and the gas valve is closed again from around 19 seconds, returning to the attached state by the end of the video. Video available from [91].

Video 5.2: FFI video of the attached plasma in the YLPD, recorded at 50000 frames per second (playback is slowed by a factor of 10000). The narrow plasma column remains steady, with some flickering in the edges. The data has been enhanced to show the features more clearly. Video available from [91].

Video 5.3: FFI video of the EIR detached plasma in the YLPD, recorded at 50000 frames per second (playback is slowed by a factor of 10000). The plasma is clearly much broader than when in the attached state, and we see the ejection of intermittent filaments of plasma in the edges of the column. The data has been enhanced to show the features more clearly. Video available from [91].

5.1.1 Mean-subtracted images

Initial analysis of the FFI images converted the raw data for each 5000-frame sequence into mean-subtracted images, as described in Section 3.5. Examples of eight consecutive frames from each of the attached and detached plasmas are shown in Figure 5.2 to illustrate the differences between the two behaviours. In both plasmas, the fluctuation amplitude of a pixel can reach up to a third of its average intensity. Figure C.1 (Appendix C) contains an example frame from each pressure value to show the evolution of the plasma column as EIR detachment is induced.

The attached plasma column (Figure 5.2a) is narrow ($\sim$ 15 mm in diameter) and relatively uniform across the width. There are some fluctuations in the intensity of the column: an $m = 1$ mode appears to be visible along the column in some of the frames, where half the pixels are above their average value, and the other side of the column is weaker than average. Dashed lines overlaid on the relevant frames show the approximate boundary between these out-of-phase regions.

The structures in the EIR detached plasma state are much more irregular. The column is broader ($\sim$ 32 mm), and filaments of bright plasma are visible at varying locations in the outer edges of the column, generally at radii beyond 6 mm. These filaments are extended azimuthally within the plane of focus, over angles of up to 180° in some cases, but are relatively narrow in the radial direction ($\sim 5 - 8$ mm). The limitations on the frame rate imposed by the required field of view and the available light levels mean that the motion of individual filaments cannot be tracked with the current data set, although the relevant timescales must be shorter than the 20 µs exposure time.

To gain further understanding of the behaviour of the plasma throughout the 100 ms data record, three reference pixels along the $y = 40$ line are considered: one in the centre of the column, and two in the edges to the left and right (illustrated in Figure 5.3). The pixels in the edges of the column are chosen to coincide with the observed filamentary structures in the EIR detached plasma. Histograms of the mean-subtracted intensity time series for these pixels are shown in Figure 5.4 (the edge pixels are not included for the attached plasma, as the narrow column width means that the signal is negligible at this radius).

The sensitivity of the FFI camera is limited, producing highly discretised data sets. However, these plots can still provide insight into the distribution of the intensities through time. The attached plasma (Figure 5.4a) has a narrow central peak, with extended, low

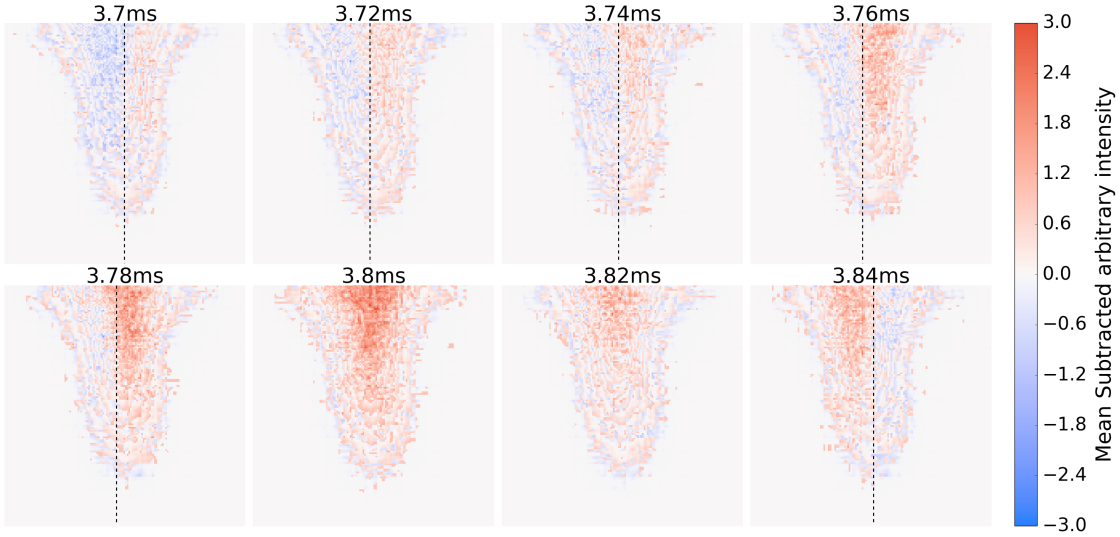

(a) Attached plasma; target chamber pressure of 3.1×10^{-4} mbar. Dashed lines indicate the approximate boundary between two out-of-phase regions in a possible $m = 1$ mode.

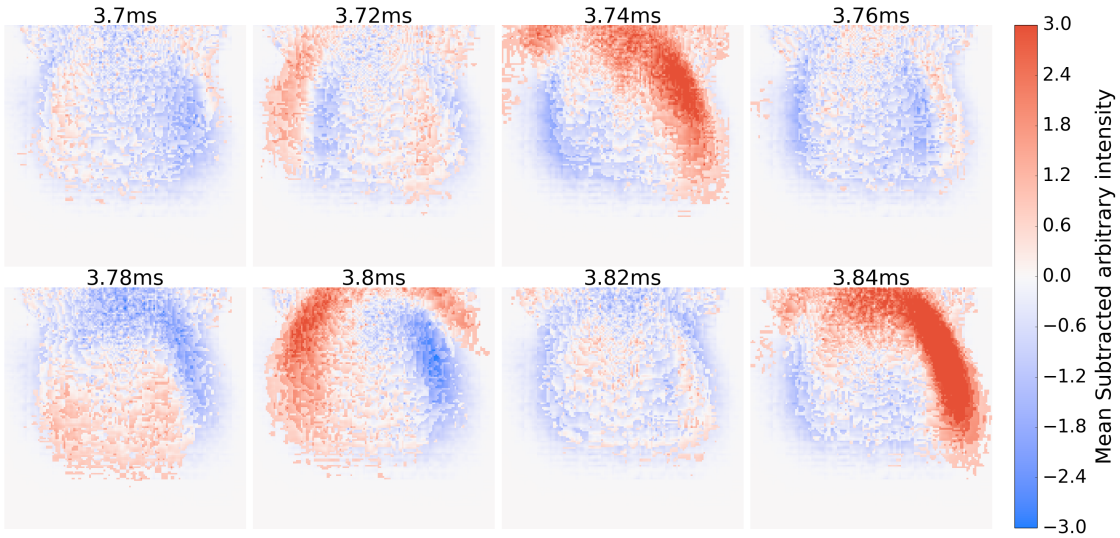

(b) EIR detached plasma; target chamber pressure of 7.25×10^{-3} mbar.

Figure 5.2: Sequences of eight consecutive mean-subtracted images of (a) the attached and (b) the EIR detached plasmas in the YLPD, recorded at a 50 kHz frame rate. Each frame is 151×151 pixels, and each pixel has a width of approximately 0.25 mm.

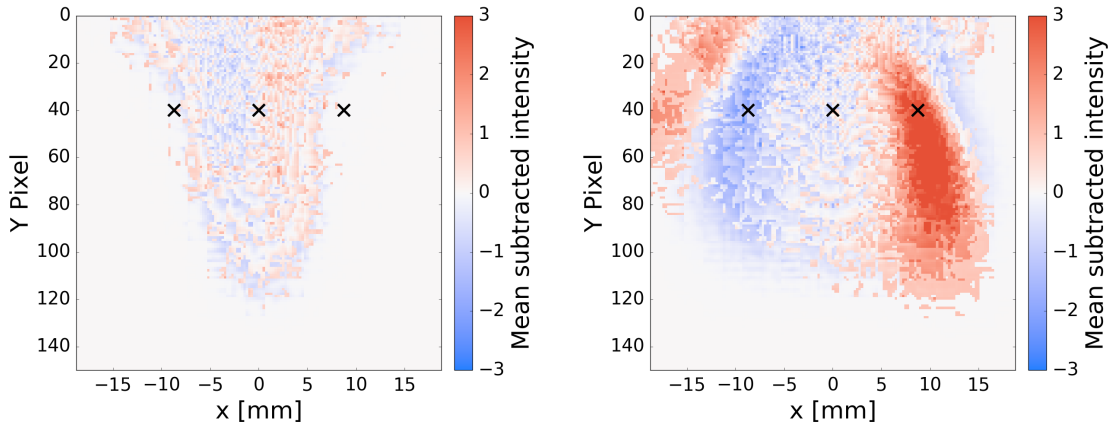

(a) Mean-subtracted image; attached.

(b) Mean-subtracted image; EIR detached.

Figure 5.3: The reference pixels chosen for analysis of the FFI image data, relative to example mean-subtracted FFI frames for both the attached and EIR detached plasmas in the target chamber of the YLPD.

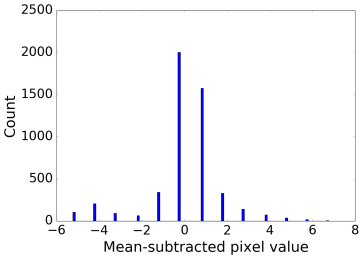

(a) Centre; attached.

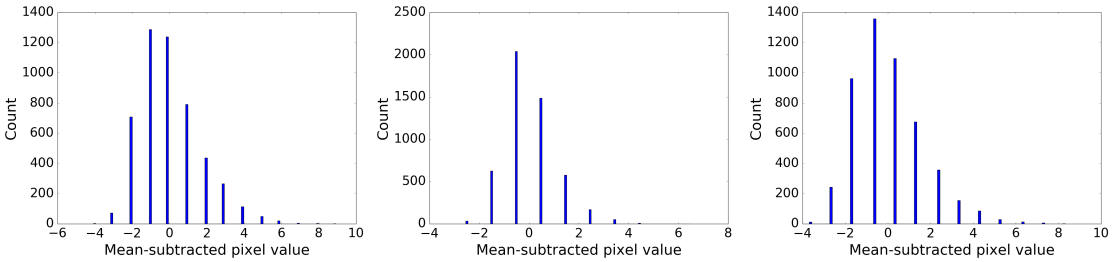

(b) LHS; EIR detached.

(c) Centre; EIR detached.

(d) RHS; EIR detached.

Figure 5.4: Histograms of the mean-subtracted intensity time series for (a) the centre reference pixel in the attached plasma; and (b)-(d) all three reference pixels in the EIR detached plasma in the YLPD.

count rate positive and negative tails. This indicates that the central column intensity is relatively stable, with occasional fluctuations yielding both bright and dark outliers.

In the detached plasma, the distribution of the central pixel (Figure 5.4c) is also narrow, but has a more pronounced positive tail and fewer negative outliers than in the attached case. The edge pixel distributions exhibit an even stronger positive skew, and the full time series of these pixels suggest that the high-intensity events are scattered throughout the observation time. It is therefore likely that the filamentary structures seen in the mean-subtracted EIR detached image frames occur on an intermittent basis.

5.1.2 Power spectra

To further investigate the potential intermittent behaviour of the EIR detached plasma, the power spectrum was calculated for each pixel across the 5000-frame time series. The frequency range is $0 - 25\,\text{kHz}$, with a resolution of 757 Hz. 2D colour maps of the 3030 Hz component across the image are shown for the attached and EIR detached plasmas in Figure 5.5, with the reference pixels chosen in the previous section highlighted. 3030 Hz has been chosen as an arbitrary example of the power distribution: the variation with frequency is minimal, with the exception of a large DC/low frequency component at 0 and 757 Hz. For completeness, all the images across the full frequency range for both states are shown in Figures C.2 and C.3 in Appendix C.

The distribution of the power components reflects the differences between the two regimes that were seen in the mean-subtracted images. The power in the attached plasma is concentrated in the centre of a narrow column ($\sim$ 7 mm across), whereas in the detached regime, the column is much wider, with two peaks in the edges. These peaks are centred at approximately $\pm 9.5\,\text{mm}$, and have widths of $\sim$ 5 mm in the x-direction, coinciding with the average positions of the bright filamentary structures that are observed in the images.

To illustrate the evolution of the power distribution as detachment is induced, Figure 5.6 is a 2D plot of the 3030 Hz component strength along the line of pixels at $y = 40$ (which lies approximately in the plane of the camera focus) as the target chamber pressure increases. The distribution remains narrow until the pressure surpasses $6 \times 10^{-3}\,\text{mbar}$, at which point the two peaks in the edges of the column are first seen. This transition, indicated by a dashed line overlaid on the plot, marks the onset of full EIR detachment. These peaks grow in strength until the final stable detachment state is reached, at a target chamber pressure of $7.25 \times 10^{-3}\,\text{mbar}$.

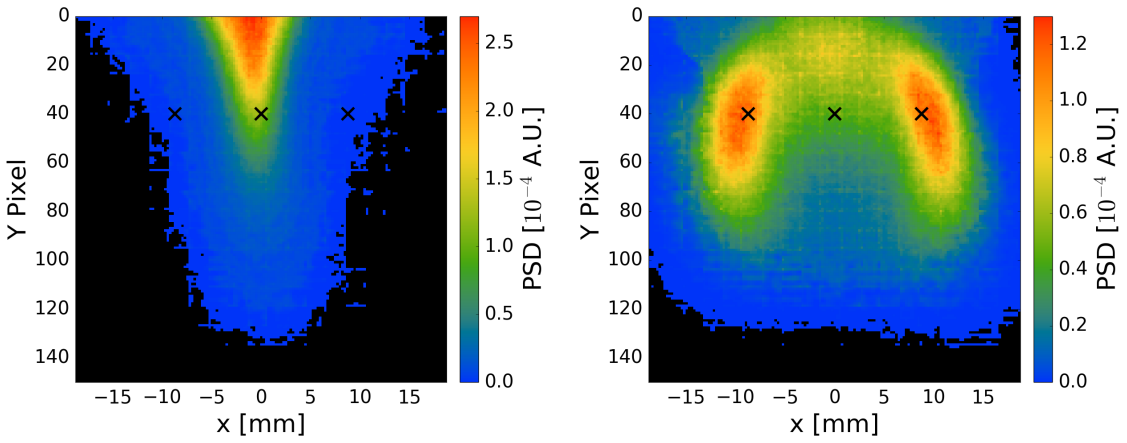

(a) Attached plasma (3.1×10^{-4} mbar). (b) EIR detached plasma (7.25×10^{-3} mbar).

Figure 5.5: The distribution of power at 3030 Hz over the FFI data range for (a) the attached and (b) the EIR detached plasmas. Black crosses mark the positions of the three reference pixels chosen for focused analyses.

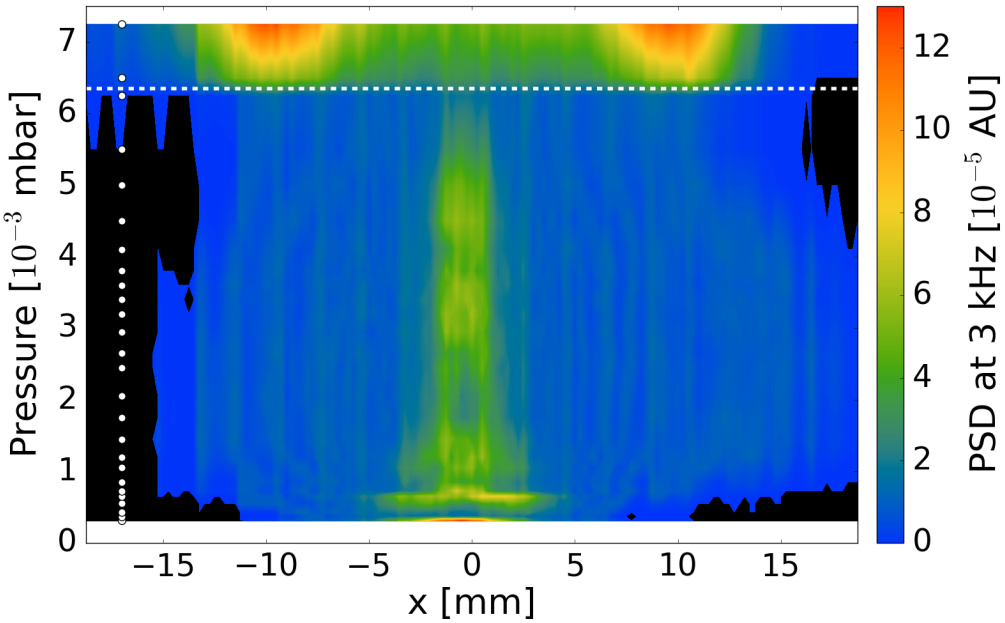

Figure 5.6: Evolution of the power component at 3030 Hz for the line of pixels at $y = 40$ as the pressure in the YLPD target chamber increases. The white scatter points show the pressures at which the data were recorded, and the white dashed line indicates the approximate pressure at which the onset of EIR detachment occurs.

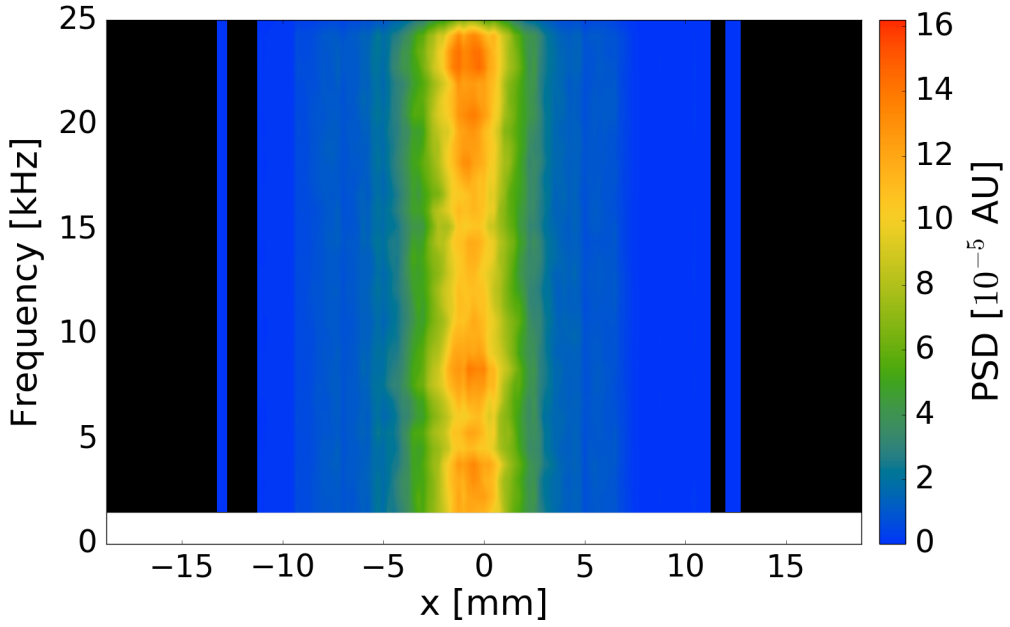

(a) Attached plasma (3.1×10^{-4} mbar).

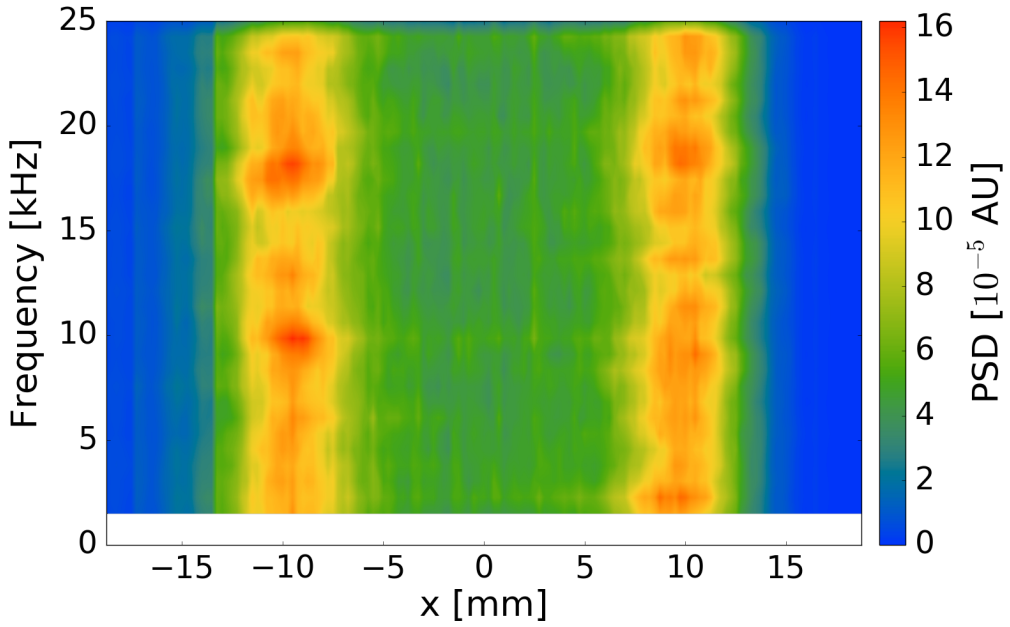

(b) EIR detached plasma (7.25×10^{-3} mbar).

Figure 5.7: Spectrograms showing the variation of the power components in the FFI data across the plasma column at $y = 40$ for (a) the attached and (b) the EIR detached plasmas. No data was available for pixels coloured black.

2D spectrograms of the frequency components of the line of pixels with $y = 40$ are shown for both the attached and detached plasma states in Figure 5.7. The DC component at the lowest frequencies is excluded, as it dominates the spectrum. These spectrograms again emphasise the differing radial power distributions of the two states. The attached data consists of a strong central region $\sim$ 7 mm across, and there is no data beyond approximately $\pm$13 mm. In contrast, the EIR detached data has a much wider distribution. There are components presents across a radial distance of almost 30 mm, and the strong peaks that were observed in Figure 5.5b at $\pm$9.5 mm (width $\sim$ 5 mm) are shown to extend over the full frequency range.

The relatively constant contributions across the full range of frequencies for both the attached and detached plasma suggest that no coherent, single frequency modes are present in this range. Instead, the fluctuations in pixel intensity are likely to be caused by intermittent events. For the EIR detached state in particular, this implies that the bright filamentary structures occur intermittently in time, rather than at a regular frequency. However, the spectral behaviour cannot be determined for either regime above the Nyquist limit of 25 kHz, which is dictated by the camera frame rate.

5.1.3 Coherence

As discussed in Section 3.5, the coherence analysis indicates the extent to which pixels share frequency components. For this, the reference pixels that were highlighted in Figures 5.3 and 5.5 are used. Figure 5.8 shows the 2D coherence plots for each of the three pixels for the attached and detached plasmas, again for the example frequency of 3030 Hz. The structure of these plots remains relatively constant across the full frequency range (as an example, the plots for all frequency components of the left-hand pixel in the detached plasma are shown in Figure C.4 in Appendix C). This supports the conclusion that the fluctuations occur intermittently, as short timescale events have wider frequency spectra.

In the attached case, the intensity of the image in the edge regions is very low due to the narrow width of the column, and the left- and right-hand pixels therefore show little to no coherence with the rest of the image. The central pixel data, on the other hand, indicates that the centre of the column is relatively coherent over a width of $\sim$ 13.5 mm.

The EIR detached plasma shows a very different structure. There is no longer a narrow beam that is coherent with the centre reference pixel; instead the region of coherence is broadened, and is weaker compared to that of the attached state. In each edge of the

column, there is a region of relatively strong coherence. These have a similar azimuthally elongated shape to the filaments seen in the mean-subtracted images (Figure 5.2b), and their positions are coincident with the positions of both the brightest regions of these filaments, and the peaks observed in the power spectrum.

There are some differences, however. The structures in the coherence plots for the edge pixels have a greater spatial extent compared to those in the power spectrum. In particular, the $x = 40$ pixel coherence (Figure 5.8d) has a weak tail that extends around the top of the column to the opposite side. In the mean-subtracted image frames, we see that the filaments' position and shape vary over time, and it is possible that this weakly coherent tail is the result of this variation. It is also important to note that the camera captures light from the plasma column behind and in front of the focal plane, which could affect the analysis (particularly at the top of the field of view, where the bright plasma enters the target chamber in the background).

5.1.4 Phase

The same reference pixels were used to study the phase differences across the images in the attached and detached regimes. 2D colour plots are shown for the 3030 Hz frequency in Figure 5.9 (again, there is little variation across the frequency spectrum, illustrated for the left-hand pixel in the detached plasma in Figure C.5 in Appendix C). In the attached case, the entire plasma appears to be in phase across the column, with very little variation except in the edges where the image intensity is low. This does not reflect the $m = 1$ mode structure that is visible in the mean-subtracted frames (Figure 5.2a), but this may be influenced by the choice of reference pixels.

The structure in the EIR detached plasma is more difficult to interpret. The central pixel appears to be in phase with the majority of the rest of the image, whereas the edge pixels are each out of phase with a region on the opposite side. These regions are quite sharply defined, with very narrow transitions between the areas that are in phase and out of phase, and could be caused by the plasma filaments: an excess of plasma on one side could deplete the opposite side of the column, leading to the phase difference.

There are also some pecularities in this data, for which the explanation is not clear. The structures in the EIR detached state do not fully reflect the distributions seen in the power and coherence plots, as they have a much greater spatial extent. Secondly, each of the three reference pixels is out of phase with a different region of the column in the

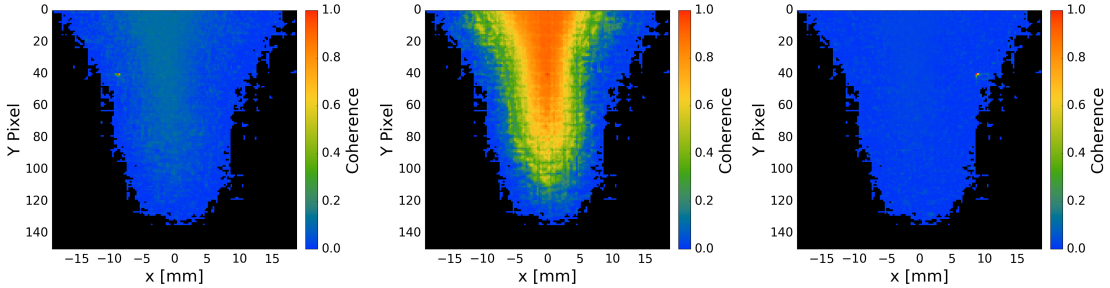

(a) LHS; attached. (b) Centre; attached. (c) RHS; attached.

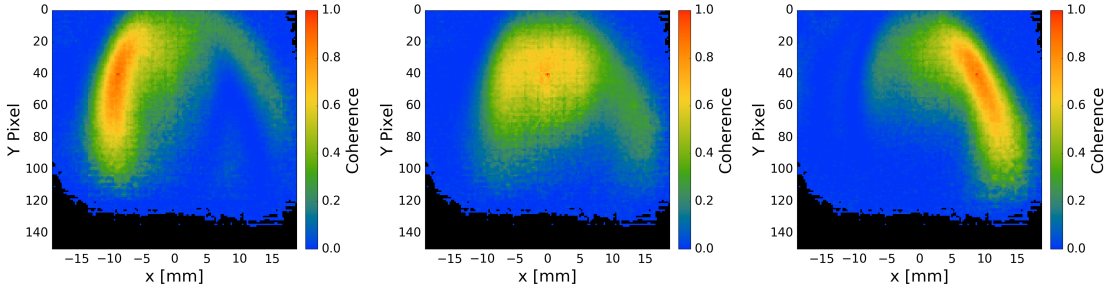

(d) LHS; EIR detached. (e) Centre; EIR detached. (f) RHS; EIR detached.

Figure 5.8: Coherence between each reference pixel and all other pixels at 3030 Hz, for the attached (top row) and EIR detached (bottom row) plasmas in the YLPD.

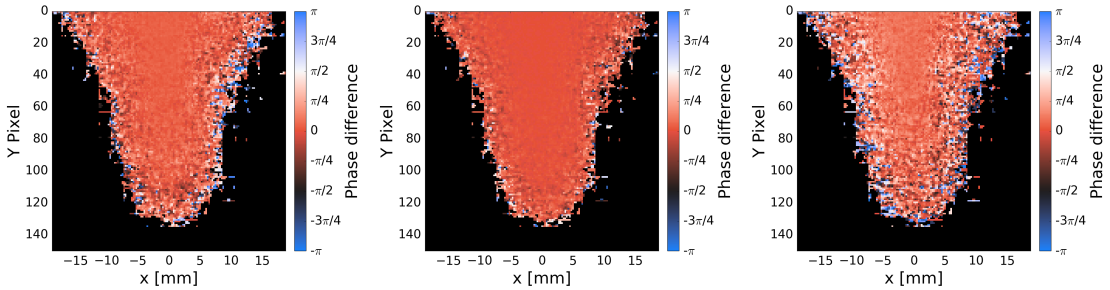

(a) LHS; attached. (b) Centre; attached. (c) RHS; attached.

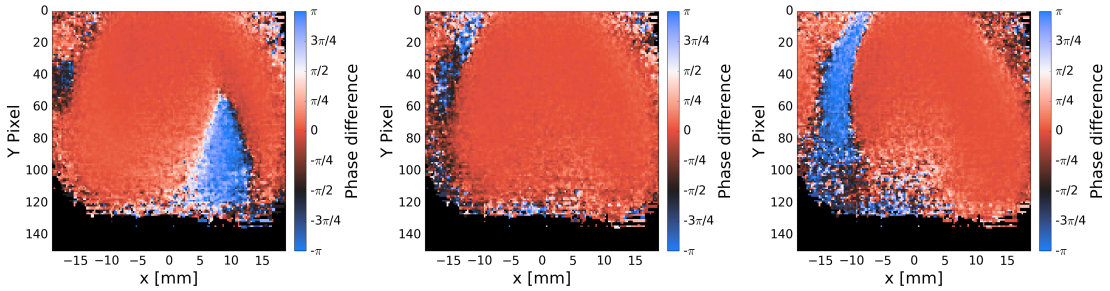

(d) LHS; EIR detached. (e) Centre; EIR detached. (f) RHS; EIR detached.

Figure 5.9: Phase difference between each reference pixel and all other pixels at 3030 Hz, for the attached (top row) and EIR detached (bottom row) plasmas in the YLPD.

detached state, but the in-phase region in each image encompasses all three of the pixels. This implies that the three reference pixels are in phase with each other, but it is unclear why the out-of-phase regions are not the same for each of the pixels. It is possible that the limited resolution of the pixel intensity, seen in Figure 5.4, and the noise (particularly in the centre of the column) reduces the effectiveness of this phase analysis.

5.1.5 Discussion of FFI results

The fast frame imaging data has first and foremost shown that bright filamentary structures appear intermittently in the edges of the plasma column in the EIR detached state. These structures are generally centred at a radius of approximately 9.5 mm, and are extended azimuthally around the column, in some cases over an angle of 180°. This broadening effect is roughly three times greater than that predicted by the three-body recombination model presented in Section 4.3, suggesting that additional processes are likely to be involved in producing the observed behaviour of the EIR detached plasma.

The broadening observed in the FFI data is in fact more pronounced than that seen in the time-averaged radial Balmer emission profiles obtained experimentally (Section 4.2.5). However, the result still supports the need for one or more additional processes to increase the width of the emission profile beyond that produced by three-body recombination alone. It is possible that the broadening mechanism could be affected by changes in the operating conditions, which may explain the increased effect in the most recent data.

The positively-skewed distribution of the mean-subtracted pixel intensity is consistent with higher intensity, filamentary events, the intermittent nature of which is suggested by the broadband power spectra. Multiple short-lived, high intensity events occur, but do not exhibit any coherent oscillatory modes. Note that the 25 kHz Nyquist frequency (dictated by the frame rate and sensitivity of the camera) limits the frequency analysis, and it is not possible to track individual filaments over their lifetime.

The importance of the broadening of the EIR detached plasma is highlighted by the differences between the attached and detached data. The mean-subtracted images illustrate the transition from the narrow, confined beam to the broadened column in the final stages, once the pressure reaches 6×10^{-3} mbar (Figure C.1, Appendix C). The transition is also visible in the 2D plot of the variation of the 3030 Hz power component with target chamber pressure along a line of pixels (Figure 5.6), which clearly shows a jump from the narrow, central peak of the attached plasma to the hollow profile of EIR detachment.

Calculations of coherence and phase difference across the image using three different reference pixels are more difficult to interpret. The coherence measurements do reflect the filamentary nature of the detached plasma to some extent, although there seems to be some blurring of the features into the central regions of the column. The phase plots indicate that the intensity fluctuations on opposite sides of the plasma are out of phase, but the plots for each reference pixel do not appear to be consistent.

In summary, the FFI data show that the broadening of the emission from the EIR detached plasma column is more significant than that predicted by only considering the process of three-body recombination. At least one alternative mechanism must therefore be included in order to fully explain EIR detachment, but the limitations of the FFI frame rate mean that this data cannot provide enough information to determine the nature of this mechanism. The emission predominantly arises from intermittent, bright filamentary events that occur on timescales that are shorter than the 20 µs exposure time, and thus it is not clear how these filamentary structures are produced or destroyed, nor how they travel. In the following section, therefore, 1 MHz floating potential measurements are used to study their behaviour further.

5.2 Fast floating potential measurements

The time series of the floating potential, V_f, of the plasma were recorded for 100 ms with 1 µs resolution at radial positions from 0 to 8 mm, for both the attached and EIR detached states (see Section 3.2.2 for details). The target chamber pressures were 3.5×10^{-4} and 1.0×10^{-2} mbar for the attached and detached cases respectively. For each position of the moveable probe, the same data was recorded simultaneously using the reference probe, radially inserted to 6 mm from the column centre on the opposite side of the plasma column. The measurements were taken with the probes AC coupled to the oscilloscope, meaning that the measured variable is $\widetilde{V}_f$: the fluctuation of V_f around its DC value. I_{sat} and T_e were measured by the Langmuir probe in the column centre and edge for both the attached and detached cases. These values are plotted in Figures 4.10 and 4.11 to demonstrate the plasma reproducibility.

First, the distribution of the moveable probe data is analysed for each radius in both the attached and detached plasmas, using histograms and skewness and kurtosis calculations (Section 5.2.1). In Section 5.2.2, the frequency spectra for each radius are plotted in a 2D spectrogram to compare the radial variation of the power distribution in the two

plasma states. The reference probe data are then used to look for time delays between the occurrence of events at different positions in the plasma, which would imply radial motion of structures inside the column (Section 5.2.3). The results are discussed in Section 5.2.4.

5.2.1 Statistical analysis

Firstly, the distribution of the $\widetilde{V}_f$ data is considered, focusing on the moveable probe. Histograms of the time series for each radial position are plotted for both the attached and EIR detached plasma states in Figures 5.10 and 5.11 respectively. These plots show the natural logarithm of the number of counts, which both increases the visibility of the lower-frequency $\widetilde{V}_f$ values and highlights the e^{-x^2} dependence of the normal distribution, where present.

In the attached case, the signal at the 3 mm position and beyond (Figures 5.10d-5.10i) has a maximum amplitude of 0.06 V, and the parabolic shape of these plots implies that the data at these radii are normally distributed. This suggests that at these positions, the probe is outside the bulk of the plasma column, and the signal is dominated by random noise. The amplitudes of the 0, 1 and 2 mm data are larger by factors of $10 - 30$, with the largest fluctuations at 1 mm, and are not straightforward Gaussian distributions. At 0 mm, the distribution appears to be formed of two overlapping peaks, whilst at 1 and 2 mm some negative skew is apparent. The causes of these distributions are not immediately clear.

The data for the EIR detached plasma show even more variation. At the centre of the column, the distribution is positively skewed, and the maximum $\widetilde{V}_f$ amplitudes are observed. $|\widetilde{V}_f|_{max}$ continually decreases as the radius increases, and none of the data from the other positions exhibit a distribution close to a Gaussian shape. From $2 - 6$ mm, the largest amplitude fluctuations are negative, whereas at 7 and 8 mm, they are positive. Note that the reference probe, situated at 6 mm on the opposite side of the column, may influence the behaviour of the plasma outside this radius. The structure that supports the probe tip has a diameter of the order of 10 mm, which is sufficiently large to produce a significant disturbance to the plasma column and reduce the accuracy of the results obtained from the moveable probe at 7 and 8 mm.

To provide further insight into these distributions, the skewness and kurtosis were calculated for the $\widetilde{V}_f$ data at each radial position. The results are plotted in Figure 5.12. The data from the attached plasma again suggests the presence of a narrow column of radius < 3 mm: inside this radius, the skewness and kurtosis are relatively large, but at

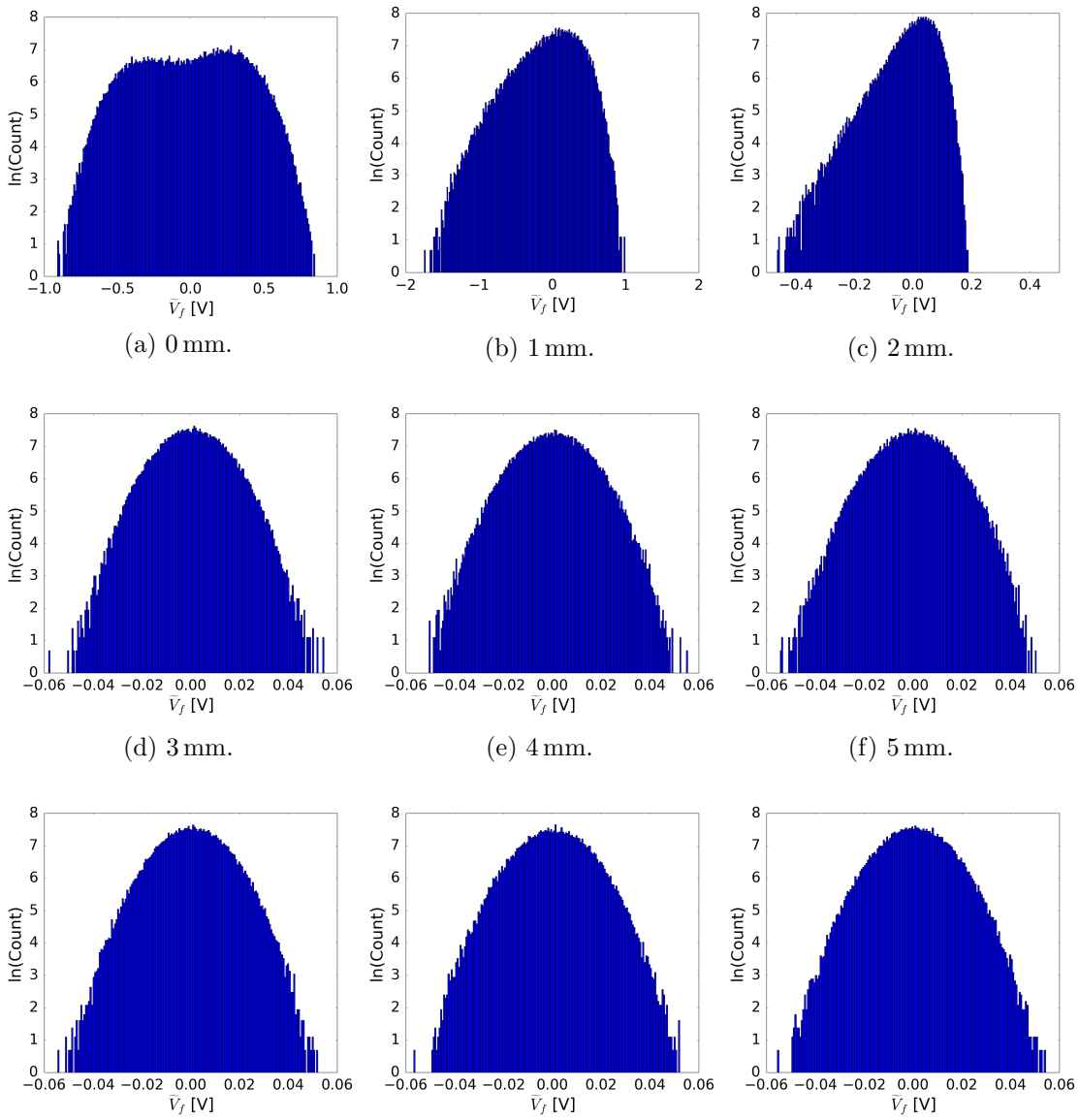

(a) 0 mm. (b) 1 mm. (c) 2 mm.

(d) 3 mm. (e) 4 mm. (f) 5 mm.

(g) 6 mm. (h) 7 mm. (i) 8 mm.

Figure 5.10: Histograms of the $\widetilde{V}_f$ time series for each radial position of the moveable probe in the attached plasma in the YLPD (target chamber pressure 3.5×10^{-4} mbar).

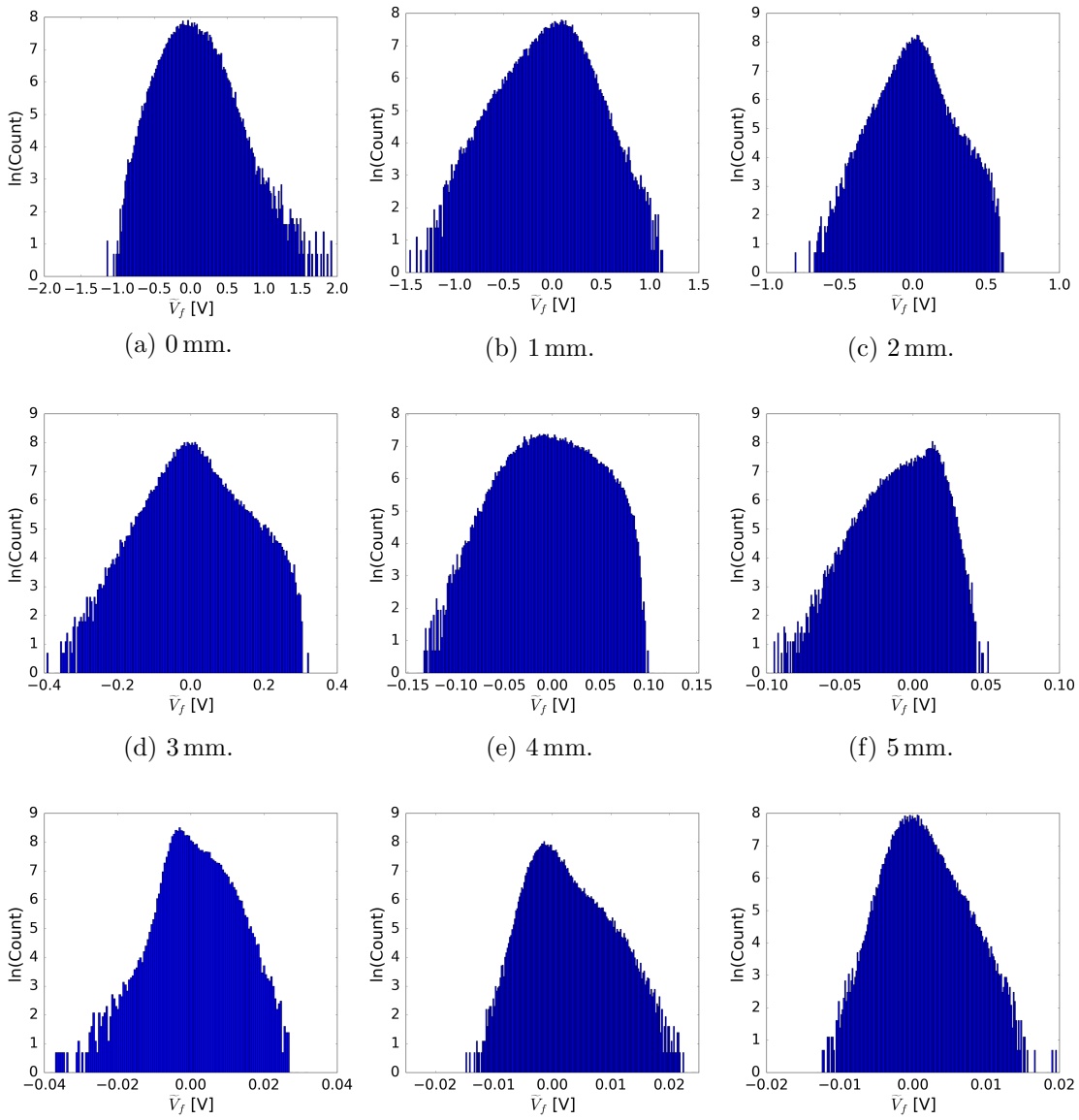

(a) 0 mm. (b) 1 mm. (c) 2 mm.

(d) 3 mm. (e) 4 mm. (f) 5 mm.

(g) 6 mm. (h) 7 mm. (i) 8 mm.

Figure 5.11: Histograms of the $\widetilde{V}_f$ time series for each radial position of the moveable probe in the EIR detached plasma in the YLPD (target chamber pressure 1.0×10^{-2} mbar).

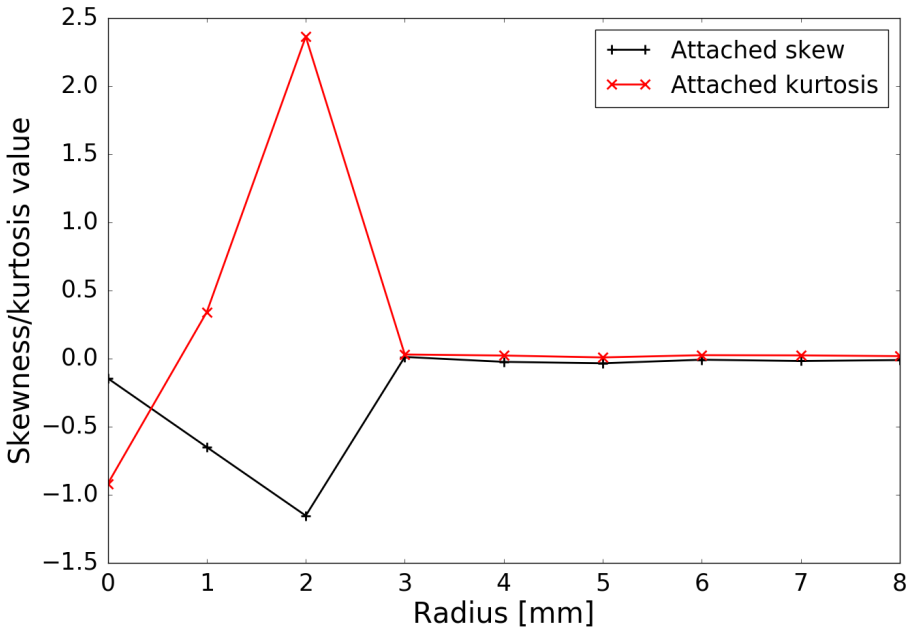

(a) Attached plasma (3.5×10^{-4} mbar).

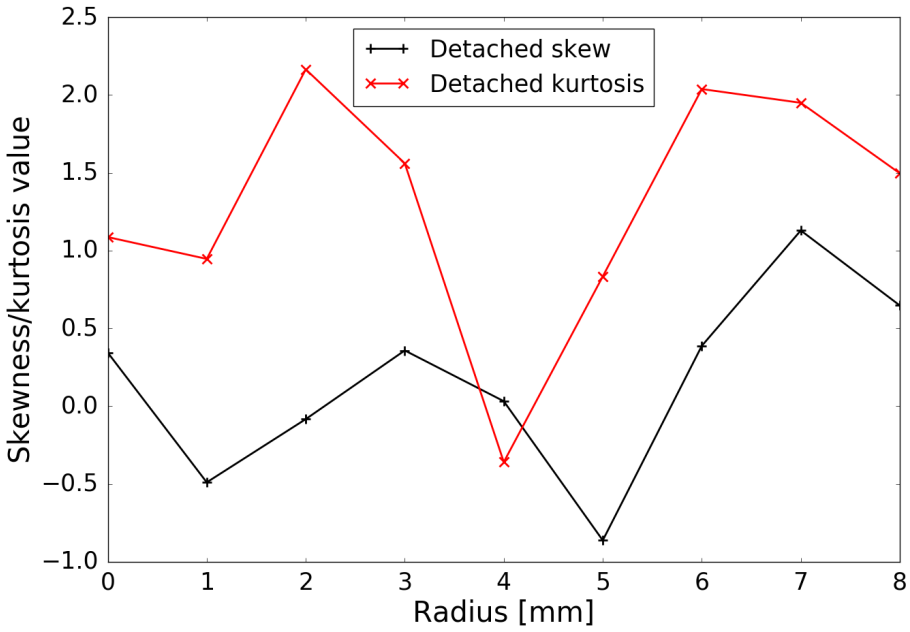

(b) EIR detached plasma (1.0×10^{-2} mbar).

Figure 5.12: Skewness and kurtosis values as functions of radial position across the plasma column in the YLPD target chamber, for (a) the attached and (b) the EIR detached cases.

3 mm and beyond they fall to zero, with very little fluctuation. This is consistent with the conclusion that at these radii the signal is dominated by normally distributed random noise, and the probe is outside the bulk of the plasma column.

The negative skewness values inside the attached column verify the negative bias identified in the histograms for these positions. The negative kurtosis at the centre of the column indicates that a relatively small number of outlying events occur here. At 1 and 2 mm, the positive kurtosis values show that the distributions at these positions have longer tails compared to a standard Gaussian.

In the EIR detached plasma, the skewness fluctuates considerably with radius, reflecting the significant variation in the histogram shapes. The kurtosis also does not exhibit any obvious trend, but remains positive at all radii except 4 mm. This indicates that at the majority of positions, the number of outlying high amplitude fluctuations is larger than would occur in a Gaussian distribution. It is difficult to draw conclusions from this data, but the broadening of the detached column is again clear. Both parameters remain relatively high out to the 8 mm position rather than falling to zero, which implies that there is still sufficient plasma at these radii to yield a signal other than noise.

5.2.2 Power spectra

To increase understanding of the $\widetilde{V}_f$ time series, the power spectra from each radial position are next considered. The resulting 2D spectrograms for the attached and detached regimes are shown in Figure 5.13. Note that the Nyquist limit for these data (recorded with a time resolution of 1 µs) is 500 kHz, compared to the 25 kHz limit for the FFI data.

Again, the spectrograms emphasise the difference in the radial extent of the two plasma states: in the attached plasma (Figure 5.13a), the spectral power is predominantly contained within a radius of 2 mm, whereas the detached plasma spectrum is still strong at low frequencies at 5 mm (Figure 5.13b). The highest amplitude frequency components in the attached plasma appear at around 300 kHz and above, with several smaller peaks below 50 kHz. In contrast, with the exception of a narrow peak at approximately 350 kHz, the spectrum for the EIR detached state is dominated by frequencies below 200 kHz. The relatively narrow peaks, at approximately 390 kHz and 350 kHz in the attached and detached spectrograms respectively, could be associated with the $\mathbf{E} \times \mathbf{B}$ rotation of the column.

The structure of the detached spectrogram differs from that obtained from the FFI data for the same state (Figure 5.7b, Section 5.1.2). There we saw a hollow profile, with

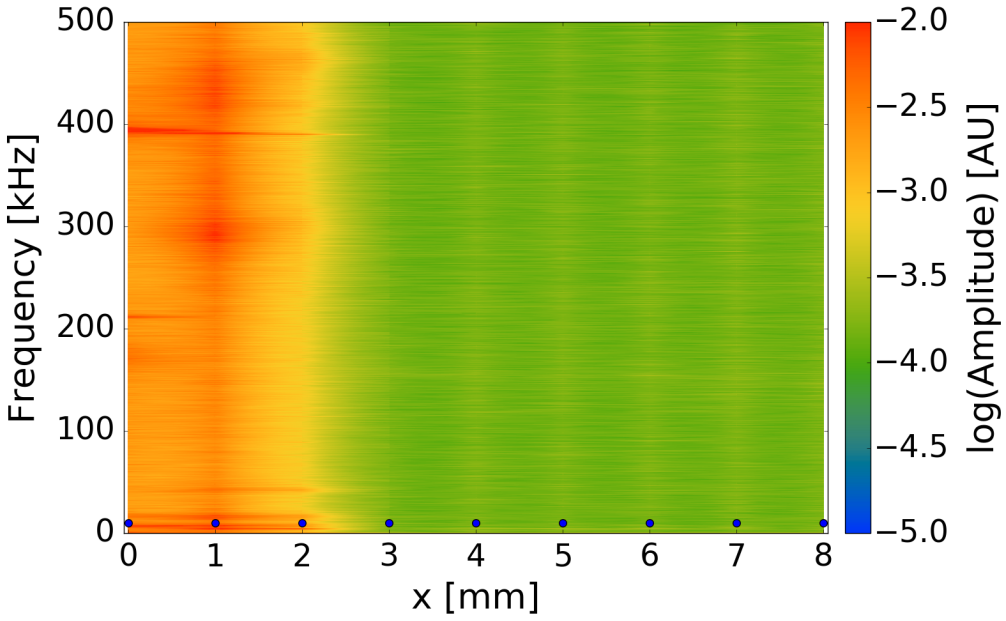

(a) Attached plasma (3.5×10^{-4} mbar).

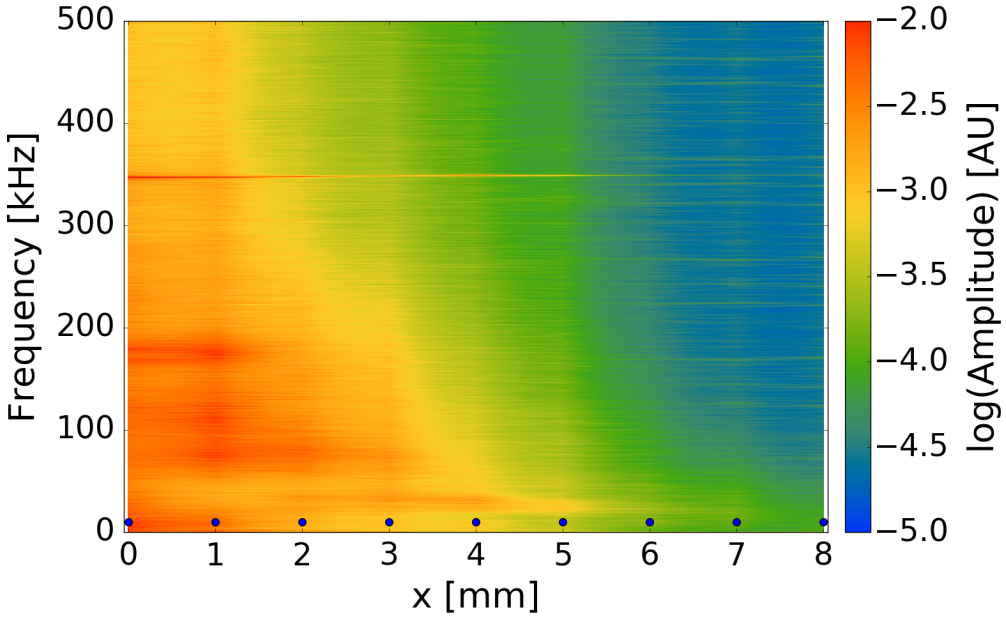

(b) EIR detached plasma (1.0×10^{-2} mbar).

Figure 5.13: Spectrograms showing the variation of the frequency components in the $\widetilde{V}_f$ time series with radial position across the plasma column in the YLPD target chamber, for (a) the attached and (b) the EIR detached cases. Blue scatter points indicate the positions at which data were recorded.

two well-defined peaks at radial positions of approximately ±9.5 mm, and lower power across the centre of the column. In the $\widetilde{V}_f$ spectrogram, however, the strongest components are seen in the centre. The radial range of the $\widetilde{V}_f$ data is smaller than the width of the FFI field of view, but the peaks are in evidence at 8 mm in the latter, and there is no increase in amplitude at the widest radii in the $\widetilde{V}_f$ spectrogram.

The ability to compare the FFI and $\widetilde{V}_f$ power spectra is restricted by the differing Nyquist frequencies of the diagnostics, but the lowest frequencies of the EIR detached $\widetilde{V}_f$ spectrogram clearly do not exhibit the hollow profile structure of the FFI power data. The most likely explanation is that the effects of EIR detachment on the floating potential and Balmer emission properties of the plasma are different. V_f, and $\widetilde{V}_f$, are determined by the balance of ion and electron densities and temperatures, whereas the photons captured by the FFI camera are emitted from neutral hydrogen atoms that are the product of three-body recombination processes. The different density and temperature dependences may be sufficient to alter how these properties fluctuate. In particular, in the hotter core of the plasma column, the recombination rate is low and there is little EIR emission to provide a signal for FFI. Secondly, the lack of any increase in the $\widetilde{V}_f$ power spectrum amplitude at the largest radii could be explained by the disturbance from the large reference probe. It is possible that removing this probe and recording moveable probe data beyond 10 mm would result in an increased power amplitude.

5.2.3 Correlation with a reference probe

We now turn to considering the relationship between the $\widetilde{V}_f$ time series recorded by the moveable and reference probes. A correlation analysis was carried out, as described in Section 3.2.2, for the 40 highest amplitude negative events in the reference probe data for each position. An example event is illustrated in Figure 5.14. The plots of average optimum time delay for the selected events at each radius are shown for both the attached and EIR detached plasmas in Figure 5.15. The errors are calculated from the standard deviation of the time delay values for the 40 events.

In the attached case, there is very little variation around the average 0 µs delay, although there are errors of up to 2 µs. Recall that the reference probe is positioned at 6 mm, which according to the earlier results is outside the bulk of the plasma column. The reference signal is therefore likely to consist predominantly of random noise, and the correlation analysis averages to zero.

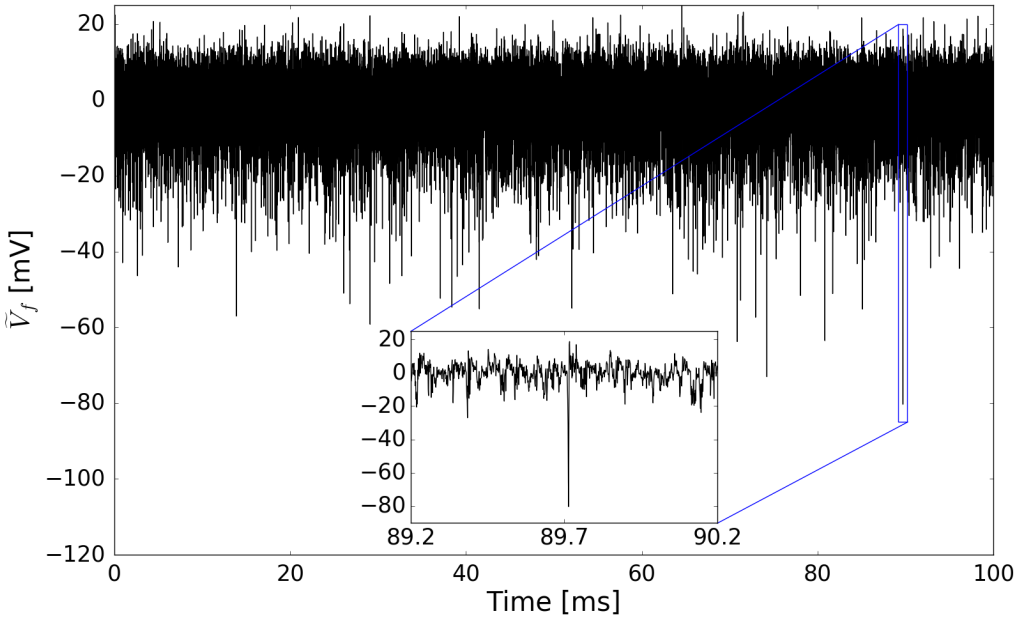

Figure 5.14: Example $\widetilde{V}_f$ time series data from the reference probe in the EIR detached plasma, with one of the selected large negative events highlighted. Inset: expanded view of the event.

The results for the EIR detached plasma exhibit more interesting behaviour. Ignoring the data at 7 and 8 mm, which, as discussed above, may be affected by the presence of the reference probe, there appears to be some structure that travels between 2 and 6 mm in a time of approximately 5 µs (indicated by the red dashed line in Figure 5.15b). Taking the minimum and maximum possible slopes of these five data points, accounting for the error bars, yields an estimate of $(650 \pm 250)\,\mathrm{m\,s^{-1}}$ for the outward radial speed of this structure. It may be expected that the time delay is zero when both probes are positioned at 6 mm, but an offset is introduced as the filamentary structures have limited azimuthal extent, and do not encircle the entire column.

Figure 5.15b may also indicate that a second structure is present, originating from the same point but travelling inwards (indicated by the blue dashed line in the figure). The data points are less well aligned here, but the estimated speed is $(380 \pm 70)\,\mathrm{m\,s^{-1}}$. It is not clear whether this is an artefact in the data, but it is possible that a disturbance of the plasma, appearing at approximately 2 mm, could propagate radially in both directions.

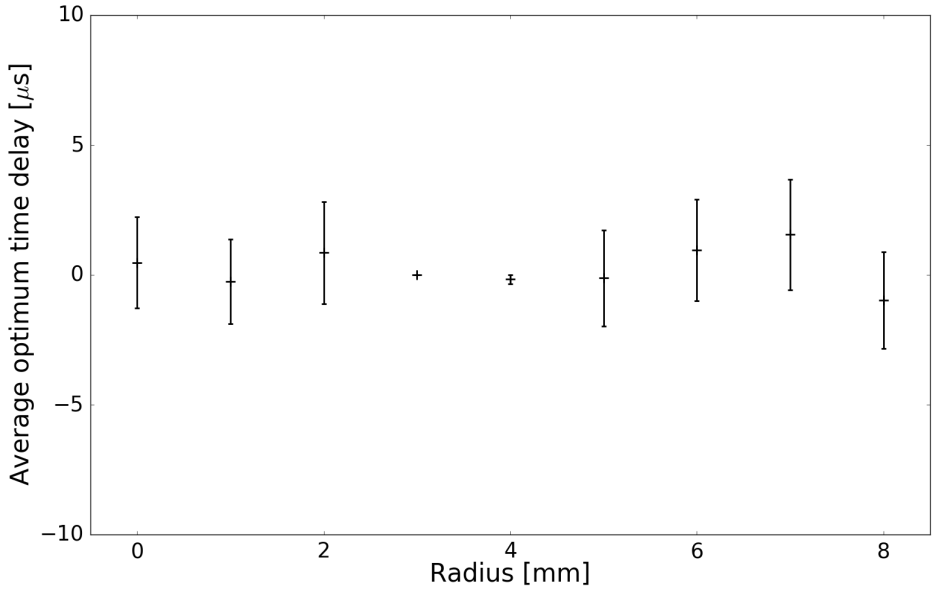

(a) Attached plasma (3.5×10^{-4} mbar).

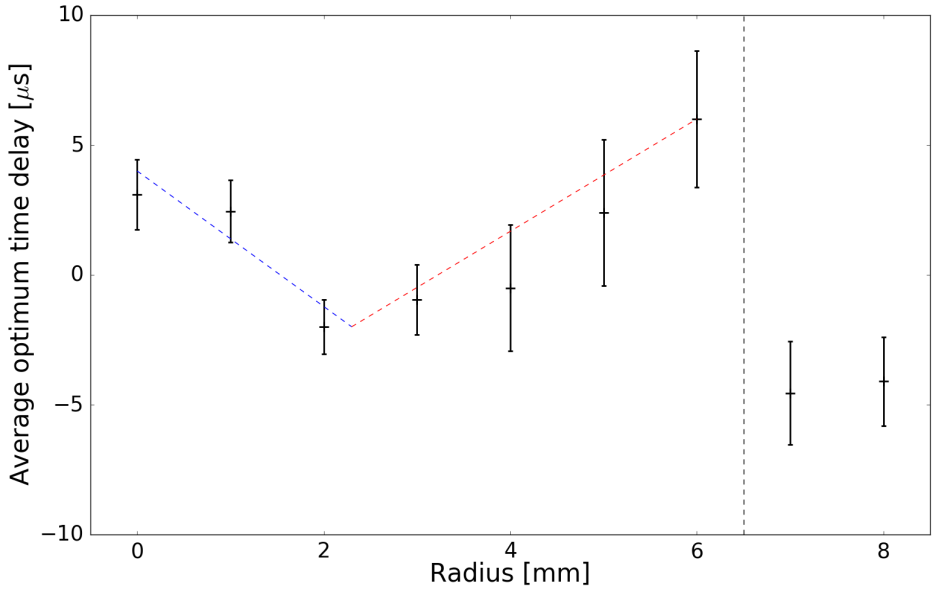

(b) EIR detached plasma (1.0×10^{-2} mbar). Data beyond the black dashed line (7 and 8 mm) is in the shadow of the reference probe. The red (outward velocity) and blue (inward velocity) dashed lines highlight the general trends in the data up to 6 mm.

Figure 5.15: Variation of the optimum time delay between the moveable and reference probe floating potential signals, as a function of radial position across the plasma column in the YLPD target chamber, for (a) the attached and (b) the EIR detached cases. Time delay values were obtained by cross-correlating the signals in the vicinity of large events in the reference signal.

5.2.4 Discussion of $\widetilde{V}_f$ results

Obtaining a complete interpretation of the $\widetilde{V}_f$ time series data is not straightforward, but the radial behaviour of the results for the attached and EIR detached states is consistent with broadening of the detached plasma column. The attached plasma data exhibits the characteristics of random noise beyond 2 mm, and the power spectrum is also confined to the 2 mm range. In the detached case, no noise-dominated signals are recorded, and the low frequency (< 200 kHz) broadband spectrum extends up to 6 mm, implying that the width of the detached plasma column is greater. However, the radial range of the data is limited by the likely disturbance caused by the reference probe, situated at 6 mm.

Time-delay correlation analysis of the reference and moveable probe $\widetilde{V}_f$ data appears to show the radial propagation of events through the EIR detached plasma (Figure 5.15b). Despite the relatively large errors, the increase in the time delay observed between the 2 and 6 mm positions is a reasonably strong indication of the radial motion of structures out of the column, with a speed of $(650 \pm 250)\,\mathrm{m\,s^{-1}}$. Inward propagation from 2 to 0 mm is also indicated, with a speed of $(380 \pm 70)\,\mathrm{m\,s^{-1}}$, although the smaller number of data points reduces the reliability of this conclusion.

It is possible that the radial propagation detected by the $\widetilde{V}_f$ analysis corresponds to the motion of the plasma filaments observed in the FFI data. In this scenario, a trigger at approximately 2 mm would result in the ejection of a filament of plasma, which, as it travels outwards, causes the observed fluctations in V_f. The inward motion suggested by the time delay data at the smallest radii could be attributed to the propagation of the region of density depletion left by the filament. An upper limit on the radial extent of the filaments is $\sim$ 3 mm, based on the maximum speed estimate ($900\,\mathrm{m\,s^{-1}}$), and an approximate V_f event duration of 3 µs. The current experimental setup means that we are unable to track the filament beyond 6 mm with the Langmuir probe, but from here it becomes visible to the FFI camera, which captures the Balmer emission produced by three-body recombination (assuming the filament has cooled as it travels).

Observations of similar radial transport of plasma filaments, or blobs, have been made on multiple machines: both in linear devices (e.g. PISCES [92], NAGDIS-II [72, 93]) and in tokamaks (e.g. NSTX [94], DIII-D [95] and Alcator C-Mod [96, 97]). In particular, the results of Boedo et al. describe intermittent transport in the scrape-off layer (SOL) of DIII-D [95]. These authors also studied large-amplitude events, with a more comprehensive set of diagnostics, and found that large positive fluctuations in the ion saturation current

(corresponding to plasma blobs) were correlated with large negative fluctuations in the floating potential, similar to those observed in the YLPD. The presence of negative V_f fluctuations in plasma blobs is also supported by $\widetilde{V}_f$ histograms from Alcator C-Mod, which have a similar, negatively-skewed distribution to those from the YLPD [96].

The DIII-D measurements also detect negative (low density) events, moving inwards towards the core of the tokamak, as well as the outward-moving high density blobs. This is again consistent with the observations in the YLPD. Furthermore, the authors measure how rapidly the blob density and temperature equilibrate with the average background values as they travel out of the SOL, and find that the temperature equalisation occurs much more quickly (on a length scale of $\sim 1\,\mathrm{cm}$ compared to $> 5\,\mathrm{cm}$ for density equalisation). Detachment in DIII-D is not considered in this work, but these results indicate that if blobs of plasma cool quickly enough as they travel radially (potentially with the aid of neutral gas puffing), recombination and detachment could occur.

In the following section, the possibility of radial transport in the YLPD is explored further. The physics of this scenario is considered, and a possible mechanism for the formation of filaments and their subsequent radial motion is proposed.

5.3 Hypothesis for filament formation

Having made fast frame imaging measurements that imply that plasma filaments are transported radially out of the column, and found some evidence for the radial motion of plasma structures in the $\widetilde{V}_f$ data analysis, the reason for this behaviour is now considered. A plausible mechanism for radial transport of filamentary plasma structures is the centrifugal instability, caused by the rotation of the linear plasma column. This is a form of the Rayleigh-Taylor instability [98], in which the rotation provides an effective gravity [99]. Centrifugal forces have been discussed in several papers on the theory of instabilities in magnetised linear plasmas (e.g. [100–102]), and observations of the centrifugal instability have been made in plasma devices such as Mistral [103, 104] and Mirabelle [99].

We begin by making some general notes pertinent to the analysis in Section 5.3.1, before outlining the mechanism of this instability (Section 5.3.2). This hypothesis, and the testing thereof, are discussed in Section 5.3.3.

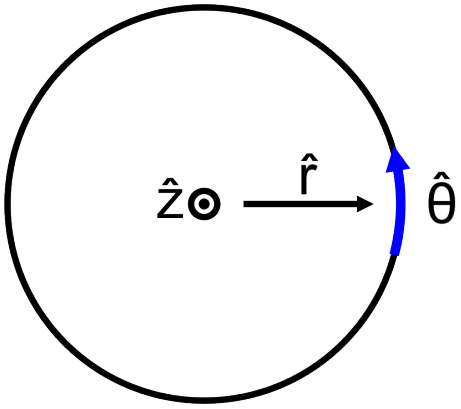

Figure 5.16: The cylindrical coordinate system describing the YLPD plasma column. The observer is situated at the target plate, looking upstream towards the plasma source at the cross-section of the column.

5.3.1 Notes on plasma physics and the coordinate system

Firstly, when describing the motion of ions and electrons in a plasma, it is common to separate the cyclotron rotation of the particles around magnetic field lines from the motion of the guiding centre of this circular path, as the cyclotron frequency of the rotation ($\Omega_{\mathrm{i,e}} = {}^{q_{\mathrm{i,e}}B}/_{2\pi m_{\mathrm{i,e}}}$) is generally faster than other types of motion [6]. In the YLPD plasma, with $B \approx 95\,\mathrm{mT}$, the approximate times taken for ions and electrons to complete one revolution (${}^{1}/_{\Omega_{\mathrm{i,e}}}$) are 0.7 µs and 0.7 ns respectively. From here, terms describing the motion of ions and electrons refer to the movement of the guiding centres of the cyclotron rotation.

The description that follows uses a cylindrical coordinate system. To orient the reader, the YLPD plasma column is directed along $\hat{z}$, travelling in the positive z direction from source to target plate. $\hat{r}$ points radially outwards from the centre of the column, and the azimuthal coordinate $\hat{\theta}$ is in the anticlockwise direction when observing the plasma from the target plate (so that $\hat{z}$ is directed towards the observer). The confining axial magnetic field is described by the vector $\mathbf{B} = B\hat{z}$. The system is illustrated in Figure 5.16.

Finally, we note that the application of a constant force $\mathbf{F}$ to a magnetised plasma will always produce a constant drift of the ion and electron guiding centres in the plane perpendicular to both $\mathbf{F}$ and $\mathbf{B}$ [6]. The general equation for the drift velocity, $\mathbf{v}_{\mathrm{D}}$, is:

$$\mathbf{v}_{\mathrm{D}} = \frac{1}{q}\frac{\mathbf{F}\times\mathbf{B}}{|\mathbf{B}|^2}. \tag{27}$$

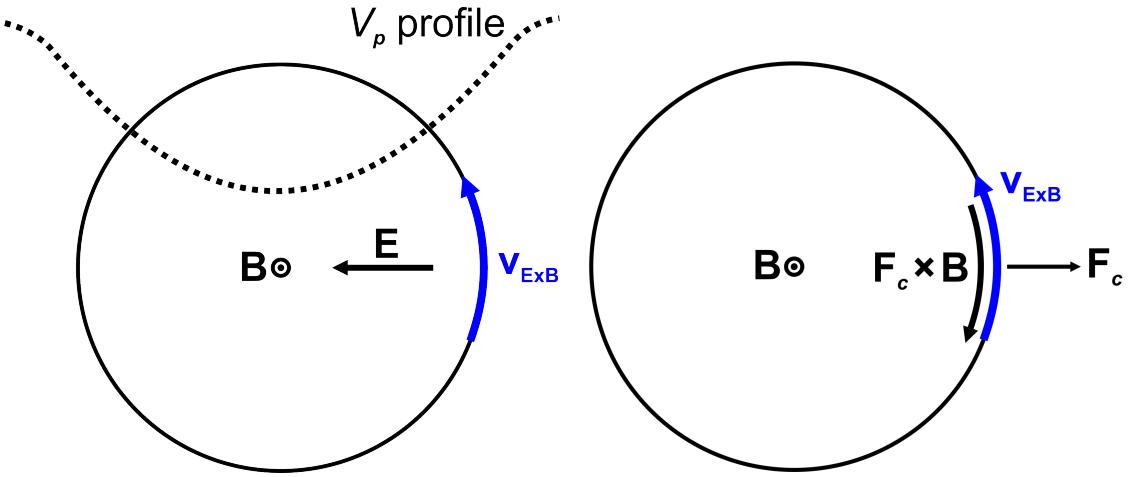

(a) The electric field derived from the radial V_p profile, and the resulting $\mathbf{E} \times \mathbf{B}$ drift velocity of the plasma.

(b) The centrifugal force felt by the rotating plasma, and the direction of the $\mathbf{F_c} \times \mathbf{B}$ ion drift velocity (reversed for the electrons).

Figure 5.17: Diagrams of (a) the plasma potential (V_p) profile across the column in the YLPD, and the resulting electric field ($\mathbf{E}$) and $\mathbf{E} \times \mathbf{B}$ drift velocity; and (b) the centrifugal force ($\mathbf{F}_c$) and the direction of the resulting ion drift velocity that arises due to the $\mathbf{F_c} \times \mathbf{B}$ rotation. Observer is situated at the target plate, looking upstream towards the source. Not to scale.

5.3.2 The centrifugal instability

The presence of an electric field across a plasma causes a common drift known as the $\mathbf{E} \times \mathbf{B}$ drift. In the YLPD plasma column, there is a positive radial gradient in the plasma potential, which produces a radial electric field directed inwards towards the centre ($\mathbf{E} = -\nabla V_p = -E\hat{r}$). This is illustrated in Figure 5.17a. The force on a particle of charge q due to an electric field is $\mathbf{F} = q\mathbf{E}$; substituting this force into (27) yields the $\mathbf{E} \times \mathbf{B}$ drift velocity:

$$\mathbf{v}_{\mathrm{E}\times\mathrm{B}} = \frac{\mathbf{E} \times \mathbf{B}}{|\mathbf{B}|^2}. \tag{28}$$

In the YLPD, the direction of this drift is anticlockwise around the column (along $\hat{\theta}$) for both ions and electrons, as shown in Figure 5.17a. The detached plasma has a potential gradient of $\sim 650\,\mathrm{V\,m^{-1}}$ beyond the centre of the column, and the axial magnetic field strength is approximately 95 mT. The $\mathbf{E} \times \mathbf{B}$ drift therefore causes the plasma to rotate anticlockwise around the column with a speed of $\sim 7000\,\mathrm{m\,s^{-1}}$.

The rotation of the plasma then results in the particles feeling an effective centrifugal force, $\mathbf{F}_c$, directed radially outwards (Figure 5.17b):

$$\mathbf{F}_c = \frac{m\, {v_{\mathrm{E}\times\mathrm{B}}}^2}{r}\,\hat{r}.$$

Substituting this force into (27) leads to a second drift velocity, which is dependent on both the mass and charge of the plasma species:

$$\mathbf{v}_c = \frac{1}{q}\frac{m\, {v_{\mathrm{E}\times\mathrm{B}}}^2}{r}\,\frac{\hat{r}\times\mathbf{B}}{|\mathbf{B}|^2}.$$

The magnitude of this centrifugal drift velocity is:

$$v_c = \frac{m\, {v_{\mathrm{E}\times\mathrm{B}}}^2}{q\, r\, B}. \tag{29}$$

The centrifugal drift acts in the clockwise direction for ions, and anticlockwise for electrons, due to the dependence on q.

If we estimate v_c for both plasma species at a radius of 2 mm, we find that:

$$v_{c,\mathrm{i}} \approx 2700\,\mathrm{m\,s^{-1}} \text{ clockwise;}$$
$$v_{c,\mathrm{e}} \approx 1.5\,\mathrm{m\,s^{-1}} \text{ anticlockwise.}$$

The mass dependence of (29) means that the effect has greater significance for the ions than the electrons. The total rotational speeds for each species are therefore:

$$v_{tot,\mathrm{i}} \approx 4300\,\mathrm{m\,s^{-1}} \text{ anticlockwise;}$$
$$v_{tot,\mathrm{e}} \approx 7000\,\mathrm{m\,s^{-1}} \text{ anticlockwise.}$$

We see that the ions travel more slowly around the column than the electrons, but if the plasma is azimuthally uniform, equilibrium is maintained.

We now consider the effect of introducing a localised density perturbation, illustrated in Figure 5.18. A small element, or 'blob', of plasma is moved radially outwards (Figure 5.18a), leaving a density deficit at its original position (Figure 5.18b). If we first focus on the blob, we see that the plasma that moves outwards is not travelling at the same speed as the plasma that is already there, thanks to the radial dependence of (29), and so the difference in the ion and electron speeds becomes important. The electrons in the displaced plasma travel faster than the ions, producing a charge separation across the blob. This results in an azimuthal electric field in the anticlockwise direction, which we denote $\mathbf{E}_p = E_p\hat{\theta}$, as shown in Figure 5.18a.

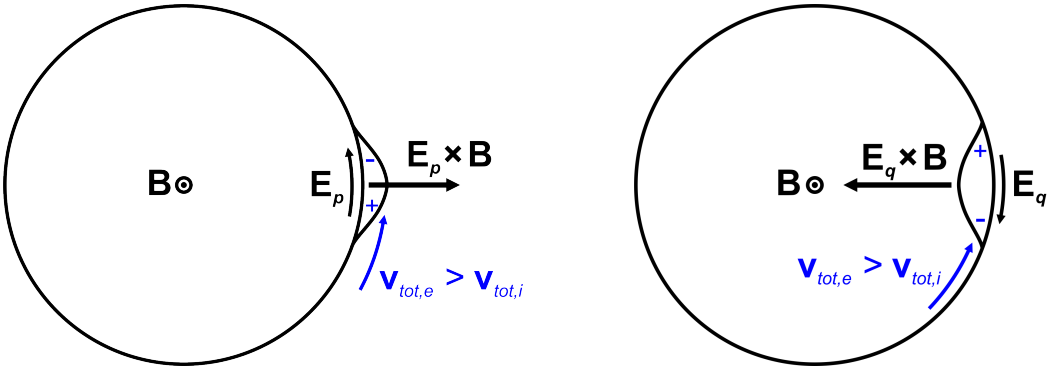

(a) Charge separation and electric field ($\mathbf{E}_p$) in the displaced plasma blob, and the resulting outward drift direction.

(b) Charge separation and electric field ($\mathbf{E}_q$) in the region of density depletion, and the resulting inward drift direction.

Figure 5.18: Diagrams of the effects of a density perturbation on the motion of the rotating plasma column, showing the charge separation and resulting electric fields and drift velocity directions for (a) the displaced plasma element; and (b) the density deficit left by the displacement. Ion and electron rotation velocities are indicated in blue. Observer is situated at the target plate, looking upstream towards the source. Not to scale.

Using (28) once more, we find that there is a second, local $\mathbf{E}\times\mathbf{B}$ drift from the force on the plasma blob due to $\mathbf{E}_p$. This drift is directed radially outwards (illustrated in Figure 5.18a) and has a magnitude of:

$$v_{\mathrm{E}_p\times\mathrm{B}} = \frac{E_p}{B}.$$

The effect of the local perturbation is therefore amplified, causing the system to become unstable. The plasma blob is ejected radially outwards, creating a filament.

Returning to the density deficit left by the removal of the blob, we find that a charge separation also arises here (Figure 5.18b). In this case, the faster electrons re-enter the region of depleted density before the ions. The charge separation is thus in the opposite direction to that in the blob, and the resulting electric field is in the clockwise direction: $\mathbf{E}_q = -E_q\hat{\theta}$. Applying the drift analysis as for the filament, we find that the local $\mathbf{E}_q \times \mathbf{B}$ drift velocity is directed radially inwards.

The overall effect of perturbing the plasma density, then, is the radial motion of a filament of plasma out of the column, and the motion of the corresponding density deficit inwards towards the centre.

Brochard, Gravier and Bonhomme describe a number of properties that can be used to distinguish between the centrifugal instability, drift waves and the Kelvin-Helmholtz

Table 5.1: Criteria for the characterisation of centrifugal instabilities, drift waves and Kelvin-Helmholtz instabilities. $v_{\mathrm{D},e}$ and $v_{\mathrm{D},i}$ are the electron and ion diamagnetic velocities respectively; $k_\perp$ and $k_\parallel$ are the perpendicular and parallel wavenumbers of the instabilities; ρ_s is the ratio of the ion sound speed to the ion cyclotron frequency; and L is the lengthscale of the machine. Adapted from [99].

Parameter	Centrifugal	Drift waves	Kelvin-Helmholtz
Phase velocity	$v_{\mathrm{E}\times\mathrm{B}}$	$\dfrac{v_{\mathrm{D},e}}{1+k_\perp^2\rho_s^2 \pm v_{\mathrm{E}\times\mathrm{B}}}$	$(0.2-0.6)\, v_{\mathrm{E}\times\mathrm{B}}$
$k_\parallel$	0	$\sim \dfrac{1}{L}$	0
Location of max. fluctuations	$\max\left(\dfrac{1}{n}\dfrac{\mathrm{d}n}{\mathrm{d}r}\right)$	Position of max. $\omega_{\mathrm{D},i} = {}^{v_{\mathrm{D},i}}/_{k_\perp}$	Position of max. velocity shear
$\max\left(\dfrac{e\widetilde{V}}{k_B T_\mathrm{e}}\right)$	1	1	$\gg 1$
$\max\left(\dfrac{e\widetilde{V}}{k_B T_\mathrm{e}}\Big/\dfrac{\widetilde{n}}{n}\right)$	≥ 1	≤ 1	$\gg 1$
Local radial variation of phase of $\widetilde{V}$	$40^\circ - 90^\circ$	$\leq 45^\circ$	$90^\circ - 180^\circ$

instability in linear plasmas, and employ them to study the instabilities in Mirabelle [99]. They base their analysis on the theory discussed by Jassby [100]. The properties of interest include the azimuthal phase velocity of the instability (the speed at which the perturbation travels around the plasma column) and the radial location of the maximum relative amplitude fluctuations, as well as the relative amplitude and phase of fluctuations in the plasma density and potential. These are summarised in Table 5.1. The data set presented in this work allows us to consider the criterion for the maximum potential fluctuation (line four of Table 5.1).

As full Langmuir probe characteristics were only recorded at the 0 and 3 mm positions, the analysis of the magnitude of fluctuations is restricted to these radial positions. At 0 mm, the measured T_e value is (2.8 ± 0.5) eV (Figure 4.11; V_f data), and the maximum fluctuation amplitude is $\sim$ 2 V. The value of ${}^{e\widetilde{V}}/_{k_B T_\mathrm{e}}$ ($= {}^{\widetilde{V}}/_{T_\mathrm{e}}$ when T_e is given in eV) is therefore around $0.6 - 0.9$. At 3 mm, $T_\mathrm{e} = 0.34 \pm 0.15$ eV as measured by the Langmuir probe (again, see the V_f data in Figure 4.11), but is estimated to be $(0.20^{+0.09}_{-0.03})$ eV by the OES diagnostic. The maximum $\widetilde{V}$ amplitude is $\sim$ 0.4 V at this position, and the maximum ratio lies in the range $1.3 - 2$ (taking the more reliable OES temperature).

These ratios are both consistent with the hypothesis. We certainly expect to see evidence for the centrifugal instability at 3 mm as the associated filamentary structures move outwards. At 0 mm, the plasma potential is at its minimum, and the electric field and associated azimuthal $\mathbf{E} \times \mathbf{B}$ drift are negligibly small. The rotation velocity of the plasma will thus be much smaller and the centrifugal instability is unlikely to be significant. The indication that drift waves occur at the centre of the column highlights the need to include the other criteria in fully identifying the instabilities in the column. This hypothesis, and the need to develop and test it further, are discussed in the following section.

5.3.3 Discussion

The centrifugal instability is a plausible mechanism for the formation of filamentary structures in the EIR detached plasma in the YLPD. The results presented in the first two sections of this chapter suggest the presence of such radially transported 'blobs' of plasma, but do not provide a fully comprehensive picture of the behaviour. Here we discuss the shortcomings of this data set, and outline what is required to develop our understanding.

Firstly, the data is insufficient to fully test the presence of instabilities according to the criteria outlined in Table 5.1. Upgrading the Langmuir probe diagnostic on the YLPD to improve the spatial range and resolution of the probe measurements would increase the accuracy with which the evolution of the filaments could be tracked, and allow detailed density and temperature profiles to be measured. Increased spatial and temporal resolution would also assist in the evaluation of the amplitude and phase of $\widetilde{n}$ and $\widetilde{V}$.

Previous observations of the centrifugal instability in the linear plasma device Mistral have shown that it leads to the formation of spiral 'arms' of plasma that grow and rotate over tens of microseconds [104]. A similar evolution in the YLPD could lead to the elongated azimuthal structures seen in the 20 µs exposure FFI images, but the $\mathbf{E} \times \mathbf{B}$ velocity in the YLPD plasma is a factor of ~ 4 higher than in the Mistral experiments, and we therefore might expect to see even more elongation than is observed.

In the case of the radial motion in the YLPD, the $(650 \pm 250)\,\mathrm{m\,s^{-1}}$ outward radial drift velocity estimated by the $\widetilde{V}_f$ measurements predicts that a filament would be displaced by $8 - 18$ mm in the radial direction in the FFI camera exposure time. This displacement would be expected to correspond to the radial widths of the structures in the images, but instead the observed widths are in the region of $5 - 8$ mm. This suggests that the higher filament velocity estimates may be more accurate, and also implies that the filaments

are likely to be relatively narrow ($< 1\,\mathrm{mm}$), limiting their apparent width during the FFI exposure time. This is reasonably consistent with the maximum filament width of $\sim 3\,\mathrm{mm}$ estimated from the duration of the V_f events, but these analyses are unable to conclusively determine the behaviour of the EIR detached plasma.

These discrepancies show that more thorough measurements of the detached plasma are needed in order to produce an enhanced model of the radial transport due to the centrifugal instability. It is also likely that the axial motion of the ions and electrons must be included in such a model: the plasma continually streams from source to target plate, and so filaments which detach from the main column will no longer be directly replenished by the upstream source. This could place a limit on their lifetime.

Optimising the FFI system and the image analysis procedures to allow a higher frame rate would enable the evolution of the emission from the plasma filaments to be captured in more detail. Characterisation of the scale of the images is also needed to properly evaluate the size and velocity of the features. However, linking the emission captured by the FFI diagnostic with the instabilities observed through probe measurements can only be fully achieved by including particle interactions as well as transport in a model of the plasma. Cooling of the filaments as they travel is key to the onset of three-body recombination, which produces the Balmer emission line photons captured by the FFI camera, and ultimately results in EIR detachment.

These improvements to the diagnostic systems would enable the radial transport in the YLPD to be characterised more thoroughly (in a similar manner to blob transport in e.g. DIII-D [95]). The inclusion of fast frame imaging of the high-n Balmer line emission and modelling of recombination would extend the studies to consider the links between radial transport and EIR detachment, which previous research has not focused on. Observations of similar radial blob transport have been made in a detached helium plasma in the linear machine NAGDIS-II [72, 105], but the relationship between the centrifugal instability and EIR detachment in hydrogen plasmas has yet to be studied in detail.

The development and experimental testing of a comprehensive theory describing EIR detachment in the YLPD is beyond the scope of this thesis, but the experiments described here have provided a foundation on which to base the next steps of this research. Having identified the presence of intermittent radial transport events in which filaments of plasma are ejected from the column, future studies can now focus on the characterisation and identification of the instability mechanism which drives them.

5.4 Summary

In this chapter, two types of fast timescale diagnostics have been used to look for fast radial transport events in the detached EIR plasma in the YLPD, and compare this state to the attached plasma. Fast frame imaging (FFI) with a camera operating at a 50 kHz frame rate showed clear evidence for filamentary structures in the plasma at radii of 6 mm and beyond, occurring intermittently on timescales faster than 20 µs. These structures are extended azimuthally, over angles of up to 180°, but limited to narrow radial widths of approximately $5 - 8$ mm.

The limited temporal resolution of the FFI data means that the evolution of individual filaments cannot currently be tracked, but comparing the attached and detached images clearly shows that the plasma broadens significantly (by at least a factor of two) when it detaches. However, there is still some discrepancy between the broadening observed in the FFI data and the location of the peaks of the Balmer emission profiles presented in Chapter 4. The peaks of the hollow profile were situated at ±6 mm, whereas the bright filaments in the images appear beyond this radius. This implies that an additional broadening mechanism, such as radial transport, is required to explain the observations. Further understanding is also needed in order to interpret the FFI coherence and phase plots.

The $\widetilde{V}_f$ data again strongly indicates the broadening of the detached plasma column compared to the attached state, in which the signal beyond the 2 mm radius only consists of random noise. The detached $\widetilde{V}_f$ time series indicate that plasma is present over the full radial range of the measurements, although the size of the reference probe limits the accuracy of the data beyond 6 mm.

A time delay correlation analysis between the reference and movable Langmuir probes, focusing on the highest amplitude negative fluctuation events in the reference time series, suggests that radial transport of structures in the plasma does occur in the EIR detached state, possibly in the inwards direction as well as out of the column. This led to the hypothesis that centrifugal instabilities in the detached plasma result in the radial propagation of blobs, or filaments, of plasma towards the edges of the column, and inward-directed transport of the corresponding depleted density region.

Calculations of the maximum ratio of the V_f fluctuation amplitude to the electron temperature at the 0 and 3 mm positions appear to be consistent with the centrifugal instability hypothesis, according to one of several criteria [99]. There are multiple criteria

which cannot be tested with this limited data set, however, and discrepancies arise between the location and extent of the filaments observed by the FFI and V_f diagnostics, and the speeds with which the simple theory predicts them to travel.

We conclude that further studies are required, both theoretical and experimental. A model of the EIR detached state must be developed that includes plasma transport in three dimensions, as well as particle interactions within the plasma and with the background neutral gas, and further measurements must be made in the YLPD to characterise the detached behaviour more thoroughly. Only then can the links between radial transport and detachment of the YLPD plasma be fully understood.

The similarities between features of the YLPD observations and previous measurements of intermittent radial transport in tokamaks have been briefly discussed, and the lack of research linking such transport to EIR detachment in these machines was highlighted. The wider impact of the YLPD observations and the resulting hypothesis for the EIR detachment mechanism are discussed further in Chapter 7. In the next chapter, we turn to the issue of power injection in tokamaks.

Chapter 6

Characterisation of negative hydrogen ion production in the RF plasma device MAGPIE

In this chapter, observations of negative hydrogen ions in the linear plasma device MAGPIE (Magnetised Plasma Interaction Experiment) are presented. The study aims to investigate the viability of helicon plasmas as caesium-free negative ion sources for neutral beam injection (NBI) in tokamaks. In the first section, we recap the requirements for tokamak NBI systems that were discussed in Section 1.2 of Chapter 1. MAGPIE and the additional diagnostic techniques employed in the study (laser photodetachment and B-dot probes) are introduced in Section 6.2. The results from the diagnostics are presented in Sections 6.3-6.6, and we summarise in Section 6.7.

This work was carried out in collaboration with C. Corr and J. Santoso at the Australian National University. The majority of the experimental work and analysis, excepting the B-dot probe measurements (obtained by J. Santoso), was carried out jointly. The rate coefficient study (Section 6.4.2) and all frequency analyses (Sections 6.5 and 6.6.2) are solely the work of this author. All simulation data were obtained by J. Santoso.

6.1 Motivation

The primary motivation for this work is the characterisation of the negative hydrogen ion population in the pulsed helicon plasma produced by MAGPIE. As introduced in Chapter 1, negative ion sources are integral to the NBI systems used for plasma heating, fuelling and

current drive in tokamaks [15, 17]. Ions are produced by an inductively coupled plasma source, and accelerated to create a high-energy beam. The ions are then neutralised, yielding a beam of neutral atoms that is injected into the tokamak.

Beam energies in excess of 1 MeV are necessary to meet the requirements of NBI systems for large tokamaks (e.g. ITER [5]). High particle energies increase the mean free path for ion-neutral interactions, meaning that the neutral beam is able to reach the core of the tokamak before depositing its energy through collisions with the plasma.

An efficient NBI system needs the neutralisation reaction to have a high cross-section once the ions have been accelerated. Comparison of the neutralisation rates for positive and negative ions shows that at high energies the process is around four times more efficient for negative ions ($\sim 55\,\%$ compared to $< 15\,\%$, as was shown in Figure 1.7) [17]. However, the efficiency of the initial production of negative ions remains an issue. Current designs use inductively coupled plasma sources, which incorporate a caesium catalyst to improve the negative ion yield [18]. This increases the complexity of the system, as the caesium must be continually replaced, and its high reactivity introduces safety concerns. It is therefore preferable to develop a negative ion source of equivalent (or greater) efficiency that does not require the use of caesium. As a guideline, an approximate threshold for the density of negative ions that such a source must produce is $1 \times 10^{17}\,\mathrm{m}^{-3}$ [106].

It has been suggested that helicon plasma sources (such as MAGPIE) could be employed as caesium-free negative ion sources, due to their efficiency at producing high density plasmas with low electron temperatures [107, 108]. However, further research into the operation and optimisation of these sources is needed in order to demonstrate that the required negative ion production rate can be sustained. This work studies the behaviour of the helicon plasma discharge in MAGPIE, focusing on its negative ion population. NBI systems in fusion reactors will operate with deuterium, but this study (and much other negative ion source research) uses hydrogen, which is the more readily available isotope.

6.2 Methods

6.2.1 MAGPIE

The Magnetised Plasma Interaction Experiment (MAGPIE) is a 1.7 m long vacuum vessel with an RF helicon antenna source, driven at 13.56 MHz [109]. A schematic diagram of the machine is shown in Figure 6.1. It consists of two sections: the source chamber, a

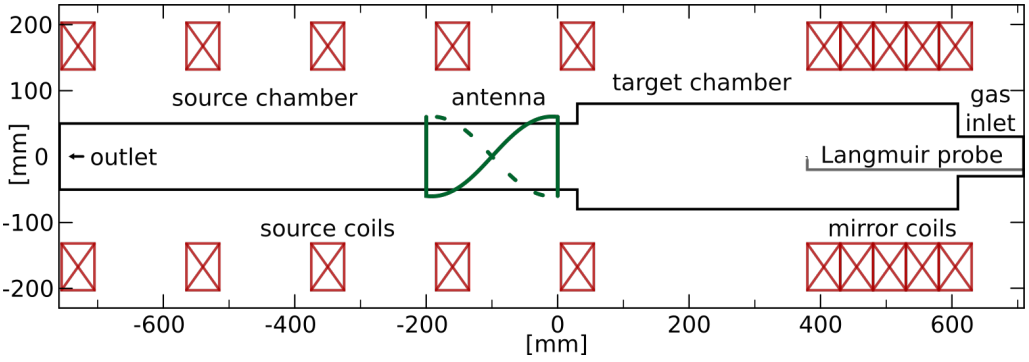

Figure 6.1: Diagram of the main chambers of the MAGPIE machine. The helicon antenna is shown in green and the magnetic field coils in red. The 0 mm position is aligned with the right hand end of the antenna [110].

borosilicate tube 1 m in length; and the aluminium target chamber, which is 0.7 m long. Each region has its own set of water-cooled magnetic field coils, shown in red in Figure 6.1, which enable tailored magnetic mirror field profiles to be created. The maximum field in the source region is 90 mT, whereas the maximum field in the target chamber is 190 mT; the higher field strength in the target region means that the highest densities occur there.

The working gas is fed into the end of the target chamber at the opposite end to the outlet, which is beyond the source region. A turbo pump at the outlet creates a fill pressure gradient in the same direction as the expected plasma density gradient. Plasma is created by coupling energy into the gas using a Nagoya III helicon antenna, 20 cm long and 12 cm in diameter (shown in green in Figure 6.1). The antenna has a left-handed, 180° helical twist, which launches $m = +1$ waves towards the target region [111]. Plasma generation using RF antennas is discussed further in e.g. [112, 113] and references therein. Helicon waves are able to propagate through higher density plasmas than other types of wave, which increases the maximum plasma density that can be produced [109].

The transparent borosilicate tube which forms the source chamber enables easy optical diagnostic access, and the end plate of the chamber has small ports for windows or diagnostics. The aluminium target chamber has two large Pyrex windows, as well as fixed ports on the sides and in the end plate.

Previous work on MAGPIE has found that negative ion densities of up to $6 \times 10^{15}\,\mathrm{m}^{-3}$ can be obtained in a hydrogen plasma with 1 kW of input power, a 10 mTorr fill pressure (1.33×10^{-2} mbar), and an axial magnetic field of a few milliTesla [108]. The electron density was $\sim 8 \times 10^{16}\,\mathrm{m}^{-3}$. In the present study, the power to the helicon antenna

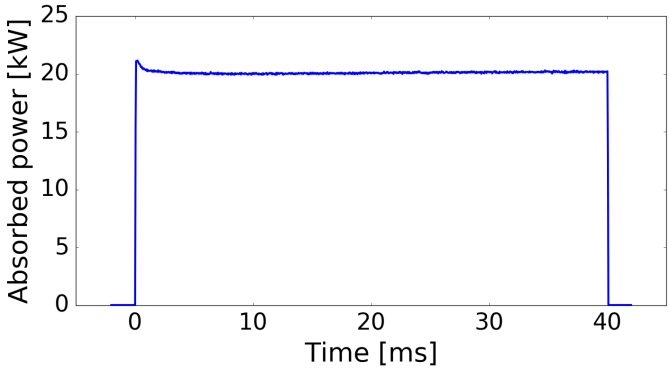

Figure 6.2: Plot of the power coupled from the helicon antenna to the plasma in MAGPIE throughout a typical 40 ms pulse.

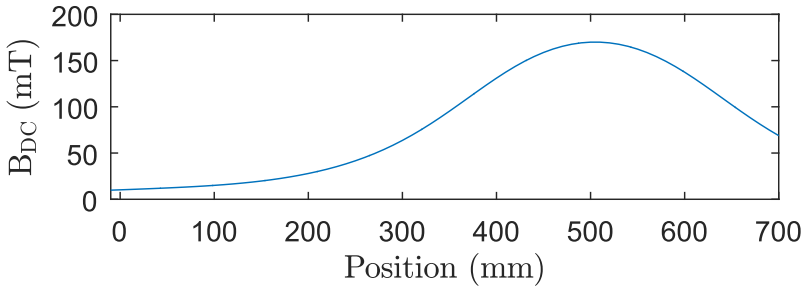

Figure 6.3: The DC magnetic field profile on-axis through the target chamber of MAGPIE for 50 A source field coil current and 800 A mirror field coil current. The right-hand edge of the antenna is at 0 mm (see Figure 6.1) [110].

is increased to 20 kW, and the evolution of the plasma throughout 40 ms RF pulses is considered in order to elucidate the behaviour of the negative hydrogen ion population. Figure 6.2 shows the absorbed power profile throughout the pulse. The confining magnetic field profile for these pulses was produced using a current of 50 A through the source field coils, and 800 A through the mirror field coils. The resulting field profile is shown in Figure 6.3; the field strength in the antenna region is $\sim$ 10 mT, with a peak field strength of $\sim$ 170 mT in the target chamber. The gas fill pressure was 10 mTorr (1.33×10^{-2} mbar).

6.2.2 Laser photodetachment

Negative ion species in a plasma can be studied with Langmuir probes, but the applicability of the technique is limited. The reliability of probe measurements is restricted by the assumptions made in the sheath analysis, and the error becomes relatively large in plasmas

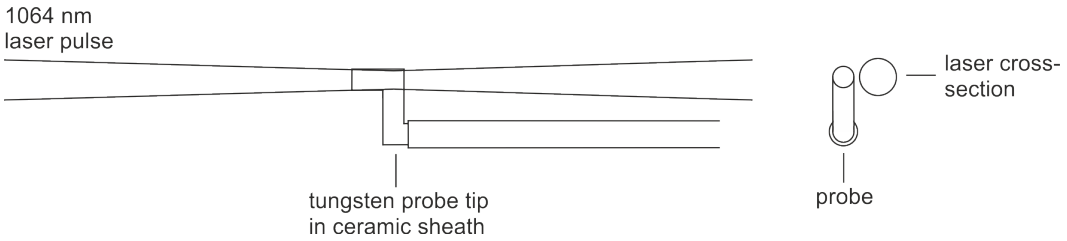

Figure 6.4: Sketch of the laser photodetachment setup in MAGPIE (not to scale). The dog-leg probe tip is first positioned within the plasma, then the laser focus and alignment are adjusted to maximise the photodetachment signal.

where the negative ion population is small compared to the electron density [114, 115]. More accurate results can be achieved using probe-based laser photodetachment, which is used to study the negative ion population through photodissociation of the ions [116]. This technique is able to measure the negative ion density local to a Langmuir probe by focusing a laser pulse in the vicinity of the probe. The concept is illustrated in Figure 6.4.

The laser wavelength is chosen so that the photons passing through the plasma have sufficient energy to dissociate a negative ion into a neutral atom and electron, without undergoing other, higher energy interactions with the plasma (particularly the ionisation of neutral atoms). For negative hydrogen ions, for which the electron affinity is 0.754 eV, a 1064 nm (1.17 eV photon energy) laser is suitable [116].

The probe is biased positively, 60 V above the plasma potential, so that all electrons and no positive ions are collected. The current drawn by the probe without the laser gives the background value, denoted I_{DC}. When a laser pulse passes through the plasma, it dissociates the negative ions and creates a population of 'photoelectrons', increasing the electron density by Δn_{e}. The photoelectrons in the region of the Langmuir probe are collected by the probe, causing a spike in the probe current of magnitude ΔI_{pd}. The fractional change in current, which we will label as η, is equal to the fractional change in density:

$$\eta = \frac{\Delta I_{\mathrm{pd}}}{I_{\mathrm{DC}}} = \frac{\Delta n_{\mathrm{e}}}{n_{\mathrm{e}}}. \tag{30}$$

The current returns to the background level after the laser pulse, once the electron population settles. The voltage from the probe is recorded by an oscilloscope (giving ΔV_{pd}) and then converted to current. Figure 6.5 illustrates an example photodetachment signal.

Assuming that all negative ions in the laser path are dissociated, no other processes occur and all photoelectrons are collected by the probe, one photoelectron is released from

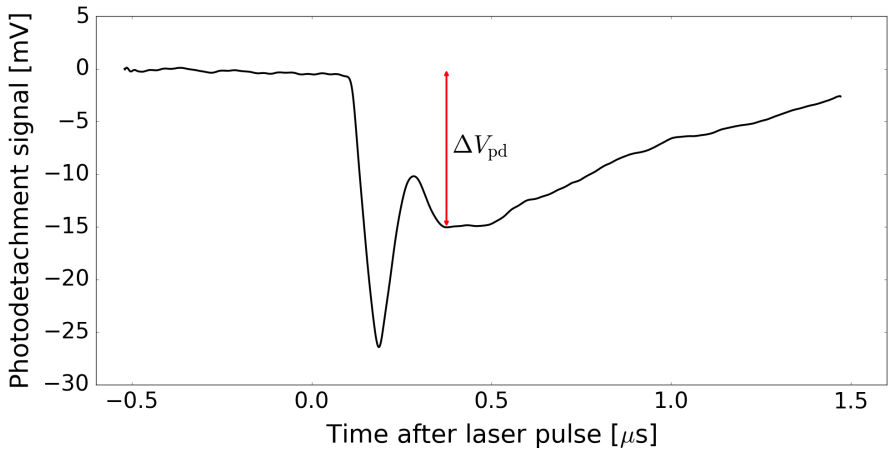

Figure 6.5: Example of a laser photodetachment signal from a hydrogen plasma in MAGPIE, showing the time evolution of the voltage drop across a positively-biased Langmuir probe in response to the photoelectron current caused by a laser pulse. The data has been background-corrected using the time evolution of the current drawn from the plasma without the laser firing. The initial large voltage drop is ignored as it is thought to be caused by probe ablation [116]. The measured signal, ΔV_{pd}, is denoted by the red arrow.

each negative ion, and Δn_{e} is equal to the negative ion density, n_{H^-}. Substituting this into (30) shows that η is the negative ion fraction within the plasma (the electronegativity):

$$\eta = \frac{n_{\mathrm{H}^-}}{n_{\mathrm{e}}}. \tag{31}$$

To calculate n_{H^-} from η, it is only necessary to multiply by n_{e}. However, as discussed in Section 3.2.1, direct Langmuir probe measurements of the electron density are not particularly reliable. Instead, we use the property of plasma quasineutrality to assume that, overall, the positive ion, electron and negative ion densities are subject to the following relationship:

$$n_{\mathrm{i}} = n_{\mathrm{e}} + n_{\mathrm{H}^-}. \tag{32}$$

Combining this expression with that for η, (31), allows us to calculate both n_{e} and n_{H^-}.

In order to obtain accurate values, it is important to set up the photodetachment diagnostic correctly. The saturation of ΔI_{pd} with both the energy of the laser pulse and the probe bias voltage must be checked. The pulse energy must be sufficient to dissociate all the negative ions in the vicinity of the probe, but should not be increased over the saturation level to minimise any other interactions between the laser and the plasma. Similarly, the probe bias voltage must be high enough to collect all the photoelectrons,

but should not be significantly over this threshold to limit the disturbance caused to the plasma. These requirements are further discussed in the review paper by Bacal [116].

The axial dog-leg Langmuir probe illustrated in Figure 6.1 was used for conventional density and temperature analyses by recording IV curves (as described in Section 3.2), as well as for laser photodetachment measurements of n_{H^-} in conjunction with a 1064 nm Nd:YAG laser. The laser was operated with a pulse energy of approximately 80 mJ and pulse length of a few nanoseconds. Details of these measurements and the results are laid out in Sections 6.3 and 6.4 respectively. The probe was also used to record time series of the floating potential throughout the 40 ms pulses, in order to analyse the frequency spectra of modes present in the plasma (Section 6.5).

6.2.3 B-dot probe

B-dot probes are so-called due to their ability to measure time-varying magnetic fields using the principle of induced voltage, V, in a loop or coil of wire (Faraday's law):

$$V = -NA\frac{\mathrm{d}B}{\mathrm{d}t},$$

where N is the number of loops in the coil and A is the area enclosed by one loop. Measuring the voltage induced in a coil of wire inserted into a plasma enables the calculation of the magnetic field strength perpendicular to the coil, B, through time. Increasing N improves the sensitivity of the measurement, but also increases the inductance of the probe. The maximum time resolution that can be recorded is reduced by a higher inductance, so the number of turns in the coil must be chosen as a compromise between the sensitivity and measurement frequency. B-dot probes and their construction and applications are discussed further in e.g. [81, 117, 118] and references therein.

The B-dot probe employed in this study consisted of a 6-turn coil, used to measure the x and y (i.e. radial) components of the magnetic field along the axis of MAGPIE. This field is induced in the plasma by the helicon antenna: the confining axial magnetic field produced by the field coils around the chamber is constant in time and therefore is not measured by the probe. The z component (along the machine) of the field produced by a Nagoya III antenna is zero on the axis of symmetry. Data were recorded at a rate of 125 MHz.

6.3 Langmuir probe IV measurements

6.3.1 Results

Langmuir probe data were taken at axial positions from 0 to 650 mm in 50 mm steps, with a final measurement at the maximum possible distance of 690 mm (positions relative to the target-end edge of the antenna; see Figure 6.1). A signal generator was used to continually sweep the bias voltage applied to the probe throughout the 40 ms pulse. The period for a full voltage cycle (positive $\rightarrow$ negative $\rightarrow$ positive) was 0.2 ms, yielding 200 up-sweep and 200 down-sweep IV-curves for each pulse. The results for each position were averaged over 16 pulses to reduce noise (using the oscilloscope), and corrected for the probe inductance. Then, the up- and down-sweeps for each 0.2 ms voltage cycle were averaged in the analysis process, producing a single IV curve for each 0.2 ms time segment between 0.6 and 39.8 ms (inclusive). These curves were then analysed (as detailed in Section 3.2) to yield the time evolution of the axial profiles of the positive ion density (n_i) and electron temperature (T_e), shown in Figures 6.6a and 6.6b respectively.

6.3.2 Discussion

The 2D density and temperature plots in Figure 6.6 show that the axial profiles vary with time during the first half of the pulse, and then relax into a steady state for the remaining ~ 20 ms. n_i initially peaks around the maximum applied magnetic field strength (~ 400 mm), with the variation between the minimum and maximum densities reaching almost two orders of magnitude. The peak then decreases in strength and travels away from the antenna (towards 550 mm). The steady state profile is more uniform along the machine: n_i varies only by a factor of $2-3$ between the minimum and maximum values.

The electron temperature exhibits a different evolution, but the timescale remains the same. At the beginning of the pulse, T_e decreases by a factor of ~ 5 between the antenna edge (at 0 mm) and 400 mm, dropping below 1 eV at this point and remaining low beyond it. The plasma then heats up as the higher temperatures propagate through the machine. After around 20 ms a steady state profile is reached, with a variation of less than a factor of two between the 0 and 690 mm positions.

From the temperature data, the propagation speed of the plasma heating front through MAGPIE is calculated to be in the region of $10-20\,\mathrm{m\,s^{-1}}$ during the first 20 ms of the pulse. This is two or three orders of magnitude below the velocities associated with typical

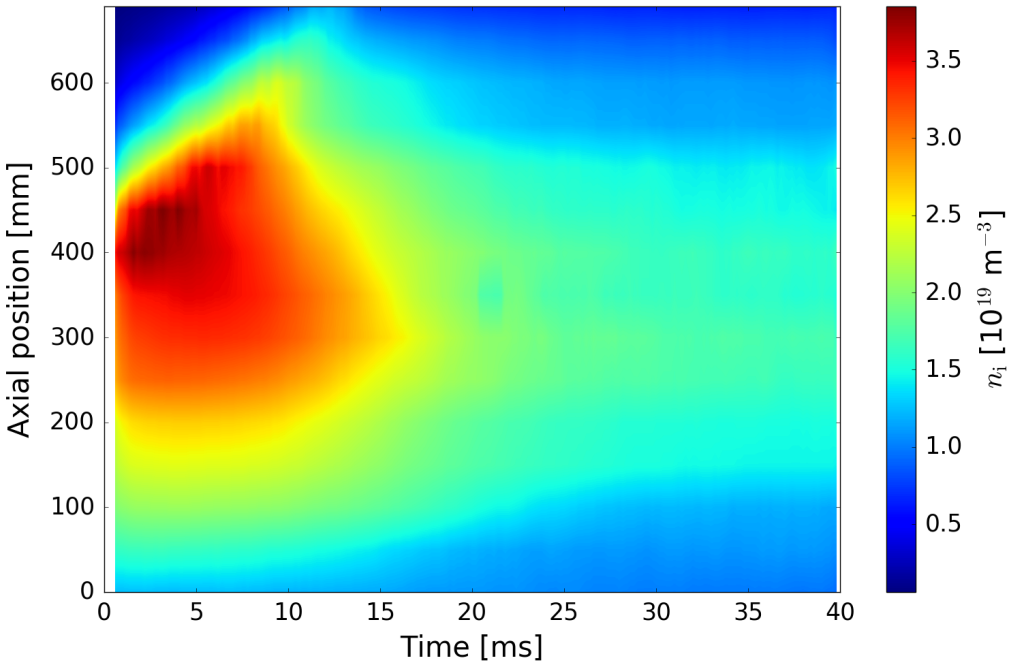

(a) Positive ion density evolution.

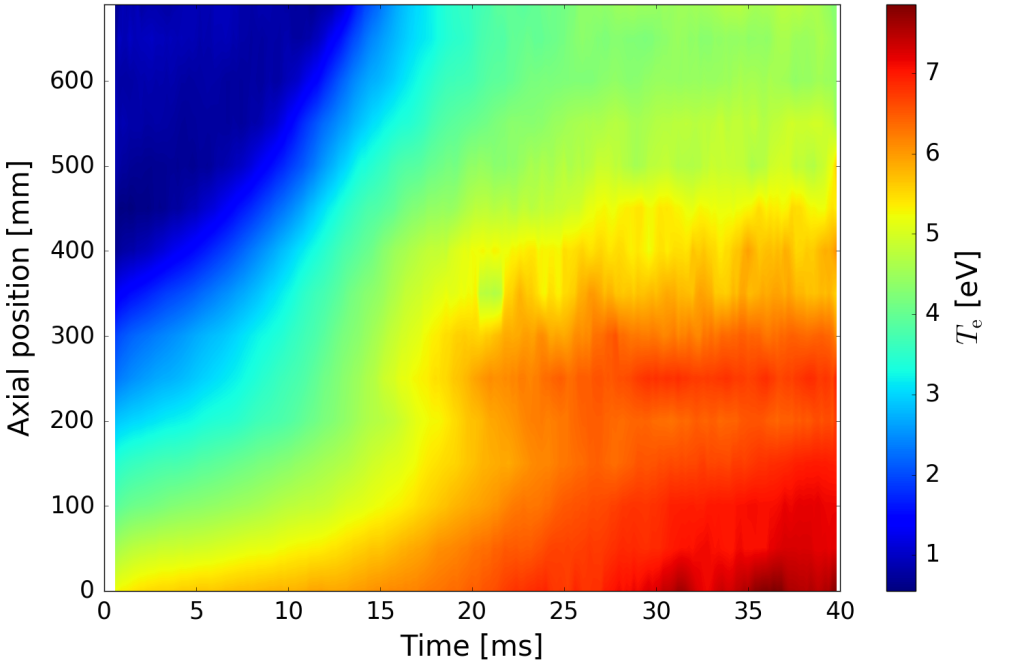

(b) Electron temperature evolution.

Figure 6.6: Time variation of axial (a) density and (b) temperature profiles throughout MAGPIE during a 40 ms pulse, as measured by the Langmuir probe.

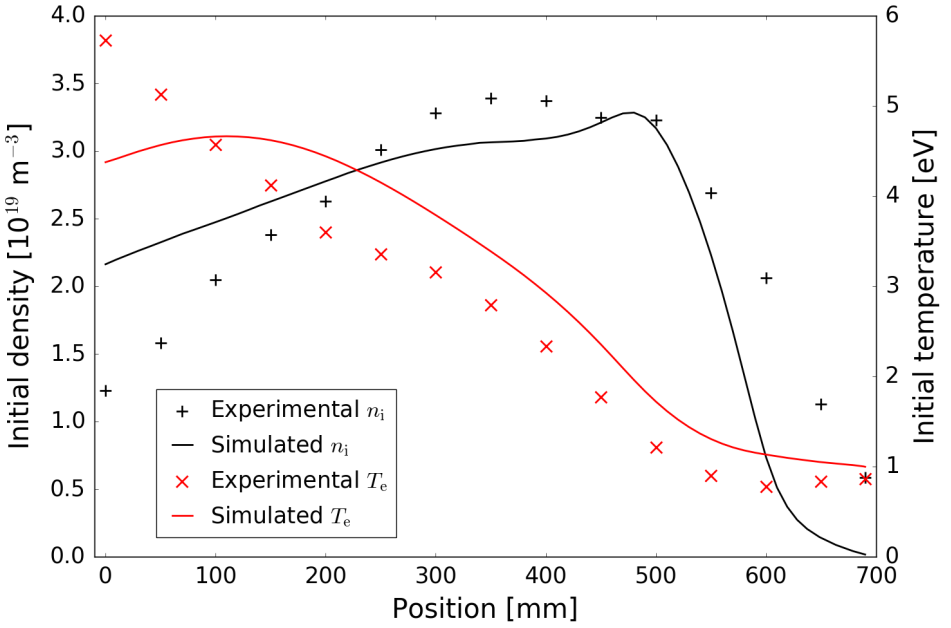

(a) Initial n_i and T_e axial profiles (taken at 6 ms).

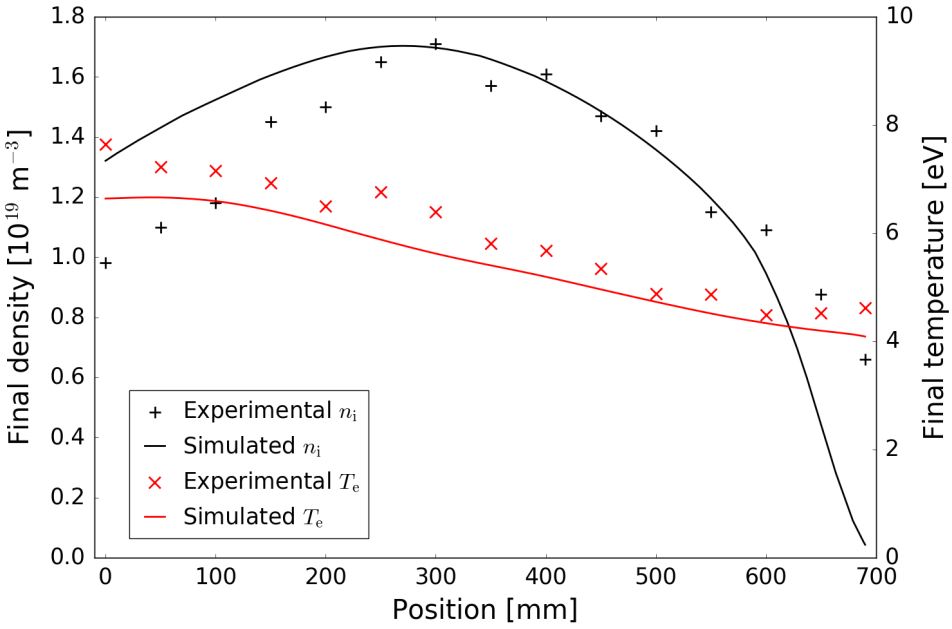

(b) Final n_i and T_e axial profiles (taken at 39.8 ms).

Figure 6.7: (a) Initial and (b) final axial profiles of experimental and simulated ion density (in black, left-hand axes) and electron temperature (in red, right-hand axes) during the 40 ms plasma pulse in MAGPIE. Experimental values are plotted as individual points; the modelled data are shown as continuous lines.

particle transport processes in plasma (e.g. the ion sound speed or ambipolar diffusion). We therefore suggest the alternative process of neutral depletion to explain the observed evolution of the plasma properties in MAGPIE [119].

Neutral depletion is caused by the coupling of plasma and neutral particle dynamics in high power discharges, or those with low neutral pressure [120]. The creation of a high density plasma necessarily reduces the amount of neutral gas, leading to regions of lower, or depleted, neutral density and limiting further ionisation. For an overview of experimental and computational neutral depletion studies, see the review by Fruchtman [120].

One such study considered neutral depletion in a helicon plasma discharge using xenon gas, in which the system was observed to reach steady state on a timescale of $\sim$ 2 s [121]. The difference between this and the 20 ms timescale seen in the hydrogen plasma in MAGPIE can be accounted for by the mass ratio of hydrogen molecules and xenon atoms, and the difference in transport rates that this causes [119]. The agreement of timescales suggests that it is the propagation of a neutral depletion channel through the plasma in MAGPIE that produces the observed time evolution of the plasma properties.

The neutral depletion hypothesis is further supported by a 2D axisymmetric simulation of the hydrogen plasma in MAGPIE, using a global model that incorporates both plasma and neutral dynamics [119]. This model is used to predict the observed plasma properties at a particular time in the pulse by choosing a neutral density profile to simulate a neutral depletion channel. Thermal expansion and diffusive transport are included, but inertial flow terms are neglected for simplicity.

Figure 6.7 shows both the experimental and simulated n_i and T_e axial profiles at times of 6 ms and 39.8 ms, as an illustration of the capabilities of the global model. The modelled values for both parameters agree relatively well with those observed experimentally, supporting the hypothesis that neutral dynamics have a significant role in determining the plasma evolution.

6.4 Photodetachment measurements

6.4.1 Results

Photodetachment data were taken at axial positions of 0, 200, 400, 500, 600, 650 and 690 mm, averaging over 32 pulses to reduce noise. The measured negative ion fraction (η) values are shown in Table 6.1. The times at which the data were recorded varied for

Table 6.1: Measurements of the negative ion fraction (η) in MAGPIE, obtained from the laser photodetachment diagnostic. Data were taken for a number of axial positions at different times during the 40 ms pulse. Values of 0 with an error of 0.005 represent positions and times where no photodetachment signal was distinguishable from the background noise. Errors that are equal to their corresponding value indicate points where an appropriate photodetachment signal appeared to be visible, but potentially could have been caused by background noise.

Time [ms]	Position [mm]						
	0	200	400	500	600	650	690
2	0 + 0.005	0 + 0.005	0.034 ± 0.012	0.04 ± 0.02	0.046 ± 0.018	0.089 ± 0.017	0.14 ± 0.06
4	0 + 0.005	0 + 0.005	-	0.04 ± 0.03	0.05 ± 0.03	0.083 ± 0.016	0.21 ± 0.09
5	0 + 0.005	0 + 0.005	0.015 ± 0.013	-	-	-	-
6	0 + 0.005	0 + 0.005	-	0.02 ± 0.02	0.07 ± 0.04	0.063 ± 0.013	0.18 ± 0.07
8	0 + 0.005	0 + 0.005	-	0.009 ± 0.009	0.030 ± 0.027	0.085 ± 0.017	0.10 ± 0.06
10	0 + 0.005	0 + 0.005	0.004 ± 0.004	0.007 ± 0.007	0.017 ± 0.017	0.046 ± 0.012	0.06 ± 0.04
12	0 + 0.005	0 + 0.005	-	0.005 ± 0.005	0.012 ± 0.012	0.0146 ± 0.008	0.026 ± 0.018
14	0 + 0.005	0 + 0.005	-	0.007 ± 0.007	0.012 ± 0.012	0.009 ± 0.009	0.019 ± 0.019
15	0 + 0.005	0 + 0.005	0.012 ± 0.012	-	-	-	-
16	0 + 0.005	0 + 0.005	-	-	0.001 ± 0.001	0.003 ± 0.003	0.011 ± 0.011
18	0 + 0.005	0 + 0.005	-	-	-	0.004 ± 0.004	-
20	0 + 0.005	0 + 0.005	0.008 ± 0.008	0.003 ± 0.003	0.009 ± 0.009	0.003 ± 0.003	0.010 ± 0.010
25	0 + 0.005	0 + 0.005	0 + 0.005	0 + 0.005	0.011 ± 0.011	0.004 ± 0.004	0.006 ± 0.006
30	0 + 0.005	0 + 0.005	0 + 0.005	0 + 0.005	0.08 ± 0.008	0.004 ± 0.004	0.007 ± 0.007
35	0 + 0.005	0 + 0.005	0 + 0.005	0 + 0.005	-	0.003 ± 0.003	-
40	0 + 0.005	0 + 0.005	0 + 0.005	0 + 0.005	0.014 ± 0.014	0.0018 ± 0.0018	0.008 ± 0.008

each position, due to limitations imposed by the minimum measurable signal and the data acquisition time. The time of recording corresponds to the time at which the laser was triggered; the measurement takes place on a scale of microseconds following the laser pulse. Data points for which no photodetachment signal was discernible are denoted by a 0 value, with an upper limit of $\eta = 0.005$ determined by the average noise level. Points which have a non-zero η but for which the error is equal to η showed an apparent photodetachment signal at the expected time, but with a low signal to noise ratio, which may have produced artefacts in the signal.

To enable comparison with the plasma density and temperature data from the Langmuir probe measurements, the η data for each position were interpolated to yield a value every millisecond from 2 to 40 ms. Both the electron and negative ion densities (n_e and n_{H^-} respectively) were calculated using (31) and (32), as set out in Section 6.2.2. The time evolution of the axial n_e and n_{H^-} profiles are plotted in Figure 6.8.

6.4.2 Discussion

The maximum observed negative ion density was $1.25 \times 10^{18}\,\mathrm{m}^{-3}$, obtained at axial positions of 400 mm (at 2 ms into the pulse) and 500 mm (at 4 ms). The error on this peak measurement is approximately $1 \times 10^{18}\,\mathrm{m}^{-3}$. The peak is transient, lasting only a few milliseconds, and travels away from the antenna. The negative ion population is effectively extinguished by 10 ms.

Comparison with the temperature plot (Figure 6.6b) shows that n_{H^-} is only significant when T_e is low, below $\sim$ 2.5 eV. This is consistent with the low temperatures required to produce negative ions from vibrationally-excited hydrogen molecules (Section 2.1.3). As the electron heating front propagates down the plasma from the antenna, the higher temperatures dissociate the negative ions and n_{H^-} decreases.

To validate the behaviour of the negative ion density evolution, the reaction rate coefficients for the formation and destruction of H^- ($\langle\sigma v\rangle_{form}$ and $\langle\sigma v\rangle_{destr}$ respectively) were modelled using the measured temperature profile. The formation reaction is:

$$e^- + H_2(v \geq 4) \longrightarrow H_2^{-*} \longrightarrow H^- + H,$$

where v indicates the vibrationally-excited molecular states included in the calculation. The contributions from lower v states are negligible [39]. The destruction equation is:

$$e^- + H^- \longrightarrow e^- + H + e^-.$$

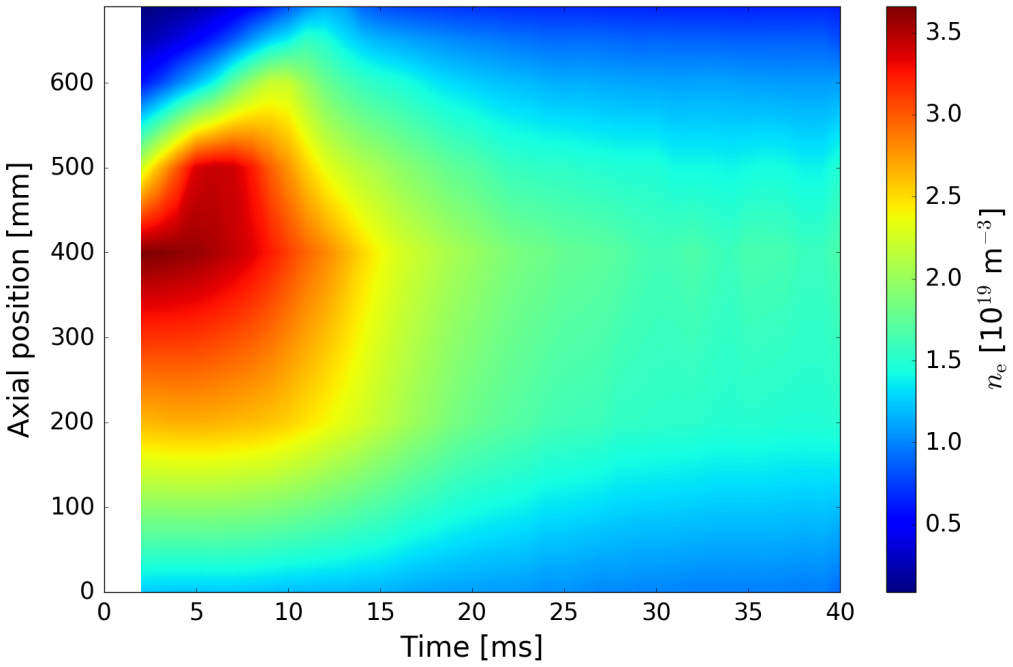

(a) Electron density evolution.

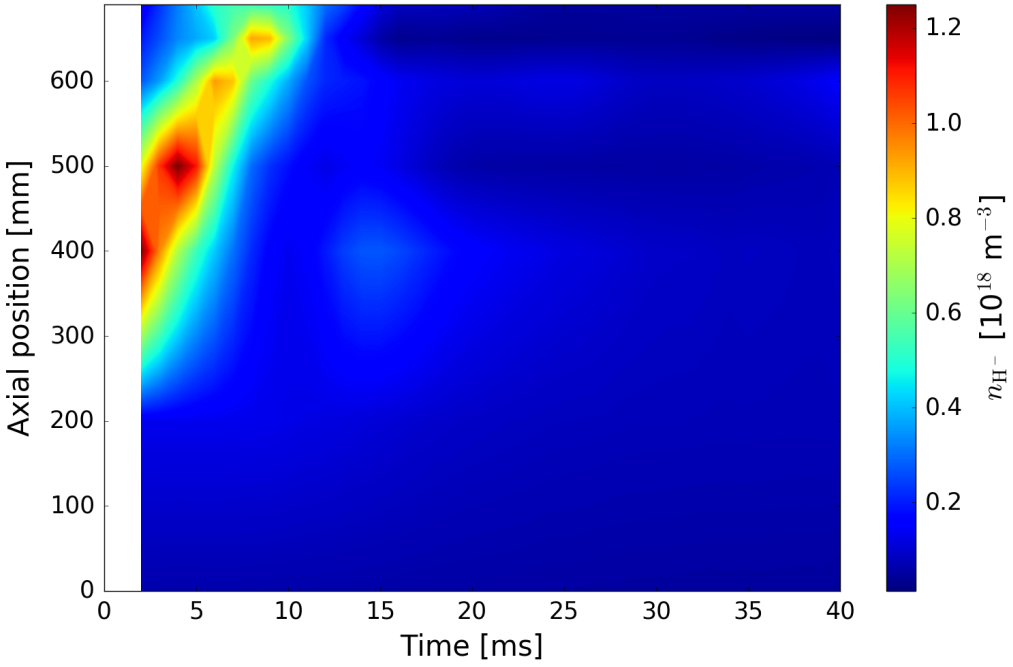

(b) Negative ion density evolution.

Figure 6.8: Time variation of axial (a) electron density and (b) negative ion density profiles throughout MAGPIE during a 40 ms pulse, measured using laser photodetachment.

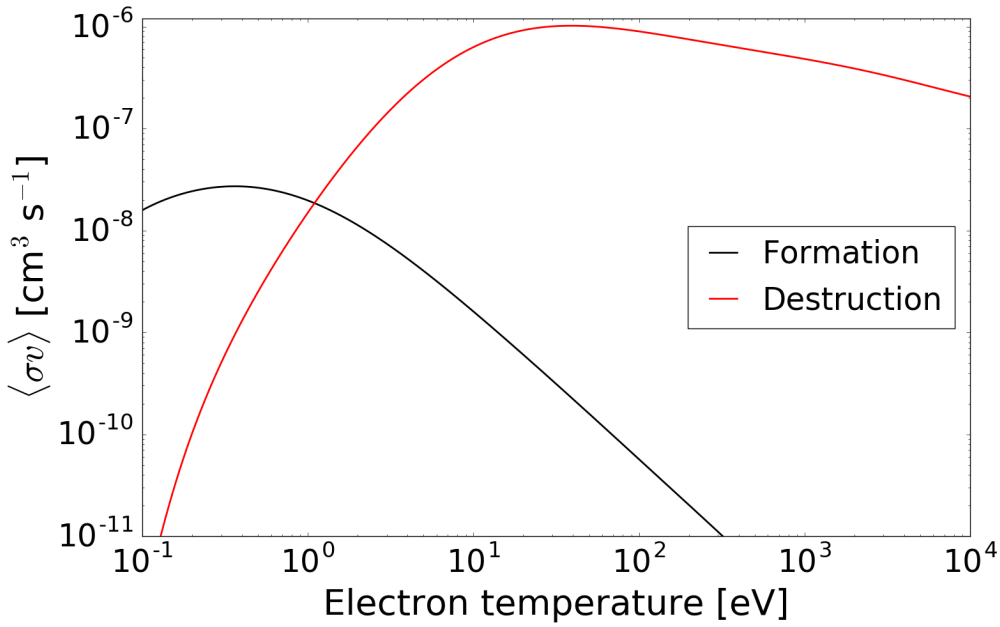

Figure 6.9: The rate coefficients, $\langle\sigma v\rangle$, for the formation and destruction of negative ions as a function of electron temperature.

The expression used to determine the rate coefficients (assuming a Maxwellian distribution of electrons) takes the form of a sum of nine terms, giving the natural logarithm of the coefficient as follows [39]:

$$\ln\langle\sigma v\rangle = \sum_{n=0}^{8} b_n (\ln T)^n,$$

where T is the electron temperature in eV. The sets of coefficients b_n used for the reactions considered here are given in Appendix D. $\langle\sigma v\rangle_{form}$ and $\langle\sigma v\rangle_{destr}$ are plotted as functions of temperature in Figure 6.9.

$\langle\sigma v\rangle_{form}$ and $\langle\sigma v\rangle_{destr}$ for the 40 ms plasma pulse in MAGPIE were calculated using the temperature measurements from the Langmuir probe. A 2D plot showing the variation of the balance between the two with axial position and time is shown in Figure 6.10. The values of $\langle\sigma v\rangle_{form}$, $\langle\sigma v\rangle_{destr}$ and n_{H^-} against time for a single axial position (500 mm, corresponding to the maximum value of n_{H^-} at 4 ms) are plotted in Figure 6.11.

The observed n_{H^-} behaviour matches the predicted rate coefficients fairly well. The 2D plot (Figure 6.10) shows that the region in which the formation reaction rate coefficient is largest coincides with the region of low electron temperature and high negative ion density. This is illustrated further by Figure 6.11, in which the initial domination of $\langle\sigma v\rangle_{form}$ is coincident with the observed increase and peak in n_{H^-}.

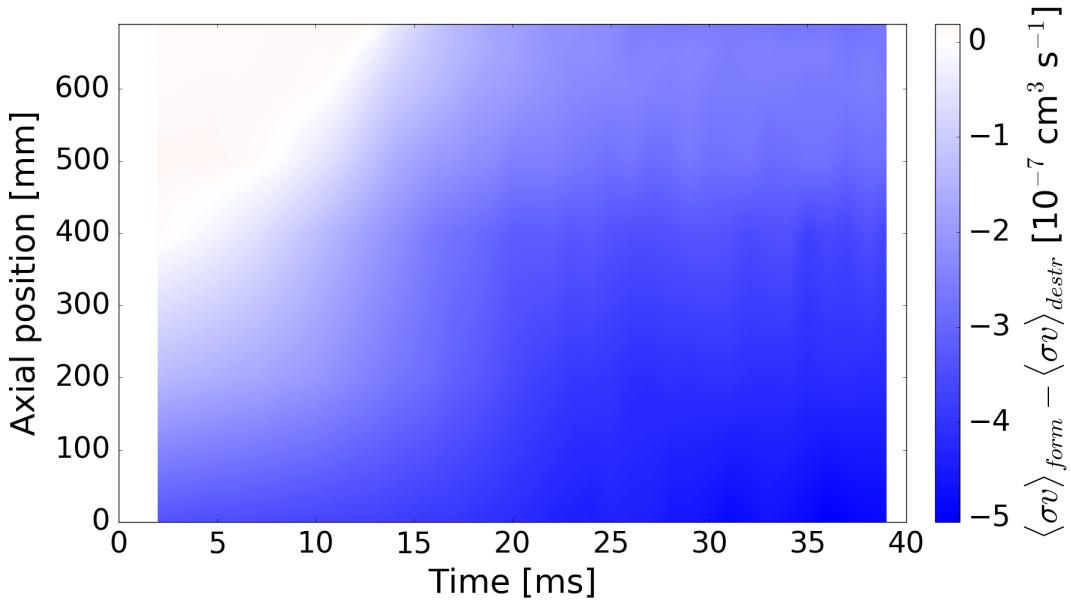

Figure 6.10: Evolution of the balance between the rate coefficients for the formation ($\langle\sigma v\rangle_{form}$) and destruction ($\langle\sigma v\rangle_{destr}$) of negative ions on axis throughout MAGPIE during a 40 ms pulse. Positive values correspond to the domination of $\langle\sigma v\rangle_{form}$.

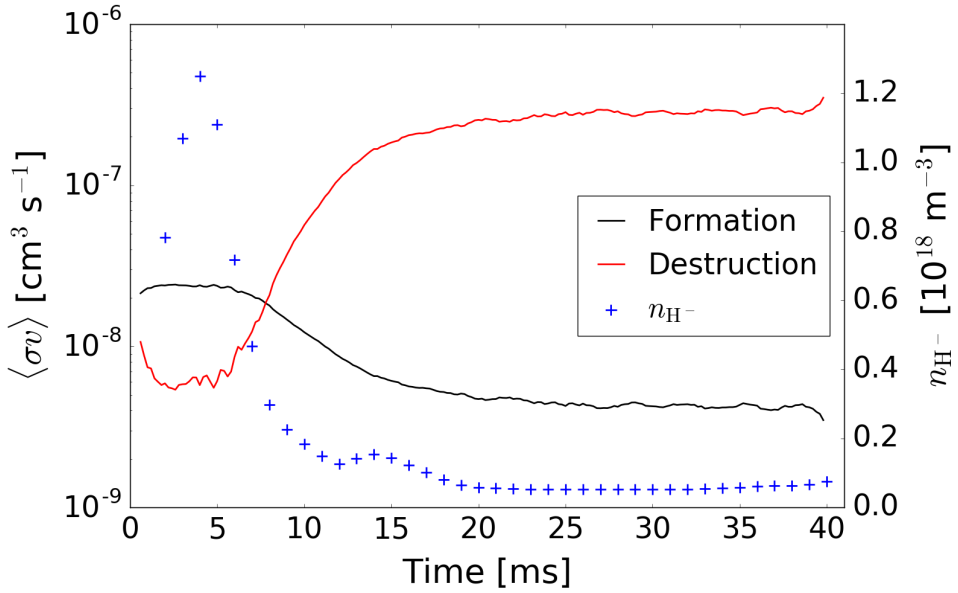

Figure 6.11: Evolution of the estimated negative ion formation and destruction rate coefficients at the 500 mm axial position throughout a 40 ms pulse (solid lines, left-hand axis). The negative ion density data (+) are plotted on the right-hand axis for comparison.

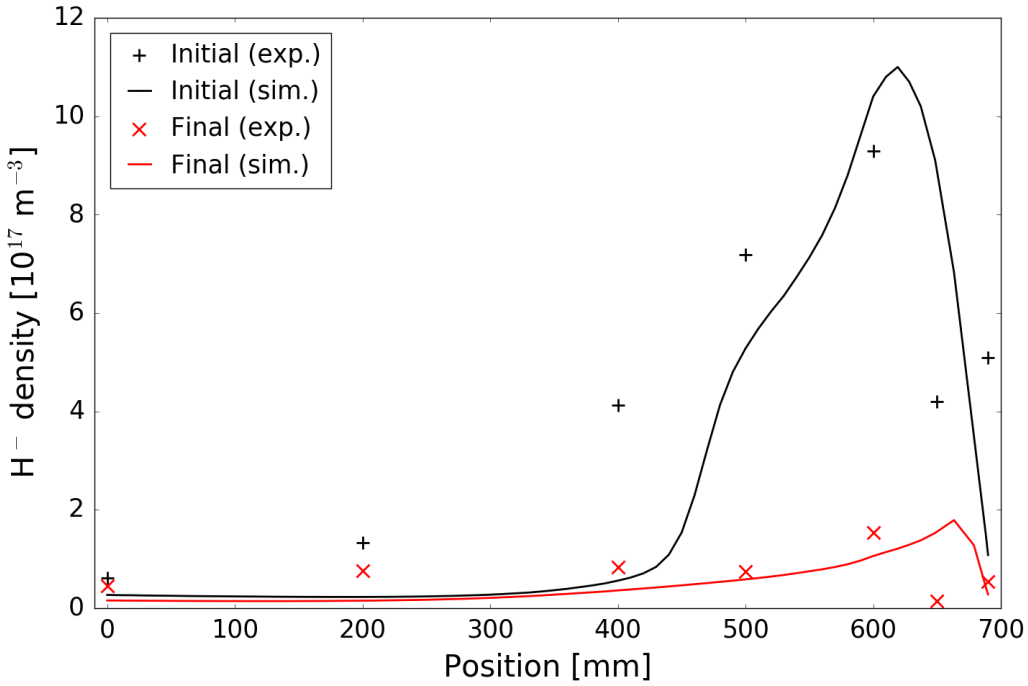

Figure 6.12: Axial experimental (scatter points) and simulated (solid lines) n_{H^-} profiles throughout MAGPIE in the initial and final stages of the 40 ms plasma pulse. Initial (6 ms) data is shown in black and final (39.8 ms) data in red.

$\langle \sigma v \rangle_{destr}$ starts to increase at approximately the same time as n_{H^-} starts to fall. $\langle \sigma v \rangle_{form}$ also begins to decrease, and n_{H^-} drops dramatically as the destructive process begins to dominate. The rate coefficients and the observed density become steady after $\sim$ 20 ms. We conclude that the qualitative behaviour of the negative ion density is consistent with that expected from consideration of the interactions of the plasma species and the temperature values measured using the Langmuir probe.

n_{H^-} profiles were also modelled using the global simulation discussed in Section 6.3.2. The initial (6 ms) and final (39.8 ms) experimental and simulated data are plotted in Figure 6.12. The agreement is relatively good: the initial peak position is approximately in the correct place, although the model underestimates n_{H^-} behind the neutral depletion front (< 450 mm). Such discrepancies are to be expected, however, as the simulation does not evolve in time, meaning that the transient nature of the neutral depletion channel and negative ion peak cannot be captured.

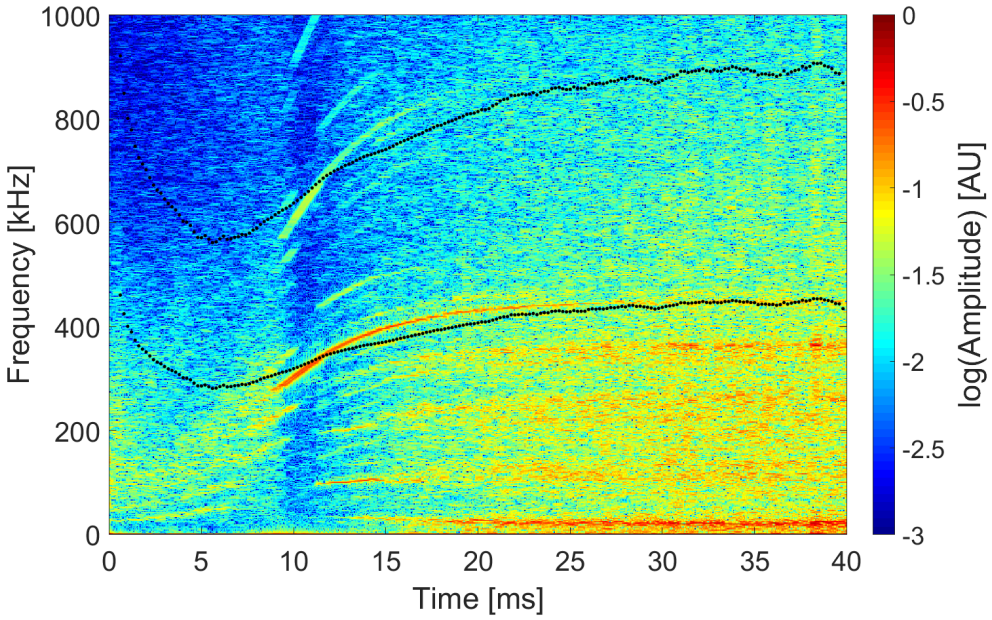

Figure 6.13: Spectrogram showing the evolution of the frequency components (up to 1000 kHz) present in the floating potential signal at an axial position of 500 mm. Overlaid in black are the fundamental and second harmonic components of the Alfvén frequency, estimated from the plasma density measurements (using a scale factor to match the peaks in the spectrogram).

6.5 V_f frequency spectra

In a similar analysis to that carried out on the YLPD, the evolution of the frequency spectrum of the plasma floating potential, V_f, was studied. The potential across the Langmuir probe was allowed to float throughout the 40 ms pulse, and the voltage across it (V_f) was recorded with a sampling rate of 40 MHz. The probe position was again chosen to be on axis at 500 mm to correspond to the observed peak in n_{H^-}.

A running fast Fourier transform analysis was applied to the data to track changes in the spectrum throughout the pulse. The width of the data window used for each spectrum was 0.5 ms, and the step between windows was 0.05 ms. Figure 6.13 shows the resulting spectrogram for the 500 mm axial position. The frequency range studied was restricted to $0 - 1000$ kHz, and hence the large RF component at 13.56 MHz is not shown.

Overlaid on this plot is the estimated behaviour of the fundamental and second harmonic modes of the Alfvén frequency, ν_A (see e.g. [122]). This is calculated from the

measured plasma density data at 500 mm according to:

$$\nu_{\mathrm{A}} = \frac{B}{\lambda\sqrt{\mu_0 m_{\mathrm{i}} n_{\mathrm{i}}}},$$

where B is taken to be the magnetic field strength from the DC field coils at 500 mm, and λ is the wavelength of the mode. λ is an unknown quantity, and its value has been chosen to match the calculated frequencies with those of the strongest peaks in the spectrum: $\lambda = 2.2$ m for the fundamental mode and 1.1 m for the second harmonic for these data. The chosen wavelengths are comparable to the 1.7 m total length of MAGPIE, and we note that, as B varies axially, the real wave structure will not replicate the ideal 'plucked string' case.

Selecting the wavelength in this way means that the predicted and observed frequencies cannot be quantitatively compared. On a qualitative basis, however, the shape of the ν_{A} evolution appears to correspond relatively well to that of the peaks seen in the spectrogram after $\sim$ 10 ms. It is therefore likely that there are Alfvénic modes present in MAGPIE throughout the remaining 30 ms of the pulse. The onset of these modes occurs at approximately the same time as the rise in the electron temperature above 2 eV and the negative ion density dropping by a factor of 10 from its peak value.

To attempt to explain the cause of the onset of these Alfvénic modes, we return to neutral depletion. If the Alfvén frequency is on a similar scale to the collision frequencies between the hydrogen ions and neutral species, these collisional interactions will damp the Alfvén waves. To investigate this, we again study the output of the 2D global model of MAGPIE (Section 6.3.2), which calculates collision frequencies between a number of species in the plasma, as well as their densities [119].

Figure 6.14a shows the predicted densities of atomic and molecular hydrogen (n_{H} and $n_{\mathrm{H_2}}$ respectively) for 6 ms and 39.8 ms into the plasma pulse. The calculated collision frequencies between hydrogen ions ($\mathrm{H^+}$) and both of these neutral species are plotted for the same times in Figure 6.14b.

Initially, the neutral depletion channel does not extend throughout MAGPIE (for the 6 ms simulation data it is set to reach 450 mm), and the atomic neutral density peaks in the mirror region at around 530 mm. The molecular hydrogen density is much lower in this region and therefore interactions with atomic hydrogen dominate. The collision frequency between H and $\mathrm{H^+}$ follows a similar distribution to that of n_{H}, with a peak height of $\sim$ 230 kHz just past 500 mm. The approximate fundamental Alfvén frequency of the plasma at 500 mm at this time is expected to be $\sim$ 280 kHz (Figure 6.13). The two

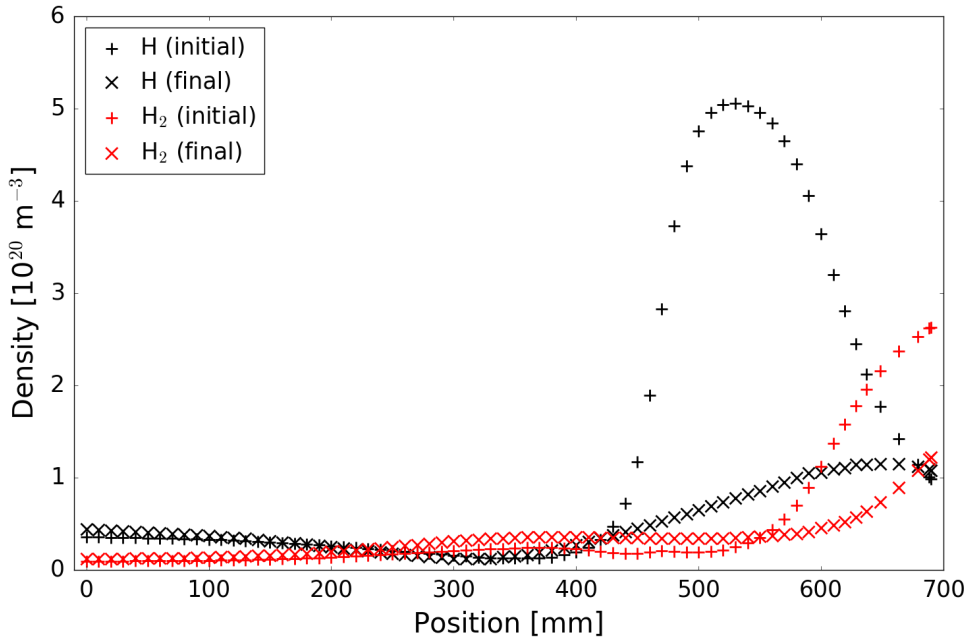

(a) Neutral atomic and molecular density profiles.

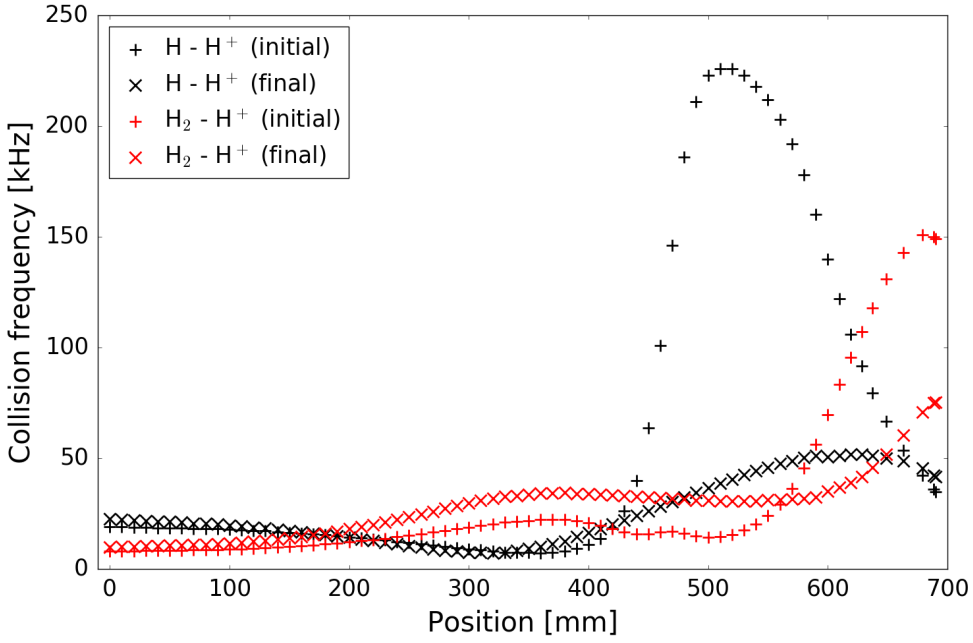

(b) Collision frequency profiles for ion-neutral interactions.

Figure 6.14: Simulated axial profiles for (a) neutral species densities and (b) H^+-neutral collision frequencies in MAGPIE towards the beginning and end of the pulse. Data for atomic hydrogen (H) are shown in black, and that for molecular hydrogen (H_2) in red. The initial values (+) simulate the profile at 6 ms into the pulse, and the final values (×) are taken at 39.8 ms.

frequencies are of the same order of magnitude, suggesting that interactions between ion and atomic neutrals could plausibly suppress the Alfvénic modes in the first ~ 15 ms.

At the end of the pulse, the neutral depletion channel has propagated to the end of the target chamber, and n_{H} has decreased sufficiently to lower the collision frequency by almost a factor of five (to around 50 kHz). The Alfvén frequency ($\sim$ 400 kHz) is dominant, meaning that Alfvénic modes are able to propagate through the plasma. The $H^+ - H_2$ collision frequency remains insignificant compared to the Alfvén frequency.

It is clear from the spectrogram that these Alfvénic modes are not the only features present. Prior to the transition at around 10 ms, there are weak modes at lower frequencies (below $\sim$ 200 kHz). More features appear after this transition, most of which show the same time evolution as the Alfvénic modes. The strongest ones appear below 400 kHz, and are regularly spaced in frequency. These may be the result of another coherent mode (potentially due to molecular ions) interacting with the Alfvén wave, creating a cascade of features. An alternative cause could be the non-uniform magnetic field profile throughout MAGPIE, but these possibilities have not yet been investigated in detail.

6.6 B-dot probe measurements

6.6.1 Evolution of the magnetic field strength

B_x and B_y data were recorded throughout the 40 ms pulse with a sampling rate of 125 MHz, at axial positions from 0 mm to 660 mm in 30 mm steps. The root mean square amplitudes of the x and y components were combined to give the average magnitude of the radial component of the magnetic field strength on axis. Figure 6.15 is a 2D colour map showing the evolution of the axial profile of this average radial field strength ($|B_r|$) throughout the pulse. The profile remains fairly constant until ~ 17 ms, at which point it undergoes significant changes. In the 50 mm closest to the antenna, and beyond ~ 150 mm, $|B_r|$ increases, but between these two regions it appears to decrease, and then slowly increase again after 30 ms. At all times, however, the field strength weakens considerably beyond the ~ 200 mm position.

Similar behaviour of the evolution of $|B_r|$ in MAGPIE has been previously observed [123]. The significant reduction of the field strength away from the antenna indicates that the helicon waves it launches are damped before travelling the length of the machine. The observation suggests that these waves are not the direct cause of the plasma heating

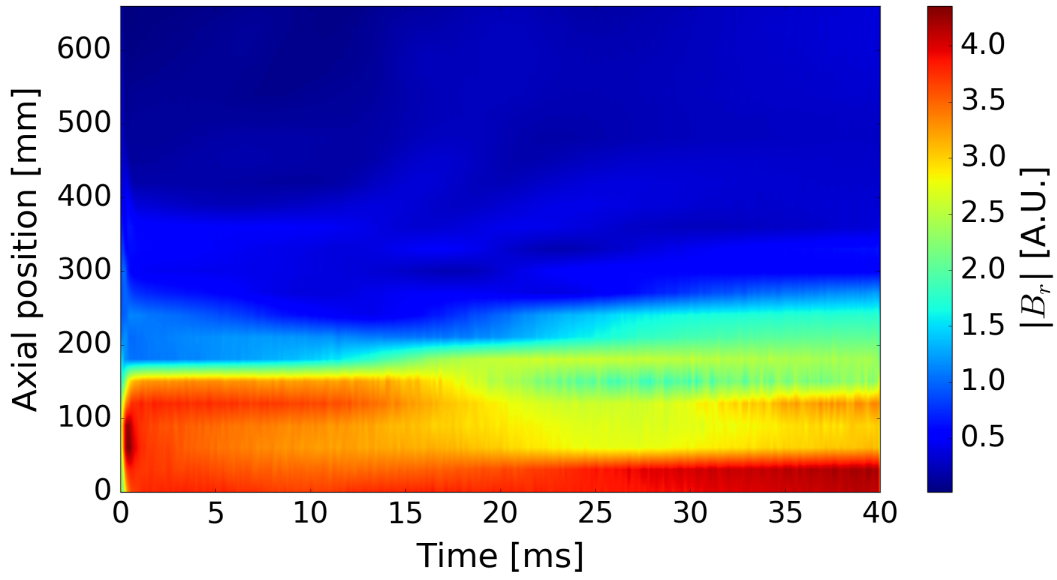

Figure 6.15: Time evolution of the root mean square amplitude of the radial component of the magnetic field strength on-axis throughout MAGPIE [110].

that is observed in the evolution of the electron temperature (Section 6.3), which does reach the full length of the target chamber. This is consistent with the hypothesis that neutral dynamics are most important in determining the plasma behaviour in MAGPIE, although it is also possible that the diffusion of hot electrons produced by the antenna causes this effect. Further study of the neutral depletion hypothesis is necessary to confirm its applicability to the plasma in MAGPIE.

6.6.2 Frequency spectra

Running fast Fourier transform analyses (as for V_f in Section 6.5) were also carried out on the raw x and y component data at a position of 510 mm. Figures 6.16a and 6.16b show the spectrograms for the B_x and B_y data respectively. Again, the frequency range is restricted to $0 - 1000$ kHz, and the large RF component at 13.56 MHz is not shown. Mode structures are visible which are similar to those in the V_f spectra. At low frequencies (< 400 kHz), the shape of the evolution of the visible peaks closely follows that of the modes in the V_f spectrogram, although the exact frequencies appear to be shifted. The peaks are also weaker relative to the background in the B data compared to the V_f data and, while the majority of the features in the B spectrograms appear after the 10 ms transition, the highest frequency mode is visible from $\sim$ 6 ms.

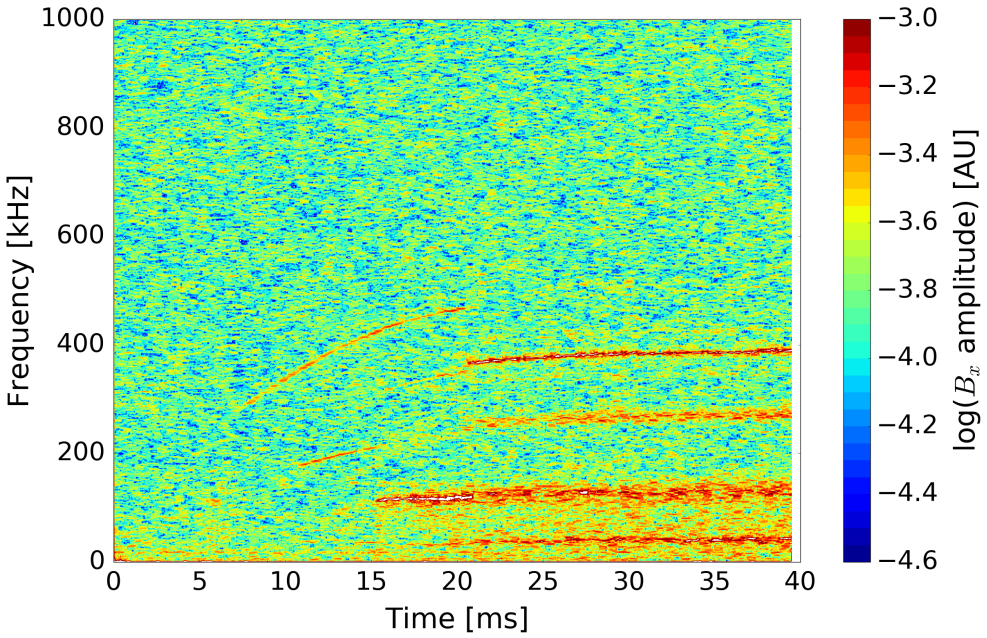

(a) B_x spectrogram.

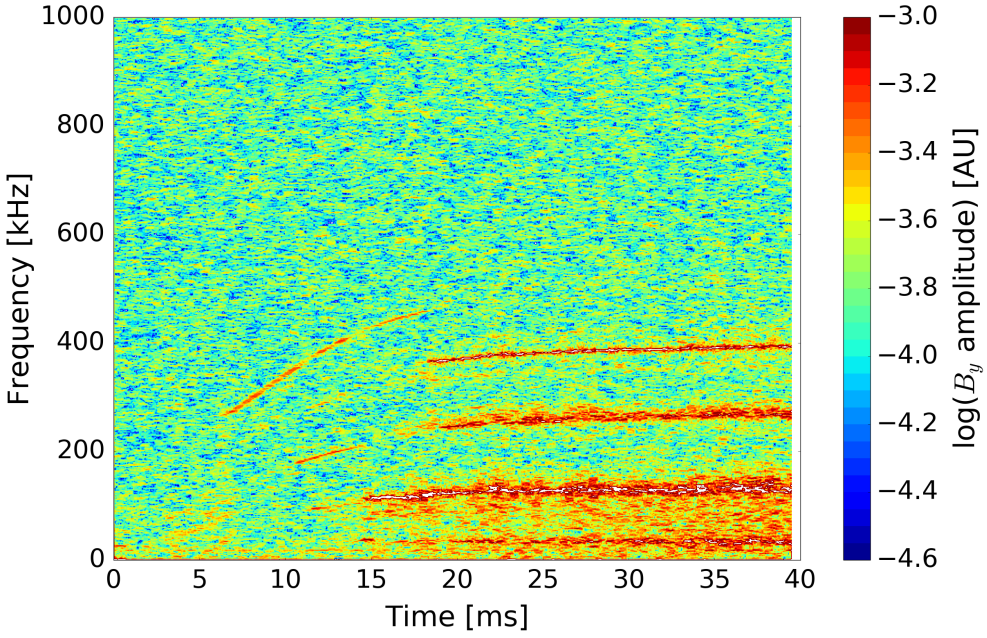

(b) B_y spectrogram.

Figure 6.16: Spectrograms showing the evolution of the frequency components (up to 1000 kHz) present in (a) the x and (b) the y components of the magnetic field from the antenna, at an axial position of 510 mm.

It is not yet clear what causes the differences between the V_f and B spectrograms. The similarity of the time evolution of the peaks suggests that the modes observed in the B data are also linked to the plasma density, and it is possible that the ion motion which propagates the Alfvén waves produces oscillations in B_x and B_y at a similar frequency. The cause of the early appearance of a coherent mode at 6 ms is less clear, but could potentially be attributed to the motion of molecular ions which is not damped by ion-neutral collisions. To study these fluctuations further, a more detailed, time-dependent simulation would be required to model the wavefields throughout MAGPIE.

6.7 Summary

The behaviour of 40 ms hydrogen plasma pulses has been observed in the helicon device MAGPIE. Peak negative ion densities of $1.25 \times 10^{18}\,\mathrm{m}^{-3}$ (error $\sim 1 \times 10^{18}\,\mathrm{m}^{-3}$) were measured in regions where the temperature dropped below 2.5 eV. This is consistent with the expected behaviour of negative ions, which are neutralised at higher temperatures.

The evolution of the plasma properties throughout the pulse occurs on a timescale of milliseconds, with a steady state axial profile reached within $\sim$20 ms. This timescale is inconsistent with those expected from consideration of e.g. the ion sound speed or diffusion, but appears to correlate well with the behaviour predicted by including neutral dynamics in the system. Scaling of previous measurements of neutral depletion timescales in xenon plasmas to account for the mass difference of hydrogen molecules is consistent with the observations made here [119,121]. We suggest that the observed plasma dynamics can be explained by the propagation of a neutral depletion channel through MAGPIE from the antenna to the target region.

Analysis of the power spectrum of the floating potential throughout the pulse revealed the possible presence of Alfvénic modes in the plasma after $\sim$ 10 ms, coinciding with the passage of the electron heating front through the plasma. These measurements are also consistent with the hypothesis that neutral dynamics and neutral depletion are dominant in the system. Simulations of the plasma in MAGPIE, including neutral dynamics, show that ion-neutral collision frequencies are initially comparable to the predicted Alfvén frequency, but are significantly lower when the Alfvénic modes are measurable. We therefore conclude that a high neutral density initially suppresses Alfvénic activity, but once the neutral depletion channel has travelled through the plasma, collisions are reduced and the ions are able to support Alfvén waves.

Measurements of the helicon magnetic wavefield strength on axis through the plasma (Figure 6.15) show that the helicon waves are strongly suppressed within 200 mm of the antenna. This further supports the hypothesis that neutral dynamics, rather than helicon wave heating, are predominantly responsible for the observed plasma evolution. The power spectra of the magnetic field components bear a strong resemblance to that of the floating potential.

The measured peak value of n_{H^-} shows promise for the use of helicon plasma sources for neutral beam injection systems, as it is an order of magnitude above the required threshold for NBI applications. However, it is clear that, with these operating parameters, the peak density is a transient feature, whereas an NBI source would require high densities to be sustained over much longer timescales in order to operate effectively. Further investigation of the properties of the plasma pulse, particularly the effects of the neutrals in the system, is needed to better understand the plasma behaviour and increase the duration of the peak negative ion density. An extension of the study to deuterium plasmas is also required in order to fully understand the implications for tokamak NBI applications [107].

Chapter 7

Conclusions and future work

The issues surrounding the input and removal of power in a tokamak are significant obstacles to the success of fusion as the clean commercial energy source of the future. This thesis focuses on studies relevant to power injection and handling using two different linear plasma devices: the York Linear Plasma Device (YLPD) and the Magnetised Plasma Interaction Experiment (MAGPIE).

How to handle the large levels of exhaust power from a fusion plasma in a tokamak is a key focus of research around the world. It is predicted that the power fluxes in ITER and future large tokamaks will be well in excess of the $10\,\mathrm{MW\,m^{-2}}$ limit imposed by the material properties of the divertor plates, and the development of methods to reduce the amount of power delivered to the divertor is therefore crucial.

Plasma detachment from the divertor plates is one such method, requiring recombination of the plasma to be induced in the vicinity of the divertor target plates. Recombination not only removes charged particles before they can impact (and damage) the plates, but also results in the emission of photons from the excited neutral particles that are produced. These photons carry energy in all directions, dissipating some of the power and hence reducing the flux to the divertor.

Detachment will be employed on ITER, and experimental tokamak research is ongoing to attempt to describe and control the process more fully. Linear plasma devices can also contribute to our understanding in this field, as they can be used to replicate divertor plasma conditions and study the processes fundamental to detachment. The linear geometry removes the complexity of the tokamak's toroidal shape, and improves the level of diagnostic access. These advantages are conducive to running steady state or high repetition rate experiments to study the basic plasma physics governing detachment.

In the case of power injection, smaller plasma sources are vital for producing the ion beams that are accelerated and neutralised for tokamak neutral beam injection (NBI) heating systems. Current NBI sources use caesium catalysts to increase the negative ion production rate of inductively coupled plasma sources. A highly reactive element, caesium introduces further safety and cost considerations, and an ideal negative ion source would be able to function without it. It is possible that helicon plasma devices could be developed to achieve a sufficiently high negative ion production rate without the need for a catalyst.

The preceding chapters presented work in both these areas. Detachment in a linear hydrogen plasma was studied in the YLPD, with a particular focus on fast, kHz timescales, and the behaviour of the negative hydrogen ion population in the helicon device MAGPIE was studied. This research has provided insight into the key phenomena in both cases, and highlighted areas in which further work is required.

We first address the study of the electron-ion recombination (EIR) regime of detachment in the steady-state, hydrogen plasma column in the YLPD, which aimed to develop understanding of the detachment process. The current level of understanding of detachment in tokamaks is restricted in particular by the lack of knowledge of anomalous transport across magnetic field lines (see e.g. [51, 124, 125]), which in turn limits the effectiveness with which detachment can be implemented. A more comprehensive understanding of cross-field transport would increase the predictive capabilities of divertor plasma models, and lead to enhanced optimisation of future fusion reactors.

In linear devices, several studies have concluded that radial transport plays a role in achieving detachment, for example in PISCES-A [68] and NAGDIS-II [71, 75]. However, the mechanisms of the process are not well understood. We have reviewed previous work in the YLPD which studied both the EIR and MAR (molecular-activated recombination) detachment regimes by injecting neutral hydrogen gas into the target chamber [85]. This previous study only considered the behaviour along the axis of the plasma column, concluding from fast Langmuir probe measurements (of the MAR regime only) that radial broadening and fast timescale events in the EIR detached plasma were unimportant.

During tests confirming that the EIR detached plasma previously studied in the YLPD could be sufficiently well replicated under altered operation conditions, visual inspection of the plasma column implied that the detached plasma column was in fact broader than in the attached state. Time-averaged hydrogen Balmer emission profiles (measured by Lisgo [88]) were presented which confirmed this. The radial profiles are hollow, with

peaks situated at ±6 mm and extending out beyond ±10 mm, compared to the attached plasma column which has a radius of less than 3 mm.

To investigate the cause of the spatial distribution of the emission, a simple calculation of the three-body recombination rate across the plasma column was carried out. This showed that combining a broadened density profile with a narrower, cooler temperature profile (chosen to match experimental data taken at the 0 and 3 mm radial positions) yielded a similar hollow emission profile to that measured experimentally. However, the overall width of the profile was smaller by a factor of ~ 2, suggesting that simply cooling and broadening the time-averaged density profile is insufficient to describe the processes occurring in the detached YLPD plasma.

This discrepancy led to the suggestion that radial transport takes place in the plasma column on timescales faster than the 1 ms resolution of the Langmuir probe diagnostic, providing an additional mechanism for the observed broadening. The remainder of the experimental investigation therefore focused on two diagnostic techniques with higher temporal resolution: fast frame imaging (FFI), with an operating frequency of 50 kHz; and 1 MHz floating potential fluctuation ($\widetilde{V}_f$) measurements using two Langmuir probes.

The FFI data showed bright filamentary structures, radially narrow ($5-8$ mm width) and azimuthally extended (up to 180°), appearing intermittently at radii larger than 6 mm. This broadening of the plasma column beyond ±6 mm is even greater than the time-averaged emission profiles showed. The filaments appear to be coherent, and out of phase with the activity on the opposite side of the column, but these analyses are difficult to interpret. They are potentially affected by the limited resolution of the pixel intensity, as well as by the foreground and background plasmas.

The radial and azimuthal extent of the filaments in the images is likely to partially result from the relatively long 20 µs exposure time of the camera, which limited the ability to track the motion of individual filaments. The actual filament sizes may therefore be much smaller than is indicated by the FFI data, a conclusion supported by the radial velocities predicted by the $\widetilde{V}_f$ time-delay correlation measurements. The long exposure time also meant that the creation and destruction of the filaments was unable to be studied.

Recording $\widetilde{V}_f$ with 1 µs resolution gave more insight into the behaviour of the EIR detached plasma. These measurements again show that the plasma column broadens by a factor of at least two when detached compared to the attached state. The large reference probe at the 6 mm position limits the radial range of these data, as it perturbs

the column beyond this radius. Nonetheless, time-delay correlation analysis between large amplitude negative events recorded by the reference probe and the $\widetilde{V}_f$ signals recorded by the moveable probe implies that some radial transport of events occurs in the plasma. The strongest evidence indicates a velocity directed out of the column, but there is also a suggestion of inward motion.

The estimated outward velocity of the plasma filaments is $(650 \pm 250)\,\mathrm{m\,s^{-1}}$, which suggests that a filament would travel a radial distance of at least 8 mm in the 20 µs FFI exposure time. This is at the upper end of the observed filament width in the FFI data, implying that the actual width of the structures may be on the order of 1 mm or less. This is consistent with the 3 mm upper limit on the width determined from the duration of the events in the V_f data, and these results appear to support the theory that radial transport is responsible for the broadening of the plasma beyond that predicted by the three-body recombination model.

Finally, a hypothesis was presented in which the centrifugal instability provides the mechanism for the observed radial transport. This mechanism arises due to the rotation of the plasma column caused by the $\mathbf{E} \times \mathbf{B}$ drift. The rotating plasma feels an effective centrifugal force, which leads to a second azimuthal drift. This second drift is dependent on both mass and charge, and the ions and electrons therefore have different velocities. A charge separation then arises across any element (or 'blob') of plasma that is displaced in the column, resulting in an azimuthal electric field and an associated $\mathbf{E} \times \mathbf{B}$ drift, this time directed radially outwards.

This mechanism could plausibly result in the intermittent ejection of 'blobs' of plasma from the column, producing the filamentary structures that have been observed. It also provides an explanation for the inward-directed motion suggested by the $\widetilde{V}_f$ correlation analysis: ejection of the blob leaves a region of depleted density, which experiences a charge separation in the opposite direction, and a resulting inward $\mathbf{E} \times \mathbf{B}$ drift.

As well as being consistent with the propagation observed in the $\widetilde{V}_f$ data, the centrifugal instability hypothesis is also supported by the maximum ratio of the $\widetilde{V}_f$ amplitude to the measured temperature in the column, which lies in the range $1.3 - 2$ at the 3 mm position. According to one of several criteria listed by Brochard et al., the presence of the centrifugal instability is suggested by values ≥ 1 [99]. However, the current data set is limited, and there are more observations that can be made to confirm whether this instability is indeed present. The data presented here have provided sufficient information to suggest a possible

explanation for the behaviour of the EIR detached plasma in the YLPD, but a more focused study is required to continue this work.

Firstly, the remaining criteria listed by Brochard et al. for instability identification can be tested to provide a more thorough assessment of the detached plasma behaviour. This will require accurate measurements of the time averaged values of density and temperature across the column, as well as fast timescale measurements of their fluctuations. To achieve this, improvements to the Langmuir probe system on the YLPD should be made to increase the spatial and temporal resolution of the diagnostic, and decrease the disturbance to the plasma column. Improving the resolution and azimuthal range of the probes will also increase the accuracy of the time-delay correlation measurements, which will allow the two-dimensional motion of the filaments to be tracked with greater precision.

The behaviour of the emission from the filaments can also be observed in more detail to increase understanding of the links between the radial transport and the three-body recombination processes that occur in the detached state. Clearly the time resolution of the FFI diagnostic must be improved, which may require a more sensitive detection system to compensate for the lower light levels. Filtering the emission to separate the high-n Balmer lines produced through three-body recombination from the H_α photons emitted from the main, ionisation-dominated plasma beam may also be of use in analysing the images with greater accuracy.

These detailed observations should not only provide stronger evidence for verification of the radial transport mechanism in the EIR detached plasma, but can also feed into the formation of a comprehensive model of the processes that take place to produce and sustain detachment in the YLPD. Ideally, such a model will describe the formation and motion of filaments, how they cool as they travel (enabling recombination to occur), and how they drain away as the plasma density is depleted. An iterative process of simulating synthetic diagnostic results and comparing them to the experimental data can be used to refine the behaviour of the model. This is particularly important for FFI, which is only able to observe the filaments when they have become cool enough to recombine and emit high-n Balmer emission.

Additional experimental information which would inform the detachment model includes measurements of the axial speed of the plasma column and the local neutral hydrogen density. A retarding-field energy analyser has previously been used to measure the axial ion speed in the YLPD (see Rusbridge et al. [77]), and could be employed to study

how the interaction with neutral hydrogen in the target chamber affects the speed along the plasma column. This would be important in understanding how the axial motion of the plasma contributes to the draining of the plasma filaments. Measuring the neutral density (for example with two-photon absorption laser-induced fluorescence [126]) would increase the accuracy with which plasma-neutral interactions, and hence the cooling of the plasma, can be modelled.

A full model of EIR detachment, including three dimensional motion of the plasma and the interactions between plasma particles and with neutrals, is an ambitious goal, but working towards this will result in a deeper understanding of how instabilities and transport in the plasma lead to its detachment. The results thus far appear to suggest that, rather than a single mechanism dominating the behaviour, there is an interplay between transport and particle interactions in which the radial transport of plasma filaments allows them to interact with neutral gas and cool sufficiently to undergo recombination.

The BOUT++ modelling framework (developed by Dudson et al. [127]) has previously been used to simulate the transport of plasma filaments in the tokamak SOL (for example in JET [128–130]). It has also been employed in studies of turbulence in linear devices (see e.g. [131, 132]), which have recently been developed to include a number of basic atomic physics processes, including ionisation, three-body recombination and charge exchange [3]. These simulations could provide a starting point for the development of a comprehensive model of EIR detachment in the YLPD.

Results from the suggested experimental and modelling work could have significant implications for our understanding of detachment in tokamaks. The presence of blobs in tokamaks has been well documented (see e.g. [133] and references therein), but there is limited knowledge of the relationship between blob transport and detachment. Some observations have been made in AUG which focus on characterising fluctuations in density and radiation, but the physics linking these processes is not fully understood [56, 57].

The mechanism proposed as an explanation for radial transport in the YLPD is not directly applicable to tokamaks, as the centrifugal instability arises only in linear devices due to the rotation of plasma column. However, mass- and charge-dependent drifts occur in tokamaks due to both the curvature and gradient of the magnetic field, and these can result in similar instabilities which may drive cross-field plasma blob transport [133, 134]. If a model can be developed to predict the recombination and detachment resulting from blob transport in a linear device, elements of the theory may be transferrable to tokamaks

to predict similar behaviour in the scrape-off layer and divertor plasma. This would lead to a much greater understanding of the detached divertor regime, and hence would be key to optimising the operation of fusion reactors.

We now return to the study of the negative hydrogen ion population in the helicon plasma device MAGPIE, which aimed to investigate the plausibility of using helicon plasma devices as caesium-free negative ion sources for neutral beam injection (NBI) systems in tokamaks (a possibility suggested by e.g. Franzen and Fantz [15]). There are several requirements which such a source must meet.

Firstly, it must be able to operate continuously in order to provide heating for steady-state tokamak operation. It must be capable of producing a sufficiently high negative ion current density (represented here by a guideline density threshold of $1 \times 10^{17}\,\mathrm{m}^{-3}$), and the negative ions must be efficiently extracted from the source. Finally, it should be capable of operating with deuterium (the relevant isotope for fusion reactors). MAGPIE is inherently a pulsed plasma source, as its operation time is limited by heating of the chamber and the magnetic field coils. The evolution of the plasma parameters was therefore studied throughout a 40 ms pulse, with a particular focus on the negative hydrogen ion density (n_{H^-}), as a first step towards determining the feasibility of such a system.

A variety of diagnostics were employed. An axial Langmuir probe was used to track the evolution of the plasma density and temperature with 0.2 ms resolution throughout the pulse. The same probe was also used to record the time series of the floating potential (V_f) with a sampling rate of 40 MHz in order to consider the power spectrum of fluctuations in the plasma at the 500 mm axial position. The addition of a 1064 nm laser enabled the use of the laser photodetachment technique to measure the axial n_{H^-} profile, and a B-dot probe was used to consider the amplitude and power spectrum of the oscillating magnetic field produced in the plasma by the helicon antenna.

The primary result is the measurement of a peak n_{H^-} value of $1.25 \times 10^{18}\,\mathrm{m}^{-3}$ (with an error of $\sim 1 \times 10^{18}\,\mathrm{m}^{-3}$). This is an order of magnitude higher than the required threshold density, and is a promising initial indication that helicon devices are capable of producing sufficient negative ions to operate an NBI system. However, the time evolution of the n_{H^-} profile throughout the 40 ms pulse shows that this peak is a transient feature. The peak is visible at the 400 and 500 mm axial positions (approximately coinciding with the maximum in the applied DC magnetic field profile) within the first 5 ms of the pulse, but decays to negligibly small values within a further 10 ms.

Inspection of the temperature profile evolution shows that the region in which negative ions are present coincides with the coldest region of the plasma, and the n_{H^-} decay occurs as this region heats up beyond 2 eV. To confirm the link between the plasma temperature and n_{H^-}, the negative ion formation and destruction rates were modelled using the measured temperature values, which yielded results that were consistent with the experimental data. The heating of the plasma destroys the vibrationally excited hydrogen molecules that are required to produce the negative ions, and neutralises those negative ions that are already present. The reduction of n_{H^-} and the heating of the coldest region of plasma therefore occur on the same timescale.

The ion density profile exhibits a general increase over the first 10 ms, with a peak at around $400 - 500$ mm, before decaying again to reach a lower magnitude, steady state distribution by 20 ms. The evolution of the frequency spectrum of the 500 mm V_f data shows a similar behaviour: coherent modes appear at approximately 10 ms, which increase in frequency before stabilising at around 20 ms. The time dependence of the mode frequencies correlates reasonably well on a qualitative basis with that predicted by calculating the Alfvén wave frequency from the density measurements through time (with the mode wavelength chosen to match the observed frequency values).

Based on the axial observations made, we suggest that neutral dynamics in the helicon plasma could be responsible for the observed behaviour, and propose neutral depletion as the driving mechanism. Neutral depletion introduces an upper density limit in high-power systems, where the large input power is able to ionise a significant fraction of the available neutrals. This depletes the reservoir of neutral 'fuel' which can create more plasma, imposing a limit on the maximum plasma density which can be obtained [120]. In MAGPIE, we propose that a neutral depletion front propagates upstream of the antenna towards the neutral gas source within the first $10 - 15$ ms, with formation and heating of plasma occurring in front of it as it travels.

Initial tests of this hypothesis were carried out using a global model to simulate the plasma parameters in the initial and final stages of the pulse. The neutral density profiles for this model were chosen to replicate neutral depletion, and the simulated results reproduce the measured density and temperature profiles reasonably well.

The results of this model are also consistent with the features observed in the evolution of the V_f power spectrum. The suppression of Alfvénic mode frequencies at 500 mm prior to 10 ms is suggested by the high plasma-neutral collision frequencies predicted by the

global model for the initial plasma state, due to the high neutral density at this position. These simulated collision frequencies have a similar magnitude to the Alfvén frequency, and could act to suppress Alfvénic oscillations in the plasma. Conversely, the predicted collision frequencies are significantly reduced in the final modelled state, and so Alfvén waves would be able to propagate as observed.

The B-dot measurements of the evolution of the magnetic wavefield produced by the helicon antenna also seem to suggest that the helicon waves are not the direct cause of plasma heating upstream of the antenna. Suppression of the helicon waves in the upstream plasma has been previously observed in MAGPIE (see [123]), and is consistent with the theory that the dominant mechanism controlling the plasma formation and heating is the neutral dynamics. The power spectra from these B-dot measurements are harder to interpret. The visible modes exhibit a similar time evolution to the Alfvénic modes in the V_f data (possibly indicating that they too are linked to the plasma density), but they occur at different frequencies, and the onset of some modes is as early as 6 ms.

These experiments to investigate the behaviour of the negative ion population in the helicon source MAGPIE have yielded promising results regarding the potential use of helicon devices as negative ion sources for tokamak NBI systems, and have led to the proposal of neutral depletion as a possible mechanism governing the evolution of the plasma. In a similar manner to the YLPD detachment study, this work has laid some important foundations on which future studies can build to further develop our understanding of the processes involved. We know that high negative ion densities are achievable, but the mechanism must be understood more fully in order to develop the technology into the steady state source of negative deuterium ions that is needed for NBI for fusion reactors.

One clear development requirement is for the transient n_{H^-} peak to be sustained throughout the plasma pulse in order to provide a continual source of negative ions. To achieve this, a more thorough understanding of the mechanism behind the creation of the negative ions is needed, which can be obtained through developing the experimental methods and the global model in tandem via an iterative feedback process.

Extending the measurements of the plasma parameters to consider their radial profiles is key, not only to improve our understanding of the plasma behaviour, but also because n_{H^-} may increase off-axis (cf. [135]). A negative ion population spread over a wide cross-sectional area will also eventually assist in their extraction. Other measurements that would be of use in improving the accuracy of the global model are the ion speed (for

example using a Mach probe, cf. [73]) and neutral density (using e.g. the two-photon absorption laser-induced fluorescence technique [126]). These additional measurements can be used to verify the simulation results, and feed back into improving the model input.

Finally, once the helicon plasma evolution can be reasonably well described, it will be necessary to test the behaviour of the source when operating in deuterium. The larger mass of this isotope may cause differences in the mechanisms governing the plasma, and it will be extremely important to understand these. An efficient extraction system will also be required in order to complete the development of a source that can be used for NBI.

Overall, the two exploratory studies described in this thesis have illustrated the capabilities of linear plasma devices in aiding the understanding of basic plasma physics processes relevant to key issues impeding the commercial success of fusion power. Detachment is extremely important for the handling of the exhaust power from a fusion plasma in the divertor region of a tokamak, and the development of a caesium-free negative ion source would be highly beneficial to the operation and maintenance of the neutral beam injection systems used for heating and fuelling tokamaks. This work has taken some important steps towards elucidating the mechanisms responsible for both detachment via electron-ion recombination processes, and high density negative hydrogen ion production in a helicon plasma source.

Appendix A

Sheath physics

Here we provide the details of the one dimensional fluid analysis used to determine the conditions in the sheath region that forms around a surface in a plasma [23]. When an object is inserted into a plasma, it charges up negatively: the electron flux in a quasineutral, thermal plasma is always greater than the ion flux (because the electron mass is much smaller, giving them a greater velocity), so the electrons reach the surface first. This sets up a negative potential around the surface, which accelerates ions and decelerates electrons to balance out the fluxes. In this analysis, we take the potential, V, relative to the plasma potential, V_p (i.e. $V_p = 0$).

In order to describe the plasma behaviour in the sheath, we begin by assuming cold ions, with temperature $T_\mathrm{i} = 0$. We can analyse the potential in the sheath region by considering the imbalance between the electron and ion densities that arises there:

$$\frac{\mathrm{d}^2 V}{\mathrm{d}x^2} = -\frac{e}{\epsilon_0}(n_\mathrm{i} - n_\mathrm{e}). \tag{A.1}$$

The ion density, n_i, can be expressed using the conservation of energy (A.2) and ion flux (A.3) throughout the sheath region (subscript *se* denotes the sheath edge):

$$\frac{1}{2} m_\mathrm{i} {v_\mathrm{i}}^2 = -eV \implies \frac{1}{2} m_\mathrm{i} {v_{se}}^2 = -eV_{se}; \tag{A.2}$$

$$n_\mathrm{i} v_\mathrm{i} = const. = n_{se} v_{se}. \tag{A.3}$$

Substituting v_{se} yields:

$$n_\mathrm{i} = n_{se} \left(\frac{V_{se}}{V} \right)^{\frac{1}{2}}. \tag{A.4}$$

For the electrons, we use a Boltzmann distribution, so that:

$$n_\mathrm{e} = n_{se} \exp\left[\frac{e(V - V_{se})}{kT_\mathrm{e}} \right]. \tag{A.5}$$

If we substitute (A.4) and (A.5) into (A.1), the Poisson equation becomes:

$$\frac{\mathrm{d}^2V}{\mathrm{d}x^2} = -\frac{e}{\epsilon_0}n_{se}\left[\left(\frac{V_{se}}{V}\right)^{\frac{1}{2}} - \exp\left(\frac{e(V-V_{se})}{kT_\mathrm{e}}\right)\right]. \tag{A.6}$$

We proceed by considering a position just inside the sheath, where the potential satisfies $V = V_{se} - \Delta$ such that Δ is small and positive. First order Taylor expansions can then be applied to both terms within the square brackets in (A.6), yielding (after some manipulation):

$$\frac{\mathrm{d}^2\Delta}{\mathrm{d}x^2} = \frac{e\Delta}{\epsilon_0}n_{se}\left[\frac{e}{kT_\mathrm{e}} - \frac{1}{2|V_{se}|}\right]. \tag{A.7}$$

As V_{se} is negative, we have written the equation in terms of its absolute value for clarity.

(A.7) has two solutions. When the right hand side is negative, the solution is oscillatory: this is unphysical and is not observed experimentally. A sheath does not form, therefore, for $V_{se} > -{}^{kT_\mathrm{e}}/_{2e}$, and the sheath analysis is invalid close to the plasma potential. The positive solution is exponential, and arises when:

$$\frac{e}{kT_\mathrm{e}} \geq \frac{1}{2|V_{se}|}.$$

Removing the absolute value, and substituting for V_{se} using (A.2), gives us the following criterion for the velocity at the sheath edge:

$$v_{se} \geq \sqrt{\frac{kT_\mathrm{e}}{m_\mathrm{i}}} = c_s. \tag{A.8}$$

This is the Bohm criterion: the velocity at the sheath edge must be greater than or equal to the ion sound speed in the plasma, c_s. A similar analysis for non-zero T_i yields the same result with the full expression for the sound speed, in which T_e is replaced by $(T_\mathrm{e} + T_\mathrm{i})$.

To further constrain v_{se}, we consider the fluid equations for conservation of particles (A.9) and momentum (A.10):

$$\frac{\mathrm{d}\Gamma}{\mathrm{d}x} = \frac{\mathrm{d}(nv)}{\mathrm{d}x} = S_p; \tag{A.9}$$

$$nF = nqE - \frac{\mathrm{d}p}{\mathrm{d}x} - nF_{drag}. \tag{A.10}$$

These equations apply to both the ion and electron species. Γ is the particle flux (the product of density, n, and velocity, v); S_p describes the particle source (from ionisation of stationary neutrals); q is the charge of the species; E is the electric field; and p the pressure. F on the left hand side is given by the classical 'mass times acceleration' formula. F_{drag} describes the frictional force on the fluid, which we assume to arise from the acceleration of newly-formed ions up to the fluid velocity. We can therefore rewrite (A.10) as:

$$nmv\frac{\mathrm{d}v}{\mathrm{d}x} = neE - \frac{\mathrm{d}p}{\mathrm{d}x} - mvS_p. \tag{A.11}$$

We first apply conservation of momentum to the electron fluid. Assuming an isothermal plasma, and that $p = nkT$, we can substitute (A.9) for the source term in (A.11), which becomes:

$$nm_{\mathrm{e}}v\frac{\mathrm{d}v}{\mathrm{d}x} = -neE - kT\frac{\mathrm{d}n}{\mathrm{d}x} - m_{\mathrm{e}}v\frac{\mathrm{d}(nv)}{\mathrm{d}x}. \tag{A.12}$$

We then approximate the spatial derivatives using a characteristic length scale of the system, L. This gives:

$$\frac{nm_{\mathrm{e}}v^2}{L} = -neE - \frac{nkT}{L} - \frac{nm_{\mathrm{e}}v^2}{L}. \tag{A.13}$$

As we saw in (A.8), the speed of particles in the sheath is characterised by the isothermal ion sound speed:

$$c_s = \sqrt{\frac{k(T_{\mathrm{e}} + T_{\mathrm{i}})}{m_{\mathrm{i}}}}. \tag{A.14}$$

If we substitute this expression for v in (A.13) in the isothermal approximation ($T_{\mathrm{e}} = T_{\mathrm{i}} = T$), and rearrange, we obtain:

$$\frac{4nkT}{L}\frac{m_{\mathrm{e}}}{m_{\mathrm{i}}} = -neE - \frac{nkT}{L}. \tag{A.15}$$

Since $m_{\mathrm{e}} \ll m_{\mathrm{i}}$, the left hand side is negligible, and we can conclude that the electron force balance is between the electric field and pressure gradient terms (first and second terms on the right hand side respectively). We therefore write:

$$neE = -kT\frac{\mathrm{d}n}{\mathrm{d}x} = -\frac{\mathrm{d}p}{\mathrm{d}x}. \tag{A.16}$$

We now turn to the ions. Conservation of momentum becomes:

$$nm_{\mathrm{i}}v\frac{\mathrm{d}v}{\mathrm{d}x} = neE - kT\frac{\mathrm{d}n}{\mathrm{d}x} - m_{\mathrm{i}}vS_p. \tag{A.17}$$

If we substitute (A.16) from the electron analysis, and then use the ion sound speed, (A.14), we find:

$$\begin{aligned} nm_{\mathrm{i}}v\frac{\mathrm{d}v}{\mathrm{d}x} &= -2kT\frac{\mathrm{d}n}{\mathrm{d}x} - m_{\mathrm{i}}vS_p; \\ nm_{\mathrm{i}}v\frac{\mathrm{d}v}{\mathrm{d}x} &= -m_{\mathrm{i}}c_s^2\frac{\mathrm{d}n}{\mathrm{d}x} - m_{\mathrm{i}}vS_p. \end{aligned} \tag{A.18}$$

Using (A.9) to write the density gradient in terms of S_p, (A.18) can be rewritten as:

$$nv\frac{\mathrm{d}v}{\mathrm{d}x} = -\frac{{c_s}^2}{v}\left(S_p - n\frac{\mathrm{d}v}{\mathrm{d}x}\right) - vS_p,$$

and rearranged to give:

$$n\frac{v^2}{{c_s}^2}\frac{\mathrm{d}v}{\mathrm{d}x} = n\frac{\mathrm{d}v}{\mathrm{d}x} - \left(1 + \frac{v^2}{{c_s}^2}\right)S_p.$$

Finally, we can introduce the Mach number, $M = {}^{v}/_{c_s}$ to subsitute for v and its derivative:

$$\frac{\mathrm{d}M}{\mathrm{d}x} = \frac{S_p}{nc_s}\frac{1+M^2}{1-M^2}. \tag{A.19}$$

Since the ions are accelerated towards the surface, the right hand side of (A.19) must be positive in order to avoid the occurrence of an unphysical singularity. This means that M must be less than or equal to unity. We have therefore further constrained the Bohm criterion (A.8) to:

$$v_{se} = c_s, \tag{A.20}$$

i.e. the plasma fluid flow becomes sonic at the sheath edge.

We can then consider the density variation within the sheath. Summing the electron and ion momentum conservation equations, (A.12) and (A.17), yields the conservation of momentum equation for the plasma fluid:

$$n(m_\mathrm{e}+m_\mathrm{i})v\frac{\mathrm{d}v}{\mathrm{d}x} = -\frac{\mathrm{d}p_\mathrm{e}}{\mathrm{d}x} - \frac{\mathrm{d}p_\mathrm{i}}{\mathrm{d}x} - (m_\mathrm{e}+m_\mathrm{i})v\frac{\mathrm{d}(nv)}{\mathrm{d}x}. \tag{A.21}$$

Neglecting m_e in comparison to m_i, and with some manipulation of the derivative in the third term on the right hand side, we obtain the relation:

$$\frac{\mathrm{d}}{\mathrm{d}x}\left(m_\mathrm{i}nv^2 + p_\mathrm{i} + p_\mathrm{e}\right) = 0. \tag{A.22}$$

The sum within the brackets is therefore constant along the fluid flow. If we again use $p = nkT$, the pressure terms can be grouped together and the constraint becomes:

$$nv^2 + n\frac{k(T_\mathrm{i}+T_\mathrm{e})}{m_\mathrm{i}} = const.$$

The second term on the left hand side is ${nc_s}^2$, and we can use the Mach number to write:

$$n(1+M^2) = const.$$

In the bulk plasma ($x = 0$), the density is denoted by n_0, and as we are assuming that the ions are stationary here, $M = 0$ and the constant is equal to n_0. The density distribution is therefore given by:

$$n = \frac{n_0}{(1+M^2)}, \tag{A.23}$$

and at the sheath edge (where $M = 1$):

$$n_{se} = \frac{n_0}{2}. \tag{A.24}$$

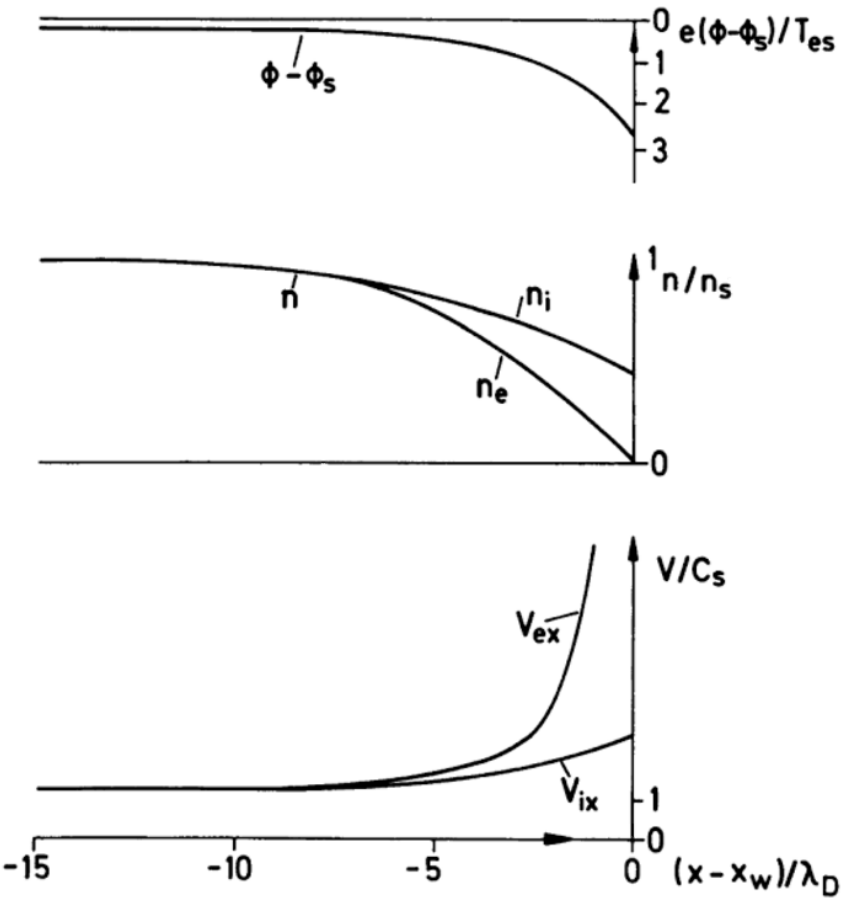

Figure A.1: Profiles of the potential (Φ); ion and electron densities (n_i and n_e); and ion and electron velocities (v_i and v_e) throughout the sheath. x_w is the position of the surface (i.e. 0 on the horizontal axis corresponds to the surface, with the bulk plasma in the negative direction). All quantities are normalised. Figure from [36].

The distributions of M, and hence v and n, can be obtained by integration of (A.19), which is detailed further in Chapter 1 of [23]. We can also find the distribution of the potential, V, by using the Boltzmann distribution, (A.5), to relate V to n and therefore M. Other analyses yield similar results, e.g. that by Chodura [36]. Example sketches of distributions for both electrons and ions are shown in Figure A.1.

Appendix B

Hydrogen excited level population coefficients

This appendix contains the coefficients used to calculate the populations of the upper levels of the hydrogen Balmer alpha (H_α, quantum number $p = 3$) and gamma (H_γ, $p = 6$) lines in the model of emission from the detached plasma in the York Linear Plasma Device (Section 4.3). The coefficients are taken from the tables of Johnson and Hinnov, and are given as functions of plasma temperature, T_e, and density, n [89].

Tables B.1 and B.2 give the coefficients $r_0(p)$ for the level populations due to recombination for the H_α and H_γ lines respectively. The population, n_{rec}, is calculated as follows:

$$n_{rec}(p) = r_0(p)\, n_{\mathrm{E}}(p),$$

where n_{E} is the Saha equilibrium density of level p (as given by (26) in Section 4.3).

The coefficients for the level populations due to collisional excitation, $r_1(p)$, are shown in Tables B.3 (H_α) and B.4 (H_γ). In this case, the equation for the population, n_{ex} is:

$$n_{ex}(p) = r_1(p)\, n(1)\, \frac{n_{\mathrm{E}}(p)}{n_{\mathrm{E}}(1)}.$$

Table B.1: The coefficents $r_0(3)$ used to calculate the population of the H_α line upper level due to recombination, $n_{rec}(3)$ [89].

T_e [eV]	n [m^{-3}]				
	1×10^{16}	1×10^{17}	1×10^{18}	1×10^{19}	1×10^{20}
0.17	2.20×10^{-05}	4.00×10^{-05}	1.10×10^{-04}	7.00×10^{-04}	6.90×10^{-03}
0.34	2.20×10^{-03}	3.10×10^{-03}	6.00×10^{-03}	2.20×10^{-02}	1.30×10^{-01}
0.69	2.60×10^{-02}	3.30×10^{-02}	5.00×10^{-02}	1.20×10^{-01}	4.30×10^{-01}
1.38	1.10×10^{-01}	1.30×10^{-01}	1.60×10^{-01}	3.00×10^{-01}	6.80×10^{-01}
2.76	2.70×10^{-01}	2.90×10^{-01}	3.40×10^{-01}	5.00×10^{-01}	8.20×10^{-01}
5.52	4.80×10^{-01}	5.00×10^{-01}	5.40×10^{-01}	6.80×10^{-01}	9.00×10^{-01}
11.03	7.30×10^{-01}	7.40×10^{-01}	7.70×10^{-01}	8.50×10^{-01}	9.50×10^{-01}
22.06	$1.00 \times 10^{+00}$	$1.00 \times 10^{+00}$	$1.00 \times 10^{+00}$	$1.00 \times 10^{+00}$	$1.00 \times 10^{+00}$

Table B.2: The coefficents $r_0(6)$ used to calculate the population of the H_γ line upper level due to recombination, $n_{rec}(6)$ [89].

T_e [eV]	n [m^{-3}]				
	1×10^{16}	1×10^{17}	1×10^{18}	1×10^{19}	1×10^{20}
0.17	3.40×10^{-02}	1.10×10^{-01}	4.00×10^{-01}	6.60×10^{-01}	7.60×10^{-01}
0.34	1.10×10^{-01}	2.70×10^{-01}	6.40×10^{-01}	8.60×10^{-01}	9.40×10^{-01}
0.69	2.40×10^{-01}	4.50×10^{-01}	7.90×10^{-01}	9.40×10^{-01}	9.80×10^{-01}
1.38	3.80×10^{-01}	6.00×10^{-01}	8.70×10^{-01}	9.70×10^{-01}	9.80×10^{-01}
2.76	5.30×10^{-01}	7.20×10^{-01}	9.10×10^{-01}	9.80×10^{-01}	$1.00 \times 10^{+00}$
5.52	6.80×10^{-01}	8.10×10^{-01}	9.40×10^{-01}	9.90×10^{-01}	$1.00 \times 10^{+00}$
11.03	8.20×10^{-01}	9.00×10^{-01}	9.70×10^{-01}	9.90×10^{-01}	$1.00 \times 10^{+00}$
22.06	9.70×10^{-01}	9.90×10^{-01}	$1.00 \times 10^{+00}$	$1.00 \times 10^{+00}$	$1.00 \times 10^{+00}$

Table B.3: The coefficents $r_1(3)$ used to calculate the population of the H_α line upper level due to collisional excitation, $n_{ex}(3)$ [89].

T_e [eV]	n [m^{-3}]				
	1×10^{16}	1×10^{17}	1×10^{18}	1×10^{19}	1×10^{20}
0.34	1.00×10^{-07}	1.00×10^{-06}	1.00×10^{-05}	1.00×10^{-04}	1.10×10^{-03}
0.69	8.20×10^{-08}	8.10×10^{-07}	8.00×10^{-06}	7.70×10^{-05}	6.10×10^{-04}
1.38	7.10×10^{-08}	7.00×10^{-07}	6.80×10^{-06}	5.90×10^{-05}	3.30×10^{-04}
2.76	6.80×10^{-08}	6.70×10^{-07}	6.30×10^{-06}	4.90×10^{-05}	2.10×10^{-04}
5.52	7.20×10^{-08}	7.00×10^{-07}	6.50×10^{-06}	4.70×10^{-05}	1.80×10^{-04}
11.03	8.10×10^{-08}	7.80×10^{-07}	7.20×10^{-06}	5.10×10^{-05}	1.90×10^{-04}
22.06	9.10×10^{-08}	8.90×10^{-07}	8.20×10^{-06}	5.80×10^{-05}	2.10×10^{-04}

Table B.4: The coefficents $r_1(6)$ used to calculate the population of the H_γ line upper level due to collisional excitation, $n_{ex}(6)$ [89].

T_e [eV]	n [m^{-3}]				
	1×10^{16}	1×10^{17}	1×10^{18}	1×10^{19}	1×10^{20}
0.34	5.20×10^{-08}	4.30×10^{-07}	2.30×10^{-06}	1.00×10^{-05}	7.20×10^{-05}
0.69	4.10×10^{-08}	3.00×10^{-07}	1.20×10^{-06}	4.00×10^{-06}	1.70×10^{-05}
1.38	3.40×10^{-08}	2.20×10^{-07}	8.70×10^{-07}	2.10×10^{-06}	6.60×10^{-06}
2.76	3.10×10^{-08}	1.90×10^{-07}	6.00×10^{-07}	1.50×10^{-06}	3.80×10^{-06}
5.52	3.20×10^{-08}	1.90×10^{-07}	5.90×10^{-07}	1.40×10^{-06}	3.20×10^{-06}
11.03	3.60×10^{-08}	2.10×10^{-07}	6.70×10^{-07}	1.60×10^{-06}	3.50×10^{-06}
22.06	4.10×10^{-08}	2.50×10^{-07}	8.20×10^{-07}	1.90×10^{-06}	4.30×10^{-06}

Appendix C

Fast frame imaging data

This appendix contains additional fast frame imaging (FFI) data to give further details of the results presented in Section 5.1 of Chapter 5.

Figure C.1 shows the full pressure evolution of the FFI data, from the attached plasma to the EIR detached state. One example frame is shown for each target chamber pressure value. We see the progression from the narrow column to the broadened detached state, with the most significant transition occurring at the penultimate pressure value, between Figures C.1x and C.1y as the pressure changes from 6.25×10^{-3} to 6.5×10^{-3} mbar.

Figure C.2 shows the full set of spectral data for the attached plasma state (3.1×10^{-4} mbar): each image is a 2D colour map of the distribution of a single frequency component across the image. The same data for the EIR detached state (7.25×10^{-3} mbar) is presented in Figure C.3.

Both data sets show very strong DC and low frequency components, which saturate the plot on the scale shown (Figures C.2(1), C.2(2), C.3(1) and C.3(2)). At higher frequencies, neither state shows significant variation in the distribution. There is some fluctuation in the peak strength (less than a factor of two), but the spatial distributions remain relatively constant: the narrow column of the attached plasma; and the broadened, double peak structure of EIR detachment. The only exception is at 25000 Hz in both cases (Figures C.2(34) and C.3(34)), which retains the structure, but is a factor of $2 - 3$ weaker.

The full set of coherence data for the left-hand reference pixel ($x = 40$, $y = 40$) across all frequency components is shown in Figure C.4. The behaviour with frequency is similar to the power distribution, with strong coherence across the majority of the image at 0 and 757 Hz, and very little variation of the filamentary structure across the rest of the spectrum.

The phase data for the same reference pixel is shown for each frequency in Figure C.5. Again, there is little to no phase difference across the plasma at 0 and 757 Hz, and the structure due to the filaments is visible across the remaining frequencies. The resolution of the 25000 Hz component is very limited (Figure C.5(34)). There is also some slight variation in how the phase changes across the column, but the general distribution of the in-phase and out-of-phase regions remains relatively constant.

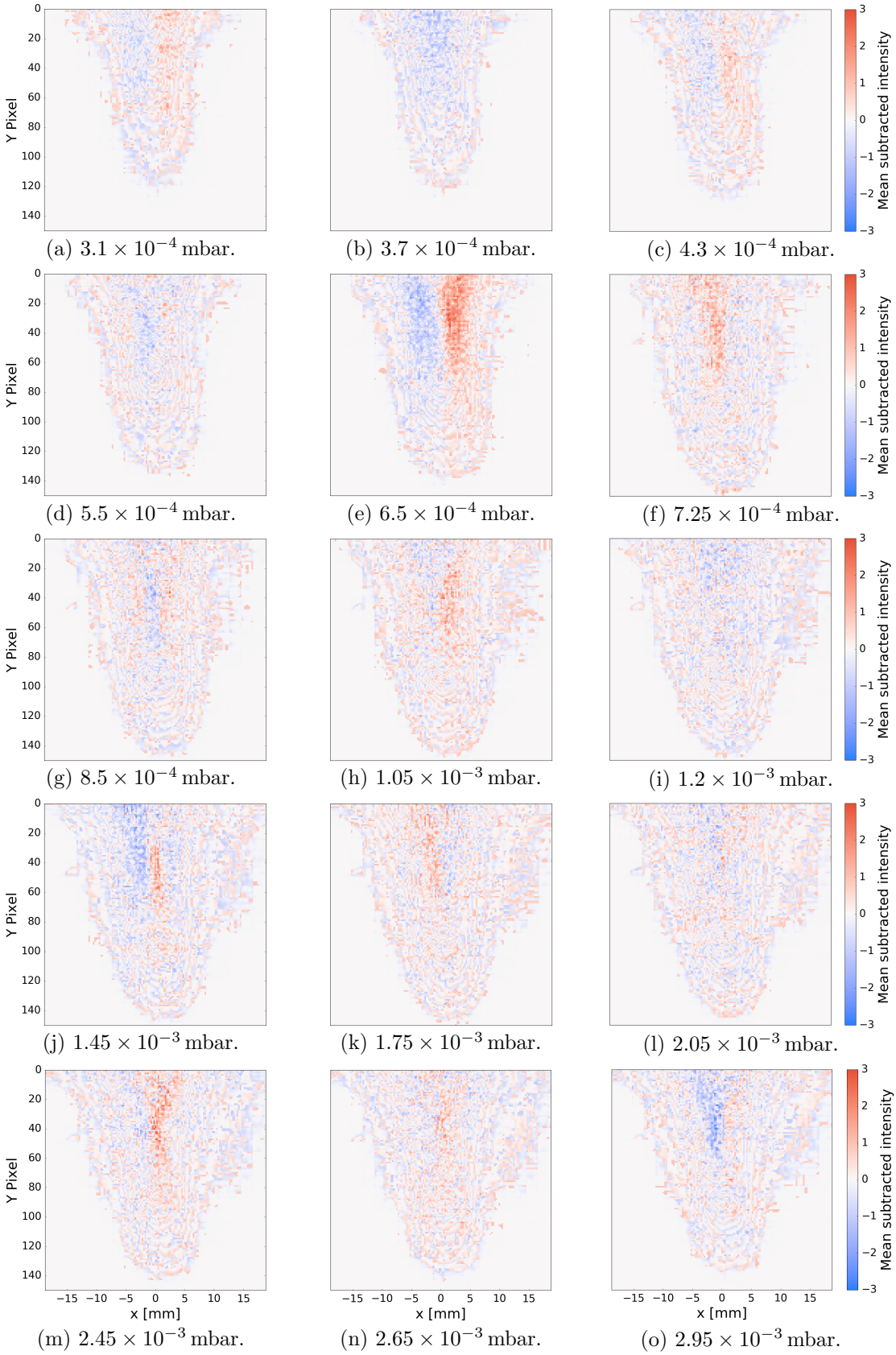

(a) 3.1×10^{-4} mbar. (b) 3.7×10^{-4} mbar. (c) 4.3×10^{-4} mbar.

(d) 5.5×10^{-4} mbar. (e) 6.5×10^{-4} mbar. (f) 7.25×10^{-4} mbar.

(g) 8.5×10^{-4} mbar. (h) 1.05×10^{-3} mbar. (i) 1.2×10^{-3} mbar.

(j) 1.45×10^{-3} mbar. (k) 1.75×10^{-3} mbar. (l) 2.05×10^{-3} mbar.

(m) 2.45×10^{-3} mbar. (n) 2.65×10^{-3} mbar. (o) 2.95×10^{-3} mbar.

Figure C.1: Example mean-subtracted FFI frames for all target chamber pressures from 3.1×10^{-4} mbar (attached) to 7.25×10^{-3} mbar (EIR detached). *Continued overleaf.*

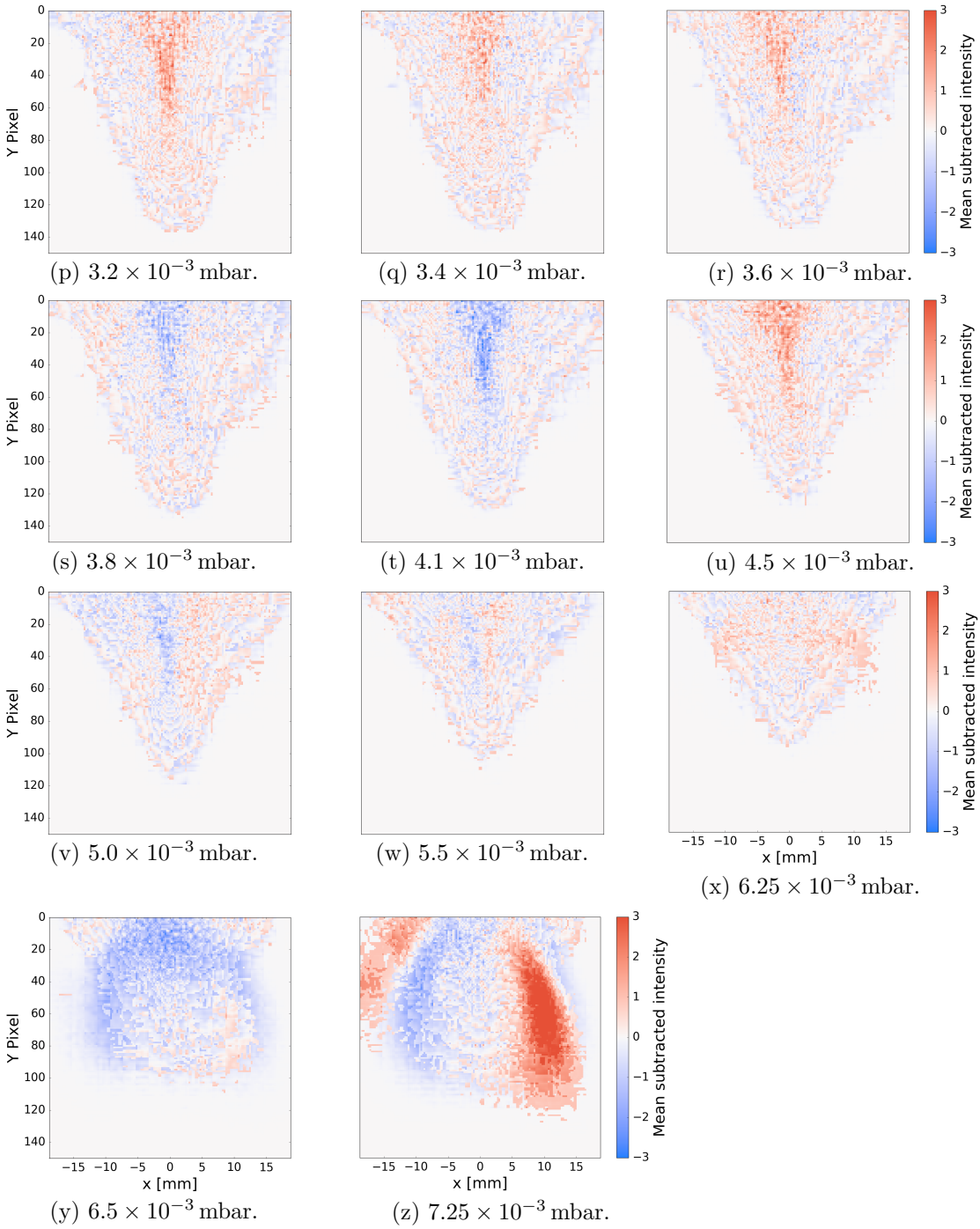

(p) 3.2×10^{-3} mbar. (q) 3.4×10^{-3} mbar. (r) 3.6×10^{-3} mbar.

(s) 3.8×10^{-3} mbar. (t) 4.1×10^{-3} mbar. (u) 4.5×10^{-3} mbar.

(v) 5.0×10^{-3} mbar. (w) 5.5×10^{-3} mbar. (x) 6.25×10^{-3} mbar.

(y) 6.5×10^{-3} mbar. (z) 7.25×10^{-3} mbar.

Figure C.1: Example mean-subtracted FFI frames for all target chamber pressures from 3.1×10^{-4} mbar (attached) to 7.25×10^{-3} mbar (EIR detached).

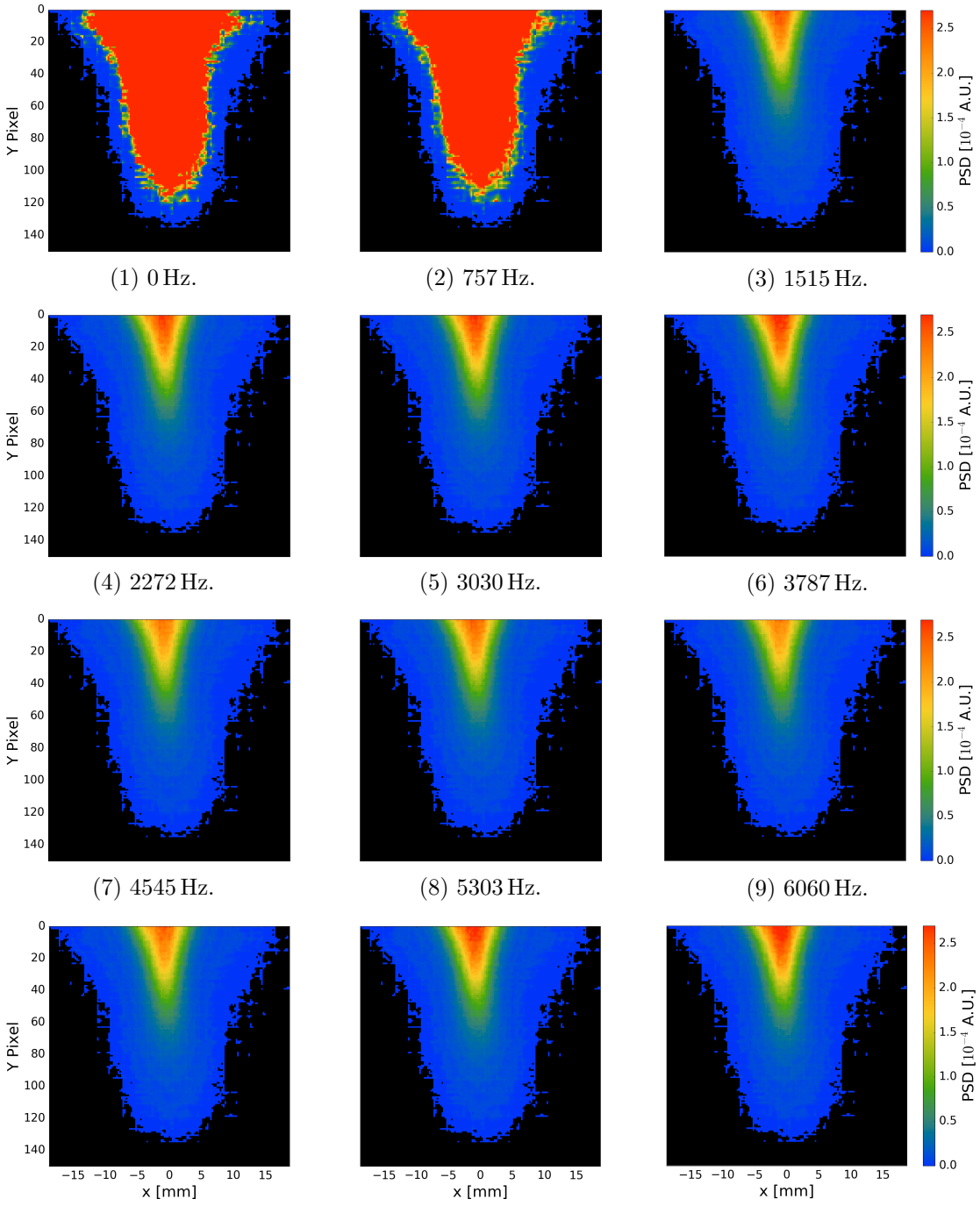

(1) 0 Hz. (2) 757 Hz. (3) 1515 Hz.

(4) 2272 Hz. (5) 3030 Hz. (6) 3787 Hz.

(7) 4545 Hz. (8) 5303 Hz. (9) 6060 Hz.

(10) 6818 Hz. (11) 7575 Hz. (12) 8333 Hz.

Figure C.2: Distribution of power components across the FFI data for the attached plasma (target chamber pressure of 3.1×10^{-4} mbar). *Continued overleaf.*

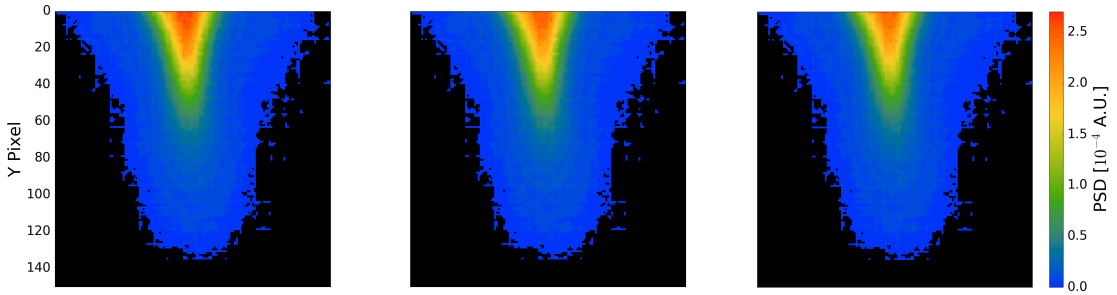

(13) 9090 Hz. (14) 9848 Hz. (15) 10606 Hz.

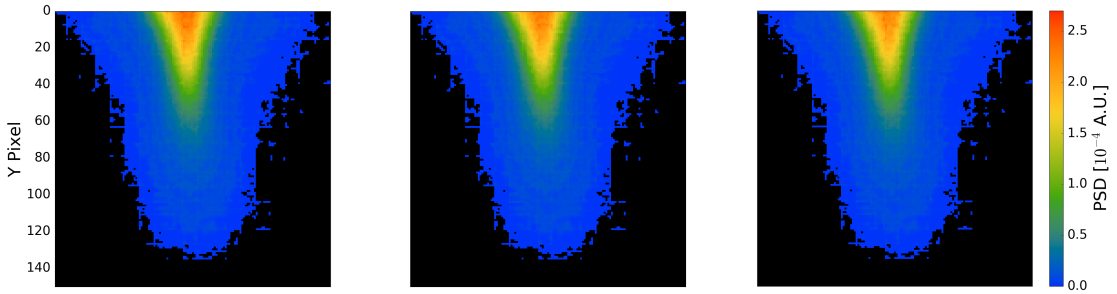

(16) 11363 Hz. (17) 12121 Hz. (18) 12878 Hz.

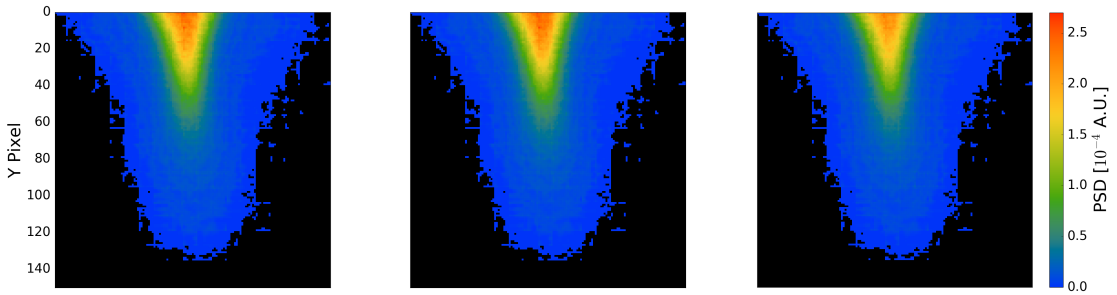

(19) 13636 Hz. (20) 14393 Hz. (21) 15151 Hz.

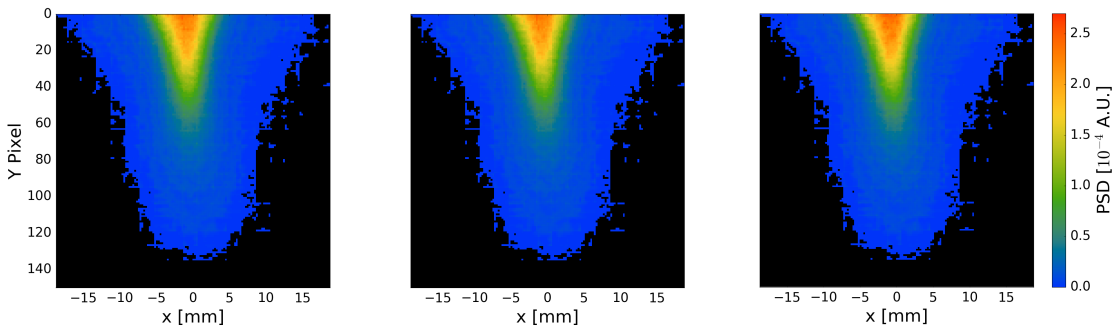

(22) 15909 Hz. (23) 16666 Hz. (24) 17424 Hz.

Figure C.2: Distribution of power components across the FFI data for the attached plasma (target chamber pressure of 3.1×10^{-4} mbar). *Continued overleaf.*

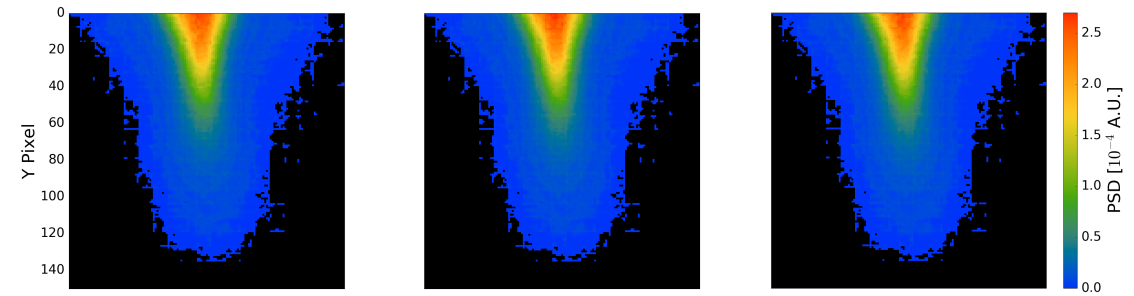

(25) 18181 Hz. (26) 18939 Hz. (27) 19696 Hz.

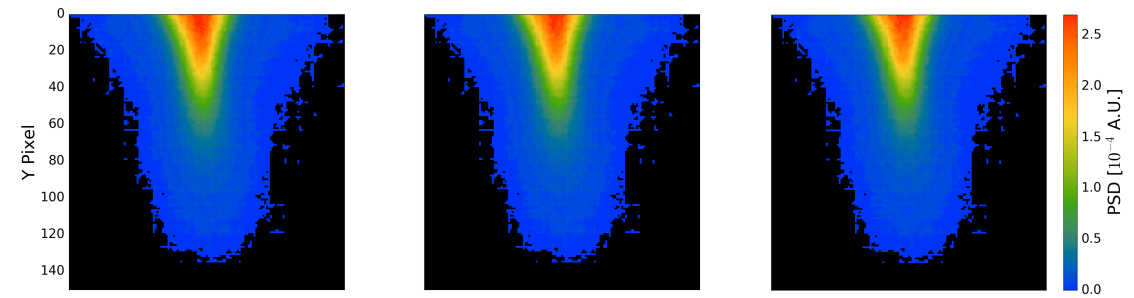

(28) 20454 Hz. (29) 21212 Hz. (30) 21969 Hz.

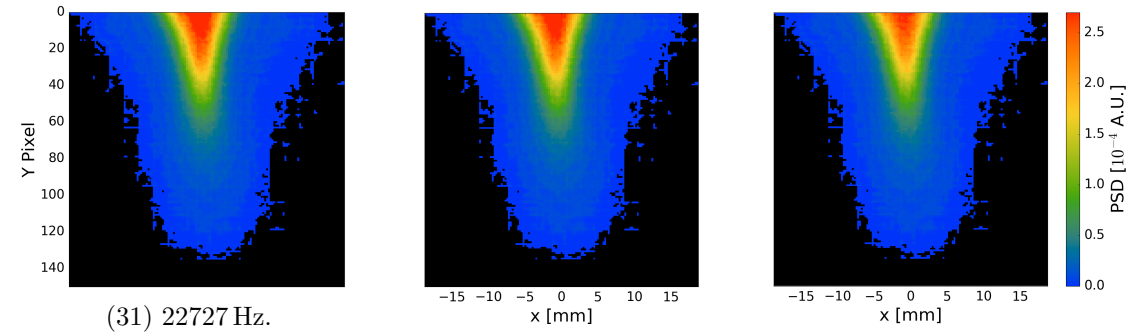

(31) 22727 Hz. (32) 23484 Hz. (33) 24242 Hz.

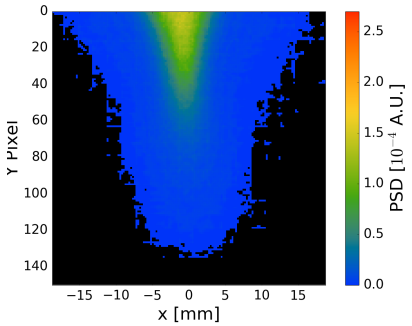

(34) 25000 Hz.

Figure C.2: Distribution of power components across the FFI data for the attached plasma (target chamber pressure of 3.1×10^{-4} mbar).

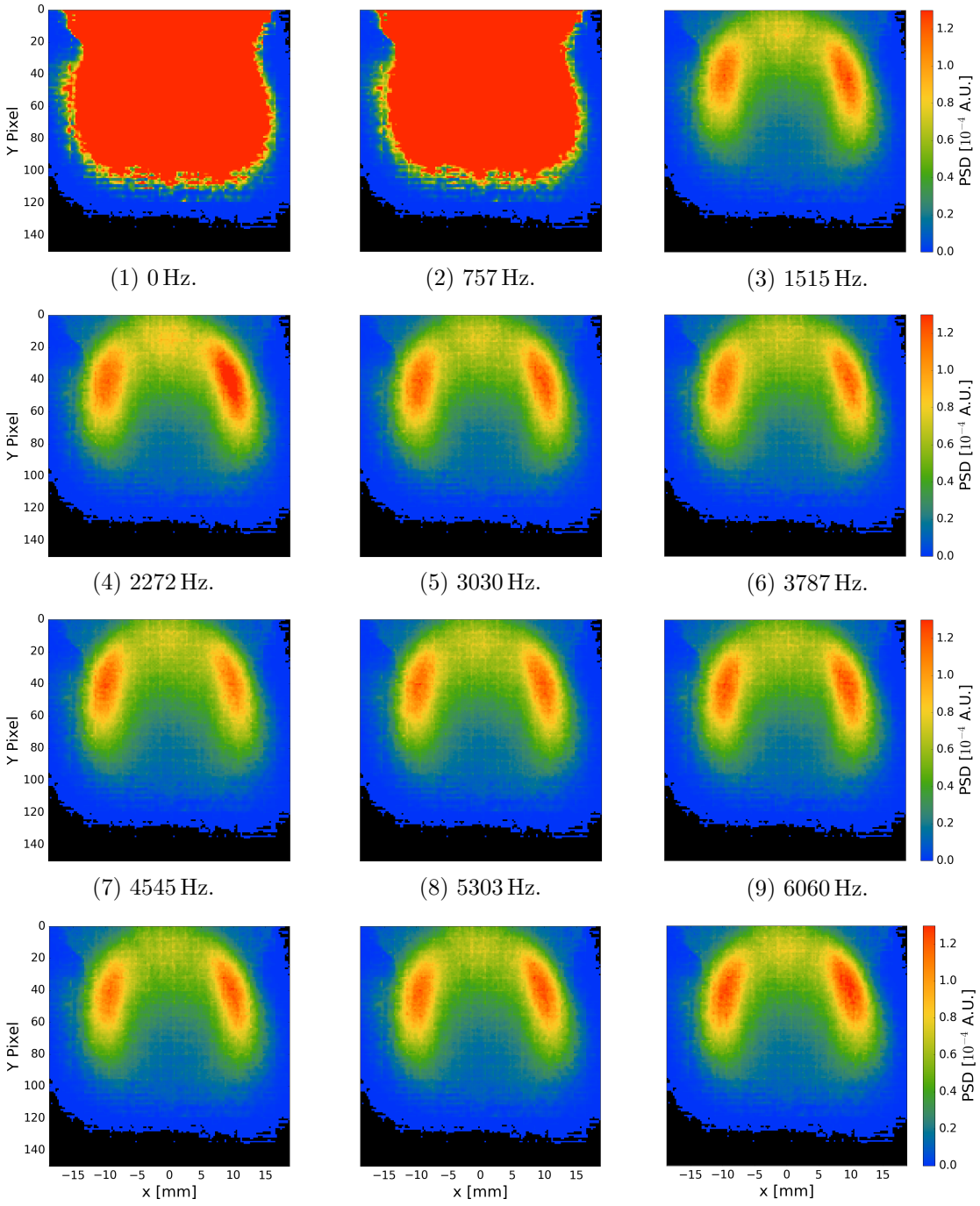

(1) 0 Hz. (2) 757 Hz. (3) 1515 Hz.

(4) 2272 Hz. (5) 3030 Hz. (6) 3787 Hz.

(7) 4545 Hz. (8) 5303 Hz. (9) 6060 Hz.

(10) 6818 Hz. (11) 7575 Hz. (12) 8333 Hz.

Figure C.3: Distribution of power components across the FFI data for the detached plasma (target chamber pressure of 7.25×10^{-3} mbar). *Continued overleaf.*

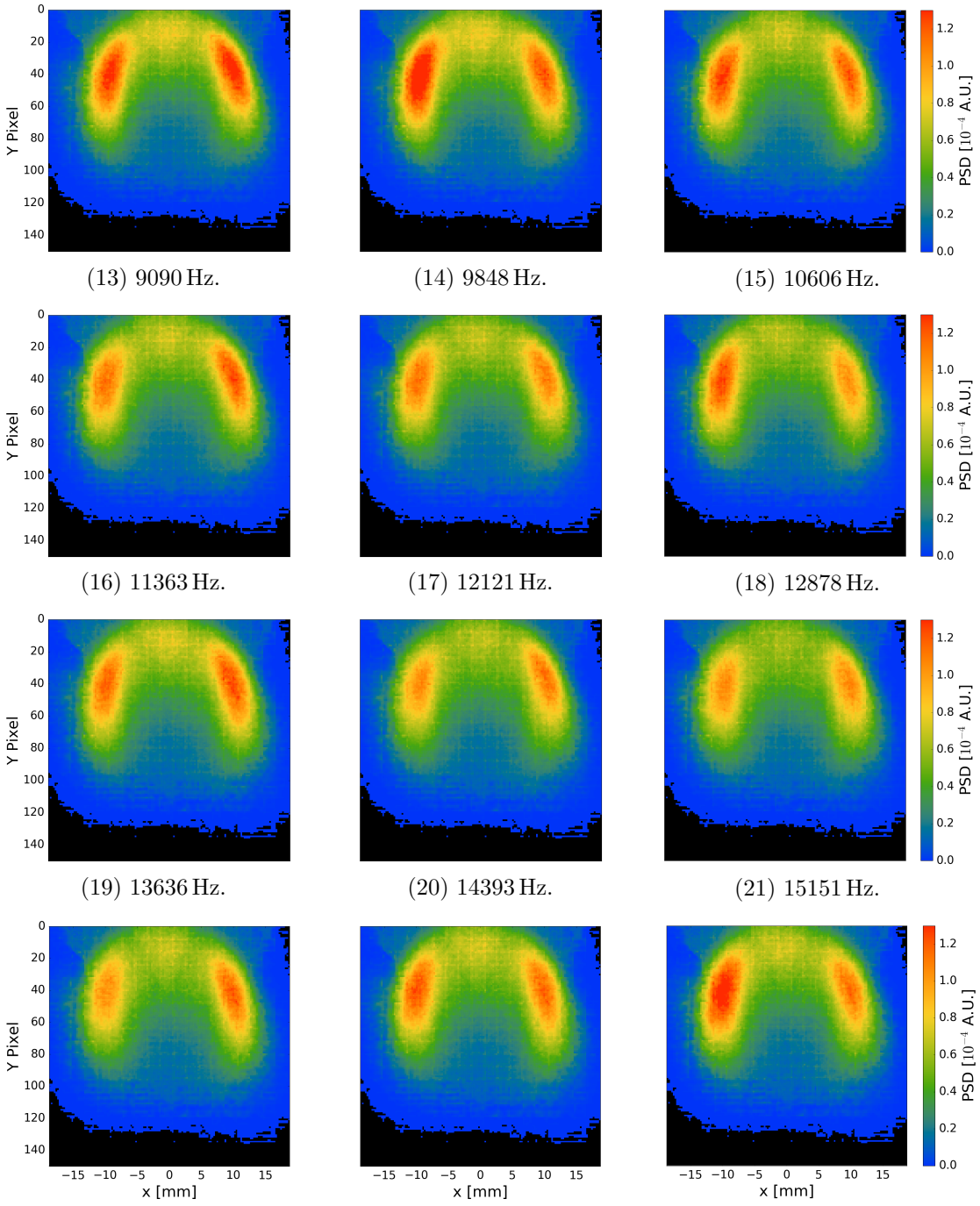

(13) 9090 Hz. (14) 9848 Hz. (15) 10606 Hz.

(16) 11363 Hz. (17) 12121 Hz. (18) 12878 Hz.

(19) 13636 Hz. (20) 14393 Hz. (21) 15151 Hz.

(22) 15909 Hz. (23) 16666 Hz. (24) 17424 Hz.

Figure C.3: Distribution of power components across the FFI data for the detached plasma (target chamber pressure of 7.25×10^{-3} mbar). *Continued overleaf.*

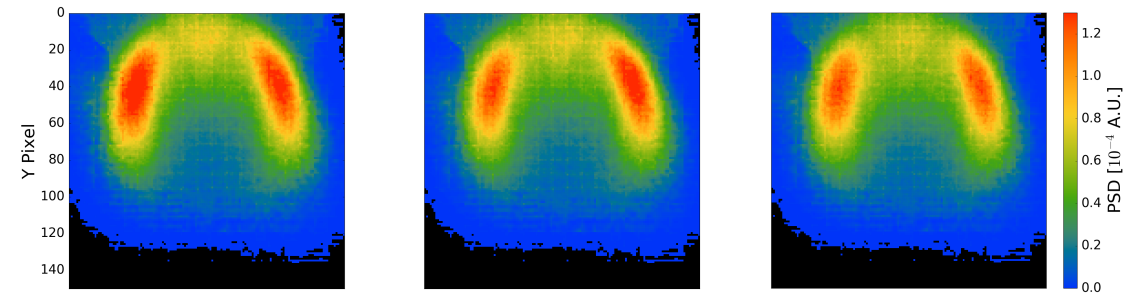

(25) 18181 Hz. (26) 18939 Hz. (27) 19696 Hz.

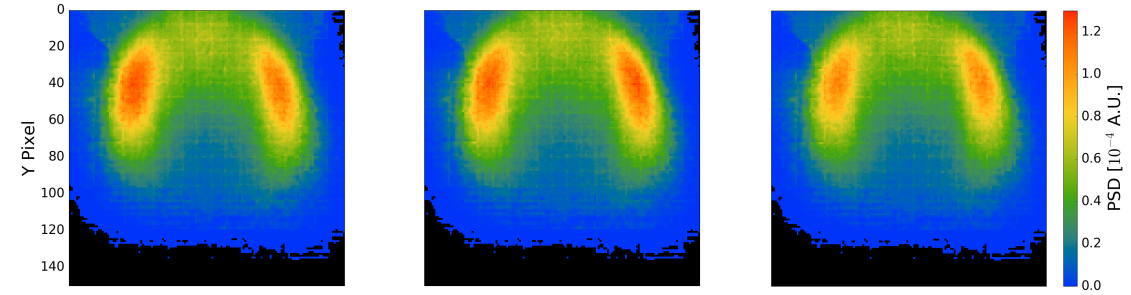

(28) 20454 Hz. (29) 21212 Hz. (30) 21969 Hz.

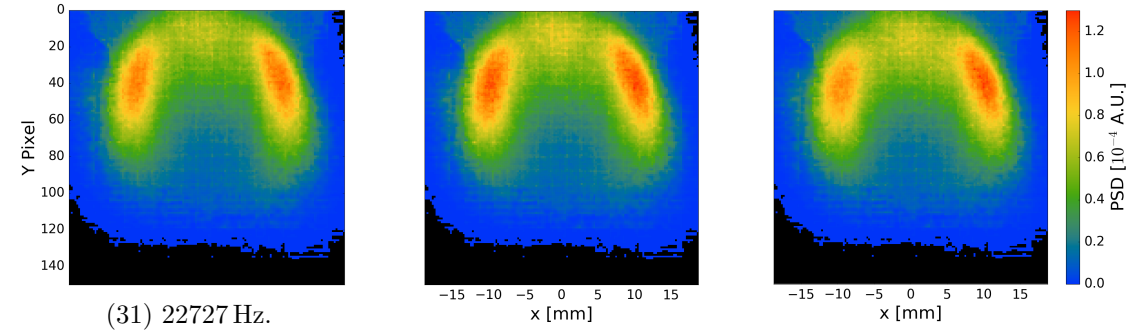

(31) 22727 Hz. (32) 23484 Hz. (33) 24242 Hz.

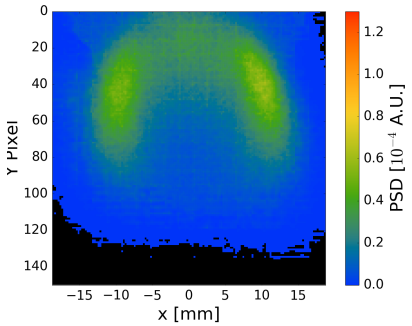

(34) 25000 Hz.

Figure C.3: Distribution of power components across the FFI data for the detached plasma (target chamber pressure of 7.25×10^{-3} mbar).

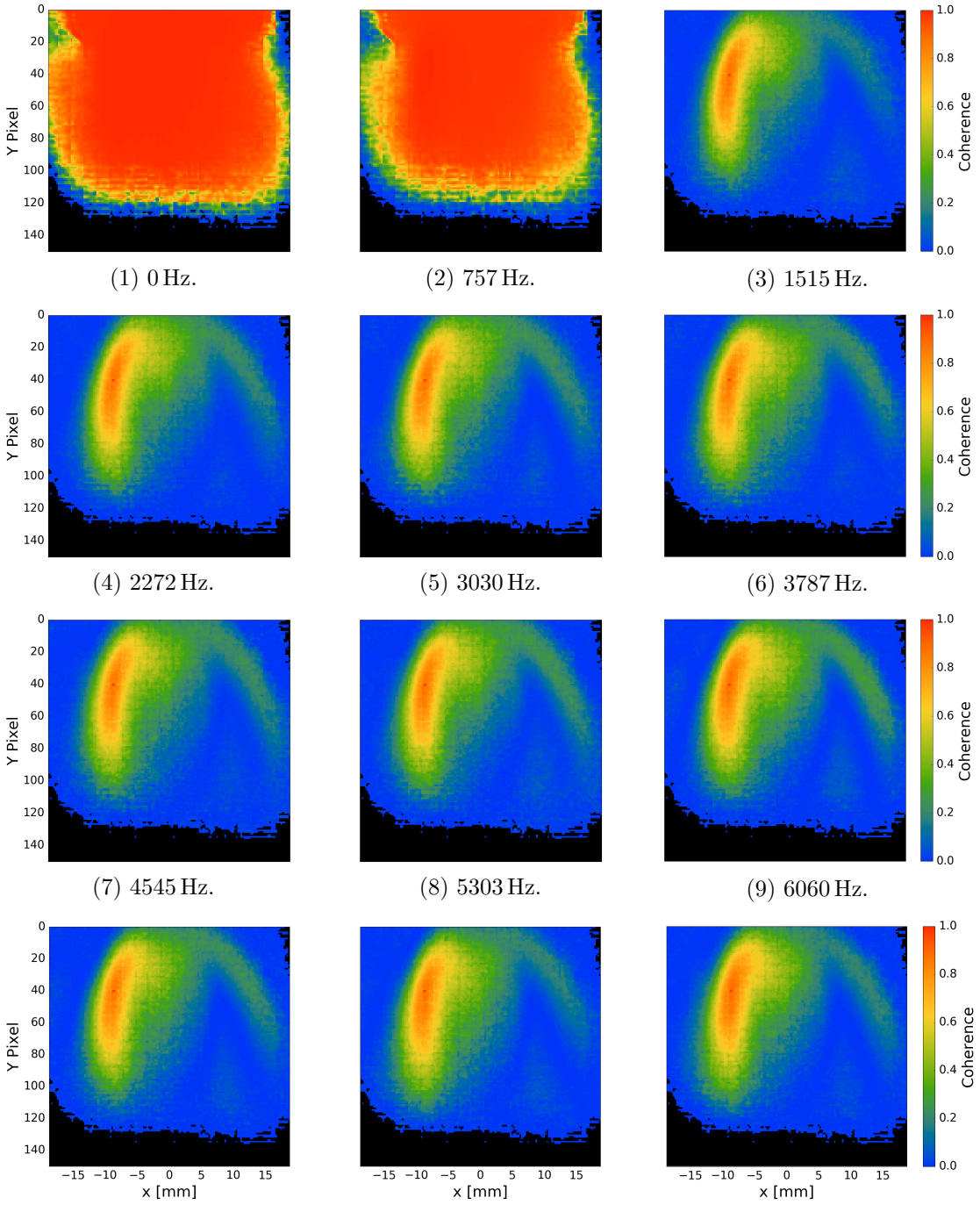

(1) 0 Hz. (2) 757 Hz. (3) 1515 Hz.

(4) 2272 Hz. (5) 3030 Hz. (6) 3787 Hz.

(7) 4545 Hz. (8) 5303 Hz. (9) 6060 Hz.

(10) 6818 Hz. (11) 7575 Hz. (12) 8333 Hz.

Figure C.4: Coherence between the left-hand reference pixel ($x = 40, y = 40$) and all other pixels in the detached plasma (target chamber pressure of 7.25×10^{-3} mbar). *Continued overleaf.*

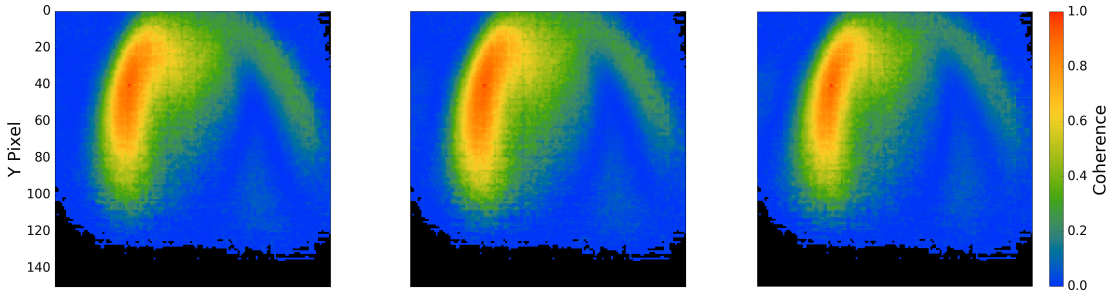

(13) 9090 Hz. (14) 9848 Hz. (15) 10606 Hz.

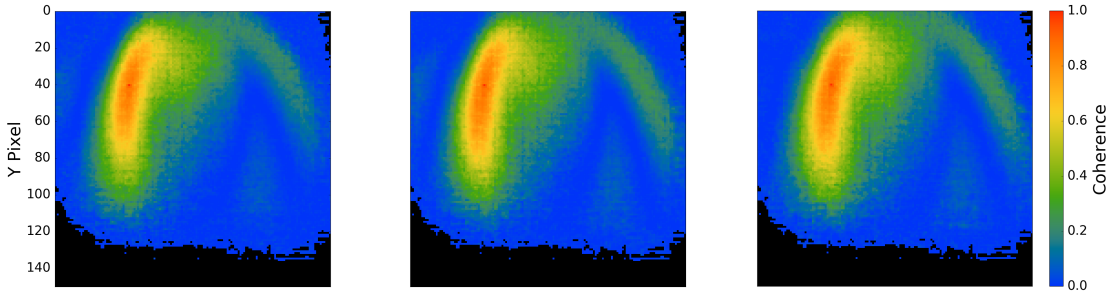

(16) 11363 Hz. (17) 12121 Hz. (18) 12878 Hz.

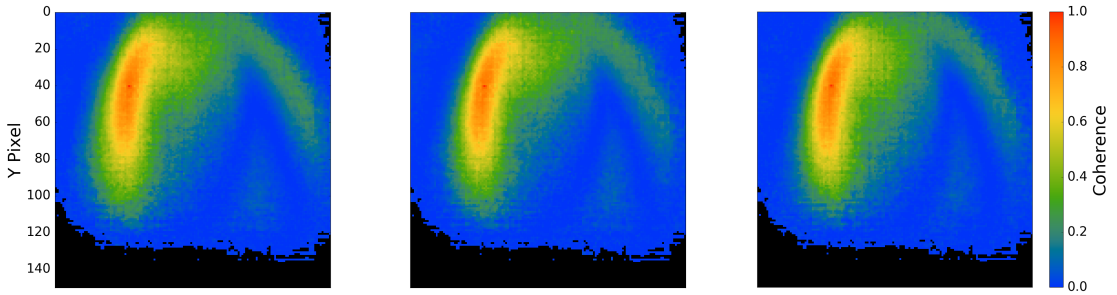

(19) 13636 Hz. (20) 14393 Hz. (21) 15151 Hz.

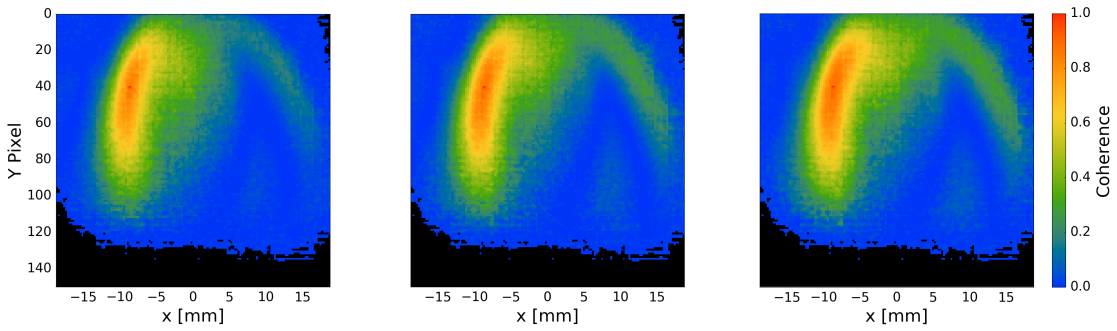

(22) 15909 Hz. (23) 16666 Hz. (24) 17424 Hz.

Figure C.4: Coherence between the left-hand reference pixel ($x = 40, y = 40$) and all other pixels in the detached plasma (target chamber pressure of 7.25×10^{-3} mbar). *Continued overleaf.*

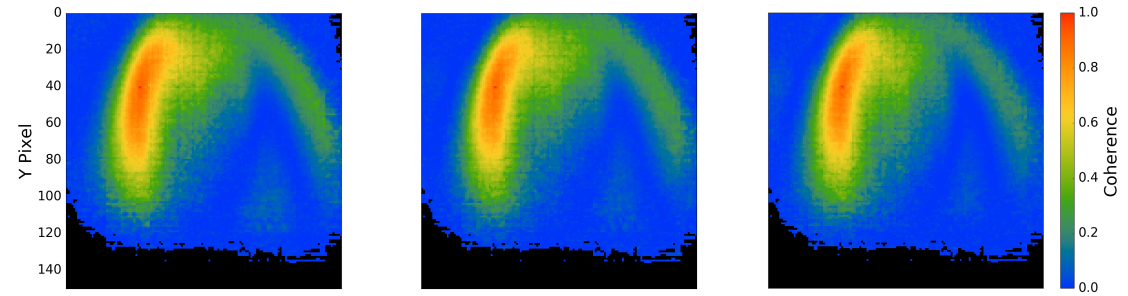

(25) 18181 Hz. (26) 18939 Hz. (27) 19696 Hz.

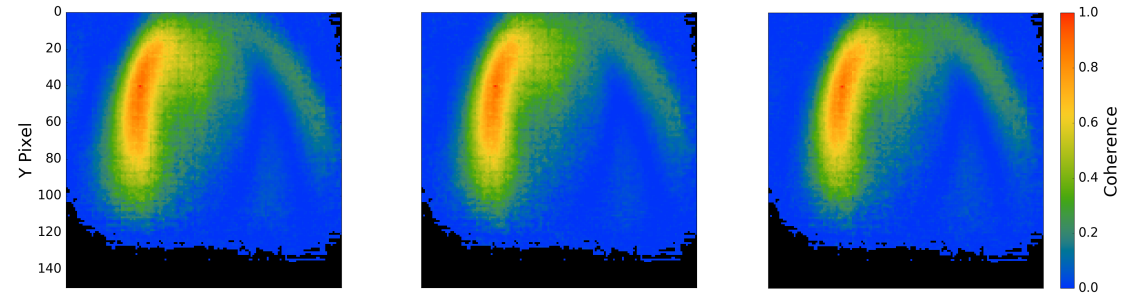

(28) 20454 Hz. (29) 21212 Hz. (30) 21969 Hz.

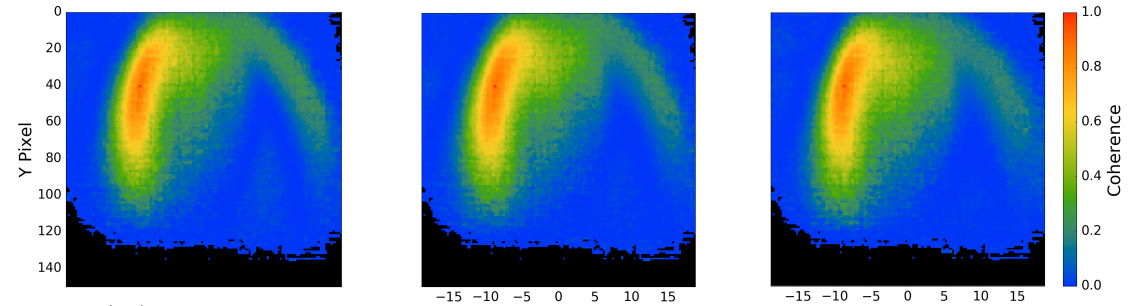

(31) 22727 Hz. (32) 23484 Hz. (33) 24242 Hz.

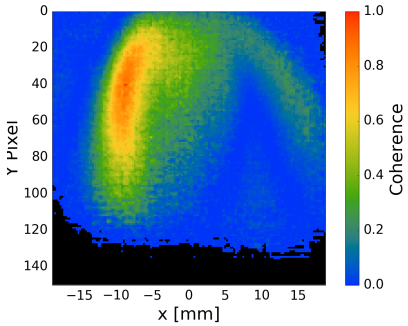

(34) 25000 Hz.

Figure C.4: Coherence between the left-hand reference pixel ($x = 40, y = 40$) and all other pixels in the detached plasma (target chamber pressure of 7.25×10^{-3} mbar).

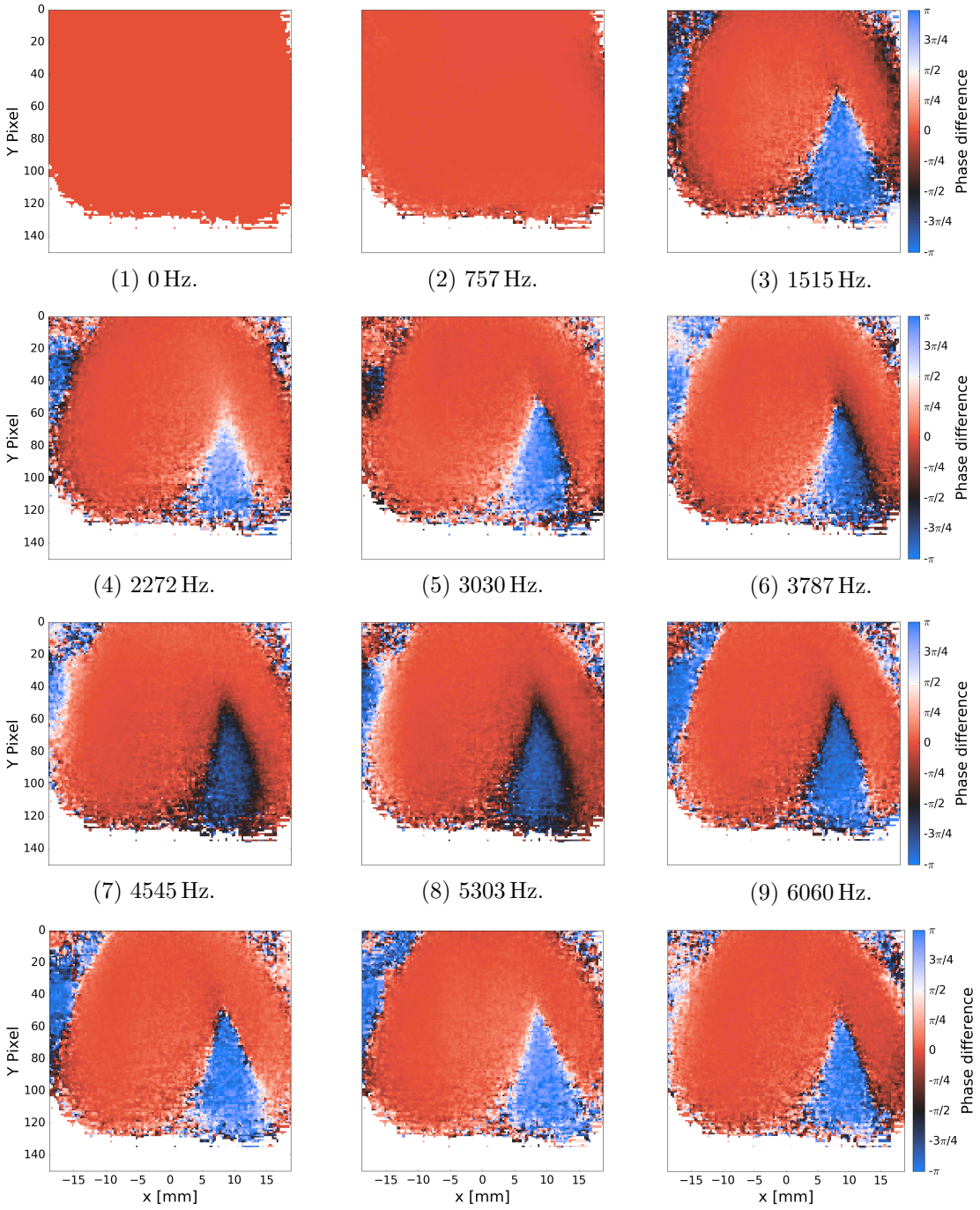

(1) 0 Hz. (2) 757 Hz. (3) 1515 Hz.

(4) 2272 Hz. (5) 3030 Hz. (6) 3787 Hz.

(7) 4545 Hz. (8) 5303 Hz. (9) 6060 Hz.

(10) 6818 Hz. (11) 7575 Hz. (12) 8333 Hz.

Figure C.5: Phase difference between the left-hand reference pixel ($x = 40, y = 40$) and all other pixels in the detached plasma (target chamber pressure of 7.25×10^{-3} mbar). *Continued overleaf.*

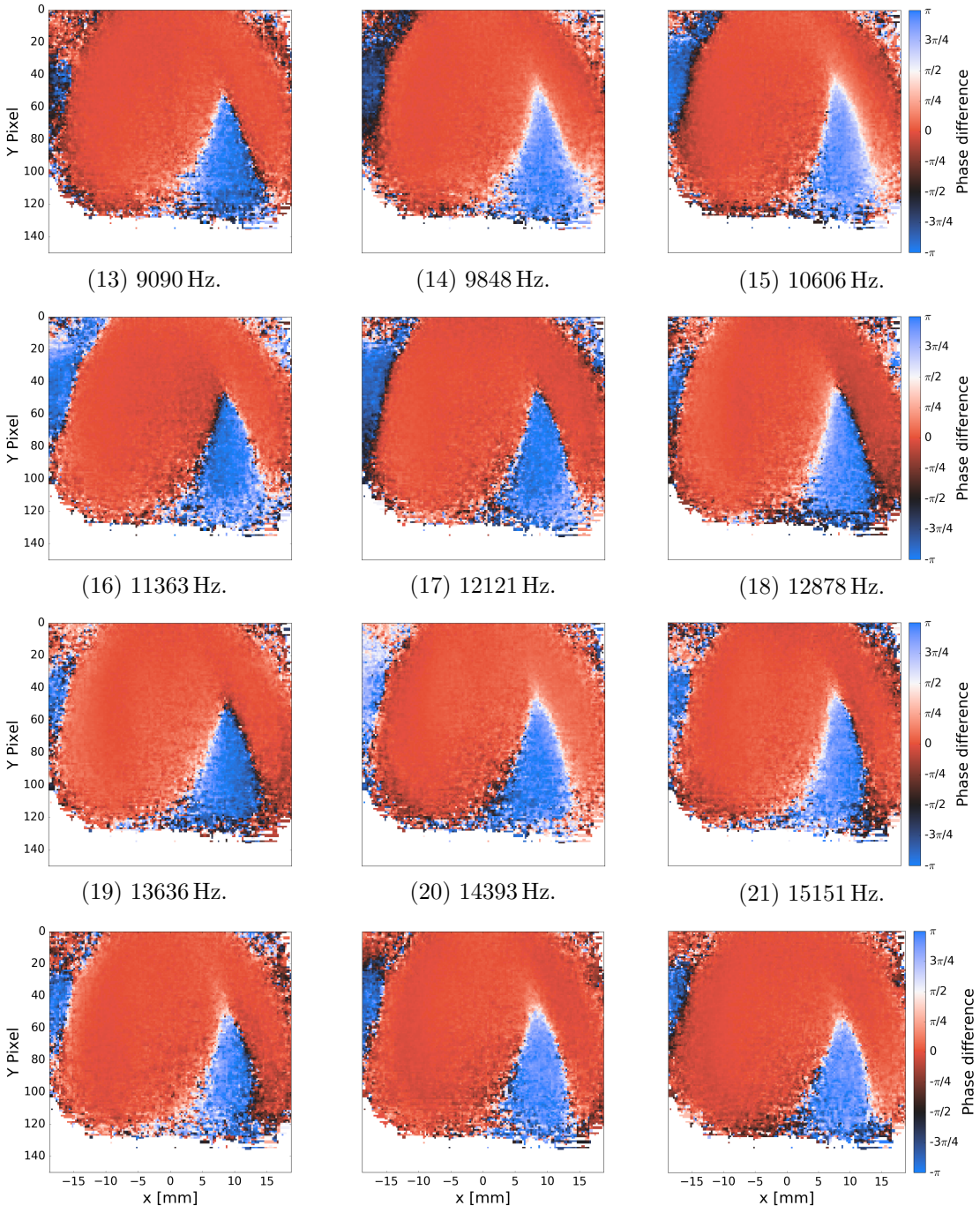

(13) 9090 Hz. (14) 9848 Hz. (15) 10606 Hz.

(16) 11363 Hz. (17) 12121 Hz. (18) 12878 Hz.

(19) 13636 Hz. (20) 14393 Hz. (21) 15151 Hz.

(22) 15909 Hz. (23) 16666 Hz. (24) 17424 Hz.

Figure C.5: Phase difference between the left-hand reference pixel ($x = 40, y = 40$) and all other pixels in the detached plasma (target chamber pressure of 7.25×10^{-3} mbar). *Continued overleaf.*

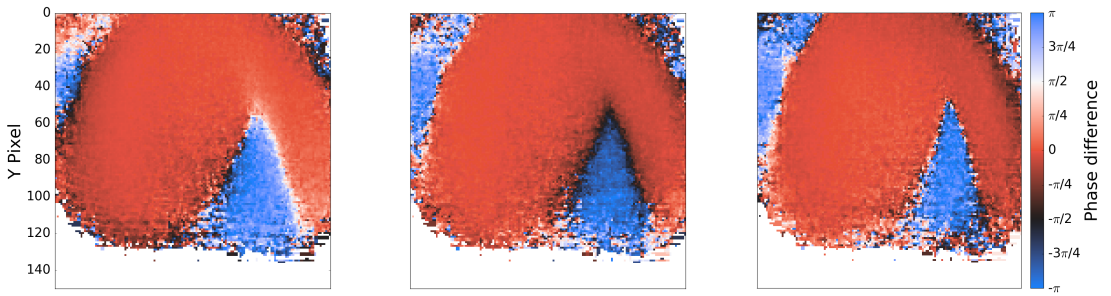

(25) 18181 Hz. (26) 18939 Hz. (27) 19696 Hz.

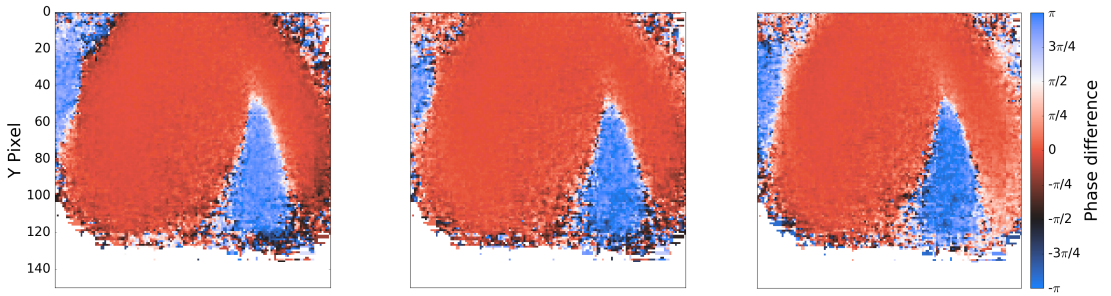

(28) 20454 Hz. (29) 21212 Hz. (30) 21969 Hz.

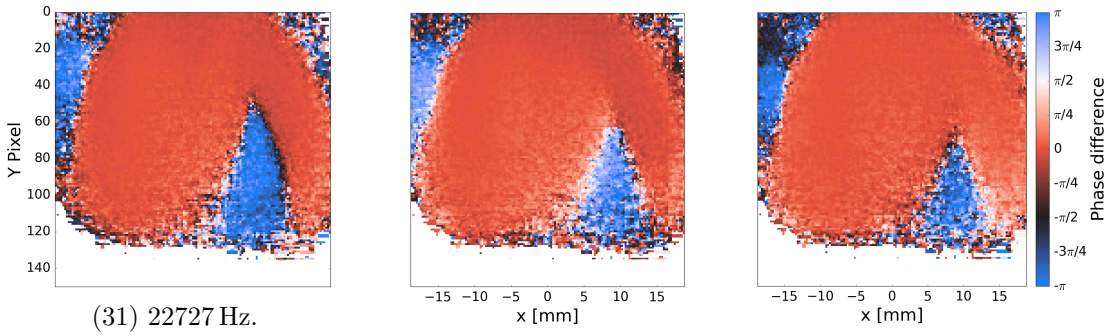

(31) 22727 Hz. (32) 23484 Hz. (33) 24242 Hz.

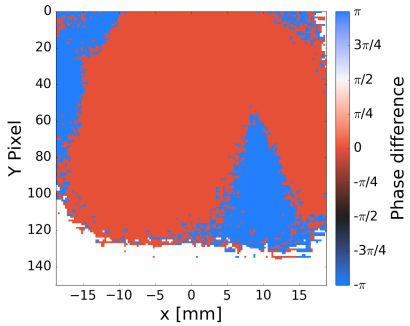

(34) 25000 Hz.

Figure C.5: Phase difference between the left-hand reference pixel ($x = 40, y = 40$) and all other pixels in the detached plasma (target chamber pressure of 7.25×10^{-3} mbar).

Appendix D

Negative ion reaction rate coefficients

The expressions for the rate coefficients for negative ion formation and destruction (as functions of temperature, T) in Section 6.4.2 both take the form [39]:

$$\ln\langle\sigma v\rangle = \sum_{n=0}^{8} b_n (\ln T)^n.$$

The coefficients b_n used for each reaction are listed in Table D.1.

Table D.1: The coefficents b_n used in the expressions for the rate coefficients for negative ion formation ($\langle\sigma v\rangle_{form}$) and destruction ($\langle\sigma v\rangle_{destr}$) [39].

n	b_n	
	$\langle\sigma v\rangle_{form}$	$\langle\sigma v\rangle_{destr}$
0	$-1.774398466232 \times 10^{+1}$	$-1.801849334273 \times 10^{+1}$
1	$-6.207038732492 \times 10^{-1}$	$2.360852208681 \times 10^{0}$
2	$-2.811412695673 \times 10^{-1}$	$-2.827443061704 \times 10^{-1}$
3	$2.540958044519 \times 10^{-2}$	$1.623316639567 \times 10^{-2}$
4	$6.643467825225 \times 10^{-3}$	$-3.365012031363 \times 10^{-2}$
5	$-8.877629159412 \times 10^{-4}$	$1.178329782711 \times 10^{-2}$
6	$-3.705776394283 \times 10^{-4}$	$-1.656194699504 \times 10^{-3}$
7	$9.313511559362 \times 10^{-5}$	$1.068275202678 \times 10^{-4}$
8	$-5.995758360037 \times 10^{-6}$	$-2.631285809207 \times 10^{-6}$

References

[1] H. V. Willett, K. J. Gibson and P. K. Browning. In *Proceedings of the 43rd EPS Conference on Plasma Physics*, page P2.042, 2016.

[2] H. V. Willett, J. Santoso, C. S. Corr and K. J. Gibson. In *Proceedings of the 44th EPS Conference on Plasma Physics*, page P2.402, 2017.

[3] J. Leddy, B. Dudson and H. V. Willett. *Nuclear Materials and Energy*, 12:994–998, 2017.

[4] J. Wesson. *Tokamaks*. Oxford University Press, 4th edition, 2011.

[5] ITER website, `http://www.iter.org`.

[6] F. F. Chen. *Introduction to plasma physics and controlled fusion*. Springer, 3rd edition, 2016.

[7] National Ignition Facility website, `https://lasers.llnl.gov/science/icf`.

[8] EUROfusion website, `http://www.euro-fusion.org`.

[9] I. H. Hutchinson. *Introduction to plasma physics*, Chapter 2, `http://silas.psfc.mit.edu/introplasma/chap2.html`.

[10] G. G. Dolgov-Savel'ev, V. S. Mukhovatov et al. *Soviet Physics JETP*, 11(2):287–295, 1960.

[11] E. Teller, editor. *Fusion*, volume 1, part A. Academic Press, 1981.

[12] M. Keilhacker, A. Gibson et al. *Nuclear Fusion*, 39(2):209–234, 1999.

[13] T. Casper, Y. Gribov et al. *Nuclear Fusion*, 54:013005, 2014.

[14] M. J. Singh, D. Boilson et al. *New Journal of Physics*, 19:055004, 2017.

[15] P. Franzen and U. Fantz. *Fusion Engineering and Design*, 89:2594–2605, 2014.

[16] Japan Atomic Energy Authority press release, 'Long-pulse control technique of neutral beam injector successfully developed', `https://www.jaea.go.jp/english/news/press/p2015073101/`.

[17] R. S. Hemsworth and T. Inoue. *IEEE Transactions on Plasma Science*, 33(6):1799–1813, 2005.

[18] E. Speth, H. D. Falter et al. *Nuclear Fusion*, 46:S220–S238, 2006.

[19] T. Eich, A. W. Leonard et al. *Nuclear Fusion*, 53:093031, 2013.

[20] A. Loarte, B. Lipschultz et al. *Nuclear Fusion*, 47:S203–S263, 2007.

[21] H. Bolt, V. Barabash et al. *Journal of Nuclear Materials*, 307-311:43–52, 2002.

[22] Y. Shimomura, M. Keilhacker, K. Lackner and H. Murmann. *Nuclear Fusion*, 23(7):869–879, 1983.

[23] P. C. Stangeby. *The plasma boundary of magnetic fusion devices*. Institute of Physics Publishing, 2000.

[24] G. F. Matthews. *Journal of Nuclear Materials*, 220-222:104–116, 1995.

[25] L. Buzi, G. De Temmerman et al. *Journal of Nuclear Materials*, 455:316–319, 2014.

[26] J. L. Barton, Y. Q. Wang et al. *Nuclear Instruments and Methods in Physics Research B*, 332:275–279, 2014.

[27] T. W. Morgan, T. M. de Kruif et al. *Plasma Physics and Controlled Fusion*, 56:095004, 2014.

[28] W. Horton, J. C. Perez, T. Carter and R. Bengtson. *Physics of Plasmas*, 12:22303–22308, 2005.

[29] A. D. Light, S. C. Thakur et al. *Physics of Plasmas*, 20:082120, 2013.

[30] G. R. Tynan, P. H. Diamond et al. *Plasma Physics and Controlled Fusion*, 51:124055, 2009.

[31] S. C. Thakur, M. Xu et al. *Physics of Plasmas*, 20:012304, 2013.

[32] G. R. Tynan, L. Schmitz et al. *Physics of Plasmas*, 1(10):3301–3307, 1994.

[33] E. Gravier, F. Brochard et al. *Physics of Plasmas*, 11(2):529–537, 2004.

[34] S. Jaeger, Th. Pierre and C. Rebont. *Physics of Plasmas*, 16:022304, 2009.

[35] C. Brault, A. Escarguel et al. *Physics Letters A*, 360:299–303, 2006.

[36] R. Chodura. *Physics of plasma-wall interactions in controlled fusion*, Chapter 4, page 113. Plenum Press, 1986.

[37] K. J. Gibson. Private communication, 2017.

[38] C. S. Pitcher and P. C. Stangeby. *Plasma Physics and Controlled Fusion*, 39:779–930, 1997.

[39] R. K. Janev, W. D. Langer, D. E. Post Jr. and K. Evans Jr. *Elementary processes in hydrogen-helium plasmas*. Springer-Verlag, 1987.

[40] D. R. Bates, A. E. Kingston and R. W. McWhirter. *Proceedings of the Royal Society of London Series A*, 267:297–312, 1962.

[41] J. Huba. *NRL plasma formulary*. Naval Research Laboratory, Washington DC, USA, 2016.

[42] S. I. Krasheninnikov, A. Yu. Pigarov, T. K. Soboleva and D. J. Sigmar. *Journal of Nuclear Materials*, 241–243:283–287, 1997.

[43] V. A. Soukhanovskii. *Plasma Physics and Controlled Fusion*, 59:064005, 2017.

[44] G. M. McCracken, M. F. Stamp et al. *Nuclear Fusion*, 38(4):619–629, 1998.

[45] A. V. Chankin, K. Itami and N. Asakura. *Plasma Physics and Controlled Fusion*, 44:A399–A405, 2002.

[46] B. Lipschultz, J. Goetz et al. *Journal of Nuclear Materials*, 220-222:50–61, 1995.

[47] J. Boedo, A. G. McLean, D. L. Rudakov and J. G. Watkins. *Plasma Physics and Controlled Fusion*, 60:044008, 2018.

[48] S. L. Allen, A. S. Bozek et al. *Plasma Physics and Controlled Fusion*, 37:A191–A202, 1995.

[49] D. Eldon, E. Kolemen et al. *Nuclear Fusion*, 57:066039, 2017.

[50] D. N. Hill. *Journal of Nuclear Materials*, 241-243:182–198, 1997.

[51] T. D. Rognlien, A. G. McLean et al. *Nuclear Materials and Energy*, 12:44–50, 2017.

[52] T. W. Petrie, J. M. Canik et al. *Nuclear Fusion*, 53:113024, 2013.

[53] J. Neuhauser, M. Alexander et al. *Plasma Physics and Controlled Fusion*, 37:A37–A51, 1995.

[54] M. Merola, F. Escourbiac et al. *Fusion Engineering and Design*, 89:890–895, 2014.

[55] S. Potzel, M. Wischmeier et al. *Nuclear Fusion*, 54:013001, 2014.

[56] P. Manz, S. Potzel et al. *Nuclear Materials and Energy*, 12:1152–1156, 2017.

[57] V. Nikolaeva, L. Guimarais et al. *Plasma Physics and Controlled Fusion*, 60:055009, 2018.

[58] S. Coda, J. Ahn et al. *Nuclear Fusion*, 57:102011, 2017.

[59] H. Reimerdes, J. Harrison et al. In *Proceedings of the 26th IAEA Fusion Energy Conference*, pages EX/2–3, 2016.

[60] G. Fishpool, J. Canik et al. *Journal of Nuclear Materials*, 438:S356–S359, 2013.

[61] E. Havlíčková, W. Fundamenski et al. *Plasma Physics and Controlled Fusion*, 55:065004, 2013.

[62] E. Havlíčková, J. Harrison et al. *Plasma Physics and Controlled Fusion*, 57:115001, 2015.

[63] D. Moulton, J. Harrison, B. Lipschultz and D. Coster. *Plasma Physics and Controlled Fusion*, 59:065011, 2017.

[64] N. Ohno. *Plasma Physics and Controlled Fusion*, 59:034007, 2017.

[65] W. L. Hsu, M. Yamada and P. J. Barrett. *Physical Review Letters*, 49(14):1001–1004, 1982.

[66] L. Schmitz, R. Lehmer et al. *Journal of Nuclear Materials*, 176-177:522–527, 1990.

[67] L. Schmitz, B. Merriman et al. *Physics of Plasmas*, 2(8):3081–3094, 1995.

[68] E. M. Hollmann, A. Yu. Pigarov et al. *Physics of Plasmas*, 9(4):1226–1232, 2002.

[69] S. I. Krasheninnikov, A. S. Kukushkin and A. A. Pshenov. *Physics of Plasmas*, 23:055602, 2016.

[70] N. Ohno, N. Ezumi et al. *Physical Review Letters*, 81(4):818–821, 1998.

[71] N. Ohno, K. Furuta and S. Takamura. *Journal of Plasma and Fusion Research*, 80(4):275–276, 2004.

[72] H. Tanaka, N. Ohno, Y. Tsuji and S. Kajita. *Contributions to Plasma Physics*, 50(3-5):256–266, 2010.

[73] S. Kado, S. Kajita et al. *Plasma Science and Technology*, 6(5):2451–2455, 2004.

[74] F. Scotti and S. Kado. *Journal of Nuclear Materials*, 390-391:303–306, 2009.

[75] E. M. Hollmann, D. G. Whyte et al. *Physics of Plasmas*, 8:3314–3320, 2001.

[76] S. Kado, H. Kobayashi, T. Oishi and S. Tanaka. *Journal of Nuclear Materials*, 313-316:754–758, 2003.

[77] M. G. Rusbridge, G. Sewell et al. *Plasma Physics and Controlled Fusion*, 42:579–602, 2000.

[78] K. J. Gibson, P. K. Browning et al. *Journal of Nuclear Materials*, 313-316:1253–1257, 2003.

[79] B. Mihaljčić, P. K. Browning and K. J. Gibson. *Physics of Plasmas*, 14:013501, 2007.

[80] J. W. Bradley, D. A. Forder and M. G. Rusbridge. *Plasma Sources Science and Technology*, 4:516–526, 1995.

[81] I. H. Hutchinson. *Principles of plasma diagnostics*. Cambridge University Press, 2002.

[82] P. C. Stangeby and G. M. McCracken. *Nuclear Fusion*, 30(7):1225–1379, 1990.

[83] R. L. Merlino. *American Journal of Physics*, 75(12):1078–1085, 2007.

[84] H. R. Griem. *Principles of plasma spectroscopy*. Cambridge University Press, 1997.

[85] B. Mihaljčić. *Studies of detached recombining plasmas in the UMIST Linear System.* PhD thesis, University of Manchester, 2004.

[86] J. R. Harrison, G. M. Fishpool et al. *Physics of Plasmas*, 22:092508, 2015.

[87] B. Law. *Statistical analysis of a linear plasma column.* Master's thesis, University of York, 2017.

[88] S. Lisgo. Private communication, 2014.

[89] L. C. Johnson and E. Hinnov. *Journal of Quantitative Spectroscopy and Radiative Transfer*, 13:333–358, 1973.

[90] D. Lumma, J. L. Terry and B. Lipschultz. *Physics of Plasmas*, 4:2555–2566, 1997.

[91] H. V. Willett and K. J. Gibson. Videos of plasma detachment in the York Linear Plasma Device, `https://doi.org/10.6084/m9.figshare.7207691`, 2018.

[92] G. Antar, S. Krasheninnikov et al. *Physical Review Letters*, 87:065001, 2001.

[93] H. Tanaka, N. Ohno et al. *Contributions to Plasma Physics*, 52(5-6):424–428, 2012.

[94] S. J. Zweben, W. M. Davis et al. *Nuclear Fusion*, 55:093035, 2015.

[95] J. A. Boedo, D. L. Rudakov et al. *Physics of Plasmas*, 10(5):1670–1677, 2003.

[96] R. Kube, O. E. Garcia et al. *Plasma Physics and Controlled Fusion*, 60:065002, 2018.

[97] O. E. Garcia, R. Kube et al. *Physics of Plasmas*, 25:056103, 2018.

[98] S. Chandrasekhar. *Hydrodynamic and hydromagnetic stability*, Chapter 11. Oxford University Press, 1961.

[99] F. Brochard, E. Gravier and G. Bonhomme. *Physics of Plasmas*, 12(6):1–7, 2005.

[100] D. L. Jassby. *Physics of Fluids*, 15(9):1590, 1972.

[101] W. Horton and J. Liu. *Physics of Fluids*, 27(8):2067–2075, 1984.

[102] M. Kono and M. Y. Tanaka. *Physical Review Letters*, 84(19):4369–4372, 2000.

[103] M. Matsukuma, Th. Pierre et al. *Physics Letters A*, 314:163–167, 2003.

[104] Th. Pierre, A. Escarguel et al. *Physical Review Letters*, 92:065004, 2004.

[105] Y. Hayashi, N. Ohno, S. Kajita and H. Tanaka. *Physics of Plasmas*, 23:012511, 2016.

[106] S. Christ-Koch, U. Fantz and M. Berger. *Plasma Sources Science and Technology*, 18(2):025003, 2009.

[107] S. Briefi and U. Fantz. *AIP Conference Proceedings*, 1515:278–283, 2013.

[108] J. Santoso, R. Manoharan, S. O'Byrne and C. S. Corr. *Physics of Plasmas*, 22:093513, 2015.

[109] B. D. Blackwell, J. F. Caneses et al. *Plasma Sources Science and Technology*, 21:055033, 2012.

[110] J. Santoso. Private communication, 2017.

[111] M. Light and F. F. Chen. *Physics of Plasmas*, 2:1084–1093, 1995.

[112] H. Kikuchi, Y. Sakawa and T. Shoji. *Journal of Plasma and Fusion Research*, 5:302–305, 2002.

[113] Y. Mori, H. Nakashima et al. *Plasma Sources Science and Technology*, 13:424–435, 2004.

[114] M. Bacal, G. W. Hamilton et al. *Review of Scientific Instruments*, 50(6):719–721, 1979.

[115] A. G. Nikitin, F. El Balghiti and M. Bacal. *Plasma Sources Science and Technology*, 5(1):37–42, 1996.

[116] M. Bacal. *Review of Scientific Instruments*, 71(11):3981–4006, 2000.

[117] R. C. Phillips and E. B. Turner. *Review of Scientific Instruments*, 36(12):1822–1825, 1965.

[118] E. T. Everson, P. Pribyl et al. *Review of Scientific Instruments*, 80:11305, 2009.

[119] J. Santoso, H. V. Willett and C. S. Corr. *Plasma Sources Science and Technology*, 2018. In press. DOI: 10.1088/1361-6595/aae705.

[120] A. Fruchtman. *Journal of Physics D: Applied Physics*, 50:473002, 2017.

[121] L. Liard, A. Aanesland and P. Chabert. *Journal of Physics D: Applied Physics*, 45:235201, 2012.

[122] T. H. Stix. *The theory of plasma waves.* McGraw-Hill, 1962.

[123] J. F. Caneses and B. D. Blackwell. *Plasma Sources Science and Technology*, 25:055027, 2016.

[124] S. I. Krasheninnikov and A. S. Kukushkin. *Journal of Plasma Physics*, 83:155830501, 2017.

[125] P. C. Stangeby. *Plasma Physics and Controlled Fusion*, 60:044022, 2018.

[126] J. Amorim, G. Baravian and J. Jolly. *Journal of Physics D: Applied Physics*, 33:R51–R65, 2000.

[127] B. D. Dudson, M. V. Umansky et al. *Computer Physics Communications*, 180(9):1467–1480, 2009.

[128] L. Easy, F. Militello et al. *Physics of Plasmas*, 21:122515, 2014.

[129] N. R. Walkden, L. Easy, F. Militello and J. T. Omotani. *Plasma Physics and Controlled Fusion*, 58:115010, 2016.

[130] F. Militello, B. Dudson et al. *Plasma Physics and Controlled Fusion*, 59:125013, 2017.

[131] B. W. Shanahan and B. D. Dudson. *Journal of Physics: Conference Series*, 561:012015, 2014.

[132] J. Leddy and B. Dudson. *Plasma Physics and Controlled Fusion*, 59:125011, 2017.

[133] D. A. D'Ippolito, J. R. Myra and S. J. Zweben. *Physics of Plasmas*, 18:060501, 2011.

[134] S. I. Krasheninnikov. *Physics Letters A*, 283(5-6):368–370, 2001.

[135] C. Marini, R. Agnello et al. *Nuclear Fusion*, 57:036024, 2017.